UNIVERSIDAD COMPLUTENSE DE MADRID
FACULTAD DE CIENCIAS QUÍMICAS

TESIS DOCTORAL

Design and synthesis of organic p-type semiconductors: toward efficient Perovskite Solar Cells

Diseño y síntesis de semiconductores orgánicos de tipo p: hacia células solares de Perovskita eficientes

MEMORIA PARA OPTAR AL GRADO DE DOCTOR

PRESENTADA POR

Javier Urieta Mora

Directores

Nazario Martín León
Agustín Molina Ontoria

Madrid

UNIVERSIDAD COMPLUTENSE DE MADRID

FACULTAD DE CIENCIAS QUÍMICAS

TESIS DOCTORAL

Design and synthesis of organic p-type semiconductors: Toward efficient Perovskite Solar Cells

Diseño y síntesis de semiconductores orgánicos de tipo p: hacia células solares de Perovskita eficientes

MEMORIA PARA OPTAR AL GRADO DE DOCTOR

PRESENTADA POR

Javier Urieta Mora

DIRECTORES

Nazario Martín León

Agustín Molina Ontoria

Madrid, 2020

UNIVERSIDAD COMPLUTENSE DE MADRID

FACULTAD DE CIENCIAS QUÍMICAS

Departamento de Química Orgánica

Design and synthesis of organic p-type semiconductors: Toward efficient Perovskite Solar Cells

Diseño y síntesis de semiconductores orgánicos de tipo p: hacia células solares de Perovskita eficientes

TESIS DOCTORAL

Javier Urieta Mora

Madrid, 2020

Design and synthesis of organic p-type semiconductors: Toward efficient Perovskite Solar Cells

Diseño y síntesis de semiconductores orgánicos de tipo p: hacia células solares de Perovskita eficientes

Directores:

Dr. Nazario Martín León

Dr. Agustín Molina Ontoria

Memoria para optar al grado de

DOCTOR EN CIENCIAS QUÍMICAS

que presenta

Javier Urieta Mora

Madrid, 2020

The results presented in this thesis have been published and listed below:

(1) I. Zimmermann, J. Urieta-Mora, P. Gratia, J. Aragó, G. Grancini, A. Molina-Ontoria, E. Ortí, N. Martín, M. K. Nazeeruddin, "High-Efficiency Perovskite Solar Cells Using Molecularly Engineered, Thiophene-Rich, Hole-Transporting Materials: Influence of Alkyl Chain Length on Power Conversion Efficiency", *Adv. Energy Mater.* **2017**, *7*, 1601674.

(2) I. García-Benito, I. Zimmermann, J. Urieta-Mora, J. Aragó, J. Calbo, J. Perles, A. Serrano, A. Molina-Ontoria, E. Ortí, N. Martín, M. K. Nazeeruddin, "Heteroatom Effect on Star-Shaped Hole-Transporting Materials for Perovskite Solar Cells", *Adv. Funct. Mater.* **2018**, *28*, 1801734.

(3) J. Urieta-Mora, I. García-Benito, A. Molina-Ontoria, N. Martín, "Hole transporting materials for perovskite solar cells: a chemical approach", *Chem. Soc. Rev.* **2018**, *47*, 8541-8571.

(4) J. Urieta-Mora, I. Zimmermann, J. Aragó, A. Molina-Ontoria, E. Ortí, N. Martín, M. K. Nazeeruddin "Dibenzoquinquethiophene- and Dibenzosexithiophene-Based Hole-Transporting Materials for Perovskite Solar Cells", *Chem. Mater.* **2019**, *31*, 6435–6442.

(5) J. Urieta-Mora, I. García-Benito, I. Zimmermann, J. Aragó, P. D. García-Fernández, G. Grancini, A. Molina-Ontoria, E. Ortí, N. Martín, M. K. Nazeeruddin, "Non-Planar and Flexible Hole-Transporting Materials from Bis-Xanthene and Bis-Thioxanthene Units for Perovskite Solar Cells", *Helv. Chim. Acta* **2019**, *102*, e1900056.

(6) J. Urieta-Mora, I. García-Benito, I. Zimmermann, J. Aragó, J. Calbo, G. Grancini, A. Molina-Ontoria, E. Ortí, N. Martín, M. K. Nazeeruddin, "Saddle-like, π-conjugated, cyclooctatetrathiophene-based, hole-transporting material for perovskite solar cells", *J. Mater. Chem. C* **2019**, *7*, 6656–6663.

(7) J. Urieta-Mora, M. Krug, W. Alex, J. Perles, I. Fernández, A. Molina-Ontoria, D. M. Guldi, N. Martín, "Homo and Hetero Molecular 3D Nanographenes Employing a Cyclooctatetraene Scaffold", *J. Am. Chem. Soc.* **2020**, *142*, 4162–4172.

(8) L. A. Illicachi, J. Urieta-Mora, J. Calbo, J. Aragó, C. Igci, I. García-Benito, C. Momblona, B. Insuasty, A. Ortiz, C. Roldán-Carmona, A. Molina-Ontoria, E. Ortí, N. Martín, M. K. Nazeeruddin, "Azatruxene-based, Dumbbell-shaped, Donor-π-bridge-Donor Hole-Transporting Materials for Perovskite Solar Cells", *Chem. Eur. J.* **2020**, *26*, 11039–11047.

List of publications not included in this thesis:

(9) I. García-Benito, I. Zimmermann, J. Urieta-Mora, J. Aragó, A. Molina-Ontoria, E. Ortí, N. Martín, M. K. Nazeeruddin, "Isomerism effect on the photovoltaic properties of benzotrithiophene-based hole-transporting materials", *J. Mater. Chem. A,* **2017**, *5*, 8317–8324.

(10) J. Urieta-Mora, I. García-Benito, I. Zimmermann, J. Aragó, A. Molina-Ontoria, E. Ortí, N. Martín, M. K. Nazeeruddin, "Tetrasubstituted Thieno[3,2-*b*]thiophenes as Hole-Transporting Materials for Perovskite Solar Cells", *J. Org. Chem.* **2020**, *85*, 1, 224-233.

Agradecimientos

El trabajo de esta Tesis Doctoral se ha realizado en el Departamento de Química Orgánica de la Universidad Complutense de Madrid y en el Laboratorio de Materiales Orgánicos de IMDEA Nanociencia bajo la dirección del Profesor Nazario Martín León y el Dr Agustín Molina Ontoria.

En primer lugar, me gustaría agradecer todo el trabajo realizado a mis directores:

Nazario, quiero agradecerte especialmente por darme la oportunidad de aprender y trabajar en tu grupo demostrándome siempre tu confianza. Desde el primer día de trabajo, he podido comprobar el amplio conocimiento y pasión por el mundo científico que transmites con entusiasmo al grupo. Ha sido un privilegio formar parte de este magnífico grupo, tanto en lo científico como en lo personal.

Agustín, quiero agradecerte todo lo que he aprendido trabajando contigo. Más allá de todo lo relacionado con la química que hemos realizado, me has formado como científico e investigador orientándome en la búsqueda bibliográfica, en el desarrollo de nuevas ideas, en la escritura de artículos o en el aprendizaje de nuevas técnicas y procedimientos. Siempre me has brindado tu confianza y eso me ha permitido dar lo mejor de mí.

En la realización de este trabajo han participado de manera sobresaliente otros grupos de investigación a los que agradezco enormemente su contribución:

En especial, al grupo de investigación del Prof. Mohammad Khaja Nazeeruddin de la Escuela Politécnica Federal de Lausanne (Suiza) por las medidas fotovoltaicas de las células solares de perovskita pero sobretodo, por darme la oportunidad de hacer una estancia en su grupo y aprender todo lo relacionado con la fabricación de dispositivos fotovoltaicos. Otra mención especial para el grupo de investigación del Prof. Enrique Ortí del Instituto de Ciencia Molecular, Universidad de Valencia (Paterna) que a través de cálculos teóricos nos han ayudado en la realización del trabajo durante mi Tesis Doctoral.

También dar las gracias a diferentes colaboradores como Javi y Zulay del servicio de resonancia de IMDEA Nanociencia, a Mª José, Maite y Josefina del Sidi de la Facultad de Ciencias Químicas de la Universidad Autónoma de Madrid y a los miembros de los distintos CAI de la Facultad de Ciencias Químicas de la Universidad Complutense de Madrid su gran ayuda y colaboración en la realización de los experimentos e interpretación de los resultados.

A continuación, me gustaría agradecer a todos los compañeros y amigos del laboratorio que he conocido estos años:

En primer lugar, a todos los miembros del grupo de Materiales Orgánicos Moleculares que han sido una ayuda inestimable durante estos años. A los químicos "mayores" del grupo: Mª Ángeles, Salvo, Beti, Carmen, David, Ángel y Andreas, y por supuesto a las secretarias Virginia y Ana que con su excepcional labor permiten que este grupo funcione. A toda la gente del laboratorio de la Complutense que siempre me han ayudado en lo personal y profesional, empezando por los doctorandos como Sara, Antonio, Rosa, Marina, Sonia, Valentina, Javi, Andrés, Alicia, Alfonso, Mikiko y Manu. Igualmente, a los doctores del grupo que han estado estos años como Marta, Laura, Chus, Paul, Rebeca, Justo, Javi y Silvia que nos han guiado para ser mejores científicos.

Al grupo de Santiago de la Moya, a Florencio, Beatriz y Josué que me introdujeron en el mundo de la investigación durante mi TFG y TFM. Mi especial gratitud para Esther, que me enseñó cómo trabajar en un laboratorio y a César, con el que he compartido grandes momentos que consiguieron que la investigación fuera el camino escogido.

A toda la gente que he conocido en IMDEA Nanociencia estos años como Emilio, José, Alberto, Alex, Leire, Sofía, Mariano, Julia, Estefanía, Arturo, Esther, etc, que siempre me han ofrecido su consejo y ayuda.

A toda la gente que conocí en Sion durante mi estancia que consiguieron que esos tres meses fueran un desafío profesional más sencillo gracias a su ayuda. En especial, mis agradecimientos para Cristina Momblona y Cristina Roldán que hacen una fantástica labor científica y me ayudaron mucho en mi estancia. No puedo olvidarme de mis apreciados Kim y Valentino que a pesar de sólo disfrutar con ellos un breve tiempo, me regalaron grandes experiencias que hicieron más fácil mi estancia.

Finalmente, mi gratitud más especial es para mis compañeros de IMDEA que han hecho que estos años de Tesis hayan sido maravillosos creando un ambiente fantástico en el laboratorio:

José, no solo aúnas ser un investigador excelente y buena persona. Además, consigues que trabajar a tu lado sea divertido a la vez que mejoras en muchos aspectos nuestra forma de trabajar. Sólo puedo desearte lo mejor para el futuro porque gente como tú merece llegar a lo más alto. Inés, desde que entré en el

laboratorio hasta en mi estancia en Suiza has sido una gran ayuda en lo personal y profesional. Mucho del trabajo que he desarrollado ha sido en colaboración contigo y por eso gran parte de esta Tesis es gracias a ti. Eider, gracias por todos los momentos compartidos estos años que han contribuido a mantener un gran ambiente de trabajo. Te deseo mucha suerte en el futuro que estoy seguro que terminará en una Tesis fantástica. También quiero acordarme de todos los que han hecho alguna estancia como Pedro, Álvaro, Luis o Mauricio. Todos habéis contribuido con vuestro trabajo a la realización de esta Tesis.

Rafa, mi compañero de vitrina, creo que eres la persona que cualquiera desearía tener a su lado en el trabajo. Eres un excelente e incansable trabajador, pero también tremendamente divertido y me has ayudado tanto con tus consejos, apoyo y buen humor que te has convertido en un gran amigo.

Agus, más allá de todo lo que ha supuesto que seas mi director y mentor científico, durante estos años te has convertido en un gran amigo y confidente. Me has aguantado en mis errores y en los tiempos no tan buenos, pero siempre has confiado en mí a la vez que seguías guiándome hacia nuevos éxitos. Has sido el espejo en el que fijarme para mejorar día a día y espero que mi trabajo sirva para ayudarte a llegar donde te mereces. De nuevo, gracias.

Y, para terminar, quiero agradecerle a mi familia todo su apoyo:

A mi tía Celia, Iñaki e Irene, por todo el cariño y ánimo que me han brindado estos años. A mis abuelos, por todo el cariño y dedicación con el que me criaron. Sé que allá donde estéis os sentiréis muy orgullosos.

A Azara, que siempre estás a mi lado, me has sufrido en el día a día con sus altibajos. Gracias a tu ánimo, apoyo y consejo has conseguido que este proyecto resulte más sencillo. Soy muy afortunado de tenerte a mi lado. Y por supuesto gracias a tu familia que me ha acogido como uno más demostrándome todo su apoyo, aprecio y cariño.

A mis padres, que siempre me han apoyado incondicionalmente. Siempre os habéis sacrificado día a día con vuestro esfuerzo y dedicación por mí, para que consiguiera todo lo que me propusiera y por ello, esta Tesis quiero dedicárosla especialmente a vosotros. Todo lo que he conseguido en mi vida os lo debo a vosotros.

TABLE OF CONTENTS

List of abbreviations and acronyms

The following terms have been used along the thesis:

2D - Two dimensional

3D - Three dimensional

ε - Molar extinction coefficient

δ - Chemical shift (ppm)

λ - Wavelength (nm) or reorganization energy

σ - Lateral conductivity (S cm^{-1})

AcOEt - Ethyl acetate

ATT - Anthratetrathiophene

a.u. - Arbitrary units

BHJ - Bulk-heterojunction

BTF - Benzotrifuran

BTP - Benzotripyrrole

BTSe - Benzotriselenophene

BTT - Benzotrithiophene

BTX - Bisthioxanthene

BX - Bisxanthene

ca. - Around, about, approximately

CD - Circular dichroism

CIGS - Copper indium gallium selenide solar cells

ClPh - Chlorobenzene

CoPh - Cyclooctatetraphenylene

CoTh - Cyclooctatetrathiophene

CV - Cyclic voltammetry

D-A - Donor-acceptor

DBQT - Dibenzoquinquethiophene

DBST - Dibenzosexithiophene

DCE - 1,2-Dichloroethane

DCM - Dichloromethane

DDQ- 2,3-dichloro-5,6-dicyanobenzoquinone

DFT - Density functional theory

DMF - *N,N*-Dimethylformamide

DMSO - Dimethyl sulfoxide

DPA - *p*-methoxydiphenylamine

DPV - Differential pulse voltammetry

DSC - Differential scanning calorimetry

DSSC - Dye-sensitized solar cells

DTP - Dithieno[3,2-*b*:2′,3′-*d*]pyrrole

$E^{0\text{-}0}$ - Optical band gap

$E_{1/2}$ - Half-wave potential

E_{HOMO} - HOMO energy

E_{LUMO} - LUMO energy

E^{ox} - Oxidation potential

EDOT - 3,4-Ethylenedixoythiophene

Eq - Equation

ESI - Electrospray ionization

ETM - Electron-transporting layer

ETM - Electron-transporting material

eV - Electron-volt

Fc - Ferrocene

FF - Fill factor

FK-102 - Tris(2-(1*H*-pyrazol-1-yl)pyridine)cobalt (II) bis(hexafluorophosphate)

FK-209 - Tris (2-(1*H*-pyrazol-1-yl)-4-*tert*-butylpyridine) cobalt (II) di[bis(trifluoromethane) sulfonimide]

FTIR - Fourier transform infrared spectroscopy

FTO - Fluorine-doped tin oxide

HOMO - Highest occupied molecular orbital

HPLC - High-performance liquid chromatography

HRMS - High-resolution mass spectrometry

HTL - Hole-transporting layer

HTM - Hole-transporting material

ITO - Indium-tin oxide

J - Coupling constant in Hz

J_{sc} Short-circuit current

J-V - Current density-voltage

Li-TFSI - Lithium bis(trifluoromethanesulfonyl)imide

LUMO - Lowest unocuppated molecular orbital

MALDI - Matrix-assisted laser desorption/ionization

$MeNO_2$ - Nitromethane

NaO^tBu - Sodium tert-butoxide

NBS - *N*-Bromosuccinimide

NG- Nanographene

NHE - Standard hydrogen electrode

NMR - Nuclear magnetic resonance spectroscopy

ODCB - 1,2-Dichlorobenzene

OFET - Organic field-effect transistor

OLED - Organic light-emitting diode

OPV - Organic photovoltaic

Pc - Phthalocyanine

PCE - Power conversion efficiency

PL - Photoluminescence

POZ - Phenoxazine

ppm - Parts-per million

PSCs - Perovskites solar cells

PTAA - Poly[bis(4-phenyl)(2,4,6-trimethylphenyl)amine]

PTZ - Phenothiazine

PVK - perovskite

rpm - Revolutions per minute

r.t. - Room temperature

SCLC - Space charge-limited current measurements

SEM - Scanning Electron Microscopy

spiro-OMeTAD - 2,2',7,7'-Tetrakis[*N*,*N*-di(4-methoxyphenyl)amino]-9,9'-spirobifluorene

TAT - Triazatruxene

$TBAPF_6$ - Tetrabutylammonium hexafluorophosphate

t-Bu - *Tert*-butyl

t-BP - 4-*Tert*-butylpiridine

T_{dec} - Decomposition temperature

T_g - Glass transition temperature

T_m - Melting temperature

TfOH - Trifluoromethanesulfonic acid

TGA - Thermogravimetric analysis

THF - Tetrahydrofuran

TLC - Analytical thin layer chromatography

TMS - Trimethylsilyl

TOF - Time of fly

TPA (TPA-OMe) - *p*-methoxytriphenylamine

UV-Vis - Ultraviolet-visible spectroscopy

V - Voltage or Volt

V_{oc} - Open circuit voltage

Summary

Introduction

Perovskite solar cells (PSCs) have become one of the most promising technologies for searching clean alternatives to fossil fuels in order to achieve a sustainable society taking advantage of the unlimited solar energy. In a few years of research, PSCs have reached promising efficiencies up to 25% which are comparable to the commercial silicon-based cells. As a means to improve the efficiencies and the stability of PSCs, the research has been closely connected to the design of highly efficient charge selective layers such as electron (ETMs) and hole-transporting materials (HTMs). Although the charge selective layer could present either inorganic or polymeric structures, organic-based small molecules have been demonstrated as the most promising alternative for the preparation of highly efficient PSCs.

Objectives

The main objective is this thesis is focused on the chemical design, synthesis and characterization of small organic molecules for its application as hole-transporting materials for perovskite solar cells. The new synthesized HTMs should compete in terms of efficiency with the benchmark spiro-OMeTAD, but with an easy attainable synthetic route for low-cost applications. As a means to design new small organic molecules for hole-transporting applications, some requirements must be followed. In this regard, an adequate HOMO energy, solubility or high conductivity and/or hole mobility should be taken into account to achieve highly efficient solar cells.

Results and discussion

1) Synthesis of HTMs based on chalcogen-rich based cores such as anthratetrathiophene (ATT), dibenzoquinquethiophene (DBQT), dibenzosexithiophene (DBST), cyclooctatetrathiophene (CoTh) and benzotriselenophene (BTSe)

This section includes the synthesis and characterization of different molecules with a common chemical design incorporating planar chalcogen-rich cores such as ATT, DBQT, DBST or BTSe endowed with electron-donor units of *p*-methoxytriphenylamine to ensure a suitable HOMO energy for the use of these

molecules as HTMs in PSCs. (**Figure S1**) Furthermore, a non-planar saddle-shaped molecule based on cyclooctatetrathiophene (CoTh) was also prepared following the same chemical approach. The new molecules were spectroscopically characterized, and its opto-electronic and thermal properties were investigated using standard techniques along with theoretical calculations, revealing their promising features to be implemented as HTMs for PCSs.

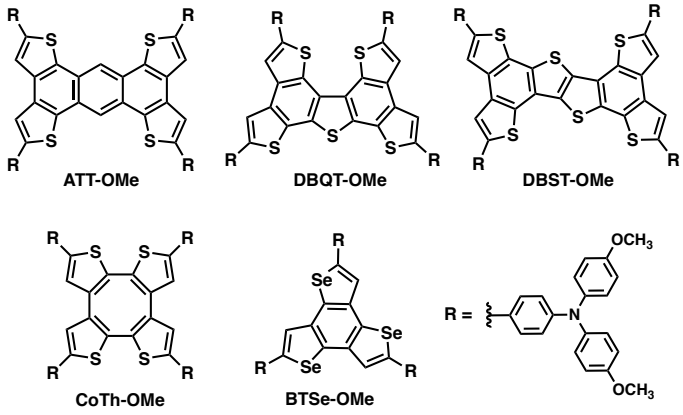

Figure S1. Chemical structure of chalcogen-rich HTMs.

In the case of ATT-based HTMs, different triphenylamines were attached in the periphery of the molecule varying the length of the alkyl chain from methoxy to butoxy, hexyloxy and decyloxy substituents. The opto-electronic properties of the corresponding HTMs were not affected by the different alkyl chain. However, as it is expected, the thermal behavior and the solubility of the HTMs were modified with the length of the alkyl chain. In combination with $[FAPbI_3]_{0.85}[MAPbBr_3]_{0.15}$-based perovskite, methoxy and butoxy-substituted ATTs reached the best power conversion efficiencies (PCEs) of 18.13 and 17.28% respectively while reduced values were measured for hexyloxy and decyloxy derivatives (**Figure S2**).

Polycyclic dibenzoquinquethiophene (DBQT) and dibenzosexithiophene (DBST) were used as scaffold for the preparation of two HTMs with a sulfur-rich structure, modifying the optical and electrochemical properties of the molecules (**Figure S1**). PSCs devices incorporating **DBQT-OMe** and **DBST-OMe** as HTMs and $[FAPbI_3]_{0.85}[MAPbBr_3]_{0.15}$-based perovskite achieved a

maximum PCE of 18.08 and 14.27% respectively (**Figure S2**). The different photovoltaic performance were attributed to the different solubility of the HTMs which allow the preparation of homogeneous films in the case of **DBQT-OMe** but not for **DBST-OMe**, which limits its photovoltaic response.

In order to preserve the sulfur-rich approach but increasing the solubility of the material that was found critical in the previous case, a non-planar sulfur-rich cores such as cyclooctatetrathiophene (CoTh) was used as framework endowed with *p*-methoxytriphenylamines. Despite the increased solubility and processability in the preparation of PSC devices, **CoTh-OMe** exhibited a reduced value of PCE of 16.30% that was ascribed to its high reorganization energy calculated by theoretical calculations and low conductivity found in OFETs devices incorporating **CoTh-OMe** (**Figure S2**).

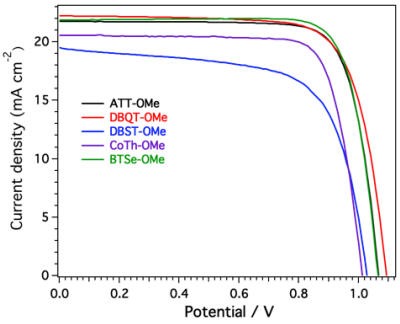

HTMs	V_{oc} (V)	J_{sc} (mA cm^{-2})	*FF*	PCE (%)
ATT-OMe	1.07	21.75	0.78	18.13
DBQT-OMe	1.09	22.23	0.74	18.08
DBST-OMe	1.03	19.68	0.71	14.27
CoTh-OMe	1.01	20.56	0.78	16.30
BTSe-OMe	1.07	21.88	0.80	18.50

Figure S2. *J-V* curves of the different chalcogen rich HTMs and its corresponding photovoltaic parameters measured for the champion device.

As a modification of the use of sulfur-based cores, a selenium-based benzotriselenophene core (BTSe) was selected to evaluate the influence of the heteroaromatic scaffold in comparison to previously reported sulfur, nitrogen and oxygen-based isostructural molecules (**Figure S1**). The impact that the heteroatom-containing central scaffold has on the electrochemical and photophysical properties, as well as on the photovoltaic performance, is systematically investigated. The isostructural HTMs exhibit suitable HOMO energy levels regarding the valence band of the perovskite, which ensure efficient hole extraction at the perovskite/HTM interface. Selenium-containing **BTSe-OMe** highlighted as the most promising HTMs among the chalcogen-based molecules with a remarkable PCE of 18.50% which surpassed its

isostructural derivatives and the reference compound of spiro-OMeTAD.

2) Synthesis of HTMs based on spiro-cyclic cores

In this section, the synthesis and characterization of spiro-containing molecules are selected as alternative to the previously prepared planar HTMs in order to achieve similar performances to the spiro-based benchmark HTM, namely spiro-OMeTAD (**Figure S3**). Spiranic-based molecules have been reported as successful choices for the design of efficient HTMs. On the one hand, two new molecules (**spiro-POZ-OMe** and **spiro-PTZ-OMe**) were synthesized and characterized using a spiro-linkage between the well-known donor frameworks phenoxazine or phenothiazine and *p*-methoxydiphenylamino-substituted fluorene. Despite the incorporation of phenoxazine or phenothiazine units into the central core in comparison to the orthogonal 9,9'-spirobifluorene, the optical and electrochemical features of **spiro-POZ-OMe** and **spiro-PTZ-OMe** are not modified in comparison to the benchmark spiro-OMeTAD. The incorporation of **spiro-POZ-OMe** and **spiro-PTZ-OMe** into mesoporous devices rendered maximum PCEs of 16.67 and 17.28% respectively, considerably lower than that measured for spiro-OMeTAD. As an alternative, planar devices were also fabricated showing an improvement in the efficiency for **spiro-POZ-OMe** (18.14 %) and **spiro-PTZ-OMe** (18.36%).

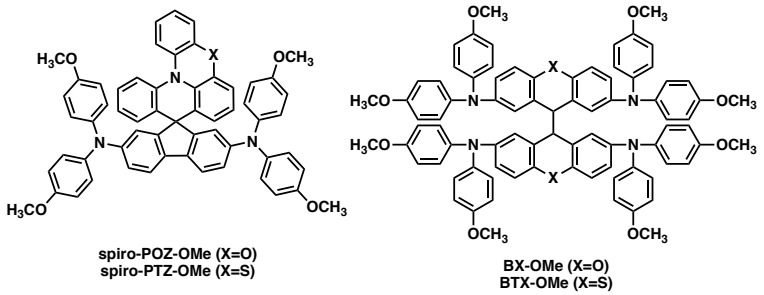

Figure S3. Chemical structure of spiro-containing (**spiro-POZ-OMe** and **spiro-PTZ-OMe**) and "spiro-like" HTMs (**BX-OMe** and **BTX-OMe**).

On the other hand, the chemical approach for the preparation of **BX-OMe** and **BTX-OMe** involves the use of covalent central C-C bond which connects the two halves of a *p*-methoxydiphenylamino-substituted xanthene or thioxanthene

units connected through sp^3-hybridized carbon atoms. This strategy renders a more flexible conformation than those of spiro-based structures providing a gradual change of the rigidity of the 3D molecular arrangement. The new HTMs display a limited absorbance in the visible region, due to the lack of conjugation between the two molecular halves, and the chemical design used has a remarkably impact on the thermal properties when compared to spiro-OMeTAD. **BX-OMe** and **BTX-OMe** have been tested in triple cation perovskite-based PSC devices exhibiting power conversion efficiencies of 14.19 and 16.55%, respectively which were notably lower than those measured for spiro-OMeTAD (19.63 %).

3) Synthesis of HTMs based on nitrogen-containing triazatruxene (TAT)

The implementation of nitrogen-based heterocycles such as carbazole, indolo[3,2-*b*]indole or indolo[3,2-*b*]carbazole as central scaffold for the synthesis of efficient HTMs have been widely reported in the bibliography during last years. One of the most highlighted nitrogen-containing heterocycles is 5*H*-diindolo[3,2-*a*:3',2'-*c*]carbazole, also known as triazatruxene (TAT), which consist on 3 units of indole fused to a central benzene ring. In this section, three new derivatives using TAT as electron-donor frameworks connected through different π-conjugated EDOT units were synthesized as it is shown in **Figure S4**. The opto-electronic properties of the DTTXs derivatives were influenced by the different linkages between the TAT units and the central EDOT. Red-shifted absorption, emission and, a stronger donor ability were observed passing from **DTTX-1** to **DTTX-2** due to the extended conjugation. In contrast, in **DTTX-3**, D-A-D system characteristics are observed with the acceptor azomethine bond and the donor TAT units, showing a charge transfer band and low-lying HOMO energy. The evaluation of the hole-transporting ability of the DTTXs family was carried out through the preparation of mesoporous PSCs devices using the state-of-art triple cation perovskite ($[(FAPbI_3)_{0.87}(MAPbBr_3)_{0.13}]_{0.92}[CsPbI_3]_{0.08}$). A remarkable PCE of 18.30% was measured for **DTTX-2** derivative which was slightly lower than that measured for the reference of spiro-OMeTAD (18.92%). In contrast, **DTTX-1** and **DTTX-3** presented reduced values for PCE of 17.48 and 12.68% respectively.

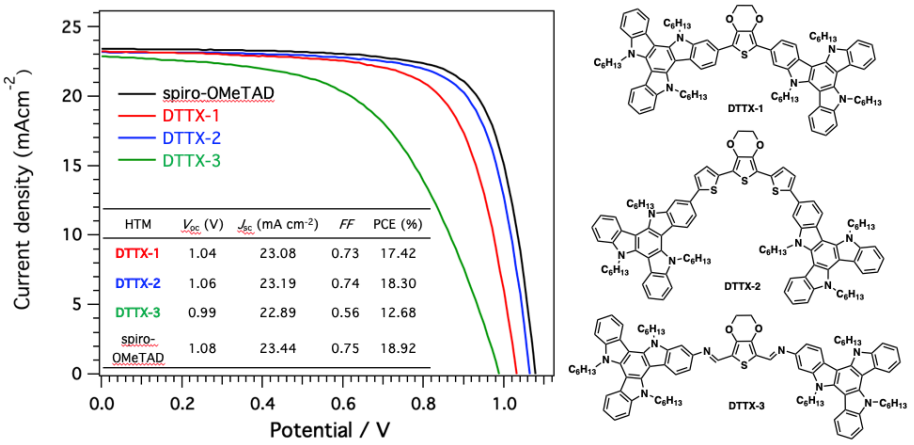

HTM	V_{oc} (V)	J_{sc} (mA cm^{-2})	*FF*	PCE (%)
DTTX-1	1.04	23.08	0.73	17.42
DTTX-2	1.06	23.19	0.74	18.30
DTTX-3	0.99	22.89	0.56	12.68
spiro-OMeTAD	1.08	23.44	0.75	18.92

Figure S4. Chemical structure of TAT-based HTMs and its photovoltaic performance.

4) Synthesis of HTMs based molecular nanographene units (CoPh-NG and CoTh-NG)

The synthesis of molecular nanographene with well-defined chemical structures and thus, its opto-electronic properties, have become an important approach for the preparation of carbon-based functional materials in electronic applications such as photovoltaics. In this section, the syntheses of two molecular nanographenes with a saddle-shaped structure conferred by the central scaffolds of cyclooctatetraphenylene (CoPh) and cyclooctratetrathiophene (CoTh) are reported (**Figure S5**). The saddle-shaped cores were functionalized in the periphery with tert-butyl-substituted hexabenzocoronenes, which represents the minimum fragment for constituting a molecular nanographene, following a straightforward synthesis. The resulting saddle-like structures of **CoPh-NG** and **CoTh-NG** are electron-rich and show good chemical and electrochemical stability. Their molecular structures were fully elucidated using single-crystal X-ray crystallography. From their crystal structure analysis was concluded that both molecular nanographenes are chiral and crystallize as a racemic mixture, which were separated using chiral HPLC in the case of **CoPh-NG**, confirming the enantiomeric nature by the mirror image of the circular dichroism (CD) spectra.

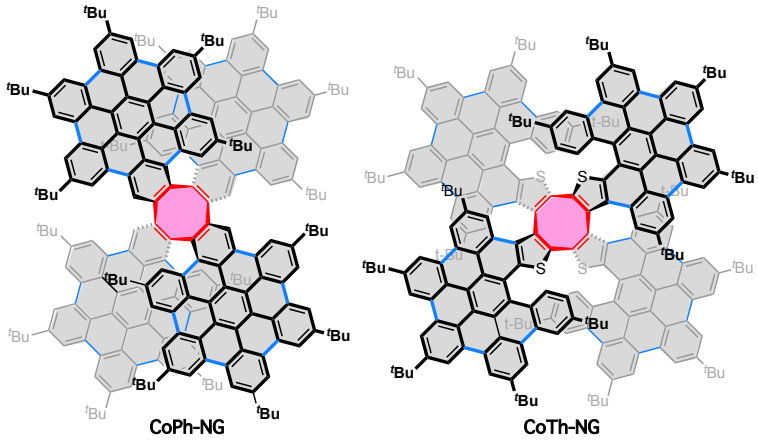

Figure S5. Chemical structure of molecular nanographenes **CoPh-NG** and **CoTh-NG**.

Conclusions

A collection of new small organic molecules focusing on low-cost and easy attainable syntheses for the design of new hole-transporting materials for perovskite solar cells have been prepared along this thesis. As a result, we have studied the influence of different central π-conjugated scaffolds functionalized with electron-donor groups in the photovoltaic response. As a general conclusion, a compromise between the thermal and opto-electronic properties of the HTMs such as solubility, molecular packing, conductivity or film morphology should be reached for maximizing the performance of the HTMs in perovskite solar cells.

Resumen

Introducción

Las células solares de perovskita (PSCs) se han convertido en una de las tecnologías más prometedoras en la búsqueda de alternativas limpias a los combustibles fósiles para alcanzar una sociedad sostenible aprovechando la energía solar ilimitada. En pocos años de investigación, PSCs han alcanzado eficiencias prometedoras por encima del 25% que son comparables a las células solares comerciales basadas en silicio. Con el fin de mejorar las eficiencias y la estabilidad de las PSCs, la investigación también ha estado relacionada con el diseño de capas selectivas de carga de alta eficiencia como los transportadores de electrones (ETMs) y de huecos (HTMs). Aunque las capas selectivas de carga pueden presentar una estructura inorgánica o polimérica, las moléculas orgánicas pequeñas han demostrado ser las alternativas más prometedoras para la preparación de PSCs de alta eficiencia.

Objetivos

El principal objetivo de esta tesis se centra en el diseño químico, la síntesis y caracterización de moléculas orgánicas pequeñas para su aplicación como materiales transportadores de huecos para células solares de perovskita con el fin de competir en términos de eficiencia con el material de referencia de spiro-OMeTAD, pero con una ruta sintética más fácilmente alcanzable para aplicaciones de bajo coste. Con el fin de diseñar nuevas moléculas orgánicas pequeñas, se deben tener en cuenta distinto requisitos como una energía del HOMO adecuada, la solubilidad o altas conductividades y/o movilidad de huevos para alcanzar células solares de alta eficiencia.

Resultados y discusión

1) Síntesis de HTMs basados en núcleos ricos en calcogenuros como antratetratiofeno (ATT), dibenzopentatiofeno (DBQT), dibenzohexatiofeno (DBST), ciclooctatetratiofeno (CoTh) y benzotriselenofeno (BTSe)

En esta sección se incluye la síntesis y caracterización de diferentes moléculas con un diseño químico común incorporando núcleos planos ricos en calcogenuros como son ATT, DBQT, DBST o BTSe funcionalizados con unidades electron-donadores de para-metoxitrifenilamina para asegurar una

energía del HOMO adecuada para el uso de estas moléculas como HTMs en PSCs (**Figura S1**). Además, una molécula no plana con forma de silla de montar basada en ciclooctatetratiofeno (CoTh) fue también preparada siguiendo la misma aproximación química. Las nuevas moléculas fueron caracterizadas de manera espectroscópica y sus propiedades ópticas, electrónicas y térmicas fueron investigadas utilizando técnicas estándar con la ayuda de cálculos teóricos, revelando sus prometedoras propiedades para ser implementadas como HTMs en PSCs.

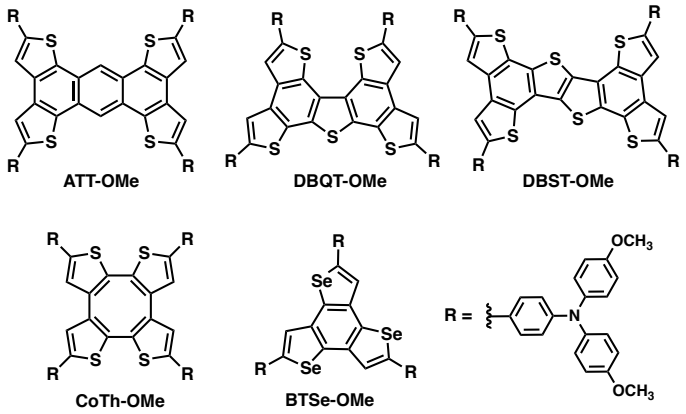

Figura S1. Estructura química de los HTM ricos en calcogenuros.

En el caso de los HTMs basados en ATT, diferentes trifenilaminas fueron acopladas en la periferia de las moléculas variando la longitud de las cadenas alquílicas desde sustituyentes metoxi a butoxi, hexiloxi o deciloxi. Las propiedades ópticas y electrónicas de los correspondientes HTMs no se vieron afectadas por las diferentes cadenas alquílicas. Sin embargo, como es esperable, el comportamiento térmico y la solubilidad de los HTMs fue modificado con la variación en la longitud de las cadenas alquílicas. En combinación con la perovskita $[FAPbI_3]_{0.85}[MAPbBr_3]_{0.15}$, los derivados de ATT sustituidos con grupos metoxi y butoxi alcanzaron las mejores eficiencias en la conversión de energía (PCEs) de 18.13 y 17.28% respectivamente, mientras que valores más reducidos fueron medidos para los derivados de hexiloxi y deciloxi (**Figura S2**).

Los policiclos dibenzopentatiofeno (DBQT) y dibenzohexatiofeno (DBST) fueron utilizados como núcleo para la preparación de dos nuevos HTMs con una

estructura rica en azufre, modificando las propiedades ópticas y electroquímicas de las moléculas (**Figura S1**). Los dispositivos de PSCs incorporando **DBQT-OMe** y **DBST-OMe** como HTMs y la perovskita $[FAPbI_3]_{0.85}[MAPbBr_3]_{0.15}$ alcanzaron una máxima eficiencia de 18.08 y 14.27% respectivamente (**Figura S2**). La diferencia en el rendimiento fotovoltaico fue atribuida a la diferencia en la solubilidad de los HTMs que permite la preparación de capas homogéneas en el caso de **DBQT-OMe** pero no para **DBST-OMe**, lo que limita su respuesta fotovoltaica.

Con la idea de preservar el diseño de moléculas ricas en azufre, pero aumentar la solubilidad de los materiales que se observó como un punto clave en el caso anterior, una molécula rica en azufre y carente de planaridad como ciclooctatetratiofeno (CoTh) fue utilizada como fragmento central funcionalizado con *para*-metoxitrifenilamina. A pesar del aumento de solubilidad y de la procesabilidad para la preparación de dispositivos de PSCs, **CoTh-OMe** mostró un valor reducido de PCE del 16.30% que fue asignado a la alta energía de reorganización estimada por cálculos teóricos y su baja conductividad encontrada en dispositivos OFETs incorporando **CoTh-OMe** (**Figura S2**).

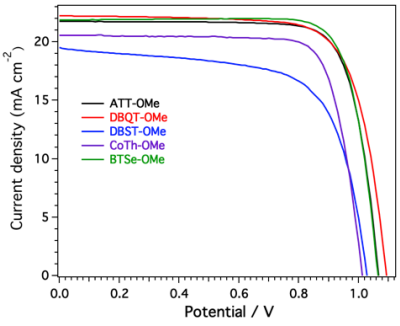

HTMs	V_{oc} (V)	J_{sc} (mA cm^{-2})	*FF*	PCE (%)
ATT-OMe	1.07	21.75	0.78	18.13
DBQT-OMe	1.09	22.23	0.74	18.08
DBST-OMe	1.03	19.68	0.71	14.27
CoTh-OMe	1.01	20.56	0.78	16.30
BTSe-OMe	1.07	21.88	0.80	18.50

Figura S2. Curvas *J-V* de los diferentes HTMs ricos en calcogenuros y sus correspondientes parámetros fotovoltaicos medidos en los mejores dispositivos.

Como una alternativa al uso de fragmentos ricos en azufre, un fragmento rico en selenio como el benzotriselenofeno (BTSe) fue seleccionada para evaluar la influencia del fragmento heterocíclico en comparación las moléculas con la misma estructura basadas en azufre, nitrógeno y oxígeno que fueron preparadas

con anterioridad (**Figura S1**). **BTSe-OMe** destacó como el HTM más prometedor entre las moléculas ricas en calcogenuros con una eficiencia notable del 18.50% que superó a los derivados con su misma estructura y la referencia de spiro-OMeTAD.

2) Síntesis de HTMs basados en fragmentos espiránicos

En esta sección, la síntesis y caracterización de moléculas que continenen unidades espiránicas fue seleccionada como alternativa a los HTMs planos preparados en la sección anterior con el fin de alcanzar rendimientos fotovoltaicos similares a los del compuesto de referencia de con fragmentos espiránico conocido como spiro-OMeTAD (**Figura S3**). Por un lado, dos nuevas moléculas (**spiro-POZ-OMe** y **spiro-PTZ-OMe**) fueron sintetizadas y caracterizadas usando un enlace espiránico entre los fragmentos conocidos de fenoxazina y fenotiazina y las unidades de fluoreno sustituidos con *para*-metoxidifenilamina. A pesar de la incorporación de unidades de fenoxazina y fenotiazina en el fragmento central en comparación al fragmento ortogonal de 9,9'-espirodifluoreno, las características ópticas y electroquímicas de **spiro-POZ-OMe** y **spiro-PTZ-OMe** no fueron modificadas con respecto al spiro-OMeTAD. La inclusión de **spiro-POZ-OMe** y **spiro-PTZ-OMe** en dispositivos mesoporosos proporcionó unas máximas PCEs de 16.67 y 17.28% respectivamente, que fueron considerablemente menores de las medidas para spiro-OMeTAD. Como alternativa, dispositivos planares de perovskita fueron fabricados mostrando una mejora en la eficiencia en el caso de **spiro-POZ-OMe** (18.14 %) y de **spiro-PTZ-OMe** (18.36 %).

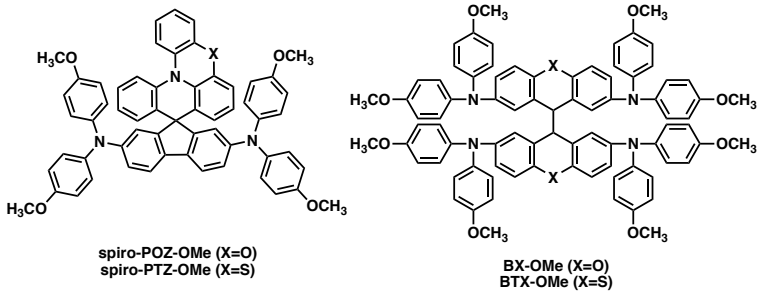

Figura S3. Estructura química de los HTMs incorporando enlaces espiránicos (**spiro-POZ-OMe** y **spiro-PTZ-OMe**) y semi-espiránicos (**BX-OMe** y **BTX-OMe**).

Por otro lado, el diseño químico para la preparación de **BX-OMe** y **BTX-OMe** involucra el uso de un enlace covalente C-C que conecta las dos mitades de xanteno o tioxanteno sustituidas con *para*-metoxidifenilaminas unidas a través de átomos de carbonos con hibridación sp^3 (**Figura S3**). Esta estrategia confiere una conformación más flexible que la que presentan las estructuras espiránicas proporcionando un cambio gradual en la rigidez de la estructura molecular en 3D. Los nuevos HTMs mostraron una absorbancia limitada en la región del visible debido a la falta de conjugación entre las dos mitades de la molécula, y el diseño químico utilizado tuvo un marcado impacto en las propiedades térmicas en comparación al spiro-OMeTAD. **BX-OMe** y **BTX-OMe** fueron probados en dispositivos en combinación con la perovskita triple catiónica alcanzando valores de PCEs de 14.19 y 16.55% respectivamente, que fueron notablemente menores de los medidos en el spiro-OMeTAD (19.63%).

3) Síntesis de HTMs basados en triazatruxeno (TAT)

La implementación de heterociclos basados en nitrógeno como son el carbazol, indolo[3,2-*b*]indol o el indolo[3,2-*b*]carbazol como fragmentos centrales para la síntesis de HTMs eficientes ha sido ampliamente publicada en la bibliografía durante los últimos años. Uno de los heterociclos que contienen nitrógeno más destacados es el 5*H*-diindolo[3,2-*a*:3',2'-*c*]carbazol, más conocido como triazatruxeno (TAT), que consiste en tres unidades de indol fusionadas a un anillo central de benceno. En esta sección, tres nuevos derivados utilizando TAT como fragmentos electrodonadores unidos a través de diferentes fragmentos de EDOT π-conjugados fueron sintetizados como se muestra en la **Figura S4**. Las propiedades ópticas y electrónicas de los derivados de DTTXs fueron influenciadas por los diferentes conectores entre las unidades de TAT y la unidad central de EDOT. Por un lado, se observó una absorción y emisión desplazada al rojo y un carácter electron-donador más fuerte al aumentar la conjugación entre el **DTTX-1** y **DTTX-2** mientras que en el caso de **DTTX-3**, se observaron las características de un sistema D-A-D entre el enlace aceptor de azometina y las unidades donadoras de TAT, mostrando una banda de transferencia de carga y una energía del HOMO más baja. La evaluación de la habilidad del transporte de huecos de la familia de los DTTXs fue realizada a través de la preparación de dispositivos mesoporosos de PSCs utilizando la perovskita triple catiónica ($[(FAPbI_3)_{0.87}(MAPbBr_3)_{0.13}]_{0.92}[CsPbI_3]_{0.08}$). Una eficiencia notable del 18.30%

fue medida para el derivado de **DTTX-2** que fue ligeramente inferior a la medida para la referencia de spiro-OMeTAD (18.92%). Por el contrario, **DTTX-1** y **DTTX-3** mostraron valores más reducidos de eficiencia del 17.48 y 12.68% respectivamente.

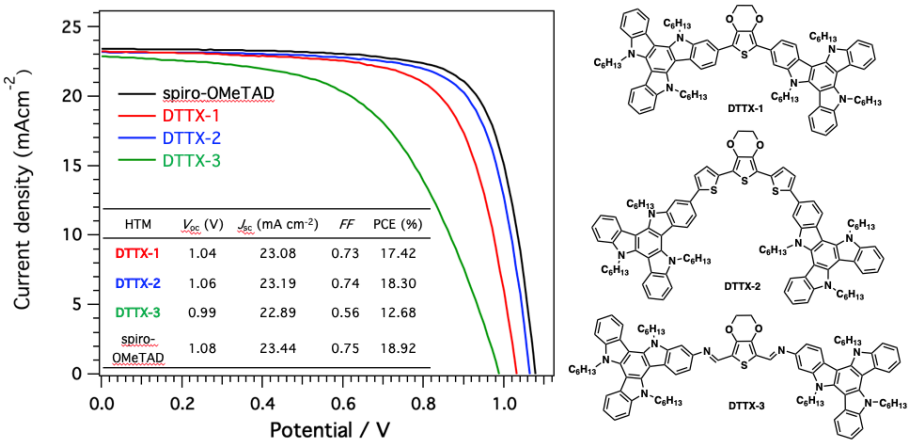

Figura S4. Estructuras químicas de los HTMs basados en TAT y su respuesta fotovoltaica.

4) Síntesis de HTMs basados en unidades de nanografenos moleculares (CoPh-NG y CoTh-NG)

La síntesis de nanografenos moleculares con estructuras químicas bien definidas y, por tanto, sus propiedades ópticas y electrónicas, se ha convertido en una de las aproximaciones para la preparación de materiales funcionales basados en carbono para aplicaciones electrónicas como las fotovoltaicas. En esta sección, se describe la síntesis de dos nanografenos moleculares con una estructura en forma de silla promovida por los fragmentos centrales de ciclooctatetrafenileno (CoPh) y ciclooctatetratiofeno (CoTh) (**Figura S5**). El núcleo en forma de silla fue funcionalizado en su periferia siguiendo una síntesis sencilla con unidades de hexabenzocoroneno sustituidos con grupos *tert*-butilo, que representa el mínimo fragmento para constituir un nanografeno molecular. Las estructuras resultantes en forma de silla de **CoPh-NG** y **CoTh-NG** son ricas en electrones y muestran buena estabilidad química y electroquímica. Las estructuras moleculares fueron completamente elucidadas por medio de difracción de rayos

X de monocristal. A través del análisis de sus estructuras cristalinas, se concluyó que ambos nanografenos moleculares son quirales y cristalizan como una mezcla racémica, que pudo ser separada utilizando HPLC quiral en el caso de **CoPh-NG**, confirmándose su carácter de enantiómeros por su imagen especular en el espectro de dicroísmo circular (CD).

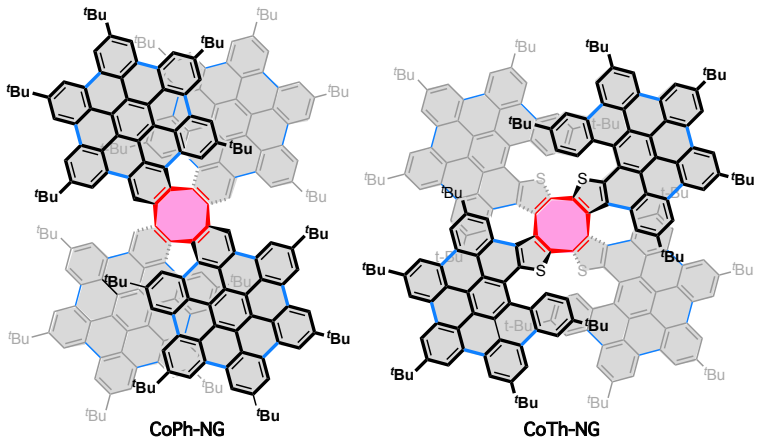

Figura S5. Estructura química de los nanografenos molecualres **CoPh-NG** y **CoTh-NG**.

Conclusiones

A lo largo de la tesis se ha preparado na colección de nuevas moléculas orgánicas pequeñas buscando síntesis fácilmente alcanzables y de bajo coste para el diseño de nuevos materiales transportadores de huecos para células solares de perovskita. Como resultado, a lo largo de esta tesis se ha estudiado la influencia de diferentes fragmentos centrales π-conjugados funcionalizados con grupos electron-donadores en la respuesta fotovoltaica. Como conclusión general, se debe alcanzar un compromiso entre las propiedades térmicas y optoelectrónicas de los HTM como la solubilidad, el empaquetamiento molecular, la conductividad o la morfología de las capas para maximizar la eficiencia de los HTMs en células solares de perovskita.

Introduction

2. INTRODUCTION

For the rational development of our society, energy and environmental issues are among the most critical challenges to face during the next years. In this regard, a key issue is to clarify the right approach to overcome the dependence of our society on fossil fuels. Actually, most of the energy consumed by humankind stems from the burning fossil fuels, such as coal, petroleum, and natural gas, while drastically reducing the reserves of our planet, of which depletion is inevitable by the end of this century. Besides, because of the uncontrolled burning of fossil fuels, greenhouse gas emissions (mainly CO_2, CH_4, and N_2O) have increased exponentially, which threatens the future for the life of the different ecosystems of our planet.[1] According to the projections made by the European Union, during the period 2000-2030, the world demand for energy will have increased by about 48%, at an approximate rate of 1.8% per year, while in 2030, global CO_2 emissions will be more than double those registered in 1990. The uncontrolled increase in emissions of greenhouse gas, mainly CO_2, has caused an increase of approximately 1.5 ºC in global temperature since 1850.[2]

These projections motivate the search for alternative sources of energy, of which renewable energies represent the most respectful approach to the environment for a sustainable and self-sufficient society.[3] The renewable energies include solar, wind, hydroelectric, biomass or geothermal sources that are projected to represent in a close future (2050) our primary resource for the production of energy, as it was accorded by 139 countries in the Paris agreement of 2016 (**Figure 1**). Unfortunately, each of the renewable energy sources has its own limitations. For example, the hydroelectricity production is geographically limited, the geothermal is limited by its high drilling costs, or the amount of biomass energy will not contribute enough for the global energy demand.

[1] S. Solomon, G.-K. Plattner, R. Knutti, P. Friedlingstein, *Proc. Natl. Acad. Sci.* **2009**, *106*, 1704 LP – 1709.

[2] I. P. O. C. Change, *Special Report of Global Warming of 1.5ºC*, **2018**.

[3] U. S. E. I. Administration, "Annual Energy Outlook 2019," can be found under https://www.eia.gov/outlooks/aeo/pdf/aeo2019.pdf, **2019**.

Nonetheless, solar energy is unarguably the largest exploitable source that potentially could guarantee our future energy demand.

Our planet has an inexhaustible energy flow coming from our Sun and deposited on the surface of the Earth calculated as 120000 TW of electromagnetic radiation (**Figure 2**). The solar energy hitting the Earth in one hour is higher than all the energy consumed by our society in one year; harvesting less than 0.02% of this energy would satisfy our present needs. For this reason, the Sun represents an inexhaustible, clean, and economical energy source our governments should target that to fulfill our future energy demand and tackle the climate change problem. In our days, none of the many routes used to convert solar energy into electricity, heat, and fuel is competitive against fossil fuels at world market price yet. Thus, research projects focused on the development of solar energy are one of the most important topics in science nowadays.

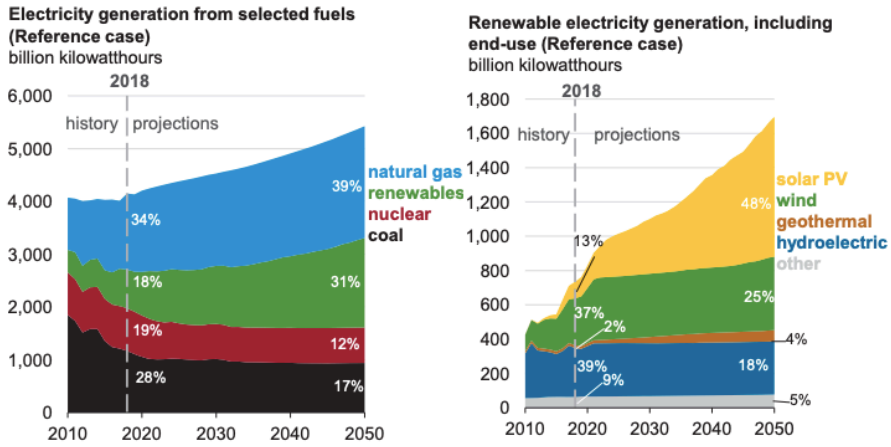

Figure 1. Electricity generation projections[3] for the next 30 years. Reproduced from ref. 3.

To date, the photovoltaic market is dominated mainly by polycrystalline silicon solar cells, representing almost 95% of the world´s total PV production. Despite Si-based solar cells could potentially sustainably supply our energy requirements, several drawbacks required for the construction of these solar cells are inspiring the research in new technologies to satisfy our energy demand. High performance Si-based solar cells involve high production costs

(monocrystalline silicon is required for efficiencies up to 15%), and the technology is bulky and heavy. For this reason, alternative technologies trying to outperform the well-established silicon solar cells are focused on low-cost production, lightweight, and flexible technologies.

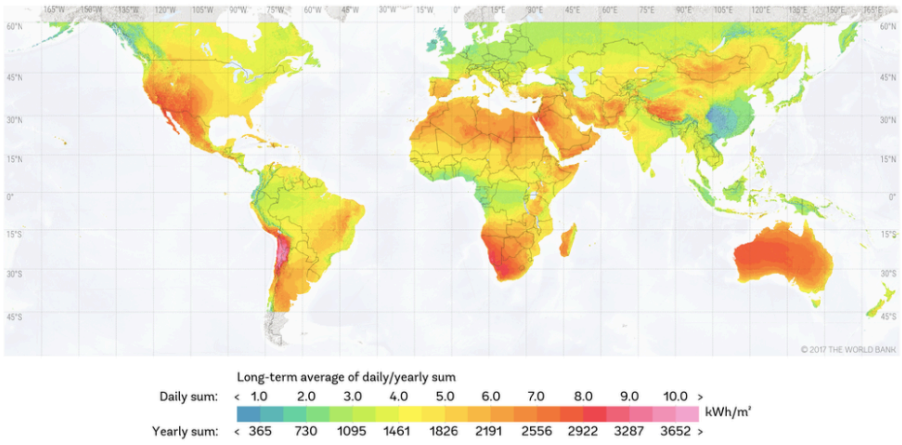

Figure 2. Daily and yearly sum of normal irradiation. Image from Global Solar Atlas.

Currently, different technologies complete the photovoltaic market together with silicon-based solar cells, such as the so-called second generation of solar cells based on thin-film (e.g., CdTe and CIGS). Furthermore, companies such as Dyesol, Infinity, Heliatek, or Solaronix are introducing in the market the third generation of solar cells using the latest technologies such as dye-sensitized solar cells (DSSCs), organic solar cells (OPVs) and Perovskite solar cells (PSCs).[4] Besides the similar power conversion efficiency (PCE) displayed by these new technologies in comparison to the benchmark polycrystalline silicon solar cells, the flexibility and lightweight of these technologies open the use of these new generation of solar cells to different applications such as solar windows, clothing or transport industry.

In this emerging field of third-generation solar cells, Perovskite solar cells (PSCs) represent the most promising technology to focus on the future development of solar energy. Amazingly promising research results (PCEs

[4] A. Extance, *Nature* **2019**, *570*, 429–432.

comparable to Si-based solar cells) have been achieved within only a few years of research incorporating low-cost production costs (from the raw materials to the manufacturing process), flexibility, and lightweight devices and additional feature such as a variety of colors.

2.1 Photovoltaic technology as a "green" alternative for producing energy.

Solar photovoltaics (PV) represent one of the most promising technologies for the production of energy from a renewable source, which is almost inexhaustible, our Sun. In this regard, future efforts for improving light-harvesting properties as well as reducing the manufacturing cost of the solar cells have to be done for a full utility of PV technologies in an energy-sustainable society that could satisfy the future global energy demand. During recent years, a wide variety of solar cells have been introduced, using different photo-active materials for the conversion of solar energy into electricity.

The first representative example of organic PV technology was presented by Tang in 1986 when it was reported a two-layers organic solar cell, which was based in the use of a copper phthalocyanine and a perylene tetracarboxylic derivative as light-absorbing materials.[5] Furthermore, seminal work was presented by O'Regan and Grätzel in 1991, introducing a new type of solar cell based on a dye-sensitized organic-based ruthenium complex, which opened a new research field during the years.[6]

In **Figure 3**, the evolution of the PCE of different technologies since their discovery is shown. It is important to highlight the rapid improvement of emerging thin-film PV, the perovskite solar cells.

Solar cells can be divided into two main categories: wafer-based solar cells and thin-film solar cells, according to the photo-active material used in the device's fabrication (**Figure 4**). Wafer-based cells are fabricated from semiconducting wafers. Thin-film cells comprise semiconducting photo-active absorbers that are

---

[5] C. W. Tang, *Appl. Phys. Lett.* **1986**, *48*, 183–185.

[6] B. O'Regan, M. Grätzel, *Nature* **1991**, *353*, 737–740.

deposited onto a transparent substrate such as glass or plastic. Among these, there are commercial and emerging thin-film solar cells.

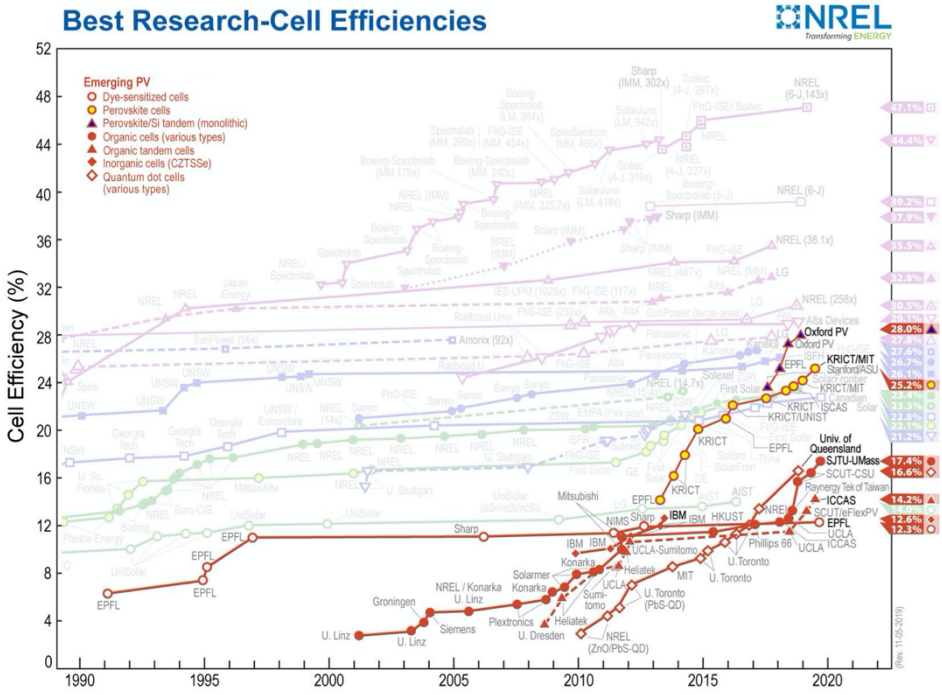

Figure 3. Chart from the National Renewable Energy Laboratory indicating the evolution of efficiencies of different solar cells during last years.

2.2 Wafer-based solar cells.

The three most important wafer-based technologies that cover the actual PV market are:

Crystalline silicon (c-Si) solar cells (25.6%). To date, silicon-based solar cells have dominated the photovoltaic market so far, producing around 90% of the current solar energy. Silicon-based materials present a nearly ideal band gap (E_g = 1.12 eV) for light-harvesting applications. Despite its outstanding properties, contact recombination causes the primary source of loss. Owing to the indirect band gap of Si, the absorption coefficient is low, and therefore thicker wafer layer is required to maximize the absorption of light. As a result, higher bulk

recombination is observed, which affects the V_{oc}. Nevertheless, it increases the material costs. Finding a correct equilibrium between cost, manufacturability, and performance have set up an optimum Si wafer thickness of 100 to 200 mm for commercial cells. Silicon-based solar cells also have an alternative in thin-film technologies. In this sense, hydrogenated amorphous silicon (H-a-Si) shows stronger absorption than crystalline silicon but, at the same time, presents a broader bandgap that does not match perfectly to the solar spectrum. Most commercial H-a-Si modules today use multi-junction cells but present much lower efficiency, which limits its market application.[7]

Gallium arsenide (GaAs) solar cells. Gallium arsenide material presents some of the optimal properties for PV applications, such as strong absorption, a direct bandgap, well-matched to the solar spectrum, and very slight non-radiative energy loss. GaAs has achieved the highest PCE for single-junction solar cells with a certified 28.8% for lab cells and 24.1% for modules.[8] The general procedure for the preparation of the GaAs layer is by epitaxial growth using chemical vapor deposition, which is a relatively energy-intensive process that difficult a high-volume manufacturing (**Figure 4**). Cost-effective production requires good film quality, more substrate reuse cycles to amortizes its cost, and low-cost wafer polishing. In addition, it is necessary encapsulation and recycling processes of commercial GaAs modules due to the toxicity of the element As.

III-V Multi-junction (MJ) solar cells. This type of multi-junction solar cell employs active layer semiconducting materials from group III (Al, Ga, In) and V (N, P, As, Sb). They are usually fabricated as a stack of two or more single-junction cells with different bandgaps to optimize the absorption of light to cover the solar spectrum along with the minimization of performance losses (**Figure 4**). Record cell efficiencies without concentration are 38.8%, 37.9%, and 31.1%

[7] M. A. Green, Y. Hishikawa, E. D. Dunlop, D. H. Levi, J. Hohl-Ebinger, M. Yoshita, A. W. Y. Ho-Baillie, *Prog. Photovoltaics Res. Appl.* **2019**, *27*, 3–12.

[8] B. M. Kayes, H. Nie, R. Twist, S. G. Spruytte, F. Reinhardt, I. C. Kizilyalli, G. S. Higashi, in *2011 37th IEEE Photovolt. Spec. Conf.*, **2011**, pp. 4–8.

for 4-junction (4J), 3J, and 2J cells, respectively.[7,9] Interestingly, III-V MJs solar cells have located at the top technology for space applications due to a very high radiation resistance, low-temperature sensitivity, and promising efficiency. On the other hand, its complex fabrication and high material costs have not allowed its application in light-harvesting applications on our planet.

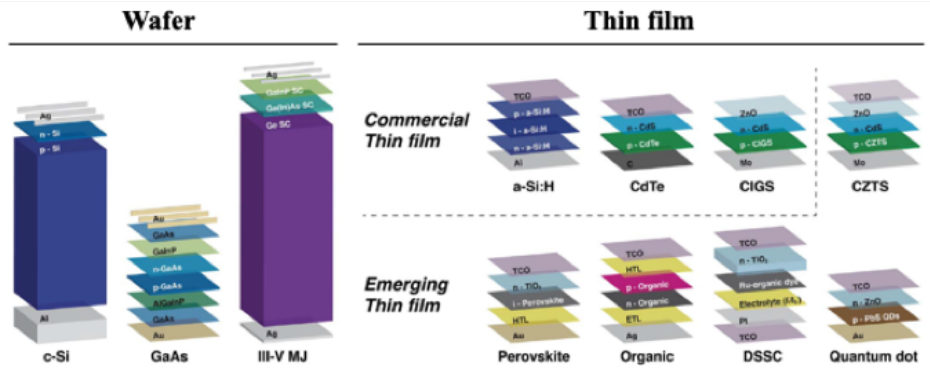

Figure 4. Schematic architectures for solar PV technologies, divided into wafer-based and thin-film structures.

2.3 Thin-film solar cells.

As it was mentioned before, attending to the thin-film technologies, it can also be divided into two other categories, as commercial or emerging thin-film technologies. Starting from the commercial thin film PV, CdTe and CIGS-based solar cells will be highlighted:

Cadmium telluride (CdTe) solar cells. CdTe is a binary semiconductor material with a cubic zinc blende structure and an ideal band gap of 1.43 eV. The highest reported certified efficiency for CdTe is 22.1% (First Solar).[7] (**Figure 4**) Nevertheless, CdTe presents relatively low open-circuit voltage attributed to recombination losses in the crystal grains and at interfaces in the material. CdTe solar modules have been extensively commercialized by several companies. As

[9] J. F. Geisz, M. A. Steiner, I. García, S. R. Kurtz, D. J. Friedman, *Appl. Phys. Lett.* **2013**, *103*, 41118.

an important point to take into account, this technology needs a recycling system due to the toxicity of element Cd.

Copper indium gallium selenide (CIGS) and copper zinc tin sulfide (CZTS) solar cells. The record efficiency of $Cu(In,Ga)(Se,S)_2$ (CIGS) thin-film solar cells has been optimized over the past 20 years, reaching a present record of 21.7% PCE, which is the best efficiency for a commercial thin-film solar cell.[10] CIGS presents a chalcopyrite crystal structure, and its band gap can be easily tuned between 1.0 and 2.4 eV by modifying the In/Ga and Se/S ratios. Due to the complex stoichiometry of CIGS, many structural phases are detected, which have been studied for the optimization of efficiencies by varying the deposition and annealing process to avoid detrimental by-products. On the other hand, copper zinc tin sulfide (CZTS) materials can crystallize to form either a kesterite or stannite crystal structure. Still, only the former is active for PV applications. The band gap of CZTS can be easily tuned over a range of 1.0 to 1.6 eV, observing the best results for a Cu-poor, Zn-rich stoichiometry with the band gap controlled by the S/Se ratio. CZTS present a record efficiency of 12.6% suffering from a high voltage loss due to recombination at defects in the bulk material and the charge extraction from the interfaces.[11,12]

Apart from the commercial thin-film technologies, new emerging thin-film devices have been presented during the last three decades. Nowadays, strong efforts in research are focused on these new emerging technologies:

Dye-sensitized solar cells (DSSC). Since the seminal work by O'Regan and Grätzel in 1991.[6] DSSCs are a particular class of devices that involves an electrochemical power generation process. These photo-electrochemical cells comprise a transparent inorganic scaffold anode (typically highly porous nanostructured TiO_2) in which the light-absorbing dye molecules (ruthenium

[10] P. Jackson, D. Hariskos, R. Wuerz, O. Kiowski, A. Bauer, T. M. Friedlmeier, M. Powalla, *Phys. status solidi – Rapid Res. Lett.* **2015**, *9*, 28–31.

[11] T. K. Todorov, K. B. Reuter, D. B. Mitzi, *Adv. Mater.* **2010**, *22*, E156–E159.

[12] W. Wang, M. T. Winkler, O. Gunawan, T. Gokmen, T. K. Todorov, Y. Zhu, D. B. Mitzi, *Adv. Energy Mater.* **2014**, *4*, 1301465.

complexes, zinc porphyrins, or other organic dyes) are anchored to the mesoporous anode.[13] PCE over 13% have been measured recently using a porphyrin sensitizer.[14] Despite these relatively low performances, dye-sensitized solar cells have been commercialized owing to their simple and low-cost fabrication, use of inexpensive materials and a variety of colors and opacities for commercial applications, mainly in the manufacture of solar windows (**Figure 5**). DSSCs have served as a model for the development of other nanostructured PV devices, such as organic solar cells and perovskite solar cells.

Organic solar cells. Organic solar devices use π-conjugated small-organic molecules or polymers to absorb light, offering inexpensive roll-to-roll fabrication on flexible substrates and a wide choice of materials for photovoltaic applications.[15,16] The photoactive layer is commonly composed of a blend of an electron-donor and an electron-acceptor. PCE up to 18%[17,18] have been obtained using a small-organic molecule as an acceptor and a donor polymer and over 17% in tandem solar cells.[19] Because of the low dielectric constant of organic materials, photo-generated exciton pairs remain tightly bound, which requires well-defined architectures such as bulk heterojunctions to achieve an efficient charge separation and extraction devices.

Quantum dot solar cells. Quantum dot (QD) solar cells take advantage of the unique properties that present semiconductor quantum dots. They can be

---

[13] A. Hagfeldt, G. Boschloo, L. Sun, L. Kloo, H. Pettersson, *Chem. Rev.* **2010**, *110*, 6595–6663.

[14] S. Mathew, A. Yella, P. Gao, R. Humphry-Baker, F. E. CurchodBasile, N. Ashari-Astani, I. Tavernelli, U. Rothlisberger, M. K. Nazeeruddin, M. Grätzel, *Nat. Chem.* **2014**, *6*, 242–247.

[15] B. Kippelen, J.-L. Brédas, *Energy Environ. Sci.* **2009**, *2*, 251–261.

[16] S. Günes, H. Neugebauer, N. S. Sariciftci, *Chem. Rev.* **2007**, *107*, 1324–1338.

[17] Q. Liu, Y. Jiang, K. Jin, J. Qin, J. Xu, W. Li, J. Xiong, J. Liu, Z. Xiao, K.Sun, S. Yang, X. Zhang, L. Ding, *Sci. Bull.* **2020**, 65, 272–275.

[18] H. Zhang, H. Yao, J. Hou, J. Zhu, J. Zhang, W. Li, R. Yu, B. Gao, S. Zhang, J. Hou, *Adv. Mater.* **2018**, *30*, 1800613.

[19] L. Meng, Y. Zhang, X. Wan, C. Li, X. Zhang, Y. Wang, X. Ke, Z. Xiao, L. Ding, R. Xia, H.-L. Yip, Y. Cao, Y. Chen, *Science* **2018**, *361*, 1094.

prepared using low-temperature solution methods, with a complete variability of their properties such as band gap by composition and size engineering. Although the most common QD solar cells so far are fabricated using PbS or PbSe as active layer,[20] the record in PCE was achieved using a perovskite $CsPbI_3$-based QD, reaching a promising efficiency of 13.4% (a new record of 16.6% has been reported by NREL although the composition is not known yet).[21]

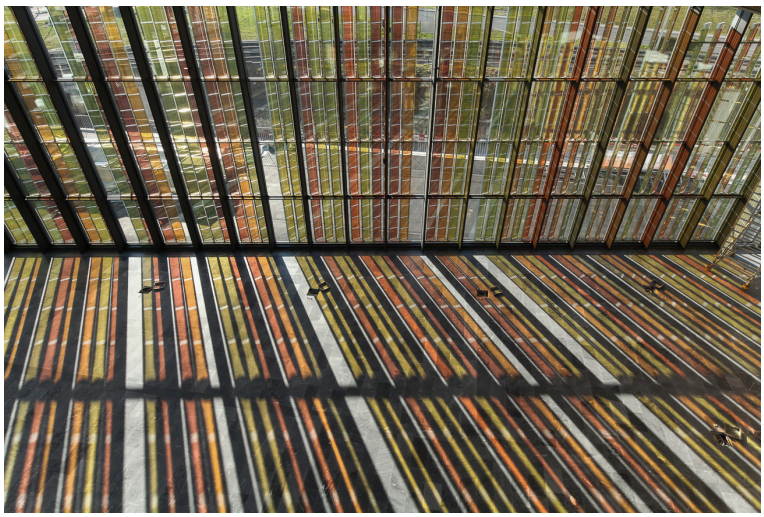

Figure 5. Up-scale solar windows at EPFL in Lausanne (Switzerland) fabricated using dye-sensitized solar cells.

Perovskite solar cells. As the most recent technology, since the first report in 2009, perovskite solar cells have emerged from solid-state dye-sensitized cells.[22] PSCs have rocketed as the most promising PV technology, reaching a

[20] C.-H. M. Chuang, P. R. Brown, V. Bulović, M. G. Bawendi, *Nat. Mater.* **2014**, *13*, 796.

[21] E. M. Sanehira, A. R. Marshall, J. A. Christians, S. P. Harvey, P. N. Ciesielski, L. M. Wheeler, P. Schulz, L. Y. Lin, M. C. Beard, J. M. Luther, *Sci. Adv.* **2017**, *3*, eaao4204.

[22] A. Kojima, K. Teshima, Y. Shirai, T. Miyasaka, *J. Am. Chem. Soc.* **2009**, *131*, 6050–6051.

certified efficiency of 23.7%[23] in just a few years of research.[24,25,26] The present thesis is focused on this type of solar cells.

[23] N. R. E. L. National Renewable Energy Laboratory, **2018**.

[24] N.-G. Park, *Mater. Today* **2015**, *18*, 65–72.

[25] A. Polman, M. Knight, E. C. Garnett, B. Ehrler, W. C. Sinke, *Science* **2016**, *352*, aad4424-9.

[26] A. Abate, J.-P. Correa-Baena, M. Saliba, M. S. Su'ait, F. Bella, *Chem. – A Eur. J.* **2018**, *24*, 3083–3100.

3. Perovskite Solar Cells (PSCs).

Since the groundbreaking discovery of Miyasaka,[22] an emerging low-cost approach for PV photovoltaic technology is entering a field widely dominated by silicon-based solar cells. The hybrid organic-inorganic perovskites solar cells have reached PCEs of 25.2% [23] similar to those of silicon-based devices in only ten years of research. Emerging from this discovery, an unleashed scientific run in terms of publications and scientific impact has sprouted, which is only comparable to those after the first report of graphene in 2004.

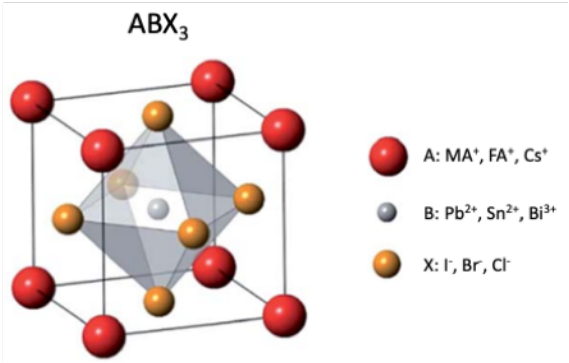

Figure 6. Crystal structures of organic-inorganic metal halide perovskites. Reproduced from ref. 28.

3.1.1 Perovskite's chemical structure.

"Perovskite" is the nomenclature for any material that possesses the same crystal structure of calcium titanium oxide ($CaTiO_3$). Perovskite takes its name from the mineral discovered by Gustav Rose in the Ural Mountains (Russia) in 1836 and named after the mineralogist Count Lev Alekseevich Perovskii.[27] Perovskites are materials described by the general formula ABX_3, where X is an anion (halides for photovoltaic applications), and A and B are cations of different sizes (A being larger than B). Typically, B is a divalent metal cation (Pb^{2+}, Sn^{2+}, Bi^{2+}). The versatility of the cation A confers to the structure a broad tunability of its

[27] R. A. B. John W. Anthony Kenneth W. Bladh, Monte C. Nichols, M. S. of America, *Handbook of Mineralogy*, **2001**.

properties. Cations A are usually small organic molecules, such as methylammonium (MA^+)[22] or formamidinium (FA^+).[28] However, larger cations, such as guanidinium (Gua^+),[29] Cesium (Cs^+),[30] or Rubidium (Rb^+)[31] have also been used.

The unit cell of perovskites is described by the A cations at the corner positions, B cations at the body center and the X anions are face-centered in an ideal cubic-symmetry (**Figure 6**). The BX_6 octahedra constitute a three-dimensional network in which they share corners. Within this framework, the A cations fill in the space between the octahedra, balancing the charge of the entire network. As aforementioned, perovskite presents an ideally cubic structure, but it is important to consider the real structure as a supramolecular assembly of two building blocks consisting of AX_{12} and BX_6 polyhedra.[32,33] This crucial distortion in the structure affects the physical properties of perovskite materials, such as electronic, optical, magnetic and dielectric properties.[34] The size of the cation A and the anion X is limited by the space that it occupies, having a great impact in the photophysical properties of the perovskite material.[35] In this regard, the crystallographic structure of perovskites can be estimated by considering the relative ion size of the constituent atoms that is expressed with

[28] G. E. Eperon, S. D. Stranks, C. Menelaou, M. B. Johnston, L. M. Herz, H. J. Snaith, *Energy Environ. Sci.* **2014**, *7*, 982–988.

[29] A. D. Jodlowski, C. Roldán-Carmona, G. Grancini, M. Salado, M. Ralaiarisoa, S. Ahmad, N. Koch, L. Camacho, G. de Miguel, M. K. Nazeeruddin, *Nat. Energy* **2017**, *2*, 972–979.

[30] M. Saliba, T. Matsui, J.-Y. Seo, K. Domanski, J.-P. Correa-Baena, M. K. Nazeeruddin, S. M. Zakeeruddin, W. Tress, A. Abate, A. Hagfeldt, M. Grätzel, *Energy Environ. Sci.* **2016**, *9*, 1989–1997.

[31] M. Saliba, T. Matsui, K. Domanski, J.-Y. Seo, A. Ummadisingu, S. M. Zakeeruddin, J.-P. Correa-Baena, W. R. Tress, A. Abate, A. Hagfeldt, M. Grätzel, *Science* **2016**, *354*, 206.

[32] F. Brivio, K. T. Butler, A. Walsh, M. van Schilfgaarde, *Phys. Rev. B* **2014**, *89*, 155204.

[33] D. B. Mitzi, *Inorg. Chem.* **2000**, *39*, 6107–6113.

[34] S. Kazim, M. K. Nazeeruddin, M. Grätzel, S. Ahmad, *Angew. Chem. Int. Ed.* **2014**, *53*, 2812–2824.

[35] H. S. Jung, N. G. Park, *Small* **2015**, *11*, 10–25.

the tolerance factor t, which is defined by Victor Goldschmidt through the **equation 1**:[36]

$$t = \frac{rA+rX}{\sqrt{2(rA+rX)}}$$

where r_A and r_X are the ionic radii of the corresponding cation A and anion X that form the perovskite material (**Figure 7**). When t = 1, the structure could be defined as a perfect cubic package, but in general, in the literature are usually found values of t between 0.8 and 0.9, which correspond to an orthorhombic structure.

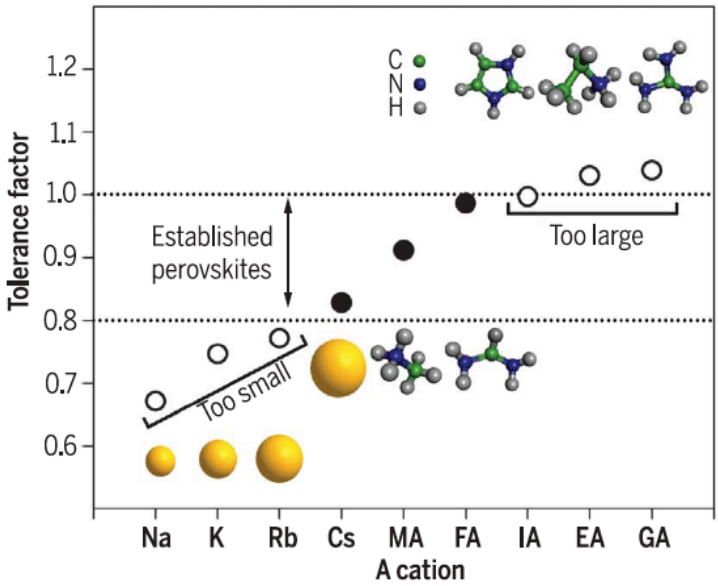

Figure 7. Tolerance factor for different A cations for the preparation of stable perovskite materials.

[36] D. B. Mitzi, in *Prog. Inorg. Chem.*, John Wiley & Sons, Inc., **1999**, pp. 1–121.

3.1.2 Perovskites: unique properties for photovoltaic applications.

From their structure, organic-inorganic lead halide perovskites display outstanding properties for photovoltaic applications.[37,38,39,40] Organic-inorganic lead halide perovskites present a panchromatic absorption which can be perfectly modulated by tuning the band gap through cation and/or anion exchange.[38] Perovskite materials present an ambipolar behavior for transporting both charges, electrons, and holes.[41,42] Under illumination, solution-processed devices exhibit reliable high performance with balanced carrier mobilities and on/off ratios of $\approx 10^4$ for both p- and n-type transports. For this reason, hybrid perovskite can be sandwiched between both electron and hole selective transport layers, which lead to different suitable device architectures. Furthermore, electron and hole diffusion lengths up to 170 μm have been measured in single-crystal $MAPbI_3$ by solution-growth methods under 1 sun illumination.[43] These diffusion lengths widely overcome the values measured for organic solar cells, which typically have been found from 10-20 nm. Also, mixed-halide crystal possessed a very low exciton binding energy (in the range of 50 meV).[44,45,46,47]

---

[37] Y. Zhao, K. Zhu, *Chem. Soc. Rev.* **2016**, *45*, 655–689.

[38] L. Zheng, Y. Ma, S. Chu, S. Wang, B. Qu, L. Xiao, Z. Chen, Q. Gong, Z. Wu, X. Hou, *Nanoscale* **2014**, *6*, 8171–8176.

[39] T. C. Sum, N. Mathews, *Energy Environ. Sci.* **2014**, *7*, 2518–2534.

[40] Y.-C. Hsiao, T. Wu, M. Li, Q. Liu, W. Qin, B. Hu, *J. Mater. Chem. A* **2015**, *3*, 15372–15385.

[41] F. Li, C. Ma, H. Wang, W. Hu, W. Yu, A. D. Sheikh, T. Wu, *Nat. Commun.* **2015**, *6*, 8238.

[42] Y. Li, W. Yan, Y. Li, S. Wang, W. Wang, Z. Bian, L. Xiao, Q. Gong, *Sci. Rep.* **2015**, *5*, 14485.

[43] Q. Dong, Y. Fang, Y. Shao, P. Mulligan, J. Qiu, L. Cao, J. Huang, *Science* **2015**, *347*, 967.

[44] V. D'Innocenzo, G. Grancini, M. J. P. Alcocer, A. R. S. Kandada, S. D. Stranks, M. M. Lee, G. Lanzani, H. J. Snaith, A. Petrozza, *Nat Commun* **2014**, *5*, 3586.

[45] J. C. Blancon, H. Tsai, W. Nie, C. C. Stoumpos, L. Pedesseau, C. Katan, M. Kepenekian, C. M. M. Soe, K. Appavoo, M. Y. Sfeir, S. Tretiak, P. M. Ajayan, M. G. Kanatzidis, J. Even, J. J. Crochet, A. D. Mohite *Science* **2017**, *355*, 1288.

[46] T. J. Savenije, C. S. Ponseca, L. Kunneman, M. Abdellah, K. Zheng, Y. Tian, Q. Zhu, S. E. Canton, I. G. Scheblykin, T. Pullerits, A. Yartsev, V. Sundström, *J. Phys. Chem. Lett.* **2014**, *5*, 2189–2194.

[47] A. Jha, H.-G. Duan, V. Tiwari, P. K. Nayak, H. J. Snaith, M. Thorwart, R. J. D. Miller, *ACS Photonics* **2018**, *5*, 852–860.

Hence, it is clear that the mechanism for conversion of light to electric current for perovskite is based on free carriers rather than *via* exciton pathways.

As it is shown in **Figure 8**, the operational mechanism of perovskite solar cells involves different steps:[48] (1) photo-excitation of the perovskite material, creating almost instantly electron-hole carriers; (2) injection of the photo-generated electron from the conduction band of the perovskite layer to the corresponding electron-transporting material; (3) injection of the photo-generated holes from the valance band of the perovskite to hole-transporting material. Then, in the ideal mechanism, these photo-generated charge carriers are subsequently transported and collected as photocurrent at the electrodes of the solar cell. Unfortunately, processes (2) and (3) compete with undesirable processes, such as the recombination of the photo-generated carriers, which can be traduced in an exciton annihilation by photoluminescence emission or non-radiative recombination (4).

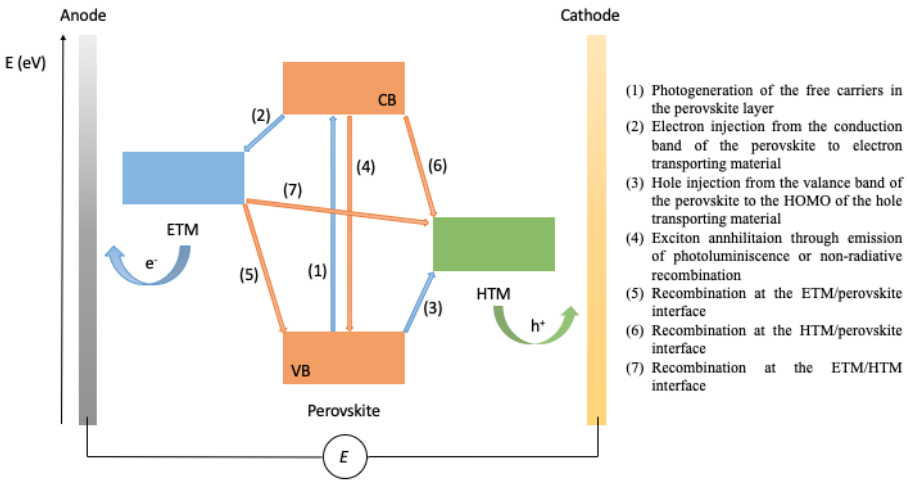

Figure 8. Schematic diagram of energy levels and charge transfer processes in a standard perovskite solar cells.

[48] A. Marchioro, J. Teuscher, D. Friedrich, M. Kunst, R. van de Krol, T. Moehl, M. Grätzel, J.-E. Moser, *Nat. Photonics* **2014**, *8*, 250.

Other processes that reduce the efficiency of the devices are related with (5) back electron transfer at the interface of ETM/perovskite, (6) back hole transfer at the interface of HTM/ perovskite, and (7) charge recombination at the ETM/HTM interface, which only occur in the case of incomplete coverage of the perovskite. It is clear that for highly efficient devices, the charge recombination processes (4-7) should occur at a lower time scale than charge generation, separation, and extraction processes (1-3).[48] Electron and hole injection occurs very efficiently in PSCs owing to the high diffusion lengths of charge carriers. To reduce the recombination at the interfaces (processes 4-7), which limits the V_{oc}, the ETM and HTM should be compact and in an ideal configuration, non-doped. Upon illumination, photo-generated electron and hole, in quasi-Fermi levels in the perovskite material, are formed close to the valence and conduction bands. The difference between these energies will determine the open-circuit voltage in perovskite solar cells.

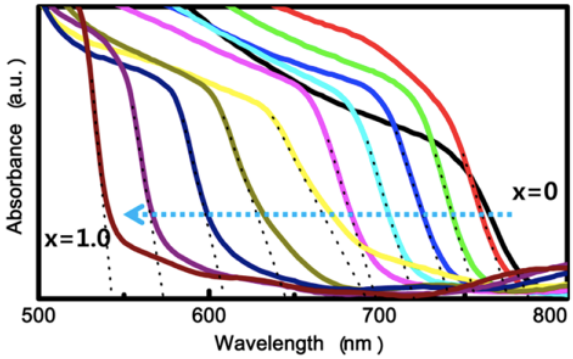

Figure 9. UV-vis absorption spectra of different $MAPb(I_{1-x}Br_x)_3$ nanocomposites. Reproduced from ref. 49.

3.1.3 Bandgap tuning by anion and cation exchange.

Different studies have demonstrated how the size of the cation A and the anion X is a useful tool for tuning the optoelectronic properties of the perovskite material.[35,49] One of the first works that beautifully exemplified this behavior

[49] J. H. Noh, S. H. Im, J. H. Heo, T. N. Mandal, S. I. Seok, *Nano Lett.* **2013**, *13*, 1764–1769.

was reported by Seok and co-workers, revealing how the sequential increase of the bromine content with respect to iodine in the standard $MAPb(I_{1-x}Br_x)_3$ perovskite lead to a modification of the absorption onset from a 786 nm wavelength (1.58 eV) to 544 nm wavelength (2.28 eV) (**Figure 9**). This band gap engineering showed an expected impact on the photovoltaic response, displaying better results when the ratio between iodine and bromine was 0.8/0.2.[49] This compositionally engineered approach has been used during these years for boosting the efficiency of PSCs up to 20%.

In 2014, Snaith and co-workers tuned the optoelectronic properties of the perovskite by varying the halide composition in a FA-based perovskite.[28] Upon increasing the bromine content in the $FAPbI_yBr_{3-y}$ perovskite, a broad bandgap tunability between 1.48 and 2.23 eV is observed, which is slightly narrow from those obtained for methylammonium-based perovskite (**Figure 10**). The authors fabricated devices with different content in bromide, observing the best efficiency of 14.2% for pure $FAPbI_3$. Noteworthy, upon increasing the content in bromine, the open-circuit voltage (V_{oc}) was boosted ($[FAPb(I_{0.8}Br_{0.2})_3]$) due to the reduced bandgap. More recently, Liu and co-workers introduced the use of the acetate anion (Ac^-) in pure $CsPbBr_3$ and $CsPbI_2Br$ perovskites as dopant for the formation of new perovskite materials $CsPbBr_{3-x}Ac_x$ and $CsPbI_{2-x}BrAc_x$.[50] Interestingly, the best results were reached by adding 4.5% of $PbAc_2$ into the $CsPbI_2Br$ perovskite, with an impressive V_{oc} of 1.30 V and a PCE of 15.6 % in planar architectures. Ac^- doping strategy result in the stabilization of the α-phase perovskite by means of increasing the tolerance factor of the crystal structure, therefore, optimizing the surface morphology and enhancing interaction with Pb.

Snaith and co-workers also studied how the band gap values can be tuned using different A cations.[28] As shown in **Figure 10b**, $CsPbI_3$ absorbs in shorter wavelength, whereas $FAPbI_3$ absorbs to longer wavelength than $MAPbI_3$, resulting in a decreased value for its band gap. It is important to mention that when increasing the ion radius of cation A, the lattice of the cell is expected to expand, which motivates a reduction in the band gap. This phenomenon is explored to push the bandgap of the perovskite absorber further towards the

[50] H. Zhao, Y. Han, Z. Xu, C. Duan, S. Yang, S. Yuan, Z. Yang, Z. Liu, S. Liu, *Adv. Energy Mater.* **2019**, *9*, 1902279.

infrared, which may lead to a more efficient conversion of the solar spectrum. Nevertheless, pure $FAPbI_3$ suffers from structural instability and is highly sensitive to humidity and solvents. One way to overcome the instability of $FAPbI_3$ is by introducing compositionally engineered perovskites that combine different A cations such as $[FAPbI_3]_{1-x}$ $[MAPbBr_3]_x$.[51,52] The first study of Grätzel and co-workers showed how the introduction of different ratio of FA/MA cations in $[MA]_x[FA]_{1-x}PbI_3$ avoided the undesirable formation of the δ-phase of pure $FAPbI_3$ perovskite which limits the device performance. Here, methylammonium cation acts as a "stabilizer" of the perovskite phase and, simultaneously, forms crystallites, which leads to notably improved PCE values.

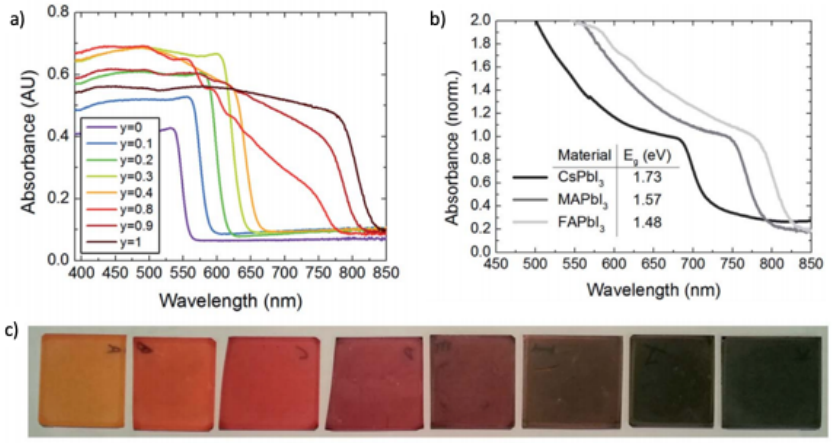

Figure 10. a) UV-Vis absorbance spectra of the $FAPbI_yBr_{3-y}$ perovskites upon increasing content of bromine; b) UV-Vis absorbance spectra of pure $CsPbI_3$, $MaPbI_3$ and $FAPbI_3$; c) Photographs of the $FAPbI_yBr_{3-y}$ perovskite layers. Reproduced from ref. 28.

The strategy of mixing small organic cations opened up new prospects for improving the photovoltaic efficiency of PSCs.[51] Going a step further in this strategy, Seok and co-workers reported the compositional engineered perovskites by combining MA/FA cations and Br/I anions, following the general

[51] N. Pellet, P. Gao, G. Gregori, T.-Y. Yang, M. K. Nazeeruddin, J. Maier, M. Grätzel, *Angew. Chem. Int. Ed.* **2014**, *53*, 3151–3157.

[52] N. J. Jeon, J. H. Noh, W. S. Yang, Y. C. Kim, S. Ryu, J. Seo, S. I. Seok, *Nature* **2015**, *517*, 476–480.

formula $[FAPbI_3]_{1-x}$ $[MAPbBr_3]_x$. The authors completed an exhaustive analysis for different compositions, showing an optimized stoichiometry of $[FAPbI_3]_{0.85}[MAPbBr_3]_{0.15}$ for the preparation of 20% efficiency devices. Later on, in 2016, Grätzel and co-workers reported the so-called "triple cation perovskite" by the incorporation of Cs in the mixed perovskite.[30] By introducing small amounts of cesium, it is observed an efficient suppress of the yellow phase impurities allowing the formation of more defect-free perovskite films. The triple cation composition films were thermally more stable and less affected by fluctuating surrounding variables such as temperature, solvent, or heating protocols. This robustness had been crucial for improving the reproducibility, enabling batch to batch reproducibility with PCEs up to 20% regularly. As an even more complex structure, the same group reported a quadruple cation composition by the incorporation of a small amount of rubidium.[31] They managed to form RbFA, RbCsFA, RbMAFA, and RbCsMAFA based perovskite and compared its properties and photovoltaic response. Quadruple cation perovskite, with a 5% of Rb, displayed 21.6% of efficiency with improved values of V_{oc} and *FF* in comparison to the triple cation-based devices. Nevertheless, the stability of this new composition was limited. Top-view scanning electron microscopy (SEM) images revealed large crystals in the RbCsMAFA devices which are beneficial for the photovoltaic performance (**Figure 11**).

Nazeeruddin and co-workers introduced the use of guanidinium (Gua) as a small cation to replace FA.[29] Gua/MA-based perovskite material exhibited superior stability and photovoltaic performance compared with classical $MAPbI_3$. The incorporation of large guanidinium cation forms a highly stable 3D crystalline structure, which can be explained using the increased number of H bonds within the inorganic framework. The reported $[MA_{1-x}Gua_x]PbI_3$ perovskite preserved the excellent optoelectronic properties associated with the organic lead halide materials, leading to very efficient devices surpassing 20% of PCE. Troshin and co-worker introduced a new cation hydrazinium for partial exchange of methylammonium lead iodide perovskite. The authors fabricated devices with different ratios of the A cation, leading to a best efficiency of 10.7% for a $MA_{0.9}HA_{0.1}PbI_3$ composition in planar devices with a considerably improved stability compared to the reference devices based on the conventional

$MAPbI_3$.[53] Very recently, the use of 1,2,4-triazole as a novel stabilizer for high efficient perovskite solar cells has been reported by Park and co-workers.[54] A maximum power conversion of 20.9% was measured, incorporating 2% of 1,2,4-triazole.

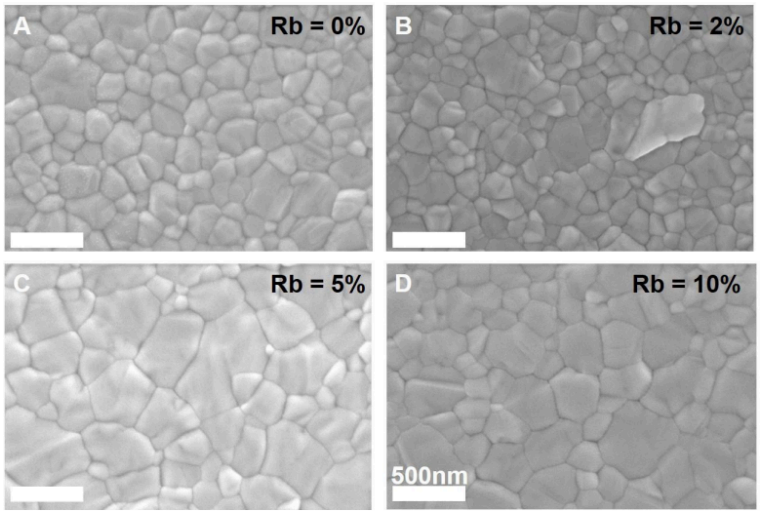

Figure 11. Top view images (SEM) of $Rb_xCsMAFA$-based perovskite with (A) 0% (B) 2% (C) 5% and (D) 10% Rb. Reproduced from ref. 31.

3.1.4 Lead-free perovskites.

Lead-containing materials are a paramount environmental concern, which limits the possibility of large-scale manufacture. As it is well-known, lead is a very toxic metallic element due to its high-water solubility and low vaporization temperature. Human exposure to lead is harmful to the nervous and reproductive systems and the hematopoietic and renal organs.[55] Lead toxicity could not be a problem if lead remains contained within the PV module by methods of

[53] A. F. Akbulatov, L. A. Frolova, D. V Anokhin, K. L. Gerasimov, N. N. Dremova, P. A. Troshin, *J. Mater. Chem. A* **2016**, *4*, 18378–18382.

[54] J. Kim, A. J. Yun, B. Gil, Y. Lee, B. Park, *Adv. Funct. Mater.* **2019**, *29*, 1905190.

[55] F. Gagan, G. Deepesh, T. Archana, *Interdiscip. Toxicol.* **2012**, *5*, 47–58.

encapsulation and recycling.[25] Nevertheless, lead-based perovskites tend to release PbI_2 as a degradation product, which is also very toxic.

Despite these possible solutions to overcome the toxicity problem of lead-based perovskite, during these years have appeared a great number of publications using partially or totally lead-free perovskite.[56,57] In this sense, tin (Sn^{2+}) has been used as a reasonable cation for substituting lead in the perovskite structure, due to its similar radii of their ion.[58,59,60] Nevertheless, Sn^{2+} presents an important drawback in its stability under air conditions because it is rapidly oxidized to Sn^{4+}, ruining the perovskite structure in air, which is considered as a bottleneck limiting the development of Sn-based PSCs with maximum power conversion efficiencies in the range of 9-12% with limited stability.[61,62] Other alternative materials based on metallic elements that have been studied for replacing lead was based in Ge^{2+}.[63,64] Power conversion efficiencies that not surpass 1% and air-stability issues of Ge^{2+} limit Ge-based perovskites future, although it can be combined with Sn ($CsGe_{0.5}Sn_{0.5}I_3$) for relatively high stable

[56] Z. Shi, J. Guo, Y. Chen, Q. Li, Y. Pan, H. Zhang, Y. Xia, W. Huang, *Adv. Mater.* **2017**, *29*, 1605005.

[57] T. Miyasaka, A. Kulkarni, G. M. Kim, S. Öz, A. K. Jena, *Adv. Energy Mater.* **2019**, 1902500.

[58] N. K. Noel, S. D. Stranks, A. Abate, C. Wehrenfennig, S. Guarnera, A.-A. Haghighirad, A. Sadhanala, G. E. Eperon, S. K. Pathak, M. B. Johnston, A. Petrozza, L. M. Herz, H. J. Snaith, *Energy Environ. Sci.* **2014**, *7*, 3061–3068.

[59] W. Ke, P. Priyanka, S. Vegiraju, C. C. Stoumpos, I. Spanopoulos, C. M. M. Soe, T. J. Marks, M.-C. Chen, M. G. Kanatzidis, *J. Am. Chem. Soc.* **2018**, *140*, 388–393.

[60] S. J. Lee, S. S. Shin, Y. C. Kim, D. Kim, T. K. Ahn, J. H. Noh, J. Seo, S. I. Seok, *J. Am. Chem. Soc.* **2016**, *138*, 3974–3977.

[61] X. Liu, K. Yan, D. Tan, X. Liang, H. Zhang, W. Huang, *ACS Energy Lett.* **2018**, *3*, 2701–2707.

[62] L.-J. Chen, C.-R. Lee, Y.-J. Chuang, Z.-H. Wu, C. Chen, *J. Phys. Chem. Lett.* **2016**, *7*, 5028–5035.

[63] C. C. Stoumpos, L. Frazer, D. J. Clark, Y. S. Kim, S. H. Rhim, A. J. Freeman, J. B. Ketterson, J. I. Jang, M. G. Kanatzidis, *J. Am. Chem. Soc.* **2015**, *137*, 6804–6819.

[64] T. Krishnamoorthy, H. Ding, C. Yan, W. L. Leong, T. Baikie, Z. Zhang, M. Sherburne, S. Li, M. Asta, N. Mathews, S. Mhaisalkar, *J. Mater. Chem. A* **2015**, *3*, 23829–23832.

and efficient PSC with a maximum PCE of 7.11%.[65] Finally, it should be mentioned the use of Bi^{3+} as a possible candidate for replacing lead-based perovskites.[66] Solar devices employing $Cs_3Bi_2I_9$ as an active layer displayed a PCE around 1%. Despite its low efficiency, Bi^{3+} could be envisioned as a dopant of lead-based conventional perovskite solar cells.

3.1.5 Perovskite solar cells devices architectures.

The first report of $CH_3NH_3PbI_3$ used as sensitizer in dye-sensitized solar cells (DSSCs) combined with a liquid electrolyte, displayed low efficiencies of 3.8% along with very limited stability.[22] The great breakthrough was introduced first by Park and co-workers by using an all-solid-state configuration. The authors deposited the perovskite onto a submicron-thick mesoscopic TiO_2 layer, whose pores were infiltrated with the perovskite material while it was capped with a hole-transporting material, spiro-OMeTAD, improving the efficiency to 9.7%.[67] Simultaneously, Snaith and co-workers presented an alternative device architecture. They used a compact layer of TiO_2 (c-TiO_2), a mesoporous scaffold of TiO_2 (m-TiO_2) where the perovskite is infiltrated and then, the hole-selective layer was spin-coated on top of the perovskite, achieving PCEs of 10.9% [68] (**Figure 12a).** Since then, this is the most used architecture for the preparation of high-efficiency PSCs.[69]

---

65 M. Chen, M.-G. Ju, H. F. Garces, A. D. Carl, L. K. Ono, Z. Hawash, Y. Zhang, T. Shen, Y. Qi, R. L. Grimm, D. Pacifici, X. C. Zeng, Y. Zhou, N. P. Padture, *Nat. Commun.* **2019**, *10*, 16.

66 B.-W. Park, B. Philippe, X. Zhang, H. Rensmo, G. Boschloo, E. M. J. Johansson, *Adv. Mater.* **2015**, *27*, 6806–6813.

67 H.-S. Kim, C.-R. Lee, J.-H. Im, K.-B. Lee, T. Moehl, A. Marchioro, S.-J. Moon, R. Humphry-Baker, J.-H. Yum, J. E. Moser, M. Grätzel, N.-G. Park, *Sci. Rep.* **2012**, *2*, 591.

68 M. M. Lee, J. Teuscher, T. Miyasaka, T. N. Murakami, H. J. Snaith, *Science* **2012**, *338*, 643–647.

69 T. Salim, S. Sun, Y. Abe, A. Krishna, A. C. Grimsdale, Y. M. Lam, *J. Mater. Chem. A* **2015**, *3*, 8943–8969.

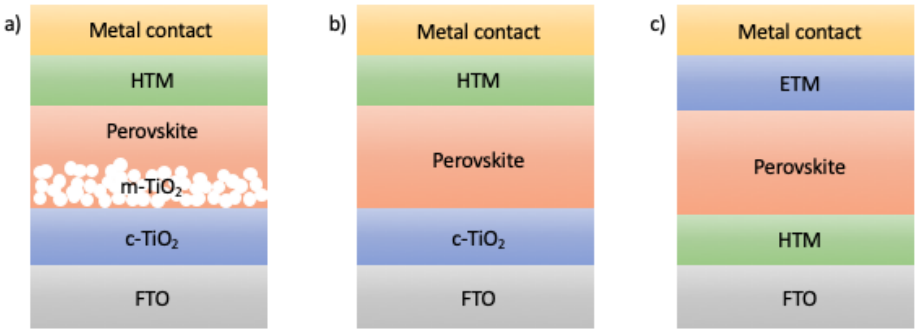

Figure 12. Schematic illustration of the most common device architectures of PSCs: a) (n–i–p) mesoporous; b) (n-i-p) planar; c) inverted (p–i–n) planar structures.

As an alternative, planar architectures have also been explored, removing the mesoporous layer of TiO_2. In planar architectures (**Figure 12b-c**) the perovskite layer is sandwiched between an electron-transporting and blocking layer, and a hole-transporting material.[70,71] The ambipolar charge transport properties of perovskite allow versatile configurations, which can be conventional (n-i-p) and inverted (p-i-n) depending on the charge-extraction layer and the selective contacts. The regular n-i-p structures (TCO/ETM/perovskite/ HTM/metal) have been extensively studied. The inverted p-i-n structure comes from organic solar cells in which the charge transport is inverted (TCO/HTM/perovskite/ETM/metal).[72] Regardless of device architecture, high PCEs up to 20% have been achieved during these years of research, which demonstrate the versatility of perovskite material for light-harvesting applications.

3.1.6 Fabrication of perovskites solar cells.

Although perovskite devices can be prepared using evaporation procedures, during this thesis, all the devices have been prepared by multi-step solution-

[70] H. Kim, K.-G. Lim, T.-W. Lee, *Energy Environ. Sci.* **2016**, *9*, 12–30.

[71] L. Meng, J. You, T.-F. Guo, Y. Yang, *Acc. Chem. Res.* **2016**, *49*, 155–165.

[72] W. Yan, S. Ye, Y. Li, W. Sun, H. Rao, Z. Liu, Z. Bian, C. Huang, *Adv. Energy Mater.* **2016**, *6*, 1600474.

processed methods (**Figure 13**). The precise deposition process of each layer is crucial for the final device efficiency (see the Experimental Section for further details). The steps involved in the preparation of perovskite solar cells comprise:

1) Etching of the FTO from the glass substrate using Zn/HCl.
2) Spray-pyrolysis of a compact TiO_2 layer from a solution of titanium diisopropoxide bis(acetylacetonate) in ethanol at 450 ºC.
3) Deposition (by spin coating) of a mesoporous layer of TiO_2 from a suspension of TiO_2 paste dispersed in ethanol followed by an annealing at 500 ºC.
4) Spin-coating the perovskite material using the anti-solvent method followed by an annealing at 100 ºC for 1 hour.
5) Spin-coating the hole-transporting material from solution.
6) Thermal deposition of the metal electrode, generally gold.

By solution-processing layer by layer, the preparation of perovskite solar cells is cheaper and relatively ease, but it lacks a precise crystallization control as compared to vacuum deposition techniques.

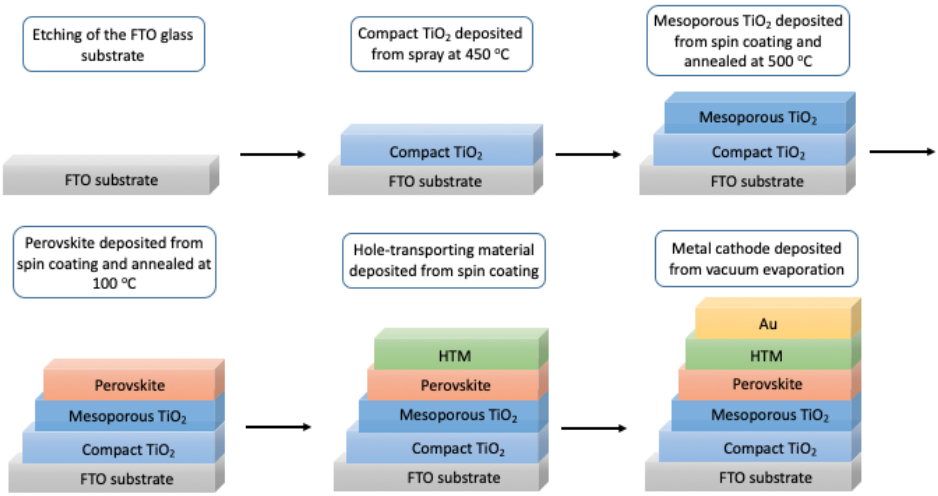

Figure 13. Schematic illustration for the fabrication of perovskite solar cells.

3.1.7 Stability of perovskite solar cells.

One of the most important factors that perovskite materials have to overcome for their future commercialization is the capacity of maintaining a stable power output under a standard working condition.[73] Perovskite devices without encapsulation shown hundreds of hours of stability when stored in the dark but undergo a rapid degradation after sustained exposure to sunlight.[74] In addition to light exposure, elevated temperature accelerates the degradation due to the moisture-induced decomposition of perovskite crystals. The lack of stability of perovskites is the most important drawback. Nevertheless, recent progress in instability issues has been achieved.[75,76] One of the most promising results in this sense was reported by Nazeeruddin and co-workers. They were able to achieve a 1-year stable perovskite solar cell employing a 2D/3D interface engineering method.[77] The combination of the 2D layer acting as a protective material against moisture, preserving the 3D perovskite results in improved stability,[78] reaching a value of efficiency of 11.9% after 1 year of irradiation. Other effective strategies that have been used are the introduction of moisture resistant layers, such as Al_2O_3 at the interface between perovskite and HTM, which is also envisioned to suppress the electron recombination between TiO_2 and HTM.[79,80,81] The use of thick carbon cathode has been explored as a

[73] T. Matsui, T. Yamamoto, T. Nishihara, R. Morisawa, T. Yokoyama, T. Sekiguchi, T. Negami, *Adv. Mater.* **2019**, *31*, 1806823.

[74] S. D. Stranks, H. J. Snaith, *Nat. Nanotechnol.* **2015**, *10*, 391.

[75] T. Leijtens, G. E. Eperon, N. K. Noel, S. N. Habisreutinger, A. Petrozza, H. J. Snaith, *Adv. Energy Mater.* **2015**, *5*, 1500963.

[76] Q. Fu, X. Tang, B. Huang, T. Hu, L. Tan, L. Chen, Y. Chen, *Adv. Sci.* **2018**, *5*, 1700387.

[77] G. Grancini, C. Roldán-Carmona, I. Zimmermann, E. Mosconi, X. Lee, D. Martineau, S. Narbey, F. Oswald, F. De Angelis, M. Grätzel, M. K. Nazeeruddin, *Nat. Commun.* **2017**, *8*, 15684.

[78] A. Mei, X. Li, L. Liu, Z. Ku, T. Liu, Y. Rong, M. Xu, M. Hu, J. Chen, Y. Yang, M. Grätzel, H. Han, *Science* **2014**, *345*, 295.

[79] S. Guarnera, A. Abate, W. Zhang, J. M. Foster, G. Richardson, A. Petrozza, H. J. Snaith, *J. Phys. Chem. Lett.* **2015**, *6*, 432–437.

[80] G. Niu, W. Li, F. Meng, L. Wang, H. Dong, Y. Qiu, *J. Mater. Chem. A* **2014**, *2*, 705–710.

[81] X. Dong, X. Fang, M. Lv, B. Lin, S. Zhang, J. Ding, N. Yuan, *J. Mater. Chem. A* **2015**, *3*, 5360–5367.

preventing layer to increase the stability of perovskite solar cells.[82,83] Another successful approach to enhance the stability of perovskite solar cells is centered on the encapsulation of perovskite solar cells. Taking into account the knowledge from organic solar cells, the most effective sealing technique for maintaining a low permeation of water vapor and oxygen, is attaching a glass or metal plate to the device using a slow-permeation epoxy-type sealant.[84,85,86]

3.1.8 Low dimensional organometal halide perovskite.

Low dimensional 2D and quasi-2D perovskites have attracted the attention of researchers recently in order to improve the stability of 3D perovskite devices.[87,88] 2D perovskites (named Ruddlesden-Popper perovskites) consist of sheets or layers ripped in a crystallographic direction from the 3D where the corner-sharing inorganic sheets are sandwiched between organic spacers. The general chemical formula is $R_2A_{n-1}B_nX_{3n+1}$, where R represents a bulky organic cation located as spacer between different layers of classical ABX_3 perovskites and n indicates the number of metal halide monolayer sheets held together (when $n = \infty$ corresponds to the conventional 3D perovskites) modulating the optoelectronic properties of the materials such as the light absorption, band-gap energy or conductivity entirely. In contrast to 3D perovskites, 2D structures show remarkably higher moisture stability due to the hydrophobic nature of the R cation intercalated in the structure as well as the highly oriented structure with a higher density packing which reduces the number of the grain boundaries,

[82] X. Xu, Z. Liu, Z. Zuo, M. Zhang, Z. Zhao, Y. Shen, H. Zhou, Q. Chen, Y. Yang, M. Wang, *Nano Lett.* **2015**, *15*, 2402–2408.

[83] F. Zhang, X. Yang, H. Wang, M. Cheng, J. Zhao, L. Sun, *ACS Appl. Mater. Interfaces* **2014**, *6*, 16140–16146.

[84] M. Jørgensen, K. Norrman, S. A. Gevorgyan, T. Tromholt, B. Andreasen, F. C. Krebs, *Adv. Mater.* **2012**, *24*, 580–612.

[85] F. Matteocci, S. Razza, F. Di Giacomo, S. Casaluci, G. Mincuzzi, T. M. Brown, A. D'Epifanio, S. Licoccia, A. Di Carlo, *Phys. Chem. Chem. Phys.* **2014**, *16*, 3918–3923.

[86] I. Hwang, I. Jeong, J. Lee, M. J. Ko, K. Yong, *ACS Appl. Mater. Interfaces* **2015**, *7*, 17330–17336.

[87] H. Lin, C. Zhou, Y. Tian, T. Siegrist, B. Ma, *ACS Energy Lett.* **2018**, *3*, 54–62.

[88] G. Grancini, M. K. Nazeeruddin, *Nat. Rev. Mater.* **2019**, *4*, 4–22.

preventing the degradation of the perovskite material in the presence of water.[89] The incorporation of 2D perovskites, therefore, bestow a longer lifetime for PSC devices but affects negatively to the photovoltaic response of the materials due to the restriction of charge transport by the organic cations acting as insulating spacing groups between the conducting 2D perovskite layers.[90] Likewise, the combination of 2D perovskites acting as a stabilizer and conventional 3D perovskites has been explored as a successful approach for increasing the lifetimes of PSCs.[77]

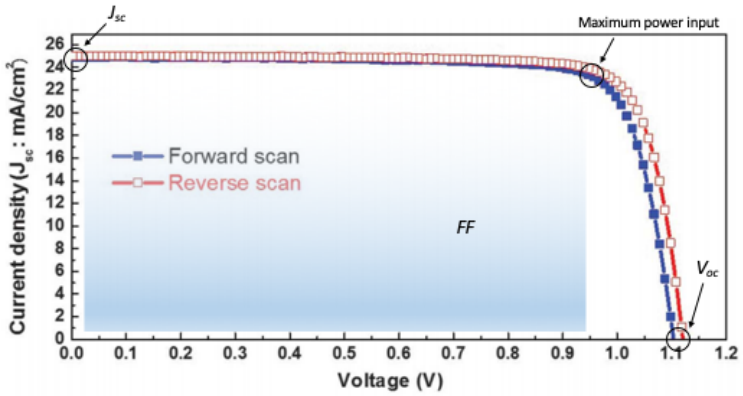

Figure 14. Typical *J-V* curves of a perovskite solar cells under illumination.

3.1.9 Photovoltaic characterization of perovskite solar cells.

The performance of perovskite solar cells is usually evaluated using *J-V* measurements obtained from a solar simulator. These measurements consist of external potentials that are applied to the PSCs and at the same time, the measurements of current generated under illumination form the solar cell (**Figure 14**). From these measurements, we can extract critical photovoltaic parameters which define the correct working of the solar cell. The open-circuit voltage (V_{oc}) is the value obtained as the applied external potential where the

[89] Y. Chen, Y. Sun, J. Peng, J. Tang, K. Zheng, Z. Liang, *Adv. Mater.* **2018**, *30*, 1–15.

[90] H. Tsai, W. Nie, J.-C. Blancon, C. C. Stoumpos, R. Asadpour, B. Harutyunyan, A. J. Neukirch, R. Verduzco, J. J. Crochet, S. Tretiak, L. Pedesseau, J. Even, M. Alam, G.Gupta, J. Lou, P. Ajayan, M. Bedzyk, M. G. Kanatzidis, A. D. Mohite, *Nature* **2016**, *536*, 312–316.

measured current is zero. Furthermore, the short-circuit current (J_{sc}) is the value of measured current when the applied external potential is zero.

The maximum power input (P_{max}) of the solar cell is determined as the product of the photocurrent and voltage reaching maximum values of current and potential (J_{max} and V_{max} respectively) which defines the fill factor value (*FF*) (**Equation 2**).

$$FF = \frac{Jmax\ Vmax}{Jsc\ Voc}$$

The optimization of these three parameters determines the power conversion efficiency of the perovskite solar cells, which is the fraction of the maximum electric power output from the incident power following the **Equation 3**:

$$PCE = \frac{Jsc\ Voc\ FF}{Pin}$$

It is important to clarify that in PSCs, the performance of the cells is highly dependent of the scan direction (forward and reverse), which is clearly shown in the *J-V* curves (**Figure 14**). This differential behavior which depend of the scan direction is called hysteresis.[91,92,93] Hysteresis behavior has been observed in other photovoltaic technologies including CIGS, CdTe and amorphous silicon. This effect has been attributed to a charge carrier accumulation and recombination in the photoactive material or neutral region of the interfaces, the existence or formation of defect states and other phenomena such as ion

[91] W. Tress, N. Marinova, T. Moehl, S. M. Zakeeruddin, M. K. Nazeeruddin, M. Grätzel, *Energy Environ. Sci.* **2015**, *8*, 995–1004.

[92] E. L. Unger, E. T. Hoke, C. D. Bailie, W. H. Nguyen, A. R. Bowring, T. Heumüller, M. G. Christoforo, M. D. McGehee, *Energy Environ. Sci.* **2014**, *7*, 3690–3698.

[93] S. van Reenen, M. Kemerink, H. J. Snaith, *J. Phys. Chem. Lett.* **2015**, *6*, 3808–3814.

migration.[94,95] These charges might have been stored previously under open circuit or forward bias, which favor high charge carrier densities within the solar cell.[96] Bias-dependent of the ionic redistribution results in the apparition of ionic space charge at the interfaces of the perovskite, which is reflected in the voltage of the perovskite. This change in the voltage could lead to different $J-V$ curves from the forward and the reverse scans. In order to quantify the discrepancy between the forward and reverse scan in perovskite solar cells and its corresponding measured photovoltaic values for the J_{sc}, V_{oc}, FF and power conversion efficiency, the hysteresis index is defined under the **Equation 4**:[97]

$$Hysteresis\ Index = \frac{PCE\ (reverse) - PCE\ (forward)}{PCE\ (reverse)}$$

[94] C. Eames, J. M. Frost, P. R. F. Barnes, B. C. O'Regan, A. Walsh, M. S. Islam, *Nat. Commun.* **2015**, *6*, 7497.

[95] H.-S. Kim, I. Mora-Sero, V. Gonzalez-Pedro, F. Fabregat-Santiago, E. J. Juarez-Perez, N.-G. Park, J. Bisquert, *Nat. Commun.* **2013**, *4*, 2242.

[96] V. W. Bergmann, S. A. L. Weber, F. Javier Ramos, M. K. Nazeeruddin, M. Grätzel, D. Li, A. L. Domanski, I. Lieberwirth, S. Ahmad, R. Berger, *Nat. Commun.* **2014**, *5*, 5001.

[97] S. N. Habisreutinger, N. K. Noel, H. J. Snaith, *ACS Energy Lett.* **2018**, *3*, 2472–2476.

3.2 Hole transporting materials for perovskite solar cells.

The aim of the present thesis is focused on the design of hole-transporting materials for its use on perovskite solar cells (PSCs). The implementation of a hole conducting layer is essential for building high-efficient PSCs because HTM has to improve the hole extraction in the perovskite/HTM interface and its transfer to the metal electrode. At the same time, the hole transporting material should prevent undesirable charge transfer or recombination processes by acting as electron blocking layer and improving the stability of the perovskite material from moisture or oxygen.[98] For those reasons, hole-transporting materials should present a HOMO energy level slightly higher in energy than the valence band of the perovskite solar cells to ensure an efficient hole injection. In contrast, the LUMO energy level has to be much higher in energy than the conduction band of the perovskite material to present electron blocking properties. Additionally, ideal HTMs should present good values of conductivity and/or hole mobility as well as high thermal stability for long-term device stability. Finally, HTMs should be prepared from a straightforward synthesis for a low-cost production of perovskite solar cells. Some of these characteristics can be found in most of the common HTMs, which are based on the use of organic compounds[99,100,101,102].

---

98 S. Maddala, C.-L. Chung, S.-Y. Wang, K. Kollimalayan, H.-L. Hsu, P. Venkatakrishnan, C.-P. Chen, Y. J. Chang, *Chem. Mater.* **2019**, *32*, 127-138.

99 N. J. Jeon, H. Na, E. H. Jung, T.-Y. Yang, Y. G. Lee, G. Kim, H.-W. Shin, S. I. Seok, J. Lee, J. Seo, *Nat. Energy* **2018**, *3*, 682–689.

100 M. Saliba, S. Orlandi, T. Matsui, S. Aghazada, M. Cavazzini, J.-P. Correa-Baena, P. Gao, R. Scopelliti, E. Mosconi, K.-H. Dahmen, F. De Angelis, A. Abate, A. Hagfeldt, G. Pozzi, M. Grätzel, M. K. Nazeeruddin, *Nat. Energy* **2016**, *1*, 15017.

101 B. Xu, J. Zhang, Y. Hua, P. Liu, L. Wang, C. Ruan, Y. Li, G. Boschloo, E. M. J. Johansson, L. Kloo, A. Hagfeldt, A. K.-Y. Jen, L. Sun, *Chem* **2017**, *2*, 676–687.

102 A. Molina-Ontoria, I. Zimmermann, I. Garcia-Benito, P. Gratia, C. Roldán-Carmona, S. Aghazada, M. Graetzel, M. K. Nazeeruddin, N. Martín, *Angew. Chem. Int. Ed.* **2016**, *55*, 6270–6274.

On the other hand, inorganic compounds[103,104] and polymeric materials.[105,106,107,108,109,110] have been also explored as useful approaches for highly efficient HTMs.

3.2.1 Role of dopants in hole transporting materials.

Most of the HTMs used in PSCs are based on organic semiconductors, which present excellent properties for photovoltaic applications such as mild processing conditions, good alignment of its energy levels, or excellent optical and electrochemical properties. These properties can be easily tuned through chemical and synthetic design.[111,112] Nevertheless, organic molecules typically show relatively low hole mobility and/or conductivity due to their intrinsic properties.[113] Hence, the addition of chemical dopants is necessary in order to increase the electronic properties, such as increasing the conductivity of the organic film or reducing its ohmic losses for achieving highly-efficient

---

[103] N. Arora, M. I. Dar, A. Hinderhofer, N. Pellet, F. Schreiber, S. M. Zakeeruddin, M. Grätzel, *Science* **2017**, *358*, 768.

[104] W. Chen, Y. Wu, Y. Yue, J. Liu, W. Zhang, X. Yang, H. Chen, E. Bi, I. Ashraful, M. Grätzel, L. Han, *Science* **2015**, *350*, 944.

[105] G. Kim, J. Lee, G. Kang, T. Kim, T. Park, *Adv. Energy Mater.* **2018**, *8*, 1870018.

[106] Y. S. Kwon, J. Lim, H.-J. Yun, Y.-H. Kim, T. Park, *Energy Environ. Sci.* **2014**, *7*, 1454–1460.

[107] F. Bella, G. Griffini, J.-P. Correa-Baena, G. Saracco, M. Grätzel, A. Hagfeldt, S. Turri, C. Gerbaldi, *Science* **2016**, *354*, 203-206.

[108] M. M. Tavakoli, J. Zhao, R. Po, G. Bianchi, A. Cominetti, C. Carbonera, J. Kong, *Adv. Funct. Mater.* **2019**, 1905887.

[109] Q. Xiao, J. Tian, Q. Xue, J. Wang, B. Xiong, M. Han, Z. Li, Z. Zhu, H.-L. Yip, Z. Li, *Angew. Chem. Int. Ed.* **2019***, 58,* 17724–17730.

[110] F. Qi, X. Deng, X. Wu, L. Huo, Y. Xiao, X. Lu, Z. Zhu, A. K.-Y. Jen, *Adv. Energy Mater.* **2019**, *9*, 1902600.

[111] K. Walzer, B. Maennig, M. Pfeiffer, K. Leo, *Chem. Rev.* **2007**, *107*, 1233–1271.

[112] J. Urieta-Mora, I. García-Benito, A. Molina-Ontoria, N. Martín, *Chem. Soc. Rev.* **2018**, *47*, 8541–8571.

[113] B. Lüssem, M. Riede, K. Leo, *Phys. Status Solidi* **2013**, *210*, 9–43.

perovskite solar cells.[114,115,116] Usually, organic-based HTMs have been heavily doped with p-type dopants to enhance their electronic properties. The basic principle for p-type dopants consists in generating additional mobile charge carriers by the addition of electron acceptors in order to remove electrons from the HOMO of the hole-transporting material producing intrinsic holes in the molecule. Therefore, the charge carrier density in the HTM is enhanced, which leads to an improved conductivity.[117]

During the last years, many p-type dopants for improving the device performance have been reported. In this context, classical organic oxidants such as 2,3,5,6-tetrafluoro-7,7,8,8-tetracyano-*p*-quinodimethane (F_4-TCNQ),[118,119] benzoyl peroxide[120] or tris(pentafluorophenyl)borane[121] have been successfully applied as p-dopants for HTMs. Moreover, organometallic compounds based on copper (II) and cobalt (III) complexes have also been described.[122,123] To date, the standard protocols of p-dopants include a combination of cobalt (III) complex (tris[2-[1H-pyrazol-1-yl]-4-tert-butylpyridine]cobalt tri[bis(trifluoromethane)sulfonimide]) (FK-209) and

---

114 U. Bach, D. Lupo, P. Comte, J. E. Moser, F. Weissörtel, J. Salbeck, H. Spreitzer, M. Grätzel, *Nature* **1998**, *395*, 583–585.

115 J. Krüger, R. Plass, L. Cevey, M. Piccirelli, M. Grätzel, U. Bach, *Appl. Phys. Lett.* **2001**, *79*, 2085–2087.

116 A. Abate, T. Leijtens, S. Pathak, J. Teuscher, R. Avolio, M. E. Errico, J. Kirkpatrik, J. M. Ball, P. Docampo, I. McPherson, H. J. Snaith, *Phys. Chem. Chem. Phys.* **2013**, *15*, 2572–2579.

117 K. Rakstys, C. Igci, M. K. Nazeeruddin, *Chem. Sci.* **2019**, *10*, 6748-6769.

118 D.-Y. Chen, W.-H. Tseng, S.-P. Liang, C.-I. Wu, C.-W. Hsu, Y. Chi, W.-Y. Hung, P.-T. Chou, *Phys. Chem. Chem. Phys.* **2012**, *14*, 11689–11694.

119 M. A. Mahmud, N. K. Elumalai, M. B. Upama, D. Wang, V. R. Gonçales, M. Wright, C. Xu, F. Haque, A. Uddin, *Phys. Chem. Chem. Phys.* **2017**, *19*, 21033–21045.

120 Q. Liu, L. Fan, Q. Zhang, A. Zhou, B. Wang, H. Bai, Q. Tian, B. Fan, T. Zhang, *ChemSusChem* **2017**, *10*, 3098–3104.

121 T. Ye, J. Wang, W. Chen, Y. Yang, D. He, *ACS Appl. Mater. Interfaces* **2017**, *9*, 17923–17931.

122 C. Chen, W. Zhang, J. Cong, M. Cheng, B. Zhang, H. Chen, P. Liu, R. Li, M. Safdari, L. Kloo, L. Sun, *ACS Energy Lett.* **2017**, *2*, 497–503.

123 J. H. Noh, N. J. Jeon, Y. C. Choi, M. K. Nazeeruddin, M. Grätzel, S. I. Seok, *J. Mater. Chem. A* **2013**, *1*, 11842–11847.

lithium bis(trifluoromethanesulfonyl) imide (LiTFSI) for increasing the device efficiency (**Figure 15**). Seok and co-workers firstly studied the combination and the synergistic effects of adding both dopant to 2,2',7,7'-tetrakis[*N*,*N*-di(4-methoxyphenyl)amino]-9,9'-spirobifluorene (spiro-OMeTAD).[123] LiTFSI is reported to boost the conductivity of the HTM but does not chemically oxidize the HTM directly. In contrast, FK-209 produces an effective electron transfer from the HTM, leaving the HTM partially oxidized (radical cation). As a consequence, higher conductivities are obtained due to the formation of additional holes, which increases in the charge carrier density. Furthermore, the co-doping produces an improvement in the open-circuit voltage (V_{oc}) due to the reduced carrier recombination at the interface between the perovskite and the HTM. Additionally, as a routine, spiro-OMeTAD is doped with tert-butylpyridine (^{t}BP) in order to improve the film formation ability on the top of the perovskite by reducing the number of pinholes and, at the same time, preventing the aggregation of lithium salts in the layer.[124] These effects lead to an increase in the photovoltaic performance and the steady-state efficiency of perovskite solar cells. On the other hand, the use of dopants in the hole-transporting materials present some disadvantages in device stability. The addition of LiTFSI and ^{t}BP accelerates cell degradation due to their hygroscopic properties.[124] The incorporation of the different complex of cobalt (III) leads to chemical degradation of the material, which has a negative impact on the long-term stability of the device.

3.2.2 Chemical design of hole transporting materials.

Since the first introduction of a solid-state HTM by Snaith and co-workers, the well-known spiro-OMeTAD,[68] a wide variety of structures, either organic or inorganic have been reported in the bibliography. Based on their chemical structures, HTMs can be divided in three categories: small organic molecules, organic polymers and inorganic compounds. In the present thesis, the

[124] E. J. Juarez-Perez, M. R. Leyden, S. Wang, L. K. Ono, Z. Hawash, Y. Qi, *Chem. Mater.* **2016**, *28*, 5702–5709.

background of hole-transporting material will be specifically focused on small organic molecules.

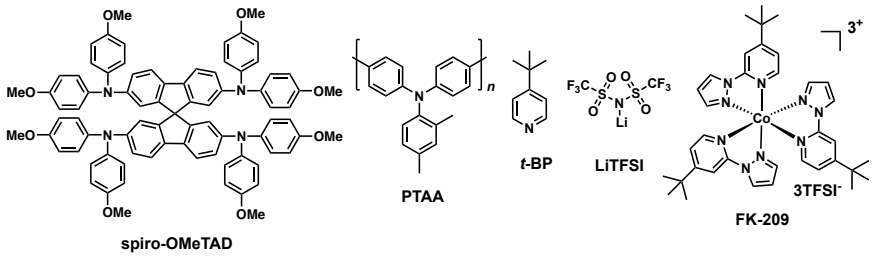

Figure 15. Chemical structures of spiro-OMeTAD, PTAA and most common dopants.

3.2.3 Hole-transporting materials based on small organic molecules.

Regarding the use of small molecules for hole-transporting applications in perovskite solar cells, spiro-OMeTAD is the benchmark molecule. The chemical structure of spiro-OMeTAD (**Figure 15**) is based on a 9,9'-spirobifluorene scaffold, which is conveniently functionalized with four units of *p*-methoxydiphenylamine. The "spiro" linkage consists of two extended π-systems connected through a tetrahedral sp^3-hybridized atom, providing an orthogonal configuration between the aromatic systems.[125] This spiro linkage usually has a beneficial impact on the morphological properties, whereas the optoelectronic properties are almost preserved. Since the first report of 9,9'-spirobifluorene in 1930,[126] spiro-based compounds have been extensively used in optoelectronic applications. On the other hand, the preparation of the 9,9'-spirobifluorene central core requires a complicated five-step synthetic protocol with a relatively low overall yield. Therefore, during the synthesis, it is required the use of harsh conditions as low temperature (-78 ºC), sensitive reagents (*n*-butyllithium or Grignard compounds) or aggressive reagents (Br_2). These drawbacks, along with a requirement of a sublimation-grade purity, make that the spiro-OMeTAD presents a high commercial cost, which limits its potential use for large-scale PV

125 T. P. I. Saragi, T. Spehr, A. Siebert, T. Fuhrmann-Lieker, J. Salbeck, *Chem. Rev.* **2007**, *107*, 1011–1065.

126 R. G. Clarkson, M. Gomberg, *J. Am. Chem. Soc.* **1930**, *52*, 2881–2891.

applications. To date, spiro-OMeTAD has been the most highlighted hole-transporting material in PSCs. Devices based on spiro-OMeTAD as HTM have achieved outstanding photovoltaic performance, surpassing 20% during the recent years.[30,127] Spiro-OMeTAD presents high solubility in common organic solvents such as toluene or chlorobenzene for almost colorless thin films, easy processability from solution, well-matched energy HOMO level and relatively high hole mobility (10^{-4} - 10^{-5} $cm^2 V^{-1} s^{-1}$).

As a consequence of its high commercial cost and its complicated future implementation in PV-technologies of spiro-OMeTAD, a wide variety of HTMs have been reported during the recent years for achieving high efficiencies in PSCs. As the most representative example, the polymer formed by triphenylamine units, poly[bis(4-phenyl)(2,4,6-trimethylphenyl)amine] (PTAA), (**Figure 15**) has been successfully introduced for preparing high efficient devices surpassing 22%.[52,128] Nevertheless, PTAA also presents an excessive commercial price of 1.980 €/g (Sigma-Aldrich), which limits its use in large-scale commercial applications. The outstanding performance of PTAA-based solar cells is based on its exceptional hole mobility (10^{-2} - 10^{-3} $cm^2 V^{-1} s^{-1}$), which is much higher than typical small organic molecules.

3.2.4 Spiro-based molecular hole-transporting materials

During recent years and motivated by the outstanding photovoltaic properties of spiro-OMeTAD, many examples of spiro-like organic structures have been reported in the literature (**Figure 16**). The photovoltaic parameters of spiro-based HTMs are summarized in **Table 1**.

Seok and co-workers introduced one of the first representative examples of spiro-like HTMs. By chemical engineering of alternative spiro-OMeTAD, the authors altered the position of the methoxy group in the periphery of the

---

[127] X. Li, D. Bi, C. Yi, J.-D. Décoppet, J. Luo, S. M. Zakeeruddin, A. Hagfeldt, M. Grätzel, *Science* **2016**, *353*, 58-62.

[128] W. S. Yang, B.-W. Park, E. H. Jung, N. J. Jeon, Y. C. Kim, D. U. Lee, S. S. Shin, J. Seo, E. K. Kim, J. H. Noh, S. I. Seok, *Science* **2017**, *356*, 1376.

dipheylamines. (HTM-1 and HTM-2)[129] (**Figure 16**). It is important to mention that the introduction of methoxy group in the structure of the hole-transporting material not only tune the HOMO level of the HTM to be aligned with the valence band edge of the perovskite but also can play a role for improving the contact in the interface between HTM/perovskite. The substitution in different positions of the -OCH_3 group affects the optoelectronic properties of the HTM, according to the Hammett strategy.[130,131] Seok and co-workers introduced HTM-1 (*ortho*-substitution of -OCH_3 group) and HTM-2 (*meta*-substitution of -OCH_3 group) and prepared devices using $MAPbI_3$ perovskite for studying its photovoltaic properties in comparison to *para*-substitution of –OCH_3 group in the spiro-OMeTAD. Power conversion efficiencies of 13.9 and 16.7% were achieved for HTM-1 and HTM-2, respectively, with similar values of V_{oc} and J_{sc}. The superior performance of HTM-2 results from its higher *FF* (0.77) than that of HTM-1, which can be attributed to its low series resistance (R_s) and high shunt resistance (R_{sh}). Furthermore, the efficiency of commercial and synthesized were similar to the reference, spiro-OMeTAD (**Table 1**).

Following the Hammett strategy, Huang and co-workers synthesized three new alternative structures for spiro-OMeTAD by the modification of the donor ability of the pendant group.[132] The -OCH_3 groups in the periphery of the diphenylamines were replaced with ethyl groups (HTM-4), methylsulfanyl (HTM-5), and *N*,*N*-dimethylamino (HTM-6) groups (**Figure 16**). As a consequence, the optical and electrochemical properties were profoundly affected, showing that the stronger π-donation ability of the -NMe_2 group leads to a higher HOMO energy (-4.82 eV) than those obtained for –OMe, -Et and -SMe (-5.16, -5.21 and -5.32 eV, respectively). Moreover, the heteroatom substitution has also a significant impact on the power conversion efficiency and charge-transport of the hole transporting materials. Power conversion

[129] N. J. Jeon, H. G. Lee, Y. C. Kim, J. Seo, J. H. Noh, J. Lee, S. I. Seok, *J. Am. Chem. Soc.* **2014**, *136*, 7837–7840.

[130] L. P. Hammett, *J. Am. Chem. Soc.* **1937**, *59*, 96–103.

[131] L. Calió, S. Kazim, M. Grätzel, S. Ahmad, *Angew. Chem. Int. Ed.* **2016**, *55*, 14522–14545.

[132] Z. Hu, W. Fu, L. Yan, J. Miao, H. Yu, Y. He, O. Goto, H. Meng, H. Chen, W. Huang, *Chem. Sci.* **2016**, *7*, 5007–5012.

efficiencies of 15.75, 15.92, and 11.92% were measured using HTM-3, HTM-4, and HTM-5 as HTM, respectively, in inverted $MAPbI_3$-based devices (**Table 1**). From SEM images, it was observed a strong influence of the grain size $MAPbI_3$ perovskite, which is affected by the different HTMs. Accordingly, the lower hydrophobic surface of HTM-5 resulted in smaller grain sizes of $MAPbI_3$ perovskite. On the other hand, larger grain sizes were formed by using spiro-OMeTAD, HTM-4, and HTM-3, which presented higher hydrophobicity.[132]

One of the most common strategies for introducing spiro-linkage is using spiro[fluorene-9,9'-xanthene] units (SFX)[133] (**Figure 16**). In this context, Hagfeldt and co-workers reported one of the first examples of spiro-cyclization of 2,7-dibromo-9-fluorenone with phenol in the presence of methanosulfonic acid giving rise to the spiro[fluorene-9,9'-xanthene] central scaffold for the preparation of HTM-6.[134] The two-armed diphenylamine substituted SFX presented a similar packing that those observed for spiro-OMeTAD, yielding an outstanding power conversion efficiency of 19.8%, which was comparable to the spiro-OMeTAD under the same conditions (20.8%). Noteworthy, using HTM-6, the devices exhibited minimized hysteresis and relatively good stability under dark and dry conditions when was combined with the mixed $[FAPbI_3]_{0.85}[MAPbBr_3]_{0.15}$ perovskite. In a different work, the same authors reported the tetra-armed SFX (HTM-7) substituted with *p*-methoxydiphenylamines mimicking the structure of spiro-OMeTAD.[135] As a consequence of the structural similarity between HTM-7 and spiro-OMeTAD, it exhibits similar HOMO energy and optical properties. Furthermore, HTM-7 showed higher values of hole mobility than the spiro-OMeTAD, which was also confirmed through theoretical calculations. The use of doped HTM-7 in combination with $MAPbI_3$-based perovskite yielded an impressive 19.84% for

133 L.-H. Xie, F. Liu, C. Tang, X.-Y. Hou, Y.-R. Hua, Q.-L. Fan, W. Huang, *Org. Lett.* **2006**, *8*, 2787–2790.

134 D. Bi, B. Xu, P. Gao, L. Sun, M. Grätzel, A. Hagfeldt, *Nano Energy* **2016**, *23*, 138–144.

135 B. Xu, D. Bi, Y. Hua, P. Liu, M. Cheng, M. Gratzel, L. Kloo, A. Hagfeldt, L. Sun, *Energy Environ. Sci.* **2016**, *9*, 873–877.

power conversion efficiency that outperforms the spiro-OMeTAD, with a noticeably short circuit current of 24.2 mA cm^{-2}.

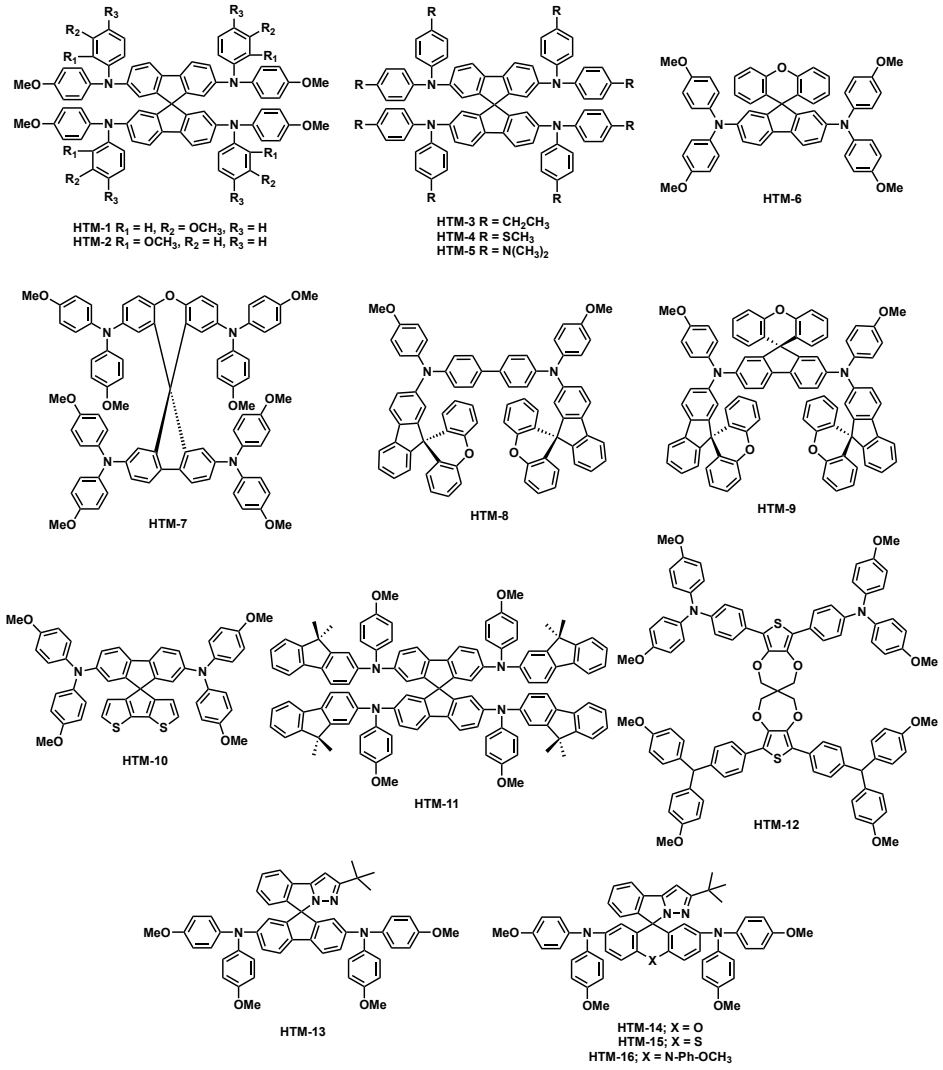

Figure 16. Chemical structures of reported spiro-based hole transporting materials.

Recently, Hagfeldt and co-workers designed two SFX-based HTMs incorporating two or three units of SFX in the structure [101] (**Figure 16**). The authors claimed that increasing the number of SFX in the structure of HTM-8

and HTM-9 improve the morphological features of the HTM in the devices, reducing the formation of pinholes. Both HTMs exhibit moderate absorbances at 493 and 525 nm after chemical doping, respectively, which correspond to the formation of the radical cation of the HTMs. The HOMO energy levels of the HTMs were slightly deeper in energy than spiro-OMeTAD, with values of -5.24 eV for HTM-8 and -5.17 eV for HTM-9, showing a proper alignment with the valence band edge of the perovskite assuring an effective extraction of the hole. This is confirmed by steady-state photoluminescence when the HTM is deposited on top of the perovskites. HTM-9 presented a more efficient quenching of the PL signal than HTM-8 and spiro-OMeTAD, which lead to a more efficient hole extraction. Both HTMs were tested in combination with $[FAPbI_3]_{0.85}[MAPbBr_3]_{0.15}$ perovskite reaching a maximum PCE of 13.6% for HTM-8 and an outstanding 20.8% using HTM-9, which is even higher than the reference of spiro-OMeTAD. The excellent solubility of HTM-9 (70 mg/mL) due to its more distorted and extended 3D structure ensures the full coverage of the perovskite layer without the formation of pinholes.

In 2016 Zakeeruddin, Grätzel, Nazeeruddin, and co-workers introduced a novel spiro-cyclopentadithiophene as a central scaffold for the synthesis of HTM-10 [100] (**Figure 16**). The new two-armed diphenylamino substituted spiro-cyclopentadithiophene showed red-shifted absorption compared to spiro-OMeTAD with similar donor ability with a HOMO energy of -5.18 eV. The HTM-10 was introduced in a conventional PSC configuration of FTO/c-TiO_2/m-TiO_2/$[FAPbI_3]_{0.85}[MAPbBr_3]_{0.15}$/HTM/Au reaching a remarkable power conversion efficiency of 20.3%, which outperformed spiro-OMeTAD and making HTM-10 one of the most promising small organic molecule for hole-transporting applications. Using theoretical calculations, the authors surmised that the interaction of spiro-OMeTAD with $MAPbI_3$ perovskite at the interface occurred mainly between the -OCH_3 groups on the periphery of the HTM and the methylammonium sites in the perovskite. On the other hand, the interface between HTM-10 and the $MAPbI_3$ perovskite revealed additional sulfur-iodine interactions. This “docking” process allows a stronger interaction, which enhanced interfacial coupling between HTM-10 and the perovskite, thus facilitating the injection of the holes.

Table 1. Photovoltaic parameters of spiro-based HTMs.

HTM	V_{OC} (V)	J_{SC} (mA cm^{-2})	*FF*	PCE (%)	Reference
HTM-1	1.01	21.1	0.65	13.9	129
HTM-2	1.02	21.2	0.78	16.7	129
HTM-3	1.07	18.2	0.80	15.75	132
HTM-4	1.06	19.2	0.78	15.92	132
HTM-5	0.96	16.6	0.75	11.92	132
HTM-6	1.13	23.4	0.73	19.8	134
HTM-7	1.14	24.2	0.71	19.84	135
HTM-8	0.95	21.3	0.67	13.6	101
HTM-9	1.15	23.4	0.77	20.8	101
HTM-10	1.15	22.7	0.76	20.2	100
HTM-11	1.14	24.91	0.81	23.20	99
HTM-12	1.02	17.6	0.73	13.44	136
HTM-13	1.05	19.5	0.69	14.19	137
HTM-14	1.07	19.10	0.79	16.08	138
HTM-15	1.10	20.60	0.80	18.06	138
HTM-16	0.77	11.28	0.58	5.02	138

Recently, Seok and co-workers reported a tailored alternative of spiro-OMeTAD by substituting a *p*-methoxyphenyl in the periphery of the diphenylamine by a fluorine-terminated unit in HTM-11[99] (**Figure 16**). HTM-11 displayed not only a slightly red-shifted absorption maximum due to the extended π-conjugation by of the fluorene units in comparison to the *p*-methoxyphenyl but also a deeper HOMO energy (-5.27 eV). HTM-11 was integrated into a conventional configuration of FTO/c-TiO_2/m-TiO_2/$[FAPbI_3]_{0.95}[MAPbBr_3]_{0.05}$/HTM-11/Au reaching an outstanding power conversion efficiency of 23.20% with a J_{sc} of 24.91 mAcm^{-2} (**Table 1**). Additionally, HTM-11 presented similar values of resistance than spiro-OMeTAD as well as similar charge extraction ability measured using photoluminescence studies. Devices based on HTM-11 presented more thermal stability than the devices using spiro-OMeTAD,

retaining 95% of its initial performance after more than 500 h at 60 °C. To date, HTM-11 can be considered as the most efficient small organic molecule to replace spiro-OMeTAD.

At the beginning of 2015 Grätzel, Nazeeruddin and co-workers introduced the thiophene-based spiro-like HTM-12 by the introduction of two propylenedioxythiophenes connected through a tetrahedral sp^3-hybridized carbon[136] (**Figure 16).** HTM-12 presents similar optoelectronic properties than those observed in spiro-OMeTAD. The authors evaluated the photovoltaic performance of HTM-12 in the presence of FK-209 dopant, showing better results for the doped-HTM with a maximum PCE of 13.4% but a remarkable efficiency of 12.7% for the non-doped HTM. These values were slightly higher than those obtained for doped spiro-OMeTAD.

Chi and co-workers introduced spiro-linkage with the incorporation of C-N bonds using a system based on phenylpyrazole/fluorene (HTM-13)[137] (**Figure 16**). The synthetic strategy is similar to the preparation of spiro-OMeTAD. HTM-13 showed an adequate HOMO energy level -5.22 eV and very similar absorption to the spiro-OMeTAD. Devices based on HTM-13, in combination with $MAPbI_3$ perovskite, reached a power conversion efficiency of 14.19%. Lately, the same authors reported two new spiro-based HTMs with C-N linkage in the structure by connecting phenylpyrazole and xanthene, thioxanthene, or acridine (HTM-14, HTM-15 and HTM-16 respectively).[138] Due to the incorporation of the new heteroatom, HTMs exhibited a blue-shifted absorption (70 nm) in comparison to spiro-OMeTAD due to its disrupted conjugation. Furthermore, the donor ability is also importantly tuned, showing a strong donor character for HTM-16 with a HOMO energy of -5.02 eV while HTM-14 and HTM-15 presented similar energies (-5.30 and -5.29 eV respectively). New HTMs were introduced in an ITO/SnO_2/C_{60}/$MAPbI_3$/HTM/MoO_3/Ag

[136] P. Ganesan, K. Fu, P. Gao, I. Raabe, K. Schenk, R. Scopelliti, J. Luo, L. H. Wong, M. Gratzel, M. K. Nazeeruddin, *Energy Environ. Sci.* **2015**, *8*, 1986–1991.

[137] Y. Wang, T.-S. Su, H.-Y. Tsai, T.-C. Wei, Y. Chi, *Sci. Rep.* **2017**, *7*, 7859.

[138] Y. Wang, Z. Zhu, C. Chueh, K. -Y Jen Alex, Y. Chi, *Adv. Energy Mater.* **2017**, *7*, 1700823.

configuration achieving maximum power conversion efficiencies of 16.08, 18.06 and 5.01% for HTM-14, HTM-15 and HTM-16, respectively (**Table 1**).

3.2.5 Carbocyclic-based molecular engineering HTMs.

One of the most common alternatives to tailor hole-transporting materials is based on the introduction in carbocyclic aromatic central scaffolds. During recent years, a wide variety of small molecules synthesized from carbocyclic structures have been combined with different periphery groups for the preparation of highly efficient PSCs (**Figure 17**). In this context, simple backbones as benzene and biphenyl have been used as central scaffolds for the synthesis of efficient HTMs, but also more complex structures such as azulene, paracyclophane or carbon nanotubes have been employed.[139] The photovoltaic parameter of carbocyclic-based HTMs are gathered in **Table 2**.

Ahmad and co-workers reported a custom-made pentacene central backbone substituted with triisopropylsilylethynyl groups (TIPS) in positions 6 and 13 as HTM [140] (HTM -17). The incorporation of the TIPS groups in the structure improves the solubility of the material, whereas allowing the supramolecular π-stacking of the molecules into 2D columnar structures.[141] HTM-17 showed a red-shifted absorption bands centered on 549, 592, and 642 nm and a deeper HOMO energy (-5.43 eV) than spiro-OMeTAD. HTM-17 was used in combination with $MAPbI_3$ perovskite as dopant-free HTM achieving a power conversion efficiency of 11.5%, which made the use of HTM-17 as the first representative example of a dopant-free HTM which is surmised to be critical for long-term stability of the devices.

In 2015, Martín and co-workers reported, for the first time, the use of tetraarylethene as backbones for the synthesis of HTM-18, which was

---

139 Y. Lu, X. Zong, Y. Wang, W. Zhang, Q. Wu, M. Liang, S. Xue, *J. Mater. Chem. C* **2019**, *7*, 14306-14313.

140 S. Kazim, F. J. Ramos, P. Gao, M. K. Nazeeruddin, M. Grätzel, S. Ahmad, *Energy Environ. Sci.* **2015**, *8*, 1816–1823.

141 J. E. Anthony, J. S. Brooks, D. L. Eaton, S. R. Parkin, *J. Am. Chem. Soc.* **2001**, *123*, 9482–9483.

functionalized with *p*-methoxydiphenylamines in the periphery.[142] Noteworthy, HTM-18 can be synthesized in two synthetic steps from commercially available 4,4'-diaminobenzophenone, through a two-fold Ullmann reaction with 4-iodoanisole followed by a McMurry coupling reaction of corresponding ketones in the presence of a titanium reagent. HTM-18 was employed in mesoporous $MAPbI_3$-based devices as dopant-free HTM, reaching a power conversion efficiency of 11.02%, which was slightly lower than the spiro-OMeTAD (13.53%) (**Table 2**). Shortly after, Ko and co-workers reported the use of HTM-18 but under doped conditions.[143] In this case, the mesoporous $MAPbI_3$-based devices displayed a power conversion efficiency of 13.09%, which was lower than the spiro-OMeTAD under the same conditions (13.87%). Very recently, HTM-18 was successfully used as dopant-free HTM for tin-based PSCs.[59] The use of the non-doped HTM-18 in combination with {en}$FASnI_3$-based perovskite displayed a remarkable PCE of 7.02%, which outperformed the values obtained for the spiro-OMeTAD (5.20%) and PTAA (6.67%).

In 2015, Scott, Murata, and co-workers reported three new hole-transporting materials introducing a chemically designed oxygen-bridged triphenylamine in combination with an atypical azulene central scaffold (HTM-19, HTM-20, HTM-21)[144,145] (**Figure 17**). Azulene-based HTM-19-21 showed strong absorptions in the UV region, which can be attributed to π–π* transitions and a broad peak in the visible region due to the intramolecular charge transfer. The incorporation of HTM-19-21 into $MAPbI_3$-based devices led to power conversion efficiencies of 16.5% for tetra-substituted HTM-19, 9.7 for HTM-20 and 8.5 for HTM-21. This superior performance of HTM-19 was attributed to its higher conductivity (similar to spiro-OMeTAD) and the better hole-extraction in the $MAPbI_3$/HTM interface. It was surmised that the face-on orientation of

142 L. Cabau, I. Garcia-Benito, A. Molina-Ontoria, N. F. Montcada, N. Martin, A. Vidal-Ferran, E. Palomares, *Chem. Commun.* **2015**, *51*, 13980–13982.

143 H. Choi, K. Do, S. Park, J.-S. Yu, J. Ko, *Chem. – A Eur. J.* **2015**, *21*, 15919–15923.

144 H. Nishimura, N. Ishida, A. Shimazaki, A. Wakamiya, A. Saeki, L. T. Scott, Y. Murata, *J. Am. Chem. Soc.* **2015**, *137*, 15656–15659.

145 M. A. Truong, J. Lee, T. Nakamura, J.-Y. Seo, M. Jung, M. Ozaki, A. Shimazaki, N. Shioya, T. Hasegawa, Y. Murata, et al., *Chem. – A Eur. J.* **2019**, *25*, 6741–6752.

HTM-19 on top of the $MAPbI_3$ layer could have a beneficial impact on the charge collection of the HTM, which was also enhanced by the two-dimensionally expanded molecular shape of the HTM-19.

Other representative examples of carbocyclic backbones for the synthesis of HTM were reported by Son and co-workers in two different works. The author employed [2,2']paracyclophane as central core for the preparation of *p*-methoxytriphenylamine tri- or tetrasubstituted HTM-22 and HTM-23 respectively[146,147] (**Figure 17**). The structure of [2,2']paracyclophane (PcP) consists of two parallel benzene rings connected through ethylene bridges. From its structure, PcP display optoelectronic and physical properties such as a strong electronic coupling through the space between the benzene rings (ring–ring spacing similar to van der Waals interactions). Furthermore, as a consequence of its dense packing in the thin-film due to the rigid shape of PcP, it is usually observed an enhancement of the charge transport ability in the three-dimensional structure. Son and co-workers reported HTM-22 and HTM-23 using three or four units of *p*-methoxytriphenylamines as donor units to achieve an adequate HOMO energy level (-5.28 eV and -5.27 eV, respectively). The optical properties of HTM-22 and HTM-23 were similar to those of spiro-OMeTAD with a maximum absorption centered at 356 and 365 nm, respectively, while the emission is strongly red-shifted (470 nm). $MAPbI_3$-based PSCs incorporating HTM-22 and HTM-23 displayed power conversion efficiencies of 16.4 and 18.0% respectively, confirming that the use of [2,2']paracyclophane as potential candidates for hole-transporting applications.

[146] S. Park, J. H. Heo, C. H. Cheon, H. Kim, S. H. Im, H. J. Son, *J. Mater. Chem. A* **2015**, *3*, 24215–24220.

[147] S. Park, J. H. Heo, J. H. Yun, T. S. Jung, K. Kwak, M. J. Ko, C. H. Cheon, J. Y. Kim, S. H. Im, H. J. Son, *Chem. Sci.* **2016**, *7*, 5517-5522.

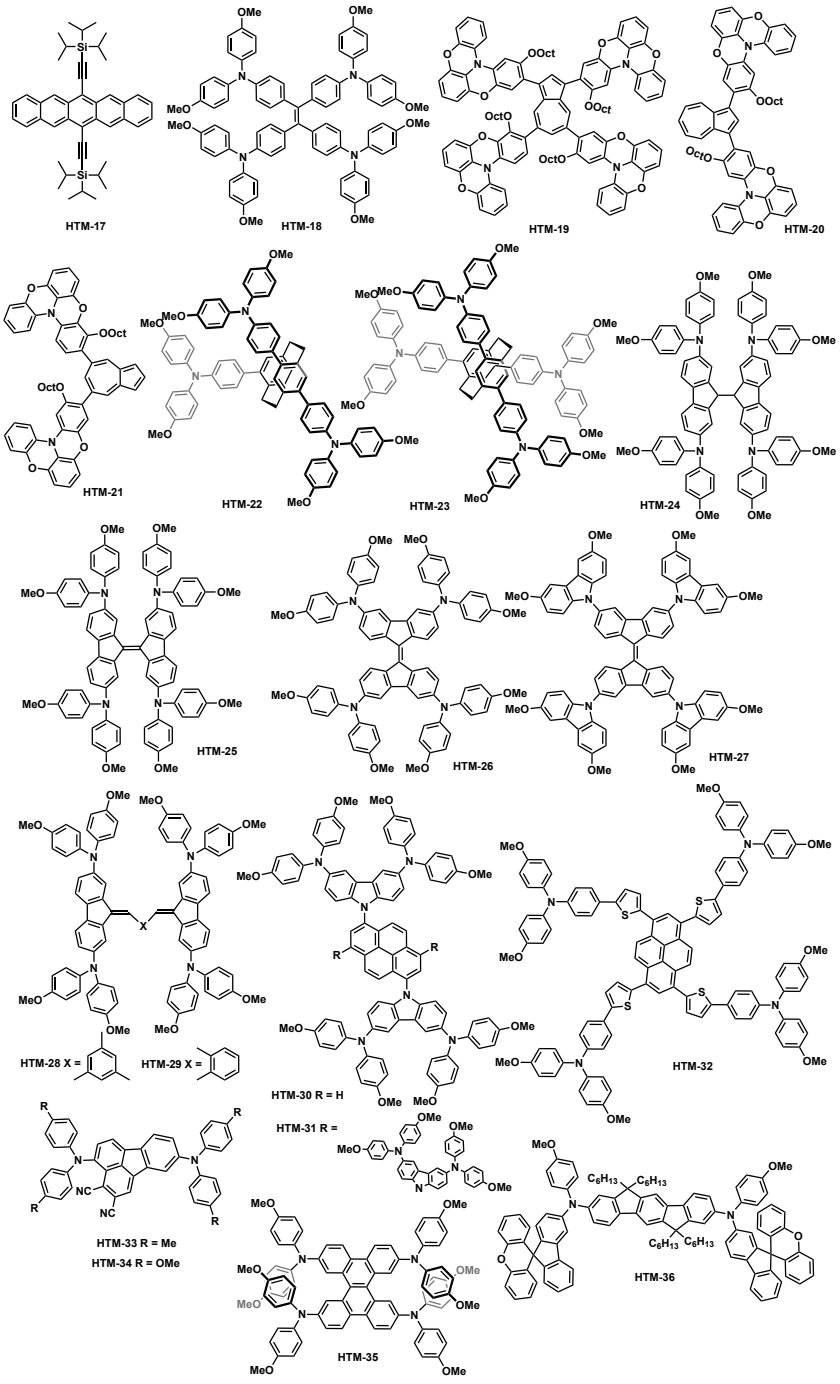

Figure 17. Chemical structures of carbocyclic-based HTMs.

In 2016 Sun, Hagfeldt and co-workers reported the synthesis of HTM-24 and HTM-25.[148] These HTMs were chemically designed for mimicking the 3D structure of spiro-OMeTAD but replacing the spiranic bond presented in spiro-OMeTAD by a rigid carbon-carbon bifluorenylidene (HTM-24) and a more flexible carbon-carbon single bond (HTM-25) (**Figure 17**). Owing to the presence of a more flexible central scaffold in HTM-25, it is observed a change in the 3D geometry in comparison to the more rigid structure of spiro-OMeTAD and HTM-24. The optoelectronic properties of HTM-24 and HTM-25, such as absorption, HOMO energy level, or conductivity, remained very similar to those displayed by spiro-OMeTAD. Both new HTMs were tested in mesoscopic devices with $[FAPbI_3]_{0.85}[MAPbBr_3]_{0.15}$-based perovskite, reaching power conversion efficiencies of 16.6 and 19.8% for HTM-24 and HTM-25, respectively, outperforming the reference of spiro-OMeTAD (18.9%) (**Table 2**). A more efficient hole extraction at the HTM-25/perovskite interface, along with an efficient hole transport, was surmised to be the reason for the superior performance of HTM-25. Very recently, our group presented two new HTMs employing the rigid bifluorenylidene as a central scaffold endowed with *p*-methoxydiphenylamine (HTM-26) and 3,6-dimethoxycabazole (HTM-27).[149] Power conversion efficiencies of 15.3 and 16.5% were achieved for HTM-26 and HTM-27, respectively, using the triple cation perovskite. Interestingly, authors demonstrated by means of photo-induced charge extraction that the HOMO energies of the HTMs are affected when the materials are deposited on top of the perovskite layer, resulting in a remarkable change of the measured V_{oc}.

Nazeeruddin, Getautis, and co-workers reported two HTMs using as a central scaffold benzene, one of the simplest carbocyclic aromatic compounds[150] (HTM-28 and HTM-29). The central benzene backbone connects two or three fluorene units through “carbon-carbon” double bond, which are functionalized

148 J. Zhang, Y. Hua, B. Xu, L. Yang, P. Liu, M. B. Johansson, N. Vlachopoulos, L. Kloo, G. Boschloo, E. M. J. Johansson, L. Sun, A. Hagfeldt, *Adv. Energy Mater.* **2016**, *6*, 1601062.

149 I. Gelmetti, N. F. Montcada, A. Pérez-Rodríguez, E. Barrena, C. Ocal, I. García-Benito, A. Molina-Ontoria, N. Martín, A. Vidal-Ferran, E. Palomares, *Energy Environ. Sci.* **2019**, *12*, 1309–1316.

150 T. Malinauskas, M. Saliba, T. Matsui, M. Daskeviciene, S. Urnikaite, P. Gratia, R. Send, H. Wonneberger, I. Bruder, M. Graetzel, et al., *Energy Environ. Sci.* **2016**, *9*, 1681–1686.

with *p*-methoxydiphenylamine in the positions 2 and 7. Both HTMs showed similar absorption spectra that spiro-OMeTAD and good alignment with the valence band of the perovskite. HTMs were tested in combination with $[FAPbI_3]_{0.85}[MAPbBr_3]_{0.15}$ perovskite reaching remarkable power conversion efficiencies of 19.47 and 17.77% for HTM-28 and HTM-29, respectively (**Table 2**). The presence of three units of the functionalized fluorene in HTM-29 produced a bulkier size structure in HTM-29 which prevents a correct packing in the solid-state. This phenomenon resulted in a lower charge mobility ability of this HTM-28, which presented lower values of hole mobility and conductivity, which are in good agreement with the trend of the photovoltaic parameters.

Pyrene has been largely employed as an aromatic scaffold for the synthesis of new materials for electronic applications. In this regard, different pyrene-based HTMs have been reported during these years.[151,152] Zhong, Meng, and co-workers reported the preparation of HTM-30 and HTM-31 using pyrene as central moiety with two or four units *p*-methoxydiphenylamine substituted carbazole, respectively (**Figure 17**). Both HTMs showed similar optoelectronic properties with a broad absorption band around 300-310 nm and a HOMO energy of -4.88 and -4.93 eV for HTM-30 and HTM-31, respectively. Both HTMs were incorporated in $[FAPbI_3]_{0.75}[MAPbI_3]_{0.17}[MAPbBr_3]_{0.08}$-based perovskite in planar configuration reaching power conversion efficiencies of 18.23 and 17.19%.[151] These values agreed with the time-resolved transient photoluminescence that confirmed a better hole extraction ability of HTM-30 in contact with the perovskite layer. Later, Hu, Zhong, and co-workers reported a new pyrene-based HTM-32 connecting *p*-methoxytriphenylamine through thiophene ring bridges to the central aromatic backbone that enables a distorted chemical structure to enhance the solubility of the molecule.[152] HTM-32 was tested in planar configuration using SnO_2 as electron-transporting layer in combination with $Cs_{0.05}FA_{0.81}MA_{0.14}PbI_{2.55}Br_{0.45}$ perovskite, rendering a PCE of 20.0% which was higher to those obtained for spiro-OMeTAD.

151 D. Li, J.-Y. Shao, Y. Li, Y. Li, L.-Y. Deng, Y.-W. Zhong, Q. Meng, *Chem. Commun.* **2018**, *54*, 1651–1654.

152 Q.-Q. Ge, J.-Y. Shao, J. Ding, L.-Y. Deng, W.-K. Zhou, Y.-X. Chen, J.-Y. Ma, L.-J. Wan, J. Yao, J.-S. Hu, Y.-W. Zhong, *Angew. Chem. Int. Ed.* **2018**, *57*, 10959–10965.

Photoluminescence studies confirmed a better hole extraction for HTM-32 in comparison with spiro-OMeTAD. XPS measurement showed two additional peaks attributed to the Pb-thiophene interaction, which reveal strong evidence for the efficient Pb-S interaction, providing a passivation of the defects between perovskite and HTM layers.

Table 2. Photovoltaic parameters of carbocyclic-based HTMs.

HTM	V_{OC} (V)	J_{SC} (mAcm^{-2})	*FF*	PCE (%)	Reference
HTM-17	0.91	20.84	0.60	11.51	140
HTM-18	0.89	17.32	0.72	11.02	142
HTM-19	1.08	21.7	0.71	16.5	144
HTM-20	0.91	15.9	0.67	9.7	144
HTM-21	0.91	17.32	0.54	8.5	144
HTM-22	1.03	21.4	0.74	16.3	146
HTM-23	1.05	21.8	0.78	17.9	147
HTM-24	1.15	24.2	0.71	19.8	148
HTM-25	1.02	22.3	0.77	17.8	148
HTM-26	0.93	22.5	0.74	15.3	149
HTM-27	0.97	24.2	0.71	16.5	149
HTM-28	1.12	23.2	0.75	19.47	150
HTM-29	1.05	19.5	0.69	14.19	150
HTM-30	1.04	23.24	0.76	18.23	151
HTM-31	0.96	22.68	0.79	17.19	151
HTM-32	1.10	23.2	0.81	20.0	152
HTM-33	1.08	20-4	0.74	16.34	153
HTM-34	1.06	22.5	0.76	18.03	153
HTM-35	1.13	24.8	0.79	22.0	154
HTM-36	1.05	21.5	0.77	17.6	157

Yan, Li, and co-workers described the use of dicyano-substituted fluoranthene as an essential block for the preparation of highly efficient dopant-free HTM-33

and HTM-34[153] (**Figure 17**). Using a well-known chemical approach from organic solar cells, the authors combine the donor *p*-methoxydiphenylamines units with the central acceptor core of dicyanofluoranthene to prepare D-A-D molecules. Based on X-ray diffraction experiments, it was observed how the cyano-substitution plays a critical role in enabling strong intermolecular interactions in the solid-state, which is expected to be beneficial for enhancing the charge transport properties of the HTMs. As a consequence of the D-A-D structure, two different absorption bands appear, which are ascribed to localized π–π* transitions and intramolecular charge transfer (ICT). The conductivity measurements confirm that the dopant-free HTMs present similar values of conductivity (6.36×10^{-5} and 1.17×10^{-4} $cm^2 V^{-1} s^{-1}$ for HTM-33 and HTM-34, respectively) in comparison to the doped spiro-OMeTAD. The dopant-free HTMs were incorporated in planar n-i-p and p-i-n architectures in combination with $[FAPbI_3]_{0.85}[MAPbBr_3]_{0.15}$ perovskite achieving power conversion efficiencies of 16.34 and 15.09% for HTM-33 and 18.03 and 17.01% for HTM-34 that outperform the corresponding undoped spiro-OMeTAD and PEDOT:PSS homologs.

Wang and co-workers reported the synthesis of a double helicene-based HTM endowed with four units of *p*-methoxydiphenylamines (HTM-35)[154] (**Figure 17**). Carbocyclic helicenes are screw-shaped, *ortho*-fused compounds with improved solubilities in comparison with planar structures and show unique electronic structures, and peculiarly complementary molecular packing.[155,156] To this end, Wang and co-workers used the simplest double helicene, dibenzo[*g*,*p*]chrysene, that consists of four benzene rings twisted away from the central naphthalene as central backbone for designing HTM-35. Using X-ray diffraction experiments and DFT calculations, the authors confirm a three-dimensional molecular stacking where the *p*-methoxydiphenylamines fit well

153 X. Sun, Q. Xue, Z. Zhu, Q. Xiao, K. Jiang, H.-L. Yip, H. Yan, Z. Li, *Chem. Sci.* **2018**, *9*, 2698–2704.

154 M. Ren, J. Wang, X. Xie, J. Zhang, P. Wang, *ACS Energy Lett.* **2019**, *4*, 2683–2688.

155 Y. Shen, C.-F. Chen, *Chem. Rev.* **2012**, *112*, 1463–1535.

156 P. J. Evans, J. Ouyang, L. Favereau, J. Crassous, I. Fernández, J. Perles, N. Martín, *Angew. Chem. Int. Ed.* **2018**, *57*, 6774–6779.

with the curved π-surfaces of the dibenzo[*g*,*p*]chrysene, observing multiple CH···π interactions and π–π stacking that reveal multidirectional hole-transport properties of HTM-35. Helicene-based HTM was introduced in mesoporous PSCs using triple cation perovskite $([FAPbI_3]_{0.87}[MAPbBr_3]_{0.08})(CsPbBr_3)_{0.05}$ reaching an impressive power conversion efficiency 22.0% (V_{oc} of 1.13 V, J_{sc} of 24.8 mA cm^{-2} and *FF* of 0.79) (**Table 2**). Additionally, HTM-35 showed long-term device stability under the dual stress of heat and full sunlight soaking.

Zhu, Li, and co-workers introduced the use of indeno[1,2-*b*]fluorene as a central π-conjugated scaffold for the preparation of HTM-36, which is decorated with SFX units in the periphery of the diphenylamine[157] (**Figure 17**). Indeno[1,2-*b*]fluorene is a pentacyclic aromatic structure that has been applied successfully to enhance intermolecular interactions and high mobilities, which could lead to dopant-free HTMs. HTM-36 was incorporated in planar PSC with a configuration of $FTO/C_{60}/MAPbI_{3-x}Cl_x/HTM/MoO_3/Ag$ in dopant-free conditions. The dopant-free HTM-36 achieved a PCE of 17.6% similar to that obtained for the doped spiro-OMeTAD. Space charge limited current (SCLC) measurements confirmed that the hole mobility of HTM-36 in dopant-free conditions is higher than that observed for spiro-OMeTAD (1.41×10^{-4} *vs.* 9.23×10^{-5} $cm^2\ V^{-1}\ s^{-1}$, respectively) demonstrating that the combination of twisted periphery groups with planar core units not only guarantees the intermolecular π–π stacking but also effectively regulates the state of molecular aggregation, boosting the hole mobility and the performance of the devices. Steady-state and time-resolved photoluminescence spectra of the perovskite films confirm a better hole extraction ability of HTM-36. Furthermore, stability measurements show an improved stability of the devices incorporating dopant-free HTM-36 sustaining a 92% of its initial PCE after 500 h of irradiation in comparison to doped spiro-OMeTAD (76%).

[157] F. Liu, F. Wu, Z. Tu, Q. Liao, Y. Gong, L. Zhu, Q. Li, Z. Li, *Adv. Funct. Mater.* **2019**, *29*, 1901296.

3.2.6 Nitrogen-based molecular engineering HTMs

Nitrogen-based aromatic central scaffolds are one of the most frequently used building blocks for electronic applications due to its chemical versatility (**Figure 18**). One of the most highlighted nitrogen-based central scaffolds is triazatruxene that consists of three indole units fused to a benzene ring in a C_{3h} symmetric planar π-conjugated structure showing high hole mobility owing to its strong π-π intermolecular interactions and electron-donating properties. Nazeeruddin and co-workers reported in 2015 a series of HTMs using triazatruxene as central scaffold endowed in position 3,8 and 13 with *p*-methoxyphenyl (HTM-37) and *p*-methoxytriphenylamine (HTM-38).[158] HTM-37 and HTM-38 showed strong absorptions at 330 and 360 nm, respectively, with a maximum of emission centered at 420 nm. The HOMO energies were founded at -5.30 and -5.26 eV for HTM-37 and HTM-38, respectively. The photovoltaic performance was evaluated using mesoscopic $[FAPbI_3]_{0.85}[MAPbBr_3]_{0.15}$-based PSCs. The average PCE of the new derivatives was measured in 17.7% (HTM-37) and 15.8% (HTM-38), which were slightly higher than the value measured for spiro-OMeTAD (17.1 %) (**Table 3**). Mayor, Su, and co-workers reported the synthesis of two isomeric triazatruxene derivatives substituted in 2,7, and 12 (HTM-39 and HTM-40).[159] HTMs were incorporated in planar $MAPbI_3$-based PSCs with a thin interlayer of poly-*N*-vinylcarbazole (PVK) in order to protect the perovskite layer from moisture along with improve the charge transport in the perovskite/HTM interface. Doped HTMs exhibited PCEs of 18.8 and 16.9% for HTM-39 and HTM-40, respectively, in combination with the PVK interlayer. In contrast, devices without this interfacial layer showed an inferior performance of 13.9% for HTM-39 and 15.5 % for HTM-40. These results were also in good agreement with the devices using spiro-OMeTAD that reached a PCE of 16.9% using PVK as an interfacial layer *vs.* 14.1% with direct contact between

[158] K. Rakstys, A. Abate, M. I. Dar, P. Gao, V. Jankauskas, G. Jacopin, E. Kamarauskas, S. Kazim, S. Ahmad, M. Grätzel, M. K. Nazeeruddin, *J. Am. Chem. Soc.* **2015**, *137*, 16172–16178.

[159] P.-Y. Su, L.-B. Huang, J.-M. Liu, Y.-F. Chen, L.-M. Xiao, D.-B. Kuang, M. Mayor, C.-Y. Su, *J. Mater. Chem. A* **2017**, *5*, 1913–1918.

perovskite/HTM. Additionally, the PVK-protection results in longer-lasting device stability in aging control experiments.

The chemical versatility of the TAT core allows the modulation of their properties through a rational design. Nazeeruddin and co-workers presented a series of triazatruxene derivatives with a D–π–A structure (HTM-41, HTM-42 and HTM-43)[160] (**Figure 18**). These HTMs were synthesized using different π-conjugated spacers, bridging the triazatruxene central core and end-capped with the dicyanovinyl groups. HTM-41, HTM-42, and HTM-43 exhibited strong absorption in the visible range due to the charge-transfer bands, with maximum centered at 487, 515, and 569 nm, respectively. Interestingly, HTM-42 presented a highly-ordered face-on organization, which should be beneficial for charge transport through the vertical direction along a stacked structure.[160] Hole mobility measurements confirmed the improvement of the charge transport in comparison with less ordered HTM-41 and HTM-43. $[FAPbI_3]_{0.85}[MAPbBr_3]_{0.15}$-perovskite based PSCs with the incorporation of undoped HTM-42 reached an impressive power conversion efficiency of 19.0%. On the other hand, dopant-free HTM-41 and HTM-43 exhibited decreased values of PCEs (8.9 and 14.9%) owing to their enhanced charge recombination from is the lower LUMO energy level.

Following the same D-π-A chemical approach, the same authors introduced two new HTMs with a flexible triphenylamine (HTM-44) and more rigid quinolizino acridine (HTM-45) as the central building block, which are endowed with thiophene π-bridges with dycianovinyl groups.[161] The D-π-A based HTMs showed similar absorption and emission bands in the visible region as well as HOMO energies (5.38 and -5.30 eV for HTM-44 and HTM-45). The incorporation of undoped HTM-44 and HTM-45 in mesoscopic devices with the conventional configuration of FTO/c-TiO_2/m-TiO_2/$[FAPbI_3]_{0.85}[MAPbBr_3]_{0.15}$/

160 K. Rakstys, S. Paek, P. Gao, P. Gratia, T. Marszalek, G. Grancini, K. T. Cho, K. Genevicius, V. Jankauskas, W. Pisula, M. K. Nazeeruddin, *J. Mater. Chem. A* **2017**, *5*, 7811–7815.

161 S. Paek, P. Qin, Y. Lee, K. T. Cho, P. Gao, G. Grancini, E. Oveisi, P. Gratia, K. Rakstys, S. A. Al-Muhtaseb, C. Ludwig, J. Ko, M. K. Nazeeruddin, *Adv. Mater.* **2017**, *29*, 1606555.

HTM/Au, provided a maximum PCE value of 18.9% for HTM-45 and 17.5% for HTM-44, outperforming undoped spiro-OMeTAD (7.5%) (**Table 3**).

Phenothiazine is another representative example of nitrogen-based scaffolds that have been extensively employed in the photovoltaic field due to its low price and its flexible electron-rich properties. In PSCs, Abate and co-workers reported a simple HTM using phenothiazine as the central scaffold, which is endowed with *p*-methoxytriphenylamine (HTM-46)[162] (**Figure 18**). HTM-46 showed a stronger donor character in comparison to spiro-OMeTAD and displayed a maximum power conversion efficiency of 17.6% in combination with the triple cation perovskite (*vs.* 17.5% of spiro-OMeTAD) which confirmed its potential for low-cost hole-transporting applications.

Seok and co-workers reported a linear fluorinated indolo[3,2-*b*]indole as the central core for the synthesis of HTM-47[163] (**Figure 18**). The introduction of fluorine atoms into the chemical structure promotes not only the intramolecular interactions (C-F···H) but also enables tighter molecular packing, which leads to improved hole mobility (1.69×10^{-3} $cm^2V^{-1}s^{-1}$) compared to spiro-OMeTAD (2.17×10^{-4} $cm^2V^{-1}s^{-1}$). The synthetic pathway toward the preparation of the core indolo[3,2-*b*]indole requires a challenging nine-step synthesis, which could limit its future application in PV technologies. The incorporation of HTM-47 into mesoscopic devices using $FAPbI_3$-based perovskite achieved an average PCE of 19.05%, with noticeable hysteresis (a maximum PCE of 19.8%), which is significantly higher than that measured for spiro-OMeTAD under the same conditions (16.8%) (**Table 3**).

[162] R. Grisorio, B. Roose, S. Colella, A. Listorti, G. P. Suranna, A. Abate, *ACS Energy Lett.* **2017**, *2*, 1029–1034.

[163] I. Cho, N. J. Jeon, O. K. Kwon, D. W. Kim, E. H. Jung, J. H. Noh, J. Seo, S. I. Seok, S. Y. Park, *Chem. Sci.* **2017**, *8*, 734–741.

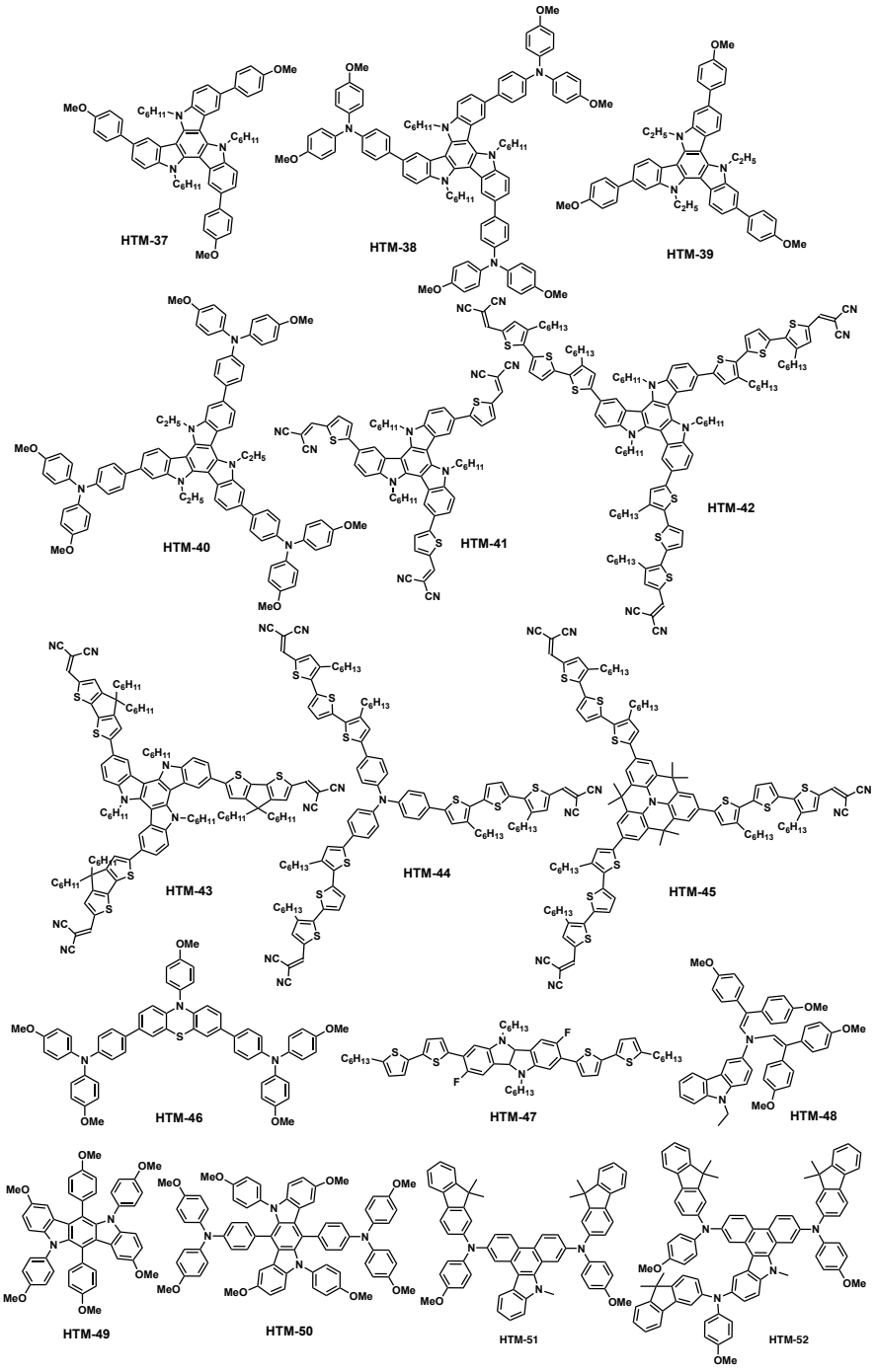

Figure 18. Chemical structures of nitrogen-based HTMs.

Carbazole is one of the most common moieties for introducing donor units in organic molecules for PV applications. Nazeeruddin and co-workers introduced a simple molecule based on a carbazole conjugated enamine derivative (HTM-48) for PSCs[164] (**Figure 18**). The synthesis only required a one-step acid-catalyzed condensation of commercial 3-amino-9-ethylcarbazole with 2,2-bis(4-methoxyphenyl)-acetaldehyde giving rise to HTM-48 in good yield. The optoelectronic properties of HTM-48 revealed a limited absorbance in the visible range, with a maximum of absorption centered at 440 nm with a low absorption coefficient and an adequate HOMO energy of -5.17 eV. HTM-48 was incorporated in mesoscopic $[FAPbI_3]_{0.85}[MAPbBr_3]_{0.15}$-based PSCs yielding PCEs of 17.8%. Additionally, HTM-48 was also tested in planar configuration with $MAPbI_{3-x}Cl_x$-based PSCs, reaching a lower value of PCE of 16.9% in comparison to spiro-OMeTAD (18.3%).

In 2019, Hagfeldt, Sun, and co-workers reported the synthesis of two HTMs using indolo[3,2-*b*]carbazole as a central scaffold endowed with *p*-methoxyphenyl (HTM-49) or *p*-methoxytriphenylamine (HTM-50).[165] Both molecules showed proper matching between the HOMO energies (-5.27 eV and -5.23 eV for HTM-49 and HTM-50, respectively) and the valence band of the mixed $[FAPbI_3]_{0.85}[MAPbBr_3]_{0.15}$ perovskite. Dopant-free HTMs were incorporated in a conventional mesoporous configuration reaching PCEs of 6.6% and 16.9% for HTM-49 and HTM-50 (**Table 3**). Despite the better optoelectronic properties of HTM-49 (low-lying HOMO energy and higher hole mobility), the performance of the cells based on HTM-49 was poorer. From the SEM and AFM images, it was surmised that the enhanced performance of HTM-50 could be attributed to its more uniform film formation on top of the perovskite layer that provided a reduced charge recombination loss and improved charge extraction ability due to its reduced tendency to aggregate.

---

[164] M. Daskeviciene, S. Paek, Z. Wang, T. Malinauskas, G. Jokubauskaite, K. Rakstys, K. T. Cho, A. Magomedov, V. Jankauskas, S. Ahmad, H. J. Snaith, V. Getautis, M. K. Nazeeruddin, *Nano Energy* **2017**, *32*, 551–557.

[165] X. Yang, Z. Yu, L. Sun, A. Hagfeldt, B. Cai, X. Jiang, *J. Mater. Chem. A* **2019**, *7*, 14835-14841.

Table 3. Photovoltaic parameters of nitrogen-based HTMs.

HTM	V_{OC} (V)	J_{SC} (mAcm^{-2})	*FF*	PCE (%)	Reference
HTM-37	1.14	20.7	0.77	18.3	158
HTM-38	1.13	20.4	0.72	16.8	158
HTM-39	1.08	22.8	0.77	18.8	159
HTM-40	1.03	22.3	0.74	16.9	159
HTM-41	1.05	16.01	0.53	8.88	160
HTM-42	1.13	21.70	0.78	19.03	160
HTM-43	1.11	19.31	0.69	14.87	160
HTM-44	1.09	20.85	0.77	17.5	161
HTM-45	1.13	21.71	0.77	18.9	161
HTM-46	1.11	21.1	0.75	17.6	162
HTM-47	1.05	23.55	0.77	19.05	163
HTM-48	1.07	2.5	0.74	17.8	164
HTM-49	0.87	15.1	0.50	6.6	165
HTM-50	1.05	22.9	0.70	16.9	165
HTM-51	1.05	22.14	0.81	18.81	166
HTM-52	1.11	22.69	0.79	20.02	166

Very recently, Zhu, Li, and co-workers reported two HTMs employing dibenzo[*a*,*c*]carbazole as the building block for the synthesis of HTM-51 and HTM-52[166] (**Figure 18**). Due to its similar chemical structure, HTM-51 and HTM-52 display related optoelectronic properties with HOMO energy values of -5.26 and -5.22 eV, respectively and absorption and emission maximum centered on 336/448 and 342/452 nm, respectively. These HTMs were incorporated in standard n-i-p PSCs with a configuration of FTO/c-TiO_2/$MAPbI_{3-x}Cl_x$/HTM/Ag, reaching remarkable PCEs of 18.81% and 20.02% for HTM-51 and HTM-52,

166 F. Liu, F. Wu, W. Ling, Z. Tu, J. Zhang, Z. Wei, L. Zhu, Q. Li, Z. Li, *ACS Energy Lett.* **2019**, *4*, 2514–2521.

respectively, which are slightly higher than the value reached for the reference of spiro-OMeTAD (18.18%) (**Table 3**). Hole mobilities were evaluated using the SCLC technique showing similar values for both HTMs (7.09×10^{-4} and 9.85×10^{-4} $cm^2V^{-1}s^{-1}$) and spiro-OMeTAD (5.37×10^{-4} $cm^2V^{-1}s^{-1}$). Hole extraction ability of the HTMs was conducted under steady-state and time-resolved photoluminescence measurements. HTM-52 was more efficient in extracting the photogenerated holes than HTM-51 and the benchmark spiro-OMeTAD.

3.2.7 Sulfur-based molecular engineering HTMs.

As the aforementioned nitrogen-based HTMs, the literature of heteroaromatic-based structures containing sulfur atoms has been widely explored (**Figure 19**). In this sense, the research community has taken advantage of the chemical versatility of thiophene for designing suitable HTMs for perovskite solar cells. Thiophene-based compounds are appealing building blocks due to their interesting optoelectronic properties for application in a variety of fields, including organic photovoltaics, organic field-effect transistors (OFETs), and organic light-emitting diodes (OLEDs).[167,168,169] The chemical structures of the sulfur-based HTMs are shown in **Figure 19,** and its photovoltaic parameters are collected in **Table 4**.

In 2014, Grätzel, Grimsdale, and co-workers reported a simple molecule combining 3,4-ethylenedioxythiophene (EDOT) end-capped with two units of *p*-methoxytriphenylamine (HTM-53) (**Figure 19**).[170] HTM-53 could be synthesized in 82% yield in just two synthetic steps. HTM-53 was incorporated in conventional mesoscopic devices using $MAPbI_3$ as photoactive layer, displaying PCEs of 10.6% as dopant-free HTM and 13.8% using the standard

[167] A. Mishra, P. Bäuerle, *Angew. Chem. Int. Ed.* **2012**, *51*, 2020–2067.

[168] H. Bronstein, Z. Chen, R. S. Ashraf, W. Zhang, J. Du, J. R. Durrant, P. Shakya Tuladhar, K. Song, S. E. Watkins, Y. Geerts, M. M. Wienk, R. A. Janssen, T. Anthopoulos, H. Sirringhaus, M. Heeney, I. McCulloch, *J. Am. Chem. Soc.* **2011**, *133*, 3272–3275.

[169] J. H. Seo, E. B. Namdas, A. Gutacker, A. J. Heeger, G. C. Bazan, *Adv. Funct. Mater.* **2011**, *21*, 3667–3672.

[170] H. Li, K. Fu, A. Hagfeldt, M. Grätzel, S. G. Mhaisalkar, A. C. Grimsdale, *Angew. Chem. Int. Ed.* **2014**, *53*, 4085–4088.

dopant combination for spiro-OMeTAD (LiTFSI, *t*-BuP, and FK-102). These values were comparable to those obtained using doped-spiro-OMeTAD (13.7%), making EDOT a promising building block for efficient HTMs. Shortly after, this chemical strategy was continued by Docampo and co-workers with the report of an analog structure, incorporating an azomethine bond. This chemical approach allows a less complicated synthetic route based on Schiff-base condensation reaction, instead of palladium-catalyzed cross-coupling reactions employed for HTM-54.[171] Using this synthetic pathway, the production of the HTM results in a cost-effective and more environmentally friendly route, with water being the only by-product. Incorporation of the azomethine bond strongly affects the optoelectronic properties of the HTM, showing a redshift and broadening the absorbance as a consequence of the increased π-conjugation and its electron-withdrawing properties, showing a lower HOMO energy level (-5.28 eV) compared to HTM-53 (-5.11 eV). HTM-54 was also tested in planar configuration devices using $MAPbI_3$ perovskite, yielding a maximum PCE of 11% in doped conditions (LiTFSI, *t*-BuP, and FK-102). Recently, the same authors completed the use of EDOT by incorporating amide functionalities to connect the *p*-methoxytriphenylamine units in HTM-55[172] (**Figure 19**). HOMO energy of HTM-55 was found to be -5.23 eV that ensures an appropriate energy alignment. HTM-55 was incorporated in a planar architecture with FTO/SnO_2/ $FA_{0.83}Cs_{0.17}Pb(I_{0.83}Br_{0.17})_3$/HTM/Au rendering an impressive 20.3% with improved stability in comparison to spiro-OMeTAD (**Table 4**).

The use of thiophene as a simple central scaffold was beautifully exemplified by Nazeeruddin and co-workers that described a highly-efficient HTM-56, following the same approach that carbocyclic-based HTM-28 and HTM-29[150] (**Figure 19**). In the chemical structure of HTM-56, thiophene is functionalized with *p*-methoxydiphenylamine-substituted fluorene units to assure a suitable HOMO energy (-5.16 eV). HTM-56 was tested in combination with $[FAPbI_3]_{0.85}[MAPbBr_3]_{0.15}$ perovskite in mesoporous configuration, achieving a

171 M. L. Petrus, T. Bein, T. J. Dingemans, P. Docampo, *J. Mater. Chem. A* **2015**, *3*, 12159–12162.

172 M. L. Petrus, K. Schutt, M. T. Sirtl, E. M. Hutter, A. C. Closs, J. M. Ball, J. C. Bijleveld, A. Petrozza, T. Bein, T. J. Dingemans, T. J. Savenije, H. Snaith, P. Docampo, *Adv. Energy Mater.* **2018**, *8*, 1801605.

remarkable PCE of 19.96%, which was higher than the efficiency measured for the reference spiro-OMeTAD (18.25%). These excellent results agreed with the measurements of lateral conductivity and hole mobility that confirmed HTM-50 as a potential candidate for replacing spiro-OMeTAD.

In 2017 Grätzel and co-workers reported two HTMs (HTM-57 and HTM-58) using 3,4-methoxythiophene as central scaffold bearing triphenylamines connected through single and double bonds[173] (**Figure 19**). In comparison with HTM-57, the light-harvesting properties HTM-58 are strongly improved, owing to the extended π-conjugation and the enhancement of the planarity. Both HTMs showed similar HOMO energies (-5.23 eV for HTM-57 and -5.21 eV for HTM-58). The hole-transport properties of pristine HTMs were evaluated for hole-only devices using time-of-flight (TOF) measurements, obtaining values of 7.66×10^{-5} and 1.34×10^{-4} $cm^2V^{-1}s^{-1}$. These HTMs were tested using a mesoscopic configuration (FTO/c-TiO_2/m-TiO_2/$MAPbI_3$/HTM/Au) under doped conditions. Noteworthy, HTM-58 displayed a maximum PCE of 20.1%, quite close to the 20.6% reached by spiro-OMeTAD. In contrast, HTM-57 devices displayed a reduced power conversion efficiency of 16.9%, which is in agreement with the reduced values of hole mobility and conductivity (**Table 4**).

Our research group described in 2016 three new hole-transporting materials using an interesting planar and rigid π-conjugated framework named benzo[1,2-*b*:3,4-*b´*:5,6-*b´´*]trithiophene (BTT). This central backbone consists of three thiophene units fused to a central benzene ring that was decorated with different donor units such as diphenylamine (HTM-59), diphenylamine-substituted carbazole (HTM-60), and triphenylamine (HTM-61)[102] (**Figure 19**). HOMO energies of -5.2 eV (for HTM-59 and HTM-60) and -5.4 eV (for HTM-61) are closely related to the different donor ability of the donor units endowed with the central benzotrithiophene. The sulfur-rich HTMs were evaluated using two different perovskites ($MAPbI_3$ and $[FAPbI_3]_{0.85}[MAPbBr_3]_{0.15}$) in standard mesoporous architectures under doped conditions. Using $MAPbI_3$ perovskite, HTM-61 showed a best PCE of 18.2% which is higher than those observed for HTM-59 (16.0%), HTM-60 (17.0%) and spiro-OMeTAD (18.1%) (**Table 4**). In

[173] F. Zhang, Z. Wang, H. Zhu, N. Pellet, J. Luo, C. Yi, X. Liu, H. Liu, S. Wang, X. Li, Y. Xiao, S. M. Zakeeruddin, D. Bi, M. Grätzel, *Nano Energy* **2017**, *41*, 469–475.

contrast, using the mixed perovskite as a photoactive layer, HTM-60 showed the best PCE of 17.5%, which is slightly higher than those measured for HTM-61 (17.3%) and HTM-59 (16.0%). The conductivity measurements showed a similar trend to that of the photovoltaic results.

Shortly after, our group reported two new HTMs by introducing isomeric structures of BTT (benzo[1,2-*b*:3,4-*b´*:6,5-b´´]trithiophene and benzo[2,1-*b*:-3, 4-*b´*:5,6-*c´´*]trithiophene) obtained by modification of the position of the sulfur atoms in the structure. These new BTTs were endowed with *p*-methoxytriphenylamine for the synthesis of HTM-62 and HTM-63[174] (**Figure 19**). Changing the arrangement of the sulfur atoms in the case of HTM-62 and HTM-63 resulted in a wider absorbance in the visible range. The absorption band of HTM-63 was significantly red-shifted in comparison to the other two three-armed compounds (HTM-61 and HTM-62) due to the enhanced π-electron delocalization of its core. It is reported that the broad absorption presented by HTM-62 could be attributed to the direct conjugation between the two *cis* thiophene rings, in contrast to the *meta* arrangement with the central benzene ring in HTM-61. The HOMO energy levels were also affected by the arrangements of the sulfur atoms, showing a stronger donor ability in HTM-63 (-5.2 eV) similar to spiro-OMeTAD, while HTM-62 showed a comparable HOMO energy (-5.3 eV) to HTM-61. Doped HTMs were applied in combination with $[FAPbI_3]_{0.85}[MAPbBr_3]_{0.15}$ perovskite in a mesoporous configuration, reaching 19.0 and 18.2% for HTM-62 and HTM-63, respectively, outperforming the previously reported HTM-61 and spiro-OMeTAD (**Table 4**). BTT was also used as the central backbone for the preparation of dopant-free HTMs by Liu and co-workers.[175] The authors followed a similar strategy to that reported in our research group, bridging the BTT central moiety with the donor triphenylamine through thiophene and EDOT moieties, reaching a notable PCE of 16.15% for dopant-free devices.

174 I. Garcia-Benito, I. Zimmermann, J. Urieta-Mora, J. Arago, A. Molina-Ontoria, E. Orti, N. Martin, M. K. Nazeeruddin, *J. Mater. Chem. A* **2017**, *5*, 8317–8324.

175 Y.-K. Peng, K.-M. Lee, C.-C. Ting, M.-W. Hsu, C.-Y. Liu, *J. Mater. Chem. A* **2019**, *7*, 24765–24770.

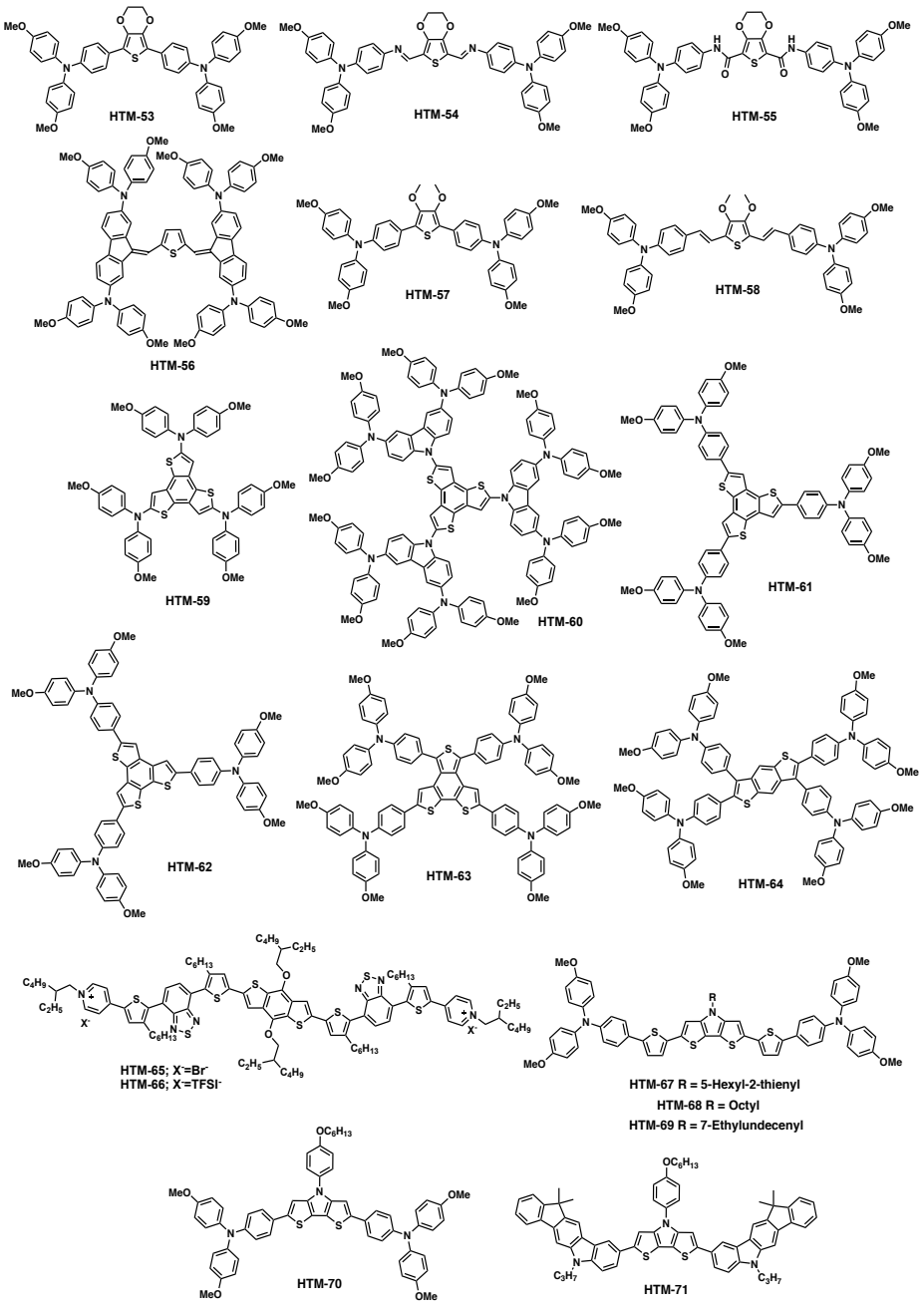

Figure 19. Chemical structure of sulfur-based HTMs.

Benzodithiophene (BDT) is another common framework that has been extensively used in organic photovoltaics.[176,177] In perovskite solar cells, BDT has also been used as a central backbone for the preparation of HTMs. Our group designed a tetrasubstituted-BDT with four units of *p*-methoxytriphenylamine (HTM-64)[178] (**Figure 19**). HTM-64 showed suitable HOMO energy (-5.36 eV) and a strong absorption in the visible region with a maximum absorption band centered at 410 nm. $[FAPbI_3]_{0.85}[MAPbBr_3]_{0.15}$-based devices in mesoporous configuration incorporating HTM-64 displayed a PCE of 18.1% that were found similar to the PCE of spiro-OMeTAD (17.8%) (**Table 4**). Previously, Sun, Kloo, and coworkers disclosed two benzodithiophene-based derivatives (HTM-65 and HTM-66) as HTMs where the BDT central framework is flanked with alkylated thiophene–benzothiadiazole π-conjugated bridges with end-capped pyridine/pyridinium units with different counter-ions (Br^- and $TFSI^-$).[179] Both HTMs were tested in dopant-free conditions in mesoscopic $[FAPbI_3]_{0.85}[MAPbBr_3]_{0.15}$-based PSCs. Under these conditions, HTM-66 reached a remarkable power conversion efficiency of 17.4%, which was comparable to the doped spiro-OMeTAD (17.9%). In stark contrast, HTM-65 yielded a very modest efficiency of 15.5%.

Dithieno[3,2-*b*:2′,3′-*d*]pyrrole (DTP) is a well-known fragment used for the preparation of electron-donor compounds in OPVs. Similarly, DTP has also been successfully applied for the preparation of highly efficient HTMs. Yan, Tang, and co-workers reported DTP as the central moiety where the donor *p*-methoxytriphenylamine is connected through thiophene units for the preparation of HTM-67 (5-hexy-2-thienyl), HTM-68 (octyl) and HTM-69 (7-

176 B. Kan, Q. Zhang, M. Li, X. Wan, W. Ni, G. Long, Y. Wang, X. Yang, H. Feng, Y. Chen, *J. Am. Chem. Soc.* **2014**, *136*, 15529–15532.

177 L. Yuan, Y. Zhao, J. Zhang, Y. Zhang, L. Zhu, K. Lu, W. Yan, Z. Wei, *Adv. Mater.* **2015**, *27*, 4229–4233.

178 R. Sandoval-Torrientes, I. Zimmermann, J. Calbo, J. Aragó, J. Santos, E. Ortí, N. Martín, M. K. Nazeeruddin, *J. Mater. Chem. A* **2018**, *6*, 5944–5951.

179 M. Cheng, K. Aitola, C. Chen, F. Zhang, P. Liu, K. Sveinbjörnsson, Y. Hua, L. Kloo, G. Boschloo, L. Sun, *Nano Energy* **2016**, *30*, 387–397.

ethylundecenyl) with different solubilizing groups[180,181] (**Figure 19**). As a consequence of its same core structure, the optoelectronic properties of the DTP-based HTMs are quite similar. They showed strong absorption bands centered at 470 nm, which are ascribed to intramolecular charge transfer from the TPA to the central DTP and HOMO energy levels around -5.10 eV. DTP-based HTMs were incorporated into n-i-p planar perovskite solar cells with a configuration of FTO/SnO_2/C_{60}-SAM/$MA_{0.7}FA_{0.3}PdI_{2.85}Br_{0.15}$/PMMA/HTM/Au reaching exceptional PCE values of 21.04, 18.37 and 20.38 % for HTM-67, HTM-68, and HTM-69, respectively, under dopant-free conditions (**Table 4**). Space charge-limited current (SCLC) measurements confirm the exceptional hole mobility values of 4.18×10^{-4}, 3.43×10^{-5} and 2.16×10^{-4} $cm^2V^{-1}s^{-1}$ for HTM-67-69, respectively.

Shortly after, Hagfeldt, Liang, and co-workers reported two new DTP-based HTMs bearing *p*-methoxytriphenylamine (HTM-70) and indeno[1,2-*b*]carbazole (HTM-71) attached to the α-positions of the central DTP core[182] (**Figure 19**). The authors demonstrated how a rational chemical design using indeno[1,2-*b*]carbazole instead of *p*-methoxytriphenylamine improves the morphology uniformity. HTM-70 and HTM-71 were incorporated in planar n-i-p PSCs with a standard configuration of ITO/SnO_2/$Cs_{0.05}(FA_{0.83}MA_{0.17})_{0.95}Pb(Br_{0.17}I_{0.83})_3$/HTMs/Au yielding PCE values of 18.59 and 20.35%, respectively, under doped conditions. Interestingly, HTM-71 confirms its potential for dopant-free applications with a remarkable 17.50% for power conversion efficiency with an improved stability in comparison to HTM-70 (14.30%) and the benchmark spiro-OMeTAD, retaining 82% of its initial PCE after 1000 h of irradiation.

---

[180] X. Yin, J. Zhou, Z. Song, Z. Dong, Q. Bao, N. Shrestha, S. S. Bista, R. J. Ellingson, Y. Yan, W. Tang, *Adv. Funct. Mater.* **2019**, *29*, 1904300.

[181] J. Zhou, X. Yin, Z. Dong, A. Ali, Z. Song, N. Shrestha, S. S. Bista, Q. Bao, R. J. Ellingson, Y. Yan, W. Tang, *Angew. Chem. Int. Ed.* **2019**, *58*, 13717–13721.

[182] J. Wang, H. Zhang, B. Wu, Z. Wang, Z. Sun, S. Xue, Y. Wu, A. Hagfeldt, M. Liang, *Angew. Chem. Int. Ed.* **2019**, *58*, 15721–15725.

Table 4. Photovoltaic parameters of sulfur-based HTMs.

HTM	V_{OC} (V)	J_{SC} (mAcm^{-2})	*FF*	PCE (%)	Reference
HTM-53	1.05	19.1	0.65	13.2	170
HTM-54	0.95	18.9	0.61	11.0	171
HTM-55	1.16	22.7	0.77	20.3	172
HTM-56	1.14	22.5	0.77	19.96	150
HTM-57	1.15	23.12	0.64	16.9	173
HTM-58	1.13	23.59	0.75	20.1	173
HTM-59	1.04	20.4	0.72	16.0	102
HTM-60	1.09	20.6	0.77	17.0	102
HTM-61	1.07	21.9	0.77	18.2	102
HTM-62	1.09	23.04	0.75	19.0	174
HTM-63	1.10	22.50	0.73	18.2	174
HTM-64	1.07	23.02	0.74	18.1	178
HTM-65	1.05	21.94	0.66	15.1	179
HTM-66	1.10	22.84	0.69	17.4	179
HTM-67	1.16	22.76	0.80	21.04	180
HTM-68	1.09	22.66	0.74	18.27	181
HTM-69	1.14	22.82	0.79	20.38	181
HTM-70	1.09	23.05	0.74	18.59	182
HTM-71	1.12	23.30	0.78	20.35	182

3.2.8 Oxygen, silicon and metallocycle-based molecular engineering HTMs.

Oxygen or silicon-based HTMs are other alternatives to the more common heteroaromatic structures based on nitrogen and sulfur. The device performances of oxygen, silicon, and metallocycle-based HTMs are summarized in **Table 5**. Thus, Shi and co-workers designed and reported two π-extended furan-based HTMs based on a dibenzofuran central unit, which was further functionalized in positions 3 and 6 with different *p*-methoxydiphenylamine moieties (HTM-71

and HTM-72)[183] (**Figure 20**). HTM-71 and HTM-72 exhibited limited absorption in the visible region and adequate HOMO energy levels according to the different electronic nature of the substituents (-5.01 eV for HTM-71 and -5.14 eV for HTM-72). These furan-based HTMs were jointly incorporated in mesoscopic devices with $MAPbI_3$ perovskite under standard doped conditions (LiTFSI, *t*-BuP, and FK-209). The best PCE was measured using HTM-71 with a maximum of 14.20, while HTM-72 showed a slightly lower 14.07%, confirming the potential of furan-based structures for hole-transporting applications.

Grätzel and co-workers described the synthesis of a planar, π-conjugated, two-dimensional heterocycle, based on xanthenoxanthene as the central scaffold (HTM-73)[184] (**Figure 20**). Interestingly, SCLC measurements of HTM-73 showed excellent hole mobility properties with a value of 8.55×10^{-4} $cm^2V^{-1}s^{-1}$, which was four times higher than that measured for spiro-OMeTAD. The molecular packing propels this excellent hole mobility in a one-dimension due to the formation of π-stacked columnar motif, where the columns link to adjacent columns with multiple C···H/π and C···H/O interactions to form a three-dimensional network. The incorporation of HTM-73 into $[Cs_{0.05}(FA_{0.83}MA_{0.17})_{0.95}]Pb(Br_{0.15}I_{0.85})_3$-based perovskite in mesoporous architecture rendered a remarkable PCE of 19.8%, showing an improved stability due to the higher hydrophobicity of HTM-73 (**Table 5**).

183 Y. Shi, K. Hou, Y. Wang, K. Wang, H. Ren, M. Pang, F. Chen, S. Zhang, *J. Mater. Chem. A* **2016**, *4*, 5415–5422.

184 N. Xu, Y. Li, R. Wu, R. Zhu, J. Zhang, S. M. Zakeeruddin, H. Li, Z.-S. Li, M. Grätzel, P. Wang, *Chem. – A Eur. J.* **2019**, *25*, 945–948.

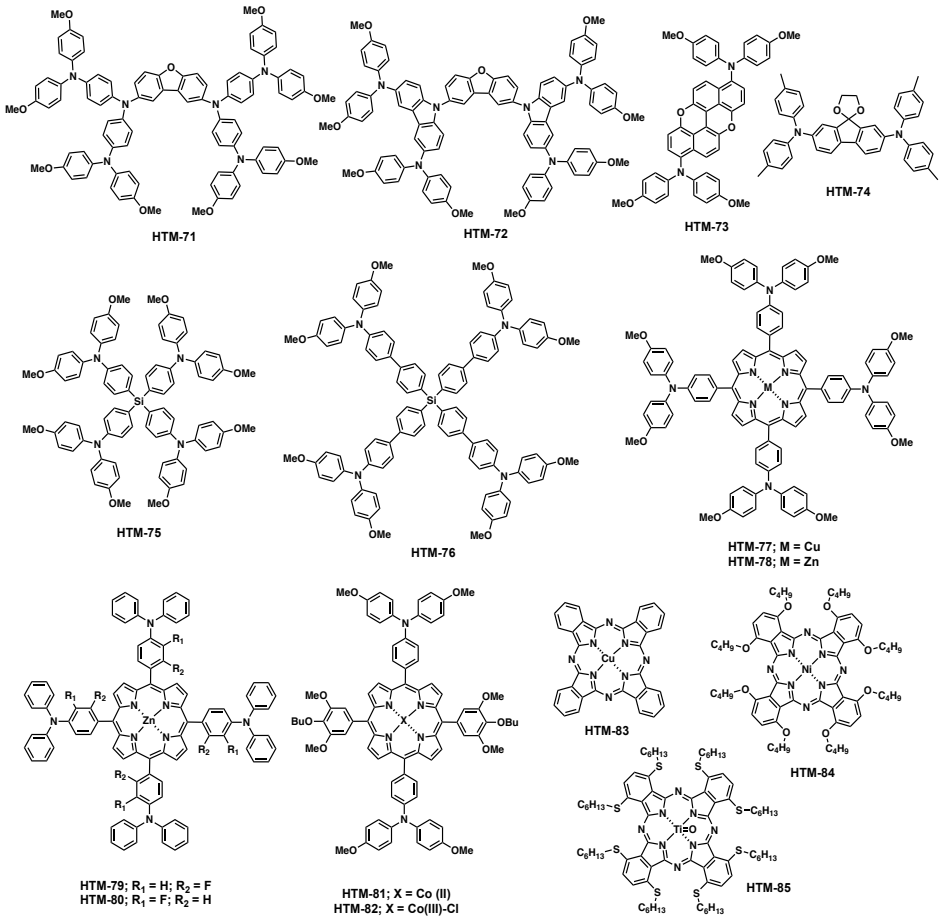

Figure 20. Chemical structures of oxygen, silicon and metallocyclic-based HTMs.

Very recently, Kelly, Berlinguette, and co-workers reported the synthesis and photovoltaic response of a simple and efficient oxygen-based HTM using two fluorene-bridged triphenylamine moieties linked to a 1,3-dioxolane group through a spiro carbon center (HTM-74)[185] (**Figure 20**). The ease chemical structure of HTM-74 allows a simple synthesis through consecutive Buchwald-Hartwig amination and acid-catalyzed condensation for preparing a cost-

185 Y. Cao, Y. Li, T. Morrissey, B. Lam, B. O. Patrick, D. J. Dvorak, Z. Xia, T. L. Kelly, C. P. Berlinguette, *Energy Environ. Sci.* **2019**, *12*, 3502-3507.

effective HTM that cannot be matched by any other compound in the bibliography. The molecular design of the dopant-free HTM was approached to ensure an appropriate HOMO energy for efficient charge extraction from the perovskite layer and with the presence of functional groups that encourage anisotropic molecular ordering of the film to achieve high electronic conductivity and hole mobility ($\approx 1 \times 10^{-3}$ $cm^2V^{-1}s^{-1}$). HTM-74 was tested in planar inverted devices with a configuration of ITO/HTM/$MA_{0.9}FA_{0.1}PbI_{3-x}Cl_x$/$C_{60}$/BCP/Ag rendering a maximum power conversion efficiency of 20.60% under dopant-free conditions, which was higher than that measured for PTTA reference (19.20%) (**Table 5**). Interestingly, the PCE of the devices using HTM-74 directly spin-coated over the perovskite layer did not surpass 11%. In contrast, after annealing the devices from 120 to 150 ºC, the output of the devices was highly improved with an optimal annealing temperature of 135 ºC.

Silicon-based materials show enhanced charge transport properties compared to their carbon counterparts, which is attributed to an effectively induced crystallinity due to the longer C–Si bond that reduces the steric hindrance.[186,187] Li and co-workers introduced two X-shaped silicon-based HTMs for p–i–n PSCs demonstrating the potential of silicon-based materials for hole-transport applications (HTM-75 and HTM-76)[188] (**Figure 20**). The introduction of silicon atoms into the structure of π-conjugated systems influences not only the optical but also the hole transport properties of the materials. Both HTMs showed limited absorption in the visible region and optimal HOMO energy levels for PSCs (-5.39 for HTM-75 and -5.34 for HTM-76). Silicon-based HTMs were incorporated in a planar p–i–n architecture that consists of ITO/HTM/$MAPbI_3$/PCBM/Al. The authors studied the influence of dopants and the annealing process in the photovoltaic response. The doped/annealed devices displayed a PCE of 14.15% for HTM-76 and 18.23% for HTM-75, while the

[186] H.-Y. Chen, J. Hou, A. E. Hayden, H. Yang, K. N. Houk, Y. Yang, *Adv. Mater.* **2010**, *22*, 371–375.

[187] M. C. Scharber, M. Koppe, J. Gao, F. Cordella, M. A. Loi, P. Denk, M. Morana, H.-J. Egelhaaf, K. Forberich, G. Dennler, R. Gaudiana, D. Waller, Z. Zhu, X. Shi, C. J. Brabec, *Adv. Mater.* **2010**, *22*, 367–370.

[188] R. Xue, M. Zhang, G. Xu, J. Zhang, W. Chen, H. Chen, M. Yang, C. Cui, Y. Li, Y. Li, *J. Mater. Chem. A* **2018**, *6*, 404–413.

undoped devices displayed much lower efficiency (**Table 5**). Furthermore, the efficiencies of the devices were boosted by depositing PCBM/C_{60}/BCP as a triple cathode buffer layer reaching a maximum PCE of 19.06 % using HTM-75.

Porphyrins and phthalocyanines (Pc) have been extensively exploited as sensitizers for DSSCs and as scaffolds for the preparation of electron-donating materials in organic solar cells.[189,190,191] These two-dimensional metallomacrocycles exhibit very appealing properties, such as intense absorption in the near-infrared region, high chemical flexibility, and thermal stability, which make them good candidates as HTMs for PSCs.[192] One of the most representative examples was described by Zhu and co-workers developing highly symmetric Zn- and-Cu-porphyrin containing TPAs at each of the four meso positions of the porphyrin (HTM-77 and HTM-78)[193] (**Figure 20**). The UV-vis spectra revealed the contribution to the light absorption by the porphyrin-based HTMs, showing in the case of HTM-77 blue-shifted Q bands and split Soret bands in comparison with HTM-78. Mesoscopic compositionally engineered perovskite $(FAPbI_3)_{0.85}(MAPbBr_3)_{0.15}$- based devices containing doped-HTM-77 and HTM-78 reached 15.36 and 17.78%, respectively, with noticeable hysteresis. HTM-77-based devices exhibit lower V_{oc}, J_{sc} and *FF* values stemming from its lower solubility and the formation of pinholes within the HTM film, which causes fast charge recombination and a lower *FF*. Additionally, HTM-78-based devices stored after 30 days (40–45% humidity at rt) retained 85% of their initial PCE, in contrast to the 45% of devices incorporating reference of spiro-OMeTAD. Latterly, Jung and co-workers introduced the use of fluorinated TPA in the meso position of Zn-based

[189] A. Yella, C.-L. Mai, S. M. Zakeeruddin, S.-N. Chang, C.-H. Hsieh, C.-Y. Yeh, M. Grätzel, *Angew. Chem. Int. Ed.* **2014**, *53*, 2973–2977.

[190] K. Gao, L. Li, T. Lai, L. Xiao, Y. Huang, F. Huang, J. Peng, Y. Cao, F. Liu, T. P. Russell, R. A. Janssen, X. Peng, *J. Am. Chem. Soc.* **2015**, *137*, 7282–7285.

[191] A. Varotto, C.-Y. Nam, I. Radivojevic, J. P. C. Tomé, J. A. S. Cavaleiro, C. T. Black, C. M. Drain, *J. Am. Chem. Soc.* **2010**, *132*, 2552–2554.

[192] M. Urbani, G. de la Torre, M. K. Nazeeruddin, T. Torres, *Chem. Soc. Rev.* **2019**, *48*, 2738–2766.

[193] S. Chen, P. Liu, Y. Hua, Y. Li, L. Kloo, X. Wang, B. Ong, W.-K. Wong, X. Zhu, *ACS Appl. Mater. Interfaces* **2017**, *9*, 13231–13239.

porphyrins for the synthesis of HTM-79 and HTM-80[194] (**Figure 20**). The incorporation of fluorine atoms into the donor units realized lower HOMO levels and enhanced dipole-induced intermolecular stacking. Notably, the position of the fluorine-substituents also influenced the HOMO levels and the molecular stacking of HTMs. HTM-79 and HTM-80 were incorporated in planar n-i-p devices in combination with $MAPbI_3$ perovskite from sol-gel methods reaching PCE values of 18.85% and 17.71%, respectively (**Table 5**). Besides, both porphyrin-based HTMs showed higher stability in comparison to the devices employing spiro-OMeTAD as HTM.

Table 5. Photovoltaic parameters of oxygen, silicon and metallocyclic-based HTMs.

HTM	V_{OC} (V)	J_{SC} (mAcm^{-2})	*FF*	PCE (%)	Reference
HTM-71	1.01	21.56	0.65	14.20	183
HTM-72	1.03	21.22	0.64	14.07	183
HTM-73	1.12	23.18	0.76	19.80	184
HTM-74	1.10	22.60	0.83	20.60	185
HTM-75	1.07	23.08	0.72	19.06	188
HTM-76	0.99	19.85	0.77	14.15	188
HTM-77	1.07	21.61	0.66	15.36	193
HTM-78	1.10	22.69	0.71	17.78	193
HTM-79	1.13	22.21	0.75	18.85	194
HTM-80	1.11	21.86	0.73	17.71	194
HTM-81	1.09	23.17	0.74	18.77	195
HTM-82	1.09	23.16	0.71	17.88	195
HTM-83	1.15	23.60	0.74	20.09	196
HTM-84	1.08	23.10	0.73	18.30	197
HTM-85	1.06	22.31	0.71	16.87	198

[194] R. Azmi, U.-H. Lee, F. T. A. Wibowo, S. H. Eom, S. C. Yoon, S.-Y. Jang, I. H. Jung, *ACS Appl. Mater. Interfaces* **2018**, *10*, 35404–35410.

Liu, Tang, and co-workers reported another porphyrin-based approach with the synthesis of cobalt (II) and (III) meso-substituted porphyrin for the preparation of highly efficient HTM-81 and HTM-82, respectively[195] (**Figure 20**). The authors showed how the incorporation of a natural organic sunscreen compound such as sinapoyl malate (SM) at the TiO_2/perovskite interface could improve the photovoltaic response. The use of UV-resistant SM protected the perovskite from the destroy by UV radiation and, more importantly, the SM interlayer tuned the interfacial chemical interactions between the TiO_2 and perovskite to enhance the electron extraction and reduce the electron recombination at the interface, thus improving device performance. The inclusion of Co-based HTM-81 and HTM-82 in mesoporous configuration with triple cation perovskite displayed power conversion efficiencies of 18.77 and 17.88%, respectively, in the presence of sinapoyl malate in the TiO_2/perovskite interface (**Table 5**). Noticeably, the use of a mixture of HTM-81 and HTM-82 as a hole-transporting layer (molar ratio 4:6 respectively) enhanced the PCE until a maximum of 20.50% with improved stability in comparison with benchmark spiro-OMeTAD.

Duong, Catchpole, and co-workers reported the use of copper phthalocyanine (CuPc) as HTM for the preparation of highly efficient PSCs (HTM-83).[196] The use of phthalocyanines was previously limited due to the cracks that usually found when CuPc is deposited form solution, which leads to severe shunts and interface recombination. The authors introduced HTM-83 into mesoporous devices with a configuration of ITO/c-TiO_2/m-TiO_2/Perovskite/HTM-83/Au using an interfacial layer between the ETM and the perovskite that consist of a blend of PCBM and PMMA. The PCE achieved by HTM-83 as-cast was 7.5% due to the defects in the deposition. Nevertheless, after a heat-treatment at 85 ºC the PCE dramatically increased to 20.09%. Using SEM images, the authors observed a rearrangement of Au particles on the metal contact migrating away from the cracks on the HTM-83 film during the heating. In addition, Au is found

---

[195] J. Cao, X. Lv, P. Zhang, T. T. Chuong, B. Wu, X. Feng, C. Shan, J. Liu, Y. Tang, *Adv. Mater.* **2018**, *30*, 1800568.

[196] T. Duong, J. Peng, D. Walter, J. Xiang, H. Shen, D. Chugh, M. Lockrey, D. Zhong, J. Li, K. Weber, T. P. White, K. R. Catchpole, *ACS Energy Lett.* **2018**, *3*, 2441–2448.

to dope HTM-83 film, and the doping effect is greatly enhanced by heat treatment resulting in the increasing PCE and excellent stability.

Sun and co-workers reported an interface modification on perovskite devices, incorporating a buffer layer of V_2O_5 on top of the nickel(II)-based phthalocyanine acting as HTM-84[197] (**Figure 20**).The performance of the new HTM/V_2O_5 was investigated in mesoscopic devices. Initially, HTM-84 was incorporated without dopants, resulting in average PCE values of 9.9%. Adding dopants (LiTFSI), efficiencies of 17% were obtained, as a result of the increased conductivity. Furthermore, incorporating an extra buffer layer (V_2O_5) on top of HTM-84 yields not only an enhanced overall efficiency until 18.30% but also lengthens the lifetime after the aging period by retaining 75% of their initial PCE after 30 days, which is in contrast to the decay observed for spiro-OMeTAD (more than 50 %) in the same time.

Very recently, McGrath, Xu and co-workers reported another illustrative example in the use of a titanium-based phthalocyanine as HTM for PSCs (HTM-85)[198] (**Figure 20**). The use of hexylthio-substituents in the non-peripheral position of the phthalocyanine is surmised to lead to stronger π-π interaction in solid state that results in a remarkable hole mobility of HTM-85 (1.17×10^{-4} cm^2 V^{-1} s^{-1}). The incorporation of dopant-free HTM-85 into n-i-p PSCs in combination with triple cation perovskite as light-absorbing material lead to PCE values of 16.87% with excellent long-term stability in comparison to the reference of doped spiro-OMeTAD (19.20%) (**Table 5**).

197 M. Cheng, Y. Li, M. Safdari, C. Chen, P. Liu, L. Kloo, L. Sun, *Adv. Energy Mater.* **2017**, *7*, 1602556.

198 Q. Hu, E. Rezaee, M. Li, Q. Chen, Y. Cao, M. Mayukh, D. V McGrath, Z.-X. Xu, *ACS Appl. Mater. Interfaces* **2019**, *11*, 36535–36543.

Objectives

4. OBJECTIVES

During recent years, PSCs have attracted the attention of the photovoltaic community due to its impressive development until values of power conversion efficiencies (25.2%) close to that achieved for silicon-based solar cells. Most of the current research in PSCs is focused on the chemical modification of the composition of the perovskite, different deposition methods, and device architectures. Nevertheless, two of the most critical points for scaling in the PV market involve the preparation of PSCs devices through cost-effective components and stability along the time, where the charge selective layers could play an important role. In this regard, the design of custom-make hole- and electron-transporting layers could be crucial to reach both high performances and long-term stability of PSCs. The two most highlighted HTMs for achieving high performances are the polymeric triphenylamine-based PTAA and the small molecule spiro-OMeTAD. However, both possess a prohibitive commercial price (exceeding 500 and 300 €/g) that hampers its application towards low-cost PSCs manufacturing (more than 30% of the overall cost of the devices). The high commercial price is associated with complicated synthetic protocols that require harsh conditions such as *n*-butyllithium at low temperatures and the use of metal-catalyzed reactions that are not easy to scale. In order to solve these problems, the design of new HTMs should include a minimized number of synthetic steps and simple work-up procedures for low-cost applications.

Taking into account the limiting points mentioned above for the preparation of organic HTMs, the main objective of the present thesis is the tailored design and synthesis of new HTMs. The new designed HTMs should compete against the benchmark spiro-OMeTAD in terms of efficiency but with a low-cost and easily attainable synthesis. Although it has not been established a clear relationship between the chemical structure of HTM and its corresponding photovoltaic performance, different chemical approaches have been demonstrated as successful options for the design of new HTMs.

It is worth to mention that the present thesis has been focused on a basic research in the design, synthesis and characterization of new organic materials for its use as hole-transporting materials in perovskite solar cells. However, commercial

prospects for the use of these materials have not yet been established.

The design of new organic HTMs will be divided into four sections related with the different chemical approaches that have been employed.

The first section involves the design and synthesis of hole-transporting molecules, including sulfur- and selenium-containing central scaffolds bearing *p*-methoxytriphenylamines as electron donor units. The use of chalcogen-rich π-conjugated cores such as anthratetrathiophene (ATT), dibenzoquinquethiophene (DBQT), dibenzosexithiophene (DBST), cyclooctatetrathiophene (CoTh) and benzotriselenophene (BTSe) should promote strong π–π interactions that could lead to excellent hole-carrier mobilities. At the same time, the presence of chalcogen atoms allows S···S or Se···Se interactions that favor the control of the molecular packing. Furthermore, strong interactions Pb···S from the perovskite layer and the HTM molecules have been reported in the bibliography for the improvement of the charge transfer in the perovskite/HTM interface leading to more efficient devices.

The next section comprises the study of spiranic HTMs. To this end, two different families of molecules, spiro-based and "spiro-like" structures, are decorated with *p*-methoxydiphenylamines, mimicking the structure of spiro-OMeTAD. Firstly, phenoxazine or phenothiazine-based spiranic molecules are selected as low-cost starting materials for the synthesis of the new asymmetric HTMs. On the other hand, the twisted spiranic carbon atom between the two halves is replaced by a covalent ''C–C'' bond. **BX-OMeTAD** and **BTX-OMeTAD** consist of two xanthene or thioxanthene units connected through sp^3-hybridized carbon atoms, rendering a more flexible conformation than those of spiro-like structures.

Section 3 presents the synthesis of three new derivatives of triazatruxene-based (TAT) molecules as end-capping groups in dumbbell-shaped molecules with different π-conjugated spacers (D-π-D). Triazatruxene units have been exploited in the literature as central scaffold bearing different electron donating groups on the periphery. In this study the novelty of our system relies in the use of TAT connected through different linkages to the EDOT spacer. As an example, the azomethine bond that allows using a less complicated synthetic route based on Schiff-base condensation chemistry instead of palladium catalyzed cross-

coupling reactions. Furthermore, this alternative path provides a cost-effective and more environmentally friendly route, with water being the only by-product.

Finally, the last section of the present thesis is focused on the design of carbon-based molecular nanographenes as a novel approach for the preparation of efficient HTMs. The chemical design combines a saddle-shaped scaffold such as cyclooctatetraphenylene (CoPh) and cyclooctatetrathiophene (CoTh) to confer a non-planar molecular structure with four units of *tert*-butyl-substituted hexabenzocoronene, which are fused to the central saddle-shaped scaffold. The chemical design incorporate four units of hexabenzocoronene, which represents the minimum fragment to be considered as a molecular nanographene. Both new compounds has been addressed by following a well-established methodology by means of consecutive Diels-Alder reaction and cyclodehydrogenation (Scholl reaction).

Results and discussion

5. RESULTS AND DISCUSSION

The design of new hole-transporting materials (HTMs) has been intensively linked to the development of perovskite solar cells (PSCs) in the search for higher PCEs as well as better long-term stabilities of PSCs.[112] In this sense, organic chemistry offers a wide variety of tools for designing and synthetizing an extensive assortment of organic molecules, "à la carte", that can be employed as central scaffolds for HTMs. These molecules must meet some general criteria, namely: (i) thermal and photochemical stability; (ii) the highest occupied molecular orbital (HOMO) must be slightly higher in energy than the valence band edge of the perovskite (-5.40 eV for $MAPbI_3$ and -5.65 eV for $(FAPbI_3)_{0.85}(MAPbBr_3)_{0.15}$) to ensure an efficient extraction of the photogenerated holes. However, there is no consensus on what are the appropriate HOMO energy values; (iii) they must possess an optimal hole mobility, or at least reasonable, for transporting the holes to the counter-electrode; (iv) high solubility is desirable for better film-forming properties; (v) reduced tendency to crystallize (T_g > 100 °C) for avoiding phase transitions during device operation; (vi) it must be easily attainable for commercialization prospects and, (vii) strong absorption is not an essential requirement for obtaining highly efficient HTMs. Considering the aforementioned requirements, small organic compounds represent excellent candidates to be used as a hole-transporting layer for photovoltaic devices owing to their tailor-making preparation and manipulation and the ability to tune their properties through precise chemical modification.

Although a clear relationship between the chemical structure of the HTMs and its photovoltaic performance is not established yet. In the literature there are a few practical chemical approaches for designing highly efficient HTMs, as it has been extensively discussed in the *Background Section*. The use of spiranic-based molecules mimicking the state-of-art spiro-OMeTAD has resulted in the design of new HTMs that outperformed the reference spiro-OMeTAD.[99,100] On the other hand, chemical designs based on donor-acceptor systems have been demonstrated to be an excellent approach for the preparation of dopant-free materials.[117] Nevertheless, the most featured design of HTMs comprises multi-armed organic molecules, in which a central π-conjugated scaffold is endowed

with electron-donor units such as di- or triphenylamine, carbazole or phenothiazine.[150,173] Thus, properties such as mobility, thermal, optical, and electrochemical, are strongly dependent on the combination of the different fragments that form the HTM.

Section 5.1 Synthesis of planar chalcogen-rich based HTMs.

During the past years, the design and synthesis of sulfur-based compounds have been extensively investigated using thiophene as key building block for the preparation of new organic compounds for different applications[199] such as organic solar cells (OSCs),[200] organic field-effect transistors (OFETs)[9,201] and organic light-emitting diodes (OLEDs).[202]

Thiophene is an electron-rich heterocycle that has been employed as a π-bridging unit for connecting different building blocks. A vast number of new thiophene-based backbones for organic electronics have been reported due to the chemical versatility of thiophene along with its rich synthetic chemistry to modify its chemical structure and properties. Benzodithiazole (BTZ), benzodithiophene (BDT), thieno[3,2-*b*]thiophene (TbT), or dithienopyrrole (DTP) represent some of the examples of chemically modified structures based on thiophene that leads to a considerable scope of π-conjugated molecules for each application.[203]

Sulfur-based small organic molecules have been successfully incorporated in PSCs, as described in the *Background* section. Our group reported some of the most representative examples with the synthesis of a series of benzotrithiophene-based HTMs (BTTs)[102,174] (**Figure 21**). Sulfur-rich central scaffolds have shown excellent hole-transporting properties due to the stacking of the planar

199 A. C. Arias, J. D. MacKenzie, I. McCulloch, J. Rivnay, A. Salleo, *Materials and Applications for Large Area Electronics: Solution-Based Approaches*, American Chemical Society, **2010**.

200 J. L. Delgado, P.-A. Bouit, S. Filippone, M. Á. Herranz, N. Martín, *Chem. Commun.* **2010**, *46*, 4853–4865.

201 C. Wang, H. Dong, W. Hu, Y. Liu, D. Zhu, *Chem. Rev.* **2012**, *112*, 2208–2267.

202 S. C. Rasmussen, S. J. Evenson, C. B. McCausland, *Chem. Commun.* **2015**, *51*, 4528–4543.

203 T. Parker, S. Marder, *Synthetic Methods in Organic Electronic and Photonic Materials*, Royal Society of Chemistry, **2015**.

structure through intramolecular π-π interactions, which lead to excellent power conversion efficiencies. Furthermore, the presence of thiophene units within the conjugated core of the HTM molecules has shown to promote the sulfur-iodine interaction with the perovskite layer leading to more efficient hole extraction as well as enhancing the passivation of the perovskite layer.[2,204,205,206] Following this strategy, BTT-based HTMs incorporated in mesoporous PSCs reached power conversion efficiencies ranging from 16-19%, demonstrating the potential of flat sulfur-based cores for highly-efficient PV applications.

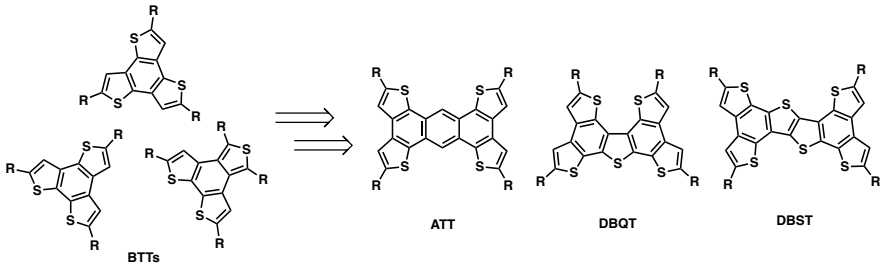

Figure 21. Chemical structures of previously reported BTT family and new planar sulfur-rich extended cores ATT, DBQT and DBST.

5.1.1 Synthesis of anthra[1,2-*b*;4,3-*b′*;5,6-*b″*;8,7-*b‴*]tetrathiophene (ATT) based HTMs.

Inspired by these promising results, we decided to continue exploring planar sulfur-rich scaffolds for the preparation of HTMs by the introduction of a more π-extended flat heteroaromatic structure based on anthra[1,2-*b*;4,3-*b′*;5,6-*b″*;8,7-*b‴*]tetrathiophene (ATT) core (**Figure 21**). ATT is a sulfur-rich polycyclic aromatic hydrocarbon with a flat and rigid π-conjugated structure, which consists of four thiophene units fused to a central anthracene moiety. As it was explained before, these structures tend to stack through strong π–π interactions and leads to excellent hole-carrier mobilities in OFETs. Furthermore, the presence of

[204] N. K. Noel, A. Abate, S. D. Stranks, E. S. Parrott, V. M. Burlakov, A. Goriely, H. J. Snaith, *ACS Nano* **2014**, *8*, 9815–9821.

[205] J. Cao, J. Yin, S. Yuan, Y. Zhao, J. Li, N. Zheng, *Nanoscale* **2015**, *7*, 9443–9447.

[206] Y. Lin, L. Shen, J. Dai, Y. Deng, Y. Wu, Y. Bai, X. Zheng, J. Wang, Y. Fang, H. Wei, W. Ma, X. C. Zeng, X. Zhan, J. Huang, *Adv. Mater.* **2017**, *29*, 1604545.

sulfur atoms allows S···S interactions in this design should favor the control of the molecular packing, which also should enhance carrier mobilities.

In the present thesis, we have introduced ATT as central backbone for the design of four new HTMs, in which the ATT planar core is endowed with *p*-alkoxytriphenylamines bearing different alkyl chain length in the periphery to study the influence of the length of the alkyl chains in the photovoltaic response. The synthetic pathway for the preparation of the ATT scaffold was reported in different works by Pei and Perepichka (**Scheme 1**).[207,208] This well-established procedure involves a four-fold Stille cross-coupling between commercially available 1,2,4,5-tetrabromobenzene and 2-(tributylstannyl)thiophene in DMF at 130 ºC, followed by the selective bromination of the α position of the thiophene employing N-bromosuccinimide (NBS) under mild conditions, which gave rise to the tetrabrominated derivative **2**. Then, $FeCl_3$-mediated Scholl reaction of compound **2** leads to the formation of the π-extended ATT (**3**). The ATT central core (**3**) was obtained in 75% overall yield (three synthetic steps) and, more importantly, no further purification was required for any of the synthetic steps, making ATT core a promising backbone for low-cost applications. Finally, *p*-alkoxytriphenylamines were covalently linked to the central ATT (**3**) by a four-fold Suzuki cross-coupling in moderate to good yields, ranging from 46% to 72%, for the preparation of methoxy (**ATT-OMe**), butoxy (**ATT-OBu**), hexyloxy (**ATT-OHex**) and decyloxy (**ATT-ODec**) substituents in the periphery of the donor triphenylamine moieties.[209] Complete structural characterization of the ATT-based HTMs was carried out using standard spectroscopic techniques such as ^{1}H and ^{13}C nuclear magnetic resonance (NMR), Fourier transform infrared (FTIR), and mass spectrometry (See Experimental Section).

---

[207] W.-J. Liu, Y. Zhou, Y. Ma, Y. Cao, J. Wang, J. Pei, *Org. Lett.* **2007**, *9*, 4187–4190.

[208] J. L. Brusso, O. D. Hirst, A. Dadvand, S. Ganesan, F. Cicoira, C. M. Robertson, R. T. Oakley, F. Rosei, D. F. Perepichka, *Chem. Mater.* **2008**, *20*, 2484–2494.

[209] I. Zimmermann, J. Urieta-Mora, P. Gratia, J. Aragó, G. Grancini, A. Molina-Ontoria, E. Ortí, N. Martín, M. K. Nazeeruddin, *Adv. Energy Mater.* **2017**, *7*, 1601674.

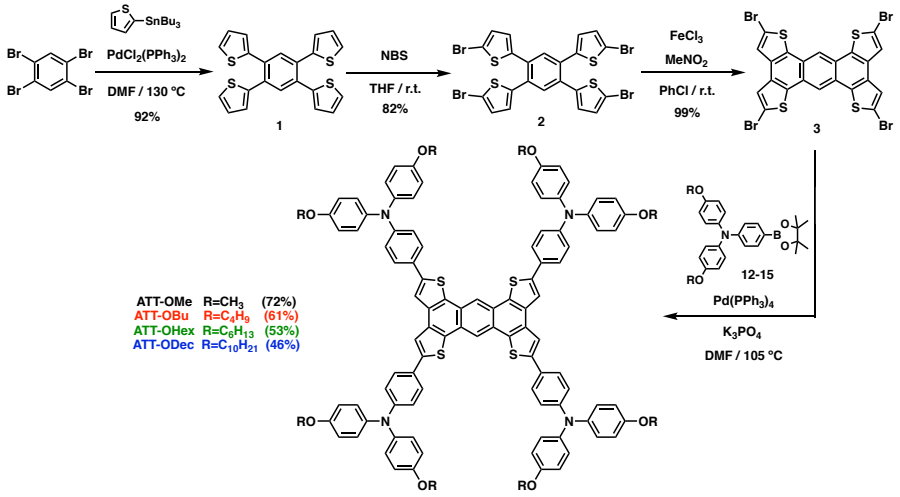

Scheme 1. Synthetic route for the preparation of ATT-based HTMs (**ATT-OMe**, **ATT-OBu**, **ATT-OHex** and **ATT-ODec**).

High-resolution mass spectrometry HR-MS [MALDI-TOF] confirmed the presence of **ATT-OMe**, **ATT-OBu**, **ATT-OHex** and **ATT-ODec** showing their corresponding molecular ion peak $[M]^+$ at 1614.4748 m/z (calcd. 1614.4697 m/z), 1950.8402 m/z (calcd. 1950.8453 m/z), 2175.1001 m/z (calcd. 2175.0957 m/z) and 2623.6028 m/z (calcd. 2623.5965 m/z), respectively. In **Figure 22** it is shown a representative example of the ^{1}H NMR of the ATT-based HTMs, in this case for **ATT-OMe**. As it is shown, the highly symmetric structure results in a quite simple spectrum with two different singlets at $\delta \approx 8.7$ and 8.0 that correspond to the protons from the central benzene and the β protons of the thiophene moieties, respectively. Moreover, the typical AA'XX' system of the *p*-substituted phenyl rings from the donor triphenylamine units appear at $\delta \approx 7.7$, 7.15, 7.0 and 6.9, with its corresponding methoxy singlet at 3.8 ppm.

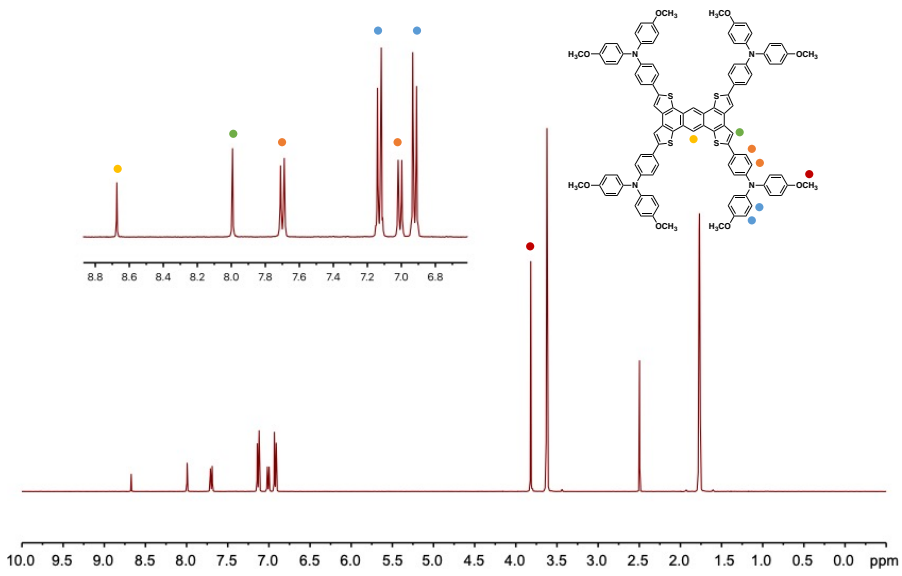

Figure 22. ^{1}H NMR spectrum (400 MHz, THF-*d8*, 298K) of **ATT-OMe**.

The syntheses of the different electron-donor triphenylamine units for the preparation of the ATT derivatives were carried out by a sequential three-step approach comprising a Buchwald-Hartwig reaction between the different *p*-alkoxyaniline with the corresponding 4-iodoalkoxybenzenes (**Scheme 2**). Thus, each triphenylamine was iodinated in the presence of I_2/H_5IO_6 under mild conditions, followed by a Miyaura borylation for the preparation of the corresponding boronic esters, which serve as reactive building blocks for further reactions.

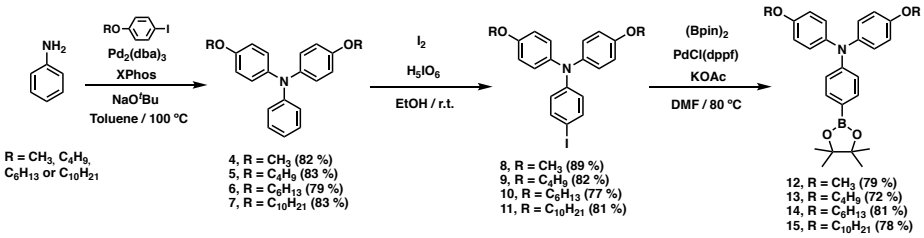

Scheme 2. Synthetic route for the preparation of the boronic esters of the different alkoxy-substituted TPAs.

5.1.2 Optical, electrochemical and thermal characterization of ATT-based HTMs.

The optical properties of the ATT-based HTMs were studied using absorption and emission spectroscopy from diluted CH_2Cl_2 solutions (**Figure 23a**). ATT-based HTMs exhibit a strong absorption band in the 300-500 nm range, with a maximum centered at 402 nm (ε = 1.5 × 10^{-5} M cm^{-1}). Thus, the limited absorption of these HTMs in the visible region should not affect the generated photocurrent due to the strong absorption of the perovskite. Theoretical calculations (B3LYP/6-31G**) of the singlet excited electronic states (S_n) ascribe this band to the intense electronic transitions $S_0 \rightarrow S_1$, $S_0 \rightarrow S_2$, $S_0 \rightarrow S_3$, and $S_0 \rightarrow S_6$ calculated at 498, 495, 458, and 440 nm, respectively. These electronic transitions are of $\pi \rightarrow \pi^*$ nature and imply one-electron excitations from the HOMO and HOMO-1 to the LUMO and LUMO+1 which are, all of them, mainly located on the ATT core. Detailed optical features of the absorption and emission spectra are collected in **Table 6**.

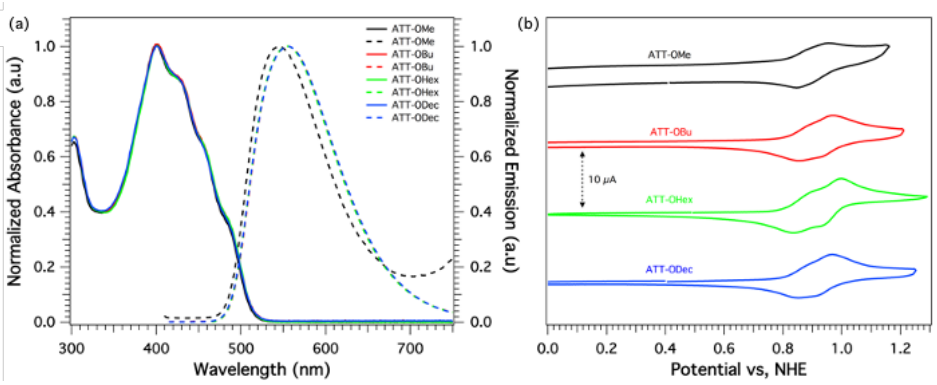

Figure 23. (a) UV–visible (solid line) and fluorescence emission (dashed line) spectra of ATT-based HTMs in CH_2Cl_2; (b) Cyclic voltammograms of ATT-based HTMs in $TBAPF_6/CH_2Cl_2$ at a scan rate of 100 mV s^{-1}.

The emission spectra (**Figure 23a**) of the HTMs exhibit a maximum centered at 554 nm for **ATT-OBu**, **ATT-OHex**, and **ATT-ODec**, whereas the emission of **ATT-OMe** is slightly blue-shifted, with a maximum at 549 nm. The large Stoke-shift between the absorption and emission maxima (~150 nm) observed for all the ATT derivatives is attributed to the participation of different singlet excited

states in the absorption, the transition to the lowest-energy S_1 being predicted at 2.49 eV (498 nm). The optical band gap ($E^{0\text{-}0}$) estimated from the intersection of the absorption and emission spectra is indeed of 2.50 eV for all of the sulfur-rich HTMs. It is important to note that no significant changes in the absorption and emission spectra were observed when increasing the length of the alkyl chains, which demonstrate that the alkyl chain length does not affect the optoelectronic properties of the respective compounds.

Table 6. Optical and electrochemical properties of ATT-based HTMs and the reference spiro-OMeTAD.

HTM	$E^{ox}_{1/2}$ [V][a]	E_{HOMO} [eV][b]	$\lambda_{max, abs}$ [nm][c]	$\lambda_{max, em}$ [nm][c]	$E^{0\text{-}0}$ [eV][d]	E_{LUMO} [eV][e]
ATT-OMe	0.88	–5.32	402	549	2.49	–2.82
ATT-OBu	0.88	–5.32	402	554	2.49	–2.83
ATT-OHex	0.87	–5.31	402	554	2.49	–2.82
ATT-ODec	0.88	–5.32	402	554	2.49	–2.83
spiro-OMeTAD	0.72	–5.16	386	319	3.05	–2.11

[a] Determined from CV measurements *vs.* normal hydrogen electrode (NHE); [b] E_{HOMO} is estimated in eV by E_{HOMO} = -4.44 eV - $E^{ox}_{1/2}$; [c] λ_{max} of absorption and emission were measured in CH_2Cl_2 solutions; [d] $E^{0\text{-}0}$ was determined at the intersection of normalized absorption and emission spectra; [e] E_{LUMO} were estimated by $E_{LUMO} = E_{HOMO} + E^{0\text{-}0}$.

The electrochemical properties of the ATT derivatives were studied by cyclic voltammetry (**Figure 23b**) in CH_2Cl_2 solutions under N_2 atmosphere at a scan rate of 100 mV s^{-1}, and the corresponding redox potentials are summarized in **Table 6**. The ATT-based HTMs are only active in the anodic scan, where two consecutive reversible oxidation waves are observed. The ATT-based derivatives show similar redox behavior with half-wave oxidation potentials of the first oxidation potential located at 0.88 V versus normal hydrogen electrode (NHE). Using this value, the energy derived for the highest-occupied molecular orbital (HOMO) of the ATT derivatives is calculated in -5.32 eV, which is slightly lower than that of spiro-OMeTAD (-5.16 eV) estimated under similar

conditions.[210] Therefore, the new sulfur-rich HTMs exhibit an excellent band alignment between the HOMO level of the HTM and the valence band edge of the perovskite material. Thus, an efficient hole injection from the HTM to the perovskite is expected, confirming the potential of ATT-based molecules for hole-transporting applications. It is worth noting that there is no significant variation in the HOMO energy by increasing the length of the alkyl chain.

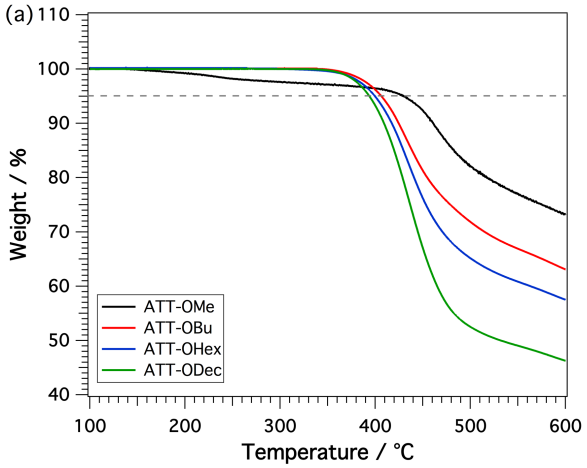

Figure 24. Thermogravimetric analysis (TGA) curves recorded for ATT-based HTMs under nitrogen at 10 ºC min^{-1} of heating rate.

Thermal behavior of the ATT-based HTMs were evaluated using thermogravimetric analysis (TGA) and differential scanning calorimetry (DSC). The thermal properties of the new HTMs are collected in **Table 7**. ATT-based derivatives exhibit good thermal stability with decomposition temperatures (T_{dec}) up to 400 ºC (5% weight loss under N_2 atmosphere) (**Figure 25**). As expected, the thermal stability increases when shortening the length of the alkyl chains. From DSC analysis (**Figure 25a-d**), by increasing the length of the alkyl chain in the periphery, a different behavior is observed. On one side, **ATT-OMe** reveals a crystalline behavior with a melting temperature (T_m) of 254 ºC and a crystallization process upon cooling (T_{cr}) of 242 ºC during the first scan, which

[210] K. Rakstys, M. Saliba, P. Gao, P. Gratia, E. Kamarauskas, S. Paek, V. Jankauskas, M. K. Nazeeruddin, *Angew. Chem. Int. Ed.* **2016**, *55*, 7464–7468.

are still observed after consecutive heating/cooling cycles. **ATT-OBu** and **ATT-OHex** present a melting temperature (T_m) of 284 and 206 ºC and a glass transition (T_g) temperature of 131 and 95 ºC, respectively, which implies the crystalline and amorphous behavior of **ATT-OBu** and **ATT-OHex**. Finally, **ATT-ODec** exhibits four consecutive phase transitions with a T_g at 60 ºC obtained from the second cycle, which indicates an amorphous nature.

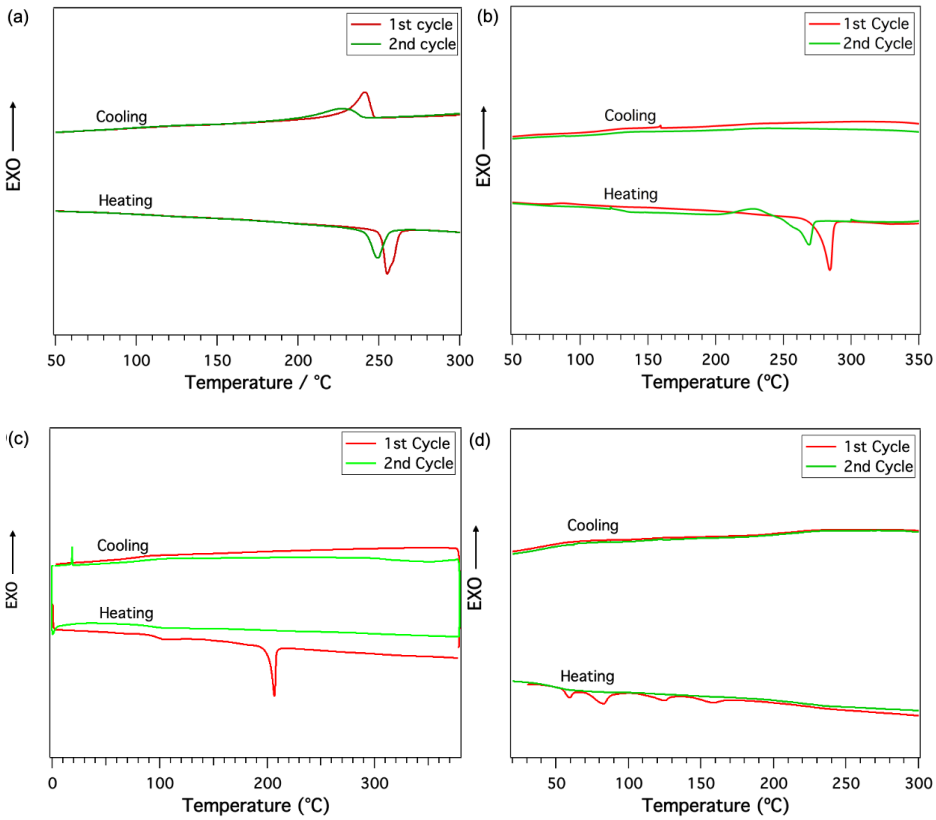

Figure 25. Differential scanning calorimetry (DSC) of (a) **ATT-OMe**, (b) **ATT-OBu**, (c) **ATT-OHex** and (d) **ATT-ODec** under nitrogen at heating rate of 20 ºC min^{-1} (first and second cycle) respectively.

Theoretical calculations were performed at the B3LYP/6-31G** level for **ATT-OMe**, its constituting fragments (the ATT central core and donor unit, the *p*-methoxytriphenylamine) and the spiro-OMeTAD as a reference to gain insights of its electronic properties. Because of these properties hardly change with the

length of the alkyl chain, only the **ATT-OMe** system was selected as a representative ATT derivative. **Figure 26a** displays the frontier molecular orbitals calculated for the ATT core, the OMeTPA units, the **ATT-OMe**, and spiro-OMeTAD. The HOMO of **ATT-OMe** clearly corresponds to the HOMO of the ATT core with significant contributions from the neighboring phenyl rings and nitrogen atoms of the *p*-methoxytriphenylamine groups, whereas the LUMO fully resides on the ATT core. It is noticeable that the HOMO is strongly destabilized, incorporating the donor groups from the ATT (-5.30 eV) to **ATT-OMe** (-4.45 eV) as a consequence of the antibonding interaction between the HOMOs of the constituting ATT core and the donor units. This destabilization enhanced the donor ability of **ATT-OMe** compared to the ATT core and determines that the HOMO energy is close to the reference spiro-OMeTAD. The HOMO of **ATT-OMe** is indeed predicted 0.29 eV lower in energy than the HOMO of the reference spiro-OMeTAD (-4.16 eV) in good agreement with the slightly higher oxidation potential measured in the CV measurements (0.88 *vs* 0.72 eV). The difference between the theoretical values predicted for the energy of the HOMO, and those obtained experimentally (**Table 6**) is that the former has been computed for the isolated molecules in gas phase. In contrast, the latter are estimated from the oxidation potentials measured in solution.

Table 7. Thermal properties of ATT-based HTMs.

	T_{dec}[°C][a]	T_m[°C][b]	T_g[°C][b]	T_{cr}[°C][b]
ATT-OMe	430	254	-	242
ATT-OBu	405	284	131	-
ATT-OHex	398	206	95	-
ATT-ODec	393	58, 82, 124, 158	60[c]	-

[a] Decomposition temperature determined from TGA (5% weight loss under N_2 atmosphere); [b] Determined from the first cycle of the DSC under nitrogen atmosphere; [c] Determined for the second cycle of the DSC under nitrogen atmosphere.

Furthermore, hole reorganization energies (λ) were also estimated in order to evaluate the ability of the ATT derivatives as HTMs. The λ values computed for the ATT core, the OMeTPA groups, **ATT-OMe**, and spiro-OMeTAD compounds are 0.126, 0.274, 0.096, and 0.139 eV, respectively. The **ATT-OMe**

compound, therefore, exhibits a very small λ value, significantly smaller than the reorganization energy calculated for the ATT core and the reference spiro-OMeTAD compound. The small λ value obtained for **ATT-OMe** is indeed comparable to the reorganization energies found for the best organic *p*-type semiconducting materials in the literature.[211] These findings clearly highlight the potential of **ATT-OMe** for hole transporting applications.

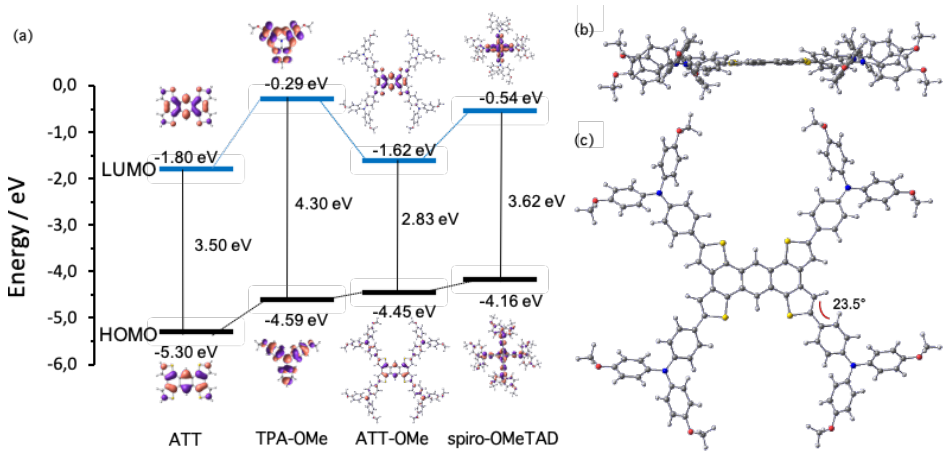

Figure 26. (a) Energy diagram showing the frontier molecular orbitals computed for ATT, TPA-OMe, **ATT-OMe** and spiro-OMeTAD compounds at the B3LYP/6-31G** level**; (**b) Lateral and top view of the optimized geometry of the **ATT-OMe**.

Optimized geometry was also predicted using theoretical calculations (**Figure 26b**). It is clear that **ATT-OMe** presents an extended π-conjugated structure; the ATT core is completely planar, and the dihedral angle between the phenyl rings connecting the peripheral donor units of the *p*-methoxytriphenylamine and the thiophene rings of the ATT core are of 23.5°. Despite the bulky structure of the donor moieties, **ATT-OMe** exhibits a quite planar structure that, in principle, can give rise to stacking aggregation in the solid-state. This fact is in good agreement with the low solubility that exhibits **ATT-OMe** in common organic solvents. As should be expected, passing from methoxy chain to butoxy,

[211] A. N. Sokolov, S. Atahan-Evrenk, R. Mondal, H. B. Akkerman, R. S. Sánchez-Carrera, S. Granados-Focil, J. Schrier, S. C. B. Mannsfeld, A. P. Zoombelt, Z. Bao, A. Aspuru-Guzik, *Nat. Commun.* **2011**, *2*, 437.

hexyloxy, and decyloxy in the periphery of the triphenylamine, the solubility of the HTMs is notably increased, and in consequence, its processability from solution.

5.1.3 Device performance and characterization of ATT-based HTMs.

The ATT-based derivatives were incorporated in solution-processed mesoporous PSC devices. The devices were prepared from a stack of thin layers onto fluorine-doped tin oxide (FTO) coated glass that serves as the conductive substrate. The different layers of the devices incorporating each new ATT-based derivative are shown in the cross-section scanning electron microscopy (SEM) image (**Figure 27a-d**). The layers forming the device are deposited consecutively starting from compact TiO_2 (~ 30 nm) serving as blocking layer, mesoporous TiO_2 (~ 200 nm) where the perovskite material is infiltrated (~ 400 nm). On the top of the perovskite, the HTM layer (~100-150 nm) is deposited from solution, and thermally evaporated gold for the electrodes (~80 nm). ATT-based HTMs were tested in combination with compositionally engineered $[FAPbI_3]_{0.85}[MAPbI_3]_{0.15}$ which displayed superior performances compared to standard $MAPbI_3$ when our group introduced benzotrithiophene-based HTMs.[13] Additional information related to the fabrication of PSCs can be found in the *Experimental Section*. The HTMs were deposited by spin-coating from chlorobenzene solution containing cobalt dopant (FK-209), Li-TFSI, and tert-butylpyridine as additives.[212] Due to the poor solubility of **ATT-OMe** at room temperature, this molecule was applied by heating the HTM solution as well as the substrate to 100 ºC; at this temperature **ATT-OMe** is completely solubilized for a concentration of 20 mM. Using this procedure, it is possible to get very smooth and uniform layers of around 150 nm thicknesses.

[212] F. Giordano, A. Abate, J. P. Correa Baena, M. Saliba, T. Matsui, S. H. Im, S. M. Zakeeruddin, M. K. Nazeeruddin, A. Hagfeldt, M. Graetzel, *Nat. Commun.* **2016**, *7*, 10379.

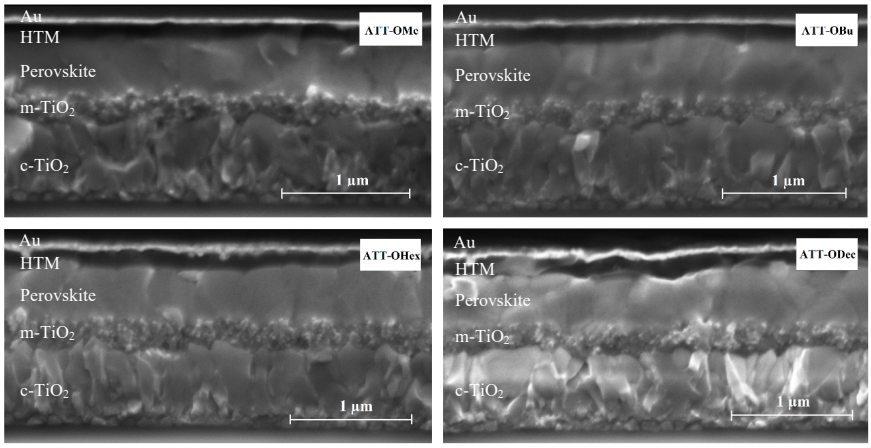

Figure 27. Cross-section SEM pictures showing the different layers in PSC devices.

The long alkyl chains on the remaining ATT derivatives increased the solubility remarkably, and 30 mM HTM concentrations spin-coated at room temperature resulted in similar thicknesses. Although good solubility is usually key for obtaining uniform HTM layers with thicknesses greater than 100 nm, we observed that the film quality became worse going for longer alkyl chains, especially for **ATT-OHex** and **ATT-ODec**. The roughness of those HTM layers can be clearly observed from the SEM images (**Figure 27**). Interestingly, the performance of the ATT-based HTMs is not affected upon heating the HTM solution until 100 ºC in contrast to the behavior showed by spiro-OMeTAD.

The performance of the PSC devices incorporating the new ATT-based HTMs and spiro-OMeTAD was measured under standard conditions of irradiation (1 sun 1.5 AMG 100 mW cm^{-2}). The *J-V* curves recorded for the four new HTMs are shown in **Figure 28a**, and the photovoltaic parameters are collected in **Table 8**. **ATT-OMe** shows the highest performance of the new sulfur-rich materials with a maximum PCE of 18.10%, similar to those measured for the benchmark spiro-OMeTAD. Upon increasing the length of the peripheral alkyl chains, the device efficiency decreases to 17.28% for **ATT-OBu**, 15.66% for **ATT-OHex**, and 9.67% for **ATT-ODec**. The same trend is also observed for the short circuit current (J_{sc}), which decreases from 21.75 mA cm^{-2} for **ATT-OMe** to 14.92 mA cm^{-2} for **ATT-ODec**. The theoretical J_{sc} values integrated from the external quantum efficiencies (EQEs) are consistent with those experimentally determined in all cases (**Figure 28b**).

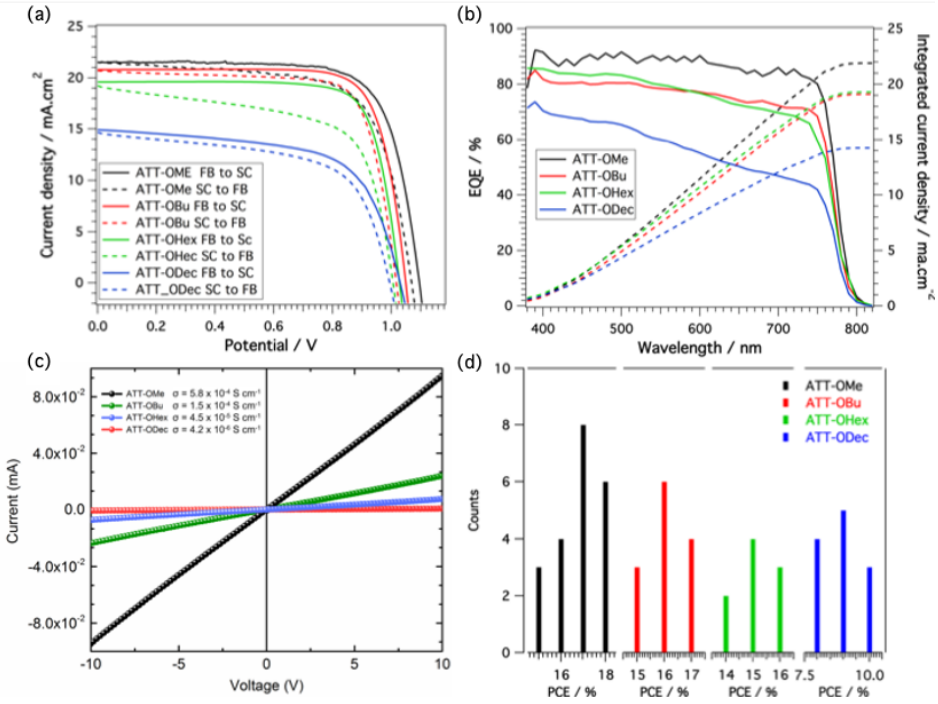

Figure 28. (a) Hysteresis curves of the ATT-based HTMs measured at 20 mV/s; (b) External quantum efficiency (EQE) and integrated current plots of ATT-based HTMs; (c) Conductivity of the ATT derivatives measured on substrates having interdigitating gold electrodes with a channel length of 2.5 μm; (d) Efficiency distribution of devices fabricated using the ATT-based HTMs.

To further investigate the observed trend in solar cell performance, we measured the conductivity of the different ATT-based hole-transporting materials. HTMs solutions doped with 6% FK-209 were spin-coated onto a substrate having interdigitating gold electrodes with a channel length of 2.5 μm. *J-V* scans between -10 and +10 V were recorded, and the conductivity of the different molecules was calculated using Ohm's law. In **Figure 28c** are represented the semi-logarithmic conductivity plots as well as the corresponding calculated conductivity values. Remarkable lateral conductivity was observed for **ATT-OMe** (5.8×10^{-4} S cm^{-1}), which is even higher than that previously measured for

spiro-OMeTAD (8.7×10^{-5} S cm^{-1}).[213] Upon increasing the length of the alkyl chains, the conductivity decreases gradually, (**ATT-OBu** = 1.5×10^{-4} S cm^{-1} and **ATT-OHex** = 4.5×10^{-5} S cm^{-1}) and for **ATT-ODec** (4.2×10^{-6} S cm^{-1}), which is two orders of magnitude lower than for **ATT-OMe**. These findings are in good agreement with the device performance. Efficient HTMs need to have high electrical conductivity to guarantee efficient charge transport.

Table 8. Device performance of the ATT derivatives compared to spiro-OMeTAD.

HTM	V_{oc} (V)	J_{sc} (mA cm^{-2})	*FF*	PCE (%)
ATT-OMe	1.07	21.75	0.78	18.13
ATT-OBu	1.05	20.94	0.78	17.28
ATT-OHex	1.03	19.60	0.77	15.66
ATT-ODec	1.03	14.92	0.63	9.67
spiro-OMeTAD	1.12	21.33	0.74	17.80

We surmised that longer alkyl chains might enhance the stacking of the ATT cores due to additional van der Waals interactions stemming from the side chains. This allows aggregation of the ATT molecules into 1D nanowire-like ensembles having highly anisotropic charge transport properties. Crystallization of those aggregates within the HTM films is expected to be oriented within the horizontal plane and thus compromising the vertical charge transport properties in the device. Increased crystallinity of ATT molecules with longer alkyl chains could also be the reason for less good film formation, which might also contribute to their lower conductivity and thus low device performance. **Figure 28d** shows the device efficiency distribution where the reproducibility was found relatively good except for the device employing **ATT-OMe** due to the difficulty in the preparation of good films caused by the low solubility of this HTM.

[213] P. Gratia, A. Magomedov, T. Malinauskas, M. Daskeviciene, A. Abate, S. Ahmad, M. Grätzel, V. Getautis, M. K. Nazeeruddin, *Angew. Chem. Int. Ed.* **2015**, *54*, 11409–11413.

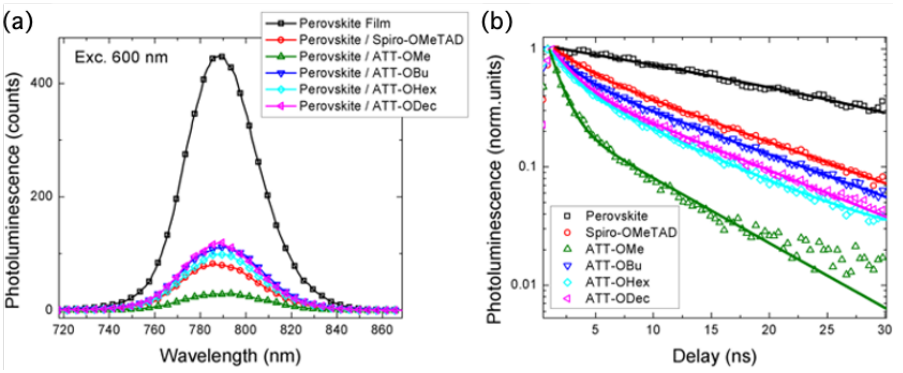

Figure 29. (a) CW photoluminescence spectra, excitation at 600 nm; (b) time-resolved photoluminescence decay at 780 nm for the pristine perovskite film deposited on glass and perovskite/HTMs samples (excitation at λ_{exc} = 460 nm).

To better understand the dynamics of hole transfer at the perovskite/ HTM interface, we carried out steady-state and time-resolved photoluminescence (PL). **Figure 29a** shows the comparison of the steady-state PL spectra measured for the pristine perovskite film and those with the HTM on top of the perovskite layer. The continuous wave (CW) PL spectra of the perovskite/HTMs show a significant reduction of the PL signal with respect to the pristine perovskite film. The quenching is indicative of interfacial hole transfer that is similarly observed for all the HTMs, with a slightly enhanced quenching for the perovskite/**ATT-OMe**. To dynamically monitor this process, we investigated the time-resolved PL (**Figure 29b**). The pristine perovskite film shows a long-living decay fitted with a mono-exponential time constant above our time window of 30 ns, in agreement with that previously observed in the literature.[214,215] On the other hand, the PL decays at the perovskite/spiro-OMeTAD, and perovskite/ATT-based HTMs exhibit faster dynamics than the pristine perovskite. The quenching observed confirms an efficient interfacial hole transfer, which is remarkably higher in the case of **ATT-OMe**. This behavior also suggests that the new molecules can effectively quench the PL, thus representing efficient hole-

[214] C. Roldán-Carmona, P. Gratia, I. Zimmermann, G. Grancini, P. Gao, M. Graetzel, M. K. Nazeeruddin, *Energy Environ. Sci.* **2015**, *8*, 3550–3556.

[215] E. Mosconi, G. Grancini, C. Roldán-Carmona, P. Gratia, I. Zimmermann, M. K. Nazeeruddin, F. De Angelis, *Chem. Mater.* **2016**, *28*, 3612–3615.

transfer materials, similar in function to spiro-OMeTAD. In addition, the interfacial dynamics further confirm the favorable hole transfer, as one should expect from the relative energy position of the HOMO level of the synthesized HTMs.

5.1.4 Synthesis of π-extended sulfur-rich DBQT and DBST-based hole-transporting materials.

As a consequence of the excellent results achieved with the introduction of flat, sulfur-containing, polycyclic aromatic structures as central scaffolds (BTTs and ATTs), we decided to study the impact of increasing the number of chalcogens atoms in more π-extended structures. Planar sulfur-rich arenes introduce extra intermolecular interactions (π–π, S···S) that affect the packing of the derivatives (face-to-edge to face to face), thus enhancing the hole-carrier mobilities that should allow the preparation of more efficient hole-transporting materials. On this basis, we have explored the synthesis of two new planar sulfur-rich central scaffolds using tetrabromothiophene and tetrabromothieno[3,2-*b*]thiophene (**19**) as starting materials following a similar strategy to that carried out for the ATT-based HTMs[216] (**Figure 21**). The new central cores consist of four fused thiophenes to a central dibenzothiophene (for **DBQT-OMe**) or dibenzothieno[3,2-*b*]thiophene (for **DBST-OMe**) which are chemically modified with four triphenylamine (TPA) units in the *α*-position of the four-terminal thiophene (**Scheme 3**).

The synthesis of DBQT and DBST cores starts with a four-fold palladium-mediated Stille cross-coupling reaction and Suzuki cross-coupling reaction between commercially available tetrabromothiophene and 2-(tributyl)stannylthiophene or tetrabromothieno[3,2-*b*]thiophene (**19**) with 2-thienylboronic acid affording compounds **16** and **20**, respectively. Then, selective *α*-bromination under mild conditions (NBS /THF/r.t.) successfully afforded the corresponding tetrabromo derivatives **17** and **21**. The π-extended central cores of dibenzoquinquethiophene (**18**) (DBQT) and dibenzosexithiophene (**22**) (DBST) were synthesized by a Lewis acid-mediated oxidative C-C coupling protocol using $FeCl_3/MeNO_2$ in chlorobenzene with excellent yields. Finally, a four-fold Suzuki cross-coupling reaction with *p*-methoxytriphenylamine (**12**) successfully furnished **DBQT-OMe** and **DBST-OMe** as orange solids in good yields (74 and 68%, respectively). Complete structural characterization of the designed **DBQT-OMe** and **DBST-OMe** was

[216] J. Urieta-Mora, I. Zimmermann, J. Aragó, A. Molina-Ontoria, E. Ortí, N. Martín, M. K. Nazeeruddin, *Chem. Mater.* **2019**, *31*, 6435–6442.

carried out using standard spectroscopic techniques such as ^{1}H NMR, ^{13}C NMR, FTIR, and mass spectrometry (MALDI-TOF) that confirmed the presence of the desired **DBQT-OMe** and **DBST-OMe** with molecular ion peaks $[M]^{+}$ at 1620.4273 (calcd. 1620.4261 m/z) and 1676.3986 (calcd. 1676.3982 m/z) m/z, respectively. (See Experimental Section for more details)

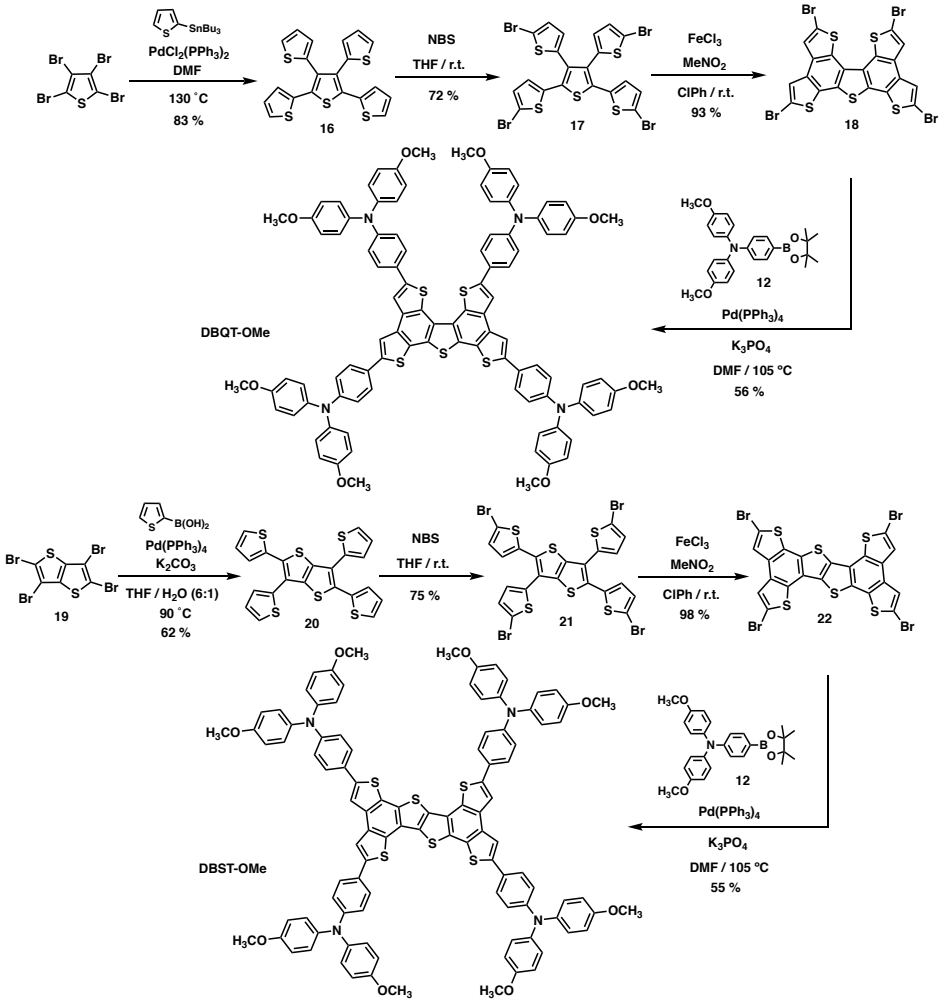

Scheme 3. Synthetic route for the preparation of π-extended HTMs **DBQT-OMe** and **DBST-OMe**.

5.1.5 Optical, electrochemical and thermal characterization of π-extended sulfur-rich DBQT and DBST-based HTMs.

The absorption and emission spectra of the π-extended HTMs in solution (CH_2Cl_2) display an intense absorption in the UV at short wavelengths of the visible region (<500 nm), in sharp contrast with the limited absorbance of spiro-OMeTAD in this region (**Figure 30a**). The absorption maxima ($\lambda_{max,abs}$) for **DBQT-OMe** and **DBST-OMe** are centered at 403 nm ($\varepsilon = 1.2 \times 10^4$ M cm^{-1}) and 431 nm ($\varepsilon = 1.4 \times 10^4$ M cm^{-1}), respectively (**Table 9**). The broader and red-shifted absorption of **DBST-OMe** compared with **DBQT-OMe** (and ATT-based molecules) is ascribed to the more extended π-conjugation of the central DBST core and agrees with the lower HOMO-LUMO gap predicted for both HTMs by DFT calculations (**Figure 30c**). B3LYP/6-31G** calculations of the lowest-lying singlet excited electronic states ascribe the broad experimental absorption band recorded for **DBQT-OMe** to six intense $S_0 \rightarrow Sn$ (n = 1-6) electronic transitions computed in the range from 430 to 505 nm. In the case of **DBST-OMe**, three intense electronic transitions ($S_0 \rightarrow S_1$, $S_0 \rightarrow S_2$, and $S_0 \rightarrow S_6$) in the range of 420-515 nm are ascribed for the more structured experimental band. The intense electronic transitions in both HTMs are of π–π* nature and imply one electron promotions from the HOMO-3, HOMO-2, HOMO-1, and HOMO to the LUMO, LUMO+1, and LUMO+2, which reside on both the core and the peripheral donor groups (**Figure 30c**). The emission maximum of **DBQT-OMe** is centered at 522 nm, whereas the maximum of **DBST-OMe** is slightly bathochromically shifted to 528 nm. Furthermore, it is observed that the intersection of the absorption and emission occurs at 477 and 481 nm for **DBQT-OMe** and **DBST-OMe**, respectively, which allow us to estimate the value of the band gap energy in 2.60 and 2.57 eV, respectively.

The redox properties of the novel HTMs, as well as the reference spiro-OMeTAD, were investigated by cyclic voltammetry in a solution of $TBAPF_6/CH_2Cl_2$ at a scan rate of 100 mV s^{-1} (**Figure 30b**). The oxidation potentials and the corresponding HOMO and LUMO energies are summarized in **Table 9**.

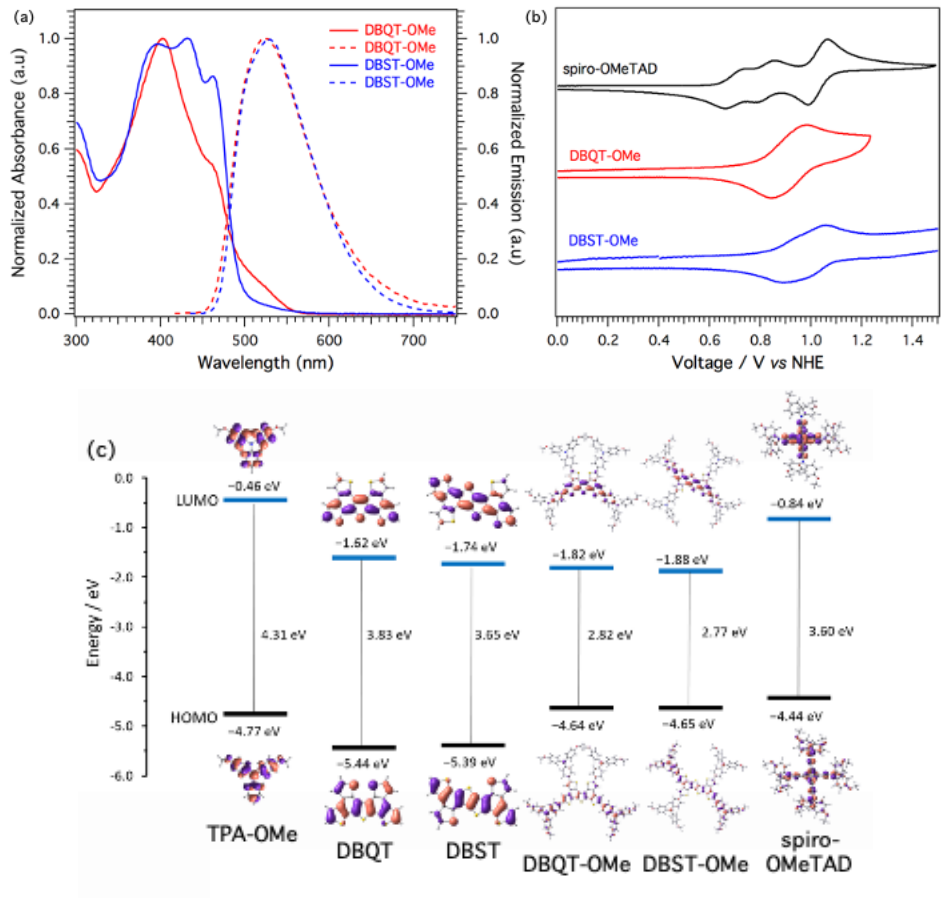

Figure 30. (a) UV-vis absorption (solid line) and fluorescence emission spectra (dashed line) of **DBQT-OMe** and **DBST-OMe** in CH_2Cl_2 solutions; (b) Cyclic voltammograms of **DBQT-OMe** and **DBST-OMe** in $TBAPF_6/CH_2Cl_2$ at a scan rate of 100 mV s^{-1}; (c) Energy diagram displaying the frontier molecular orbitals computed at the B3LYP/6-31G** level for the new HTMs, its fragments and the spiro-OMeTAD.

The cyclic voltammogram of **DBQT-OMe** shows one oxidation wave with $E_{1/2}$ value of 0.88 V vs. NHE. The broad shape of the oxidation wave seems to result from the overlapping of two different oxidation waves that can be tentatively assigned to consecutive oxidation processes where four electrons are simultaneously extracted from the TPA units. Similarly, **DBST-OMe** exhibits two close waves with $E_{1/2}$ values at 0.93 and 1.02 V vs. NHE, respectively. The different central moieties do not have a strong impact on the electrochemical

properties of the resulting HTMs. The HOMO energies calculated from the first oxidation potential for **DBQT-OMe** and **DBST-OMe** are -5.32 and -5.37 eV, respectively, which are ~ 0.2 eV lower than the HOMO energy displayed for spiro-OMeTAD (-5.16 eV) and very similar to the previously reported ATT-based molecules (-5.21 eV). A similar trend is observed for the HOMO energies predicted by theoretical calculations (**Figure 30c**). Therefore, an efficient hole extraction from the perovskites to the HTMs is ensured due to the excellent band alignment with the valence band edge of the compositionally engineered $[FAPbI_3]_{0.85}[MAPbBr_3]_{0.15}$ perovskite (-5.4 eV).

To gain a better understanding of the electronic properties of the new sulfur-rich HTMs, density functional theory (DFT) calculations were performed at the B3LYP/6-31G** level in the presence of the solvent (CH_2Cl_2). Their respective cores (DBQT and DBST), the pendant *p*-methoxytriphenylamine units (TPA), and the reference spiro-OMeTAD compound were also computed for comparison purposes. In **Figure 30c** are displayed the frontier molecular orbitals calculated for TPA, the DBQT and DBST cores, the **DBQT-OMe** and **DBST-OMe**, and the spiro-OMeTAD. The highest-occupied molecular orbital (HOMO) of the DBQT and DBST cores, computed at -5.44 and -5.39 eV, respectively, are significantly lower in energy than the HOMO of the TPA-donor units (-4.77 eV) in accord with their weaker electron-donor character. In line with the molecular structure, the HOMOs of DBQT and DBST mainly spread over the most effective conjugated path, and their topology resembles those obtained for oligothiophene derivatives.[217] The HOMO energies of the tetra-substituted HTMs are significantly destabilized (-4.64 and -4.65 eV) as a consequence of the incorporation of the TPA units. This destabilization, which implies an enhancement of the electron-donor character, shifts up the HOMO levels close to that computed for the reference spiro-OMeTAD (-4.44 eV). Interestingly, the HOMO of both **DBQT-OMe** and **DBST-OMe** are located not only over the respective cores but also over the TPA moieties connected to the thiophene rings where the conjugation is more effective.

---

[217] J. Aragó, P. M. Viruela, E. Ortí, R. Malavé Osuna, B. Vercelli, G. Zotti, V. Hernández, J. T. López Navarrete, J. T. Henssler, A. J. Matzger, Y. Suzuki, S. Yamaguchi, *Chem. – A Eur. J.* **2010**, *16*, 5481–5491.

Table 9. Photophysical, electrochemical and thermal properties of **DBQT-OMe**, **DBST-OMe** and spiro-OMeTAD.

HTMs	$\lambda_{max,\ abs}$ (nm)[a]	$\lambda_{max,\ em}$ (nm)[a]	$E^{ox}{}_{1/2}$ (V)[b]	E_{HOMO} (eV)[c]	$E^{0\text{-}0}$ (eV)[d]	E_{LUMO} (eV)[e]	T_{dec} (°C)[f]	T_g (°C)[g]
DBQT-OMe	403	522	0.88	–5.32	2.60	–2.72	423	149
DBST-OMe	431	528	0.93	–5.37	2.57	–2.80	450	209
spiro-OMeTAD	386	319	0.72	–5.16	3.05	–2.11	449	125

[a] λ_{max} of absorption and emission were measured in CH_2Cl_2 solutions; [b] Determined from CV measurements vs normal hydrogen electrode (NHE); [c] E_{HOMO} is estimated in eV by E_{HOMO} = -4.44eV - $E^{ox}{}_{1/2}$; [d] $E^{0\text{-}0}$ was determined at the intersection of normalized absorption and emission spectra; [e] E_{LUMO} was estimated by $E_{LUMO} = E_{HOMO} + E^{0\text{-}0}$; [f] Decomposition temperature determined from TGA (5% weight loss under a N_2 atmosphere; [g] Determined from the second cycle of the DSC under a N_2 atmosphere.

Hole reorganization energies (λ) were also calculated at the B3LYP/6-31G** level in gas phase to evaluate the capability of the **DBQT-OMe** and **DBST-OMe** for hole-transporting applications. The λ values estimated for **DBQT-OMe** and **DBST-OMe** are 0.142 and 0.129 eV, respectively. Note that the λ calculated values are notably smaller than those obtained for their constituting fragments (0.180, 0.200 and 0.274 eV for DBQT, DBST and TPA, respectively) due to the fact that charge extraction involves both the sulfur-rich core and the peripheral TPA moieties (especially those linked to the thiophene rings involved in the more effective conjugation path of the planar core). Both **DBQT-OMe** and **DBST-OMe** exhibit low reorganization energy similar to those found for other excellent p-type semiconducting organic materials[218] and in the same range as that obtained for the reference spiro-OMeTAD (0.139 eV) and the **ATT-OMe** (0.126 eV).[20] Therefore, **DBQT-OMe** and **DBST-OMe** present a great

[218] Y. Yao, H. Dong, W. Hu, *Adv. Mater.* **2016**, *28*, 4513–4523.

potential as hole-transporting materials for PSC devices owing to its small λ value and the appropriate energy level alignment with the valence band edge of the perovskite.

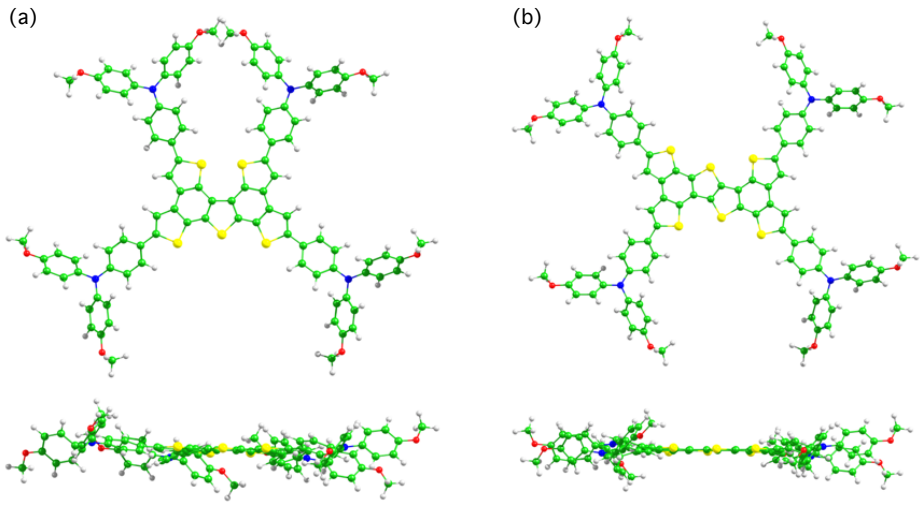

Figure 31. (a) Top and (b) side views of the optimized geometries calculated for **DBQT-OMe** and **DBST-OMe** performed at the B3LYP/6-31G** level in CH_2Cl_2.

Additional DFT calculations were carried out to predict the molecular structure of **DBQT-OMe** and **DBST-OMe** at the B3LYP/6-31G** level (**Figure 31**). The DBQT and DBST cores can be visualized as formed by two benzotrithiophene (BTT) units that were previously reported by our group.[102,174] In the case of DBQT, the two BTT units share the central thiophene ring and define a conjugated all-syn 2,2′,5′,2″-terthiophene with the external thiophene rings. As a consequence of the fused benzene rings, the central thiophene ring exhibits longer C-C bonds (1.417-1.479 Å) than the external thiophene rings (1.372-1.432 Å), which display values similar to those observed for non-fused thiophene oligomers. In the case of the DBST core, the two BTT units define a central fused thieno[3,2-*b*]-thiophene unit with C-C bond lengths more similar to those expected for fused oligothiophenes. Therefore, both the DBQT and the DBST core present an effective conjugation path between the thiophene rings connected by the 2,2′-positions. The introduction of the four TPA units in **DBQT-OMe** and **DBST-OMe** hardly causes any substantial change in the bond distances of the conjugated core, and more important, that both HTMs preserve

the planarity of the fused polycyclic core, particularly in the case of **DBST-OMe**.

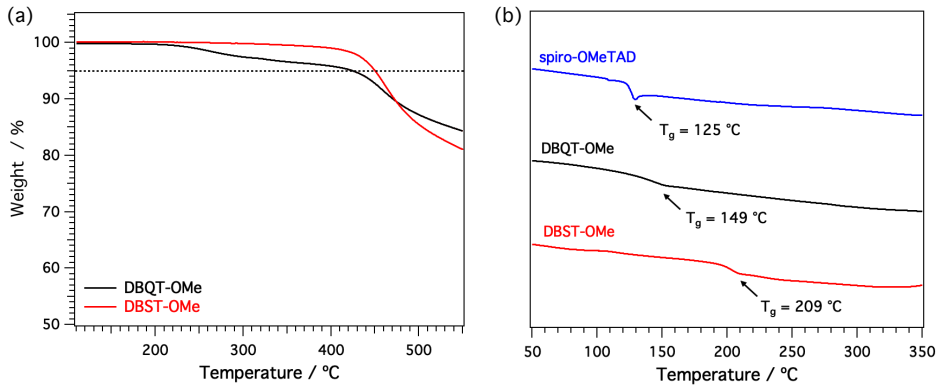

Figure 32. (a) Thermogravimetric analysis of **DBQT-OMe** and **DBST-OMe** under nitrogen at 10 °C min^{-1} of heating rate; (b) Differential scanning calorimetry of spiro-OMeTAD, **DBQT-OMe** and **DBST-OMe** under nitrogen at a heating rate of 20 °C min^{-1} (second cycle).

Thermogravimetric analysis (TGA) of the new π-extended sulfur-rich HTMs revealed their good thermal stability (5% weight loss under N_2 atmosphere) up to 450 °C for **DBST-OMe** and 423 °C for **DBQT-OMe**, which demonstrates the thermal robustness of these HTMs (**Figure 32a**). The latter exhibits a slight weight loss (3%) in the range of 150-350 °C, which is attributed to traces of solvent molecules trapped after purification of the material. Detailed thermal features are collected in **Table 9**. The thermal behavior of **DBQT-OMe** and **DBST-OMe** was studied by means of differential scanning calorimetry (DSC) (**Figure 32b**). Glass transition temperatures (T_g) were determined from the second heating cycle. Both molecules exhibit reduced tendency to crystallize with a glass transition temperature of 149 °C for **DBQT-OMe** and 209 °C for **DBST-OMe**, which confirms their amorphous behavior. T_g is indeed higher for the two new HTM derivatives in comparison with that for spiro-OMeTAD (T_g = 125 °C), which is attributed to improved molecular packing, indicating higher stability in the amorphous state.

5.1.6 Device performance and characterization of DBQT and DBST-based HTMs.

In order to evaluate the hole-transporting ability of the π-extended **DBQT-OMe** and **DBST-OMe**, solution-processed perovskite solar cells were prepared along with the benchmark spiro-OMeTAD. The photovoltaic devices were fabricated following a standard procedure for the well-studied n-i-p configuration with a mixed ion perovskite $[FAPbI_3]_{0.85}[MAPbBr_3]_{0.15}$ as the active light-harvesting material.

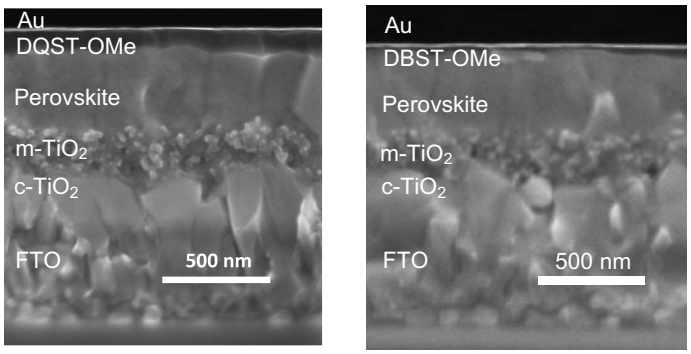

Figure 33. Cross-sectional images of the different layers of devices incorporating **DBQT-OMe** (left) and **DBST-OMe** (right) as HTMs.

The solar cells consist of a stack of thin-film layers deposited onto a FTO substrate. Compact and mesoporous TiO_2 was used as the electron-selective contact, sandwiching the light-absorbing perovskite material with the HTM. The perovskite layer was obtained using a one-step spin-coating process using chlorobenzene as a quenching solvent, as previously described by Jeon *et al*.[52] The HTMs were applied on top of the perovskite film by spin-coating their corresponding solutions in chlorobenzene for **DBQT-OMe** and spiro-OMeTAD and tetrachloroethane for **DBST-OMe**. Tetrachloroethane was used instead of chlorobenzene due to the low solubility of **DBST-OMe**. FK-209, Li-TFSI, and tert-butylpyridine were added as additives to enhance the performance of the new HTMs and spiro-OMeTAD. Finally, the top of the HTM is covered with gold that acts as an electrode for the device. The individual thin-film layers of the prepared PSC devices can be observed from the cross-sectional scanning

electron microscopy (SEM) image shown in **Figure 33**, where **DBQT-OMe** and **DBST-OMe** were deposited as the HTM.

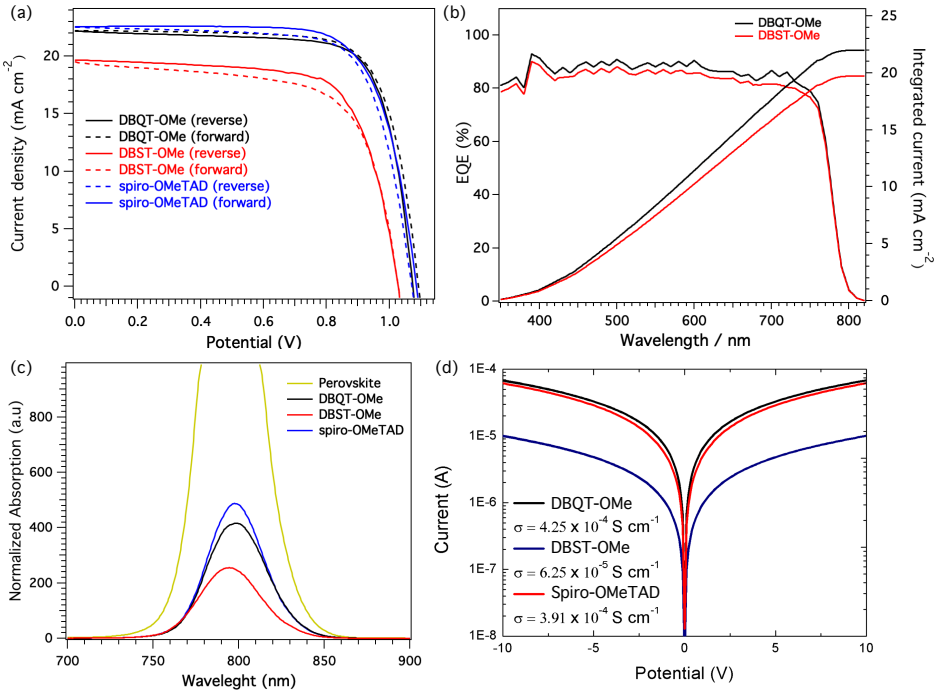

Figure 34. (a) Hysteresis curves of **DBQT-OMe**, **DBST-OMe** and spiro-OMeTAD measured at 20 mV/s; (b) External quantum efficiency (EQE) and integrated current plots; (c) Steady-state photoluminescence spectra (excitation at 600 nm); (d) Conductivity of **DBQT-OMe**, **DBST-OMe** and spiro-OMeTAD measured on substrates having interdigitating gold electrodes with a channel length of 2.5 µm.

Device efficiencies were investigated under AM 1.5G (100 mW cm^{-2}) simulated sunlight. The *J-V* curves of the champion devices using **DBQT-OMe** and **DBST-OMe** and the benchmark spiro-OMeTAD are shown in **Figure 34a**. Devices fabricated with **DBQT-OMe** showed superior PCE than **DBST-OMe** based PSCs (**Table 10**). Efficiencies up to 18.08% (V_{oc} of 1.09 V, J_{sc} = 22.2 mA cm^{-2} and a fill factor of 74.4%) could be obtained using **DBQT-OMe**, whereas for **DBST-OMe** the champion device exhibited an efficiency of 14.27% (V_{oc} = 1.03 V; J_{sc} = 19.7 mA cm^{-2}; *FF* = 70.6%) measured under the same conditions. Almost negligible hysteresis was observed for **DBQT-OMe** with a performance difference between reverse and forward scan of only 1%, whereas for **DBST-**

OMe, the difference in PCE was around 6%. The performance of spiro-OMeTAD was very close to that obtained for **DBQT-OMe** with a power conversion efficiency of 17.96% (V_{oc} = 1.08 V; J_{sc} = 22.6 mA cm^{-2}; *FF* = 73.1%). The lower performance of **DBST-OMe** is surmised to be caused by its low solubility and, therefore difficult processability. Tetrachloroethane was used as an alternative solvent which leads to the formation of a very thin HTM layer of only 20-50 nm and less uniform than for **DBQT-OMe**, as can be seen from the SEM image (**Figure 33** right). This indicates the formation of pinholes within the HTM layer, which would explain the reduced V_{oc} and J_{sc} of the **DBST-OMe** devices due to direct contact of the gold layer with the perovskite material. The J_{sc} obtained from the *J-V* measurements, and the integrated current densities from the external quantum efficiencies (EQEs) are in good agreement, within 5% (**Figure 34b**).

Table 10. Device performance of the **DBQT-OMe** and **DBST-OMe** compared to spiro-OMeTAD.

HTM	V_{oc} (V)	J_{sc} (mA cm^{-2})	*FF*	PCE (%)
DBQT-OMe	1.09	22.23	0.74	18.08
DBST-OMe	1.03	19.68	0.71	14.27
spiro-OMeTAD	1.08	22.60	0.73	17.96

To have a better understanding of the charge extraction processes, steady-state photoluminescence (PL) was recorded. As shown in **Figure 34c**, the pristine perovskite film exhibits a strong PL signal steaming from the radiative recombination of the photogenerated charge carriers. A significantly decreased PL signal is observed upon deposition of the HTMs on top of the perovskite layer, provoked by an efficient quenching of the photogenerated charge carriers. This suggests a good hole extraction for both **DBST-OMe** and **DBQT-OMe** comparable to spiro-OMeTAD, which is in agreement with the well-aligned HOMO energy levels. The more planar molecular structure predicted for **DBST-OMe** results in a more efficient hole extraction than for **DBQT-OMe**, which may be attributed to better contact between the perovskite and the HTM. Intriguingly, the improved charge extraction capability of **DBST-OMe** does not

translate into better photovoltaic performance. As mentioned before, the poor solubility of the former resulted in non-homogeneous and poor film-forming ability. The surface coverage of the perovskite layer by **DBST-OMe** is not uniformly distributed, leading to the formation of pinholes, which significantly affects not only the charge collection but also the device performance.

Further justification for the PSC efficiencies obtained with the different HTMs could be obtained by conductivity measurements from OFETs devices having interdigitating gold electrodes (**Figure 34d**). The conductivity observed for **DBQT-OMe** (4.25×10^{-4} S cm^{-1}) was slightly higher than that of spiro-OMeTAD (3.91×10^{-4} S cm^{-1}). However, the conductivity of **DBST-OMe** (6.25×10^{-5} S cm^{-1}) was around one order of magnitude lower than **DBQT-OMe**, which further corroborates its lower values found for J_{sc}, *FF*, and therefore, lower PCEs.

5.1.7 Synthesis of non-planar sulfur-rich cyclooctatetrathiophene-based hole-transporting material (CoTh-OMe).

Once we have confirmed the potential of planar sulfur-rich molecules for the synthesis of hole-transporting materials, our next step was the design and synthesis of alternative non-planar central moieties incorporating chalcogen atoms. One beautiful example of this type of structures is the connection of four thiophene units at positions 2 and 3, resulting in a special, flexible, π-conjugated skeleton with an 8 π-electron annulene core, named cyclooctatetrathiopene (CoTh). The non-planar structure of this scaffold could, in principle, be transformed into a planar geometry by an aromaticity conversion for the reduced 10 π dianion or the oxidized 6 π dication according to the Hückel's (4n + 2) rule.

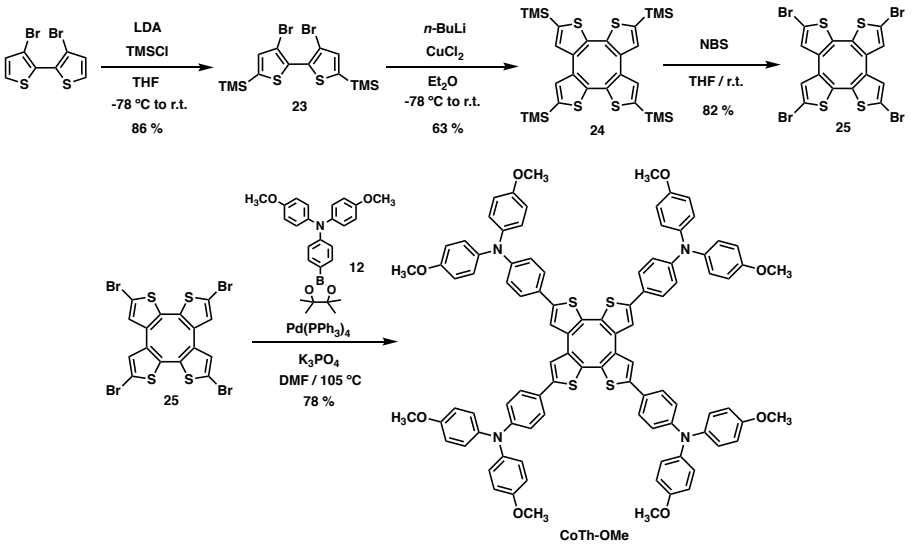

Scheme 4. Synthetic route for the preparation of saddle-shaped HTM **CoTh-OMe**.

CoTh was firstly synthesized with low yields of 18 and 23% by Woltermann and co-workers in 1978 via $CuCl_2$ or $FeCl_3$-mediated oxidative homocoupling of 3,3'-dilithio-2,2'-bithiophene and 2,2'-dilithio-3,3'-bithiophene, respectively.[219] More recently, Wang and co-workers improved the synthesis of

[219] T. Kauffmann, B. Greving, R. Kriegesmann, A. Mitschker, A. Woltermann, *Chem. Ber.* **1978**, *111*, 1330–1336.

CoTh fragment by introducing TMS-protecting groups in the α-position of bithiophene units, leading to an improved 40% of yield.[220,221] We followed this strategy with a slightly modification using an attainable starting material such as 3,3'-dibromo-5,5'-bis(trimethylsilyl)-2,2'-bithiophene (**23**) which was treated in the presence of *n*-butyllithium and copper chloride ($CuCl_2$) to form the central CoTh motif (**24**) in good yield (63%). Then, selective bromination of the TMS-protected group using *N*-bromosuccinimide (NBS) followed by a four-fold Suzuki cross-coupling reaction with the boronic ester of *p*-methoxytriphenylamine (**12**) successfully afforded **CoTh-OMe** in a three-step protocol with a good overall yield of 44 % (**Scheme 4**).[222]

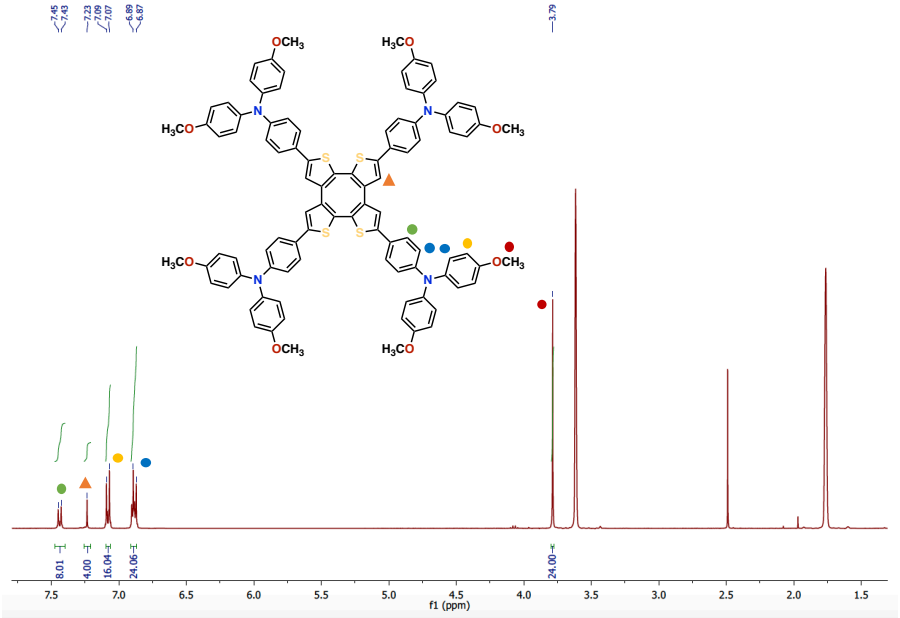

Figure 35. ^{1}H NMR of **CoTh-OMe** in THF-*d*$_8$ (400 MHz, 298 K).

[220] Y. Wang, Z. Wang, D. Zhao, Z. Wang, Y. Cheng, H. Wang, *Synlett* **2007**, *2007*, 2390–2394.

[221] Y. Wang, D. Gao, J. Shi, Y. Kan, J. Song, C. Li, H. Wang, *Tetrahedron* **2014**, *70*, 631–636.

[222] J. Urieta-Mora, I. García-Benito, I. Zimmermann, J. Aragó, J. Calbo, G. Grancini, A. Molina-Ontoria, E. Ortí, N. Martín, M. K. Nazeeruddin, *J. Mater. Chem. C* **2019**, *7*, 6656–6663.

A complete structural characterization of the **CoTh-OMe** was carried using standard spectroscopic techniques such as ^{1}H and ^{13}C nuclear magnetic resonance (NMR), Fourier transform infrared (FTIR), and mass spectrometry which confirms the presence of **CoTh-OMe** with a molecular ion peak $[M]^{+}$ at 1540.4560 m/z (calcd. 1540.4547 m/z). **Figure 35** shows the corresponding ^{1}H NMR signals of **CoTh-OMe**. The highly symmetric structure of the new HTM leads to simple NMR spectra which exhibits only two singlets (δ = 7.23 ppm) corresponding to the four β protons of the thiophene rings and the methoxy substituents of the triphenylamine units (δ = 3.79 ppm) while the aromatic protons of the triphenylamine show the typical AA'BB' signals of these systems.

5.1.8 Optical, electrochemical and thermal characterization of non-planar sulfur-rich CoTh-OMe.

We evaluated the optical properties of the new **CoTh-OMe** HTM using absorption and emission spectroscopy from CH_2Cl_2 solutions (**Figure 36a**), and the recorded maximum absorption and emission wavelengths are summarized in **Table 11**. From the UV-Vis absorption spectrum, two broad absorption bands in the range of 250 to 500 nm are observed. The first band at the shorter wavelength, with its maximum centered at 290 nm, can be ascribed to the characteristic optical features of the peripheral *p*-methoxytriphenylamine units. In contrast, the second broad absorption band spreading over the 350-500 nm range is attributed to the π-conjugation of the central scaffold by introducing the electron-donating TPA units. For **CoTh-OMe**, it is reasonable to expect the appearance of charge transfer bands stemming from the direct conjugation between the donor TPA units and the central backbone CoTh, acting as the acceptor moiety. This interaction could explain the broad shoulder observed in the absorption band located at around 400 nm. Regarding the emission spectrum of **CoTh-OMe** shows a broad fluorescence band peaking at 550 nm with a large Stokes' shift. Furthermore, we have estimated the optical band gap ($E^{0\text{-}0}$) from the intersection of the absorption and emission bands at 470 nm, corresponding to 2.70 eV, which is significantly narrower than that recorded for spiro-OMeTAD (3.05 eV).

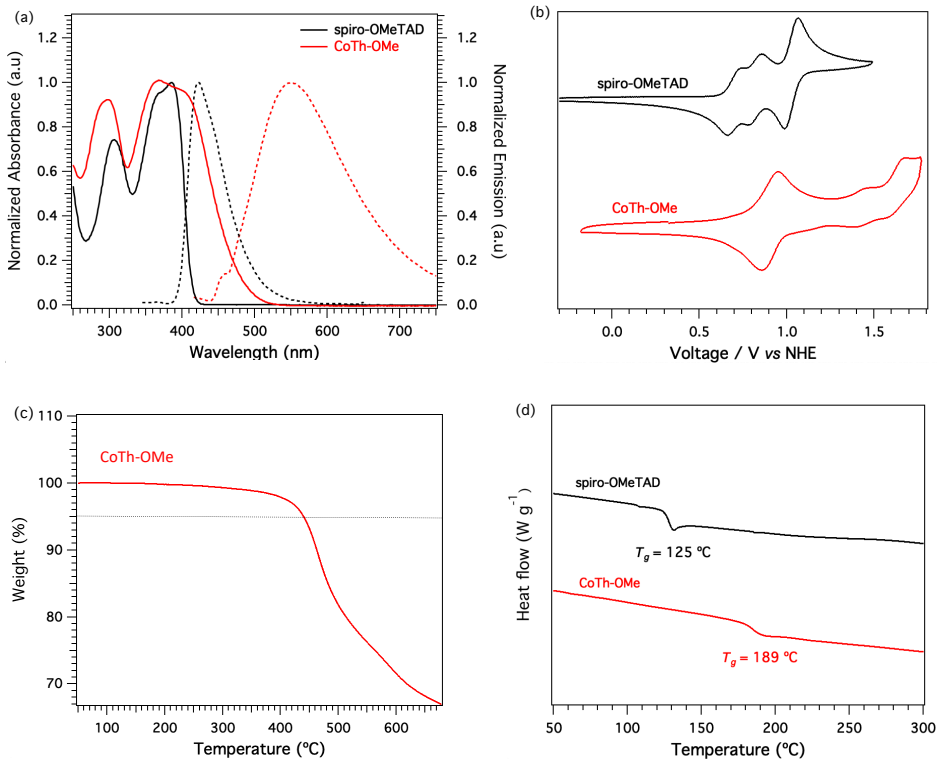

Figure 36. (a) UV-vis absorption spectra (solid line) and fluorescence emission spectra (dashed line) of **CoTh-OMe** and spiro-OMeTAD recorded in CH_2Cl_2; (b) Cyclic voltammetry of **CoTh-OMe** and spiro-OMeTAD in CH_2Cl_2 containing 0.1 M $TBAPF_6$ at a scan rate of 100 mV s^{-1}; (c) Thermogravimetric analysis recorded for **CoTh-OMe** under nitrogen at 10 °C min^{-1} of heating rate; (d) Differential scanning calorimetry curves of **CoTh-OMe** and spiro-OMeTAD under nitrogen at a heating rate of 20 °C min^{-1} (second cycle).

The electrochemical properties of **CoTh-OMe** were evaluated by cyclic voltammetry (CV) in CH_2Cl_2 solution using 0.1 M of tetrabutylammonium hexafluorophosphate ($TBAPF_6$) at room temperature, and at a scan rate of 100 mV s^{-1} (**Figure 36b**). As it can be observed, **CoTh-OMe** shows a weaker donor ability in comparison to the benchmark spiro-OMeTAD, with a reversible oxidation wave at a half-wave potential ($E_{1/2}$) of 0.91 V vs. normal hydrogen electrode (NHE). Hence, the HOMO energy level of **CoTh-OMe** can be estimated around -5.35 eV, while the HOMO energy of the spiro-OMeTAD is

upshifted to -5.16 eV. Therefore, the **CoTh-OMe** possesses suitable band alignment with the valence band edge of the perovskite (ca. -5.65 eV), which may lead to efficient injection of the photogenerated holes from the perovskite to the HTM. Taking into account the optical band-gap estimated from the intersection of the absorption and emission spectra, we could estimate a LUMO energy of -2.61 eV for **CoTh-OMe**.

Table 11. Optical, electrochemical and thermal properties of **CoTh-OMe** and spiro-OMeTAD.

HTM	$\lambda_{max,\ abs}$ [nm][a]	$\lambda_{max,\ em}$ [nm][a]	$E^{0\text{-}0}$ [eV][b]	$E^{ox}{}_{1/2}$ [V][c]	E_{HOMO} [eV][d]	E_{LUMO} [eV][e]	T_{dec} [°C][f]	T_g [°C][g]
CoTh-OMe	396	548	2.70	0.91	-5.35	-2.61	438	189
spiro-OMeTAD	386	419	3.05	0.72	-5.16	-2.11	449	125

[a] λ_{max} of absorption and emission measured in CH_2Cl_2 solutions; [b] $E^{0\text{-}0}$ was determined at the intersection of normalized absorption and emission spectra; [c] Determined from CV measurements *vs* normal hydrogen electrode (NHE); [d] E_{HOMO} is calculated in eV by $E_{HOMO} = -4.44\ eV - E^{ox}{}_{1/2}$; [e] E_{LUMO} were estimated by $E_{LUMO} = E_{HOMO} + E^{0\text{-}0}$; [f] Decomposition temperature determined from TGA (5% weight loss under a N_2 atmosphere). [g] Determined from the second cycle of the DSC under a N_2 atmosphere.

Thermal properties of **CoTh-OMe** were evaluated using TGA and DSC as it is illustrated in **Figure 36c-d**. **CoTh-OMe** exhibits good thermal stability and decomposes above 400 °C. The morphological stability of the amorphous hole-transporting material film upon heating is determined by the glass transition temperature (T_g). DSC analysis of **CoTh-OMe** shows that after consecutive heating/cooling cycles, only a T_g value of 186 °C was observed, which confirms the amorphous nature and reduced tendency to crystallize of **CoTh-OMe**. In contrast, spiro-OMeTAD can exist in both crystalline and amorphous states, with a T_g of 125 °C.

The structural and electronic properties of the **CoTh-OMe** were also investigated by theoretical calculations using DFT at the B3LYP/6-31G** level in the presence of the solvent (CH_2Cl_2). In **Figure 37a**, the frontier molecular orbitals calculated for **CoTh-OMe** and spiro-OMeTAD are shown along with its constituting fragments. The highest-occupied molecular orbital (HOMO) of the

CoTh core, computed at -5.64 eV, is noticeably lower in energy than the HOMO of TPA (-4.77 eV) indicating, as expected, a much higher electron-donor character of the triphenylamine units. Therefore, for **CoTh-OMe**, the incorporation of the TPA units results in a destabilization of the HOMO level (-4.62 eV), improving its electron-donor character, which is closer to the HOMO level calculated for spiro-OMeTAD (-4.44 eV). The energy difference of 0.19 eV observed in CV measurements matched perfectly with the value predicted theoretically (0.18 eV) (**.**

Table *11* 11). Interestingly, the HOMO of **CoTh-OMe** is located not only over the central core but also over the peripheral TPA moieties connected to the thiophene rings of CoTh. It is important to remark that an important charge transfer occurs from the terminal TPA groups to the sulfur-rich central core. The electronic structure of the **CoTh-OMe** HTM is, therefore, predicted to be significantly polarized, and it is confirmed by the absorption spectra of **CoTh-OMe** that reveal charge-transfer bands in the 350-400 nm region (**Figure 37a**).

Table 12. Mulliken atomic charges (in e) computed for the central CoTh core and the TPA units of **CoTh-OMe** in different oxidized states.

Molecular fragment	Neutral	Cation	Dication	Trication	Tetracation
CoTh	−0.508	−0.227	−0.116	−0.102	−0.067
TPA-1	0.127	0.307	0.529	0.775	1.017
TPA-2	0.127	0.307	0.529	0.775	1.017
TPA-3	0.127	0.307	0.529	0.776	1.017
TPA-4	0.127	0.307	0.529	0.776	1.017

To gain a better understanding of the oxidation processes, the oxidized species (up to the tetracation) of **CoTh-OMe** were calculated at the B3LYP/6-31G** level in CH_2Cl_2. In line with the distribution of the HOMO (**Figure 37a**), the charge for the radical cation species is drawn from the core (*ca.* 0.28e) and the TPA units (0.18e from each unit) (**Table 12**). Upon further oxidation, the charge is steadily extracted from the four TPA units. They hold a similar charge of *ca.* +1.0e for the tetracation and the core loses the excess of electron density found

in the neutral state. It should be stressed that for **CoTh-OMe** the ionization energies (IEs) required for going from the neutral molecule to the cation (IE1), from the cation to the dication (IE2), from the dication to the trication (IE3) and from the trication to the tetracation (IE4) are computed to have comparatively close values (4.51, 4.76, 5.01 and 5.05 eV, respectively), the largest difference being found between IE1 and IE2 (0.25 eV). The closeness of the IEs explains the electrochemical behavior found for **CoTh-OMe** exhibiting a broad four-electron oxidation wave (**Figure 36b**).

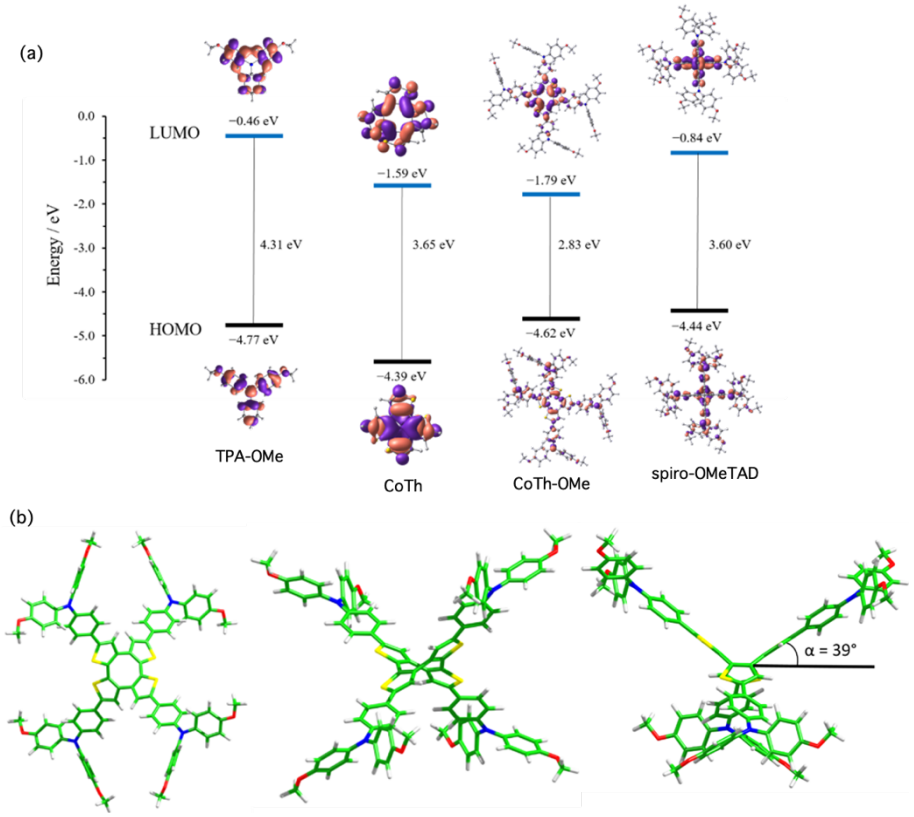

Figure 37. (a) Energy diagram displaying the frontier molecular orbitals for **CoTh-OMe** and spiro-OMeTAD; (b) Top and side views of the geometric structure of **CoTh-OMe** computed at the B3LYP/6-31G** level in CH_2Cl_2.

To evaluate the capability of the **CoTh-OMe** system as HTM, hole reorganization energies (λ) were estimated at the B3LYP/6-31G** level in gas phase. The λ value calculated for **CoTh-OMe** is 0.188 eV, which is notably

smaller than the values obtained for its constituting fragments (0.468 and 0.274 eV for CoTh and TPA, respectively). The charge extraction process involves both the core and the TPA units that lead to a decrease value of λ. Although **CoTh-OMe** exhibits a low reorganization energy, the predicted value is larger than that computed for spiro-OMeTAD (0.139 eV).

The molecular structure of **CoTh-OMe** is entirely determined by the central cyclooctatetrathiophene unit (CoTh), which shows a C_2-symmetry saddle-like structure with two opposite thiophene rings pointing up and the other two pointing down (**Figure 37b**). The distortion from planarity of the central CoTh moiety is characterized by the folding angle α defining the tilting of the thiophene rings with respect to the central molecular plane (39 º for **CoTh-OMe**) The thiophene rings condensed to the cyclooctatetraene moiety preserve their characteristic structural pattern with a clear single-double carbon-carbon (C-C) alternating backbone. The insertion of the four TPA units into the CoTh motif hardly causes any substantial change in the structural shape and in the bond distances of the conjugated core. Regarding the latter, a slight lengthening of the single C-C and carbon-sulfur bonds and a shortening of the double C-C bonds of the thiophene rings is predicted.

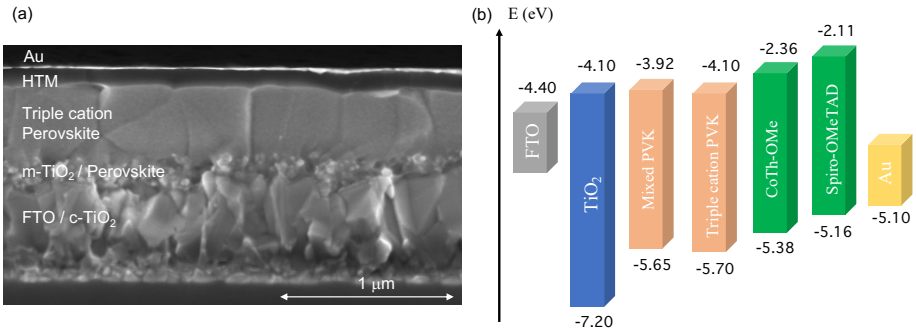

Figure 38. (a) SEM cross-section image of a PSC containing **CoTh-OMe** as HTM; (b) Energy diagram of the different components used in the mesoporous PSCs.

5.1.9 Device performance and characterization of CoTh-based HTM.

The new non-planar and sulfur-rich **CoTh-OMe** was incorporated as HTM in mesoscopic solution-processed PSC devices according to the procedures described in the *Experimental Section*. The different layers constituting the PSC

device can be seen from the schematic illustration and the cross-section scanning electron microscopy (SEM) image displayed in **Figure 38a**. The energy-level diagram of the prepared devices shows a good matching between the HOMO energy and the valence band edge of the mixed cation-mixed anion perovskite and also with the triple cation perovskite (**Figure 38b**). This provides sufficient driving force for an efficient hole-extraction from the perovskite to the HTM.

The incorporation of **CoTh-OMe** into conventional mesoscopic PSC devices was tested using two different perovskite material such as state-of-art $[FAPbI_3]_{0.85}[MAPbBr_3]_{0.15}$ and $[(FAPbI_3)_{0.87}(MAPbBr_3)_{0.13}]_{0.92}[CsPbI_3]_{0.08}$. The corresponding current density-voltage ($J-V$) characteristics obtained from the best-performing device along with the reference of spiro-OMeTAD are illustrated in **Figure 39a** under 1 sun AM 1.5 G (100 mW cm^{-2}) simulated sunlight, and the corresponding photovoltaic parameters are gathered in **Table 13**. The $[FAPbI_3]_{0.85}[MAPbBr_3]_{0.15}$-based devices employing doped **CoTh-OMe** afford a maximum PCE of 16.3% with a short-circuit current (J_{sc}) of 20.6 mA cm^{-2}, a field factor (FF) of 0.78 and an open-circuit voltage (V_{oc}) of 1.01 V (**Table 13**). As a reference, doped spiro-OMeTAD-based PSCs reaches a superior performance with a maximum PCE of 18.8% (J_{sc} of 22.35 mA cm^{-2}, FF of 0.77 and V_{oc} of 1.09 V). The performance of the spiro-OMeTAD can be significantly increased by changing the perovskite composition to the triple cation perovskite $[(FAPbI_3)_{0.87}(MAPbBr_3)_{0.13}]_{0.92}[CsPbI_3]_{0.08}$. The champion-device displays a PCE of 19.94% with improved values of J_{sc} of 23.3 mA cm^{-2} and a V_{oc} of 1.12 V. On the contrary, the incorporation of **CoTh-OMe** into triple cation-based PSC exhibits lower efficiency than those using the mixed cation-mixed anion perovskite. The devices afford a maximum PCE of 15.88% with an improved J_{sc} of 22.3 mA cm^{-2} but significantly lower value of FF (0.69). The small difference in the performances is probably raised from the homogeneity of the **CoTh-OMe** film (from a chlorobenzene solution of 20 mM of concentration) deposited on top of the perovskite layer and the accumulation of charges at the perovskite/HTM interface. The **CoTh-OMe** thin film was indeed more uniform, covering all the surface when employing the mixed-cation perovskite than when deposited onto the triple-cation perovskite. This results in a significant difference in the FF, which is higher in the case of the mixed cation-based perovskite and leads to a better PCE using this perovskite. The devices statistics obtained using

CoTh-OMe for the different perovskites are in good agreement with the performance of the best device for each perovskite (**Figure 39c**).

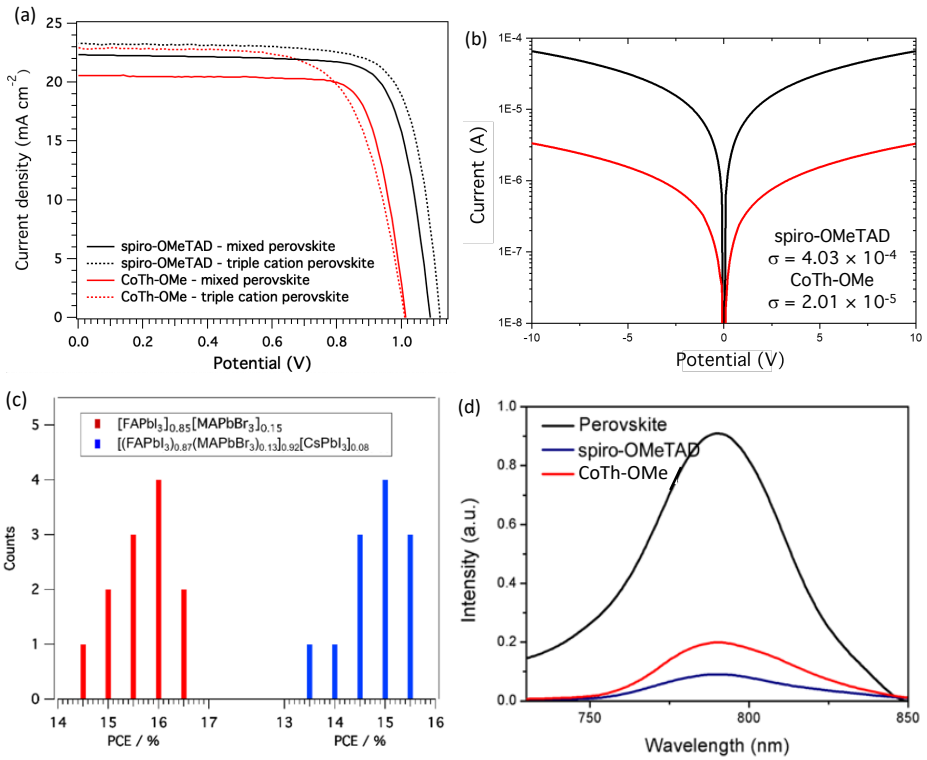

Figure 39. (a) Current density-voltage (*J-V*) curves of **CoTh-OMe** and spiro-OMeTAD in mesoscopic PSCs; (b) Conductivity of **CoTh-OMe** and spiro-OMeTAD measured on substrates having interdigitated gold electrodes with a channel length of 2.5 μm; (c) Efficiency distribution of devices incorporating **CoTh-OMe** fabricated with each perovskite; (d) Steady state photoluminescence measured using an excitation wavelength of 580 nm.

To further investigate the lower efficiency observed for **CoTh-OMe**, lateral conductivity of the HTM was measured on organic field-effect transistor (OFET) substrates. The corresponding current-voltage curves were recorded in the range from -10 to 10 V, and lateral conductivity values were calculated using Ohms law (**Figure 39b**). The same concentration as for the device preparation was used, adding 6% of FK-209 as dopant for both **CoTh-OMe** (20 mM) and spiro-OMeTAD (70 mM). The resulting conductivity of spiro-OMeTAD (4.03×10^{-4}

S cm^{-1}) is one order of magnitude higher than the conductivity of **CoTh-OMe** (2.01×10^{-5} S cm^{-1}), which further confirms the lower efficiency of the latter due to the reduced hole transport that could lead to an accumulation of charges at the perovskite/HTM interface.

Table 13. Device performance of **CoTh-OMe** with $[FAPbI_3]_{0.85}[MAPbBr_3]_{0.15}$ (mixed) and $[(FAPbI_3)_{0.87}(MAPbBr_3)_{0.13}]_{0.92}[CsPbI_3]_{0.08}$ (triple cation) perovskite and the reference spiro-OMeTAD.

HTM	Perovskite	V_{oc} (V)	J_{sc} (mA cm^{-2})	*FF*	PCE (%)
CoTh-OMe	Mixed	1.01	20.56	0.78	16.30
	Triple cation	1.01	22.95	0.69	15.88
Spiro-OMeTAD	Mixed	1.09	22.35	0.77	18.80
	Triple cation	1.12	23.29	0.77	19.94

To gain more insight into the charge extraction processes at the perovskite/HTM interface, steady-state photoluminescence (PL) was recorded into glass substrates with the corresponding HTM and triple cation perovskite (**Figure 39d**). The pristine perovskite film shows a strong PL signal, which stems from the radiative recombination of the photogenerated charge carriers. After the deposition of the HTM on top of the perovskite, the intensity of the PL signal is significantly reduced. This quenching is caused by the efficient extraction of the photogenerated charge carriers and is remarkably enhanced at the perovskite/spiro-OMeTAD interface. Compared to spiro-OMeTAD, **CoTh-OMe** exhibits limited quenching, which suggests a less efficient hole extraction from the perovskite layer, which leads to recombination and charge accumulation processes.

5.1.10 Synthesis of planar π-conjugated benzotriselenophene-based hole-transporting material (BTSe-OMe).

The synthesis of planar star-shaped molecules for hole-transporting applications has been developed in our research group during the last recent years.[102,174] As it was mentioned in the *Background* and *Objectives* sections, the use of benzotrithiophene as central scaffold for the design of efficient hole-transporting materials gives rise to a new family of HTMs with isostructural geometry respect to **BTT-3** by chemical modification of the central heteroaromatic π-conjugated core (**Figure 40**). In this regard, our research group described the syntheses and characterization of two new star-shaped derivatives based on *N*-phenyl substituted benzotripyrrole (**BTP-OMe**) and benzotrifuran (**BTF-OMe**) and, in the present thesis, it has been extended to the study of a benzotriselenophene-based molecule (**BTSe-OMe**).

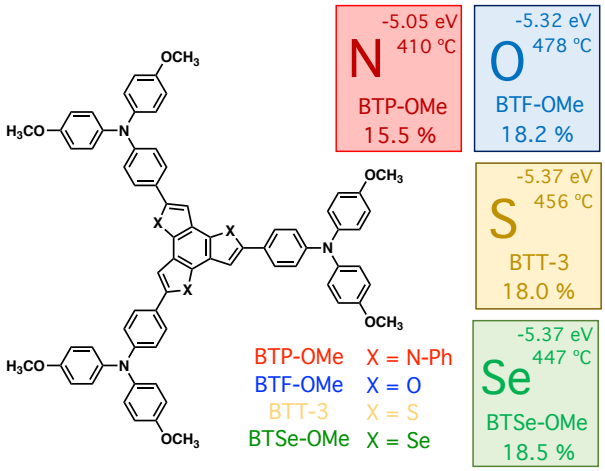

Figure 40. Chemical structures of star-shaped **BTP-OMe**, **BTF-OMe**, **BTSe-OMe** and **BTT-3**.

The star-shaped structure showed by **BTT-3** is expected to be slightly more planar in the benzotrifuran derivative (**BTF-OMe**) due to the smaller size of the oxygen atom (atomic radius = 64 pm) compared to sulfur (104 pm) or selenium (118 pm), which could eventually lead to significant morphological changes in the molecular packing. In contrast, **BTP-OMe** is expected to display a more distorted structure due to the *N*-phenyl substitution of the central pyrrole rings,

which could affect negatively to the charge extraction and the hole transport. Typically, selenium-containing small molecules and polymers show narrower band gaps owing to the more polarizable nature of the Se atoms, which lead to improved delocalization of electrons and, therefore, to a better conjugation.

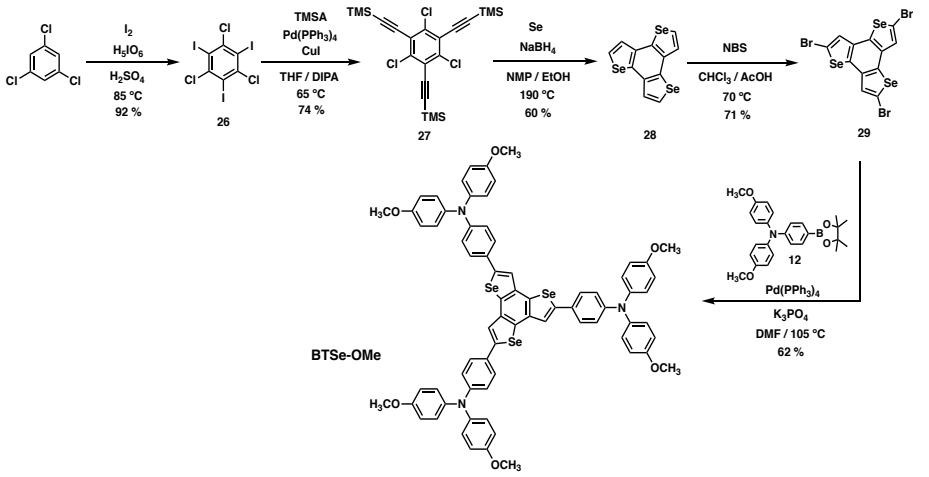

Scheme 5. Synthetic approach for the preparation of **BTSe-OMe**.

The synthesis of **BTSe-OMe** was conducted following a similar synthetic approach that was previously described by our group[102,223] (**Scheme 5**). A three-fold Sonogashira cross-coupling reaction over the previously prepared 2,4,6-trichloro-1,3,5-triiodobenzene (**26**) led to the formation of derivative **27** that reacts in a triple cyclization reaction in the presence of selenium powder and $NaBH_4$ under harsh conditions to form the selenium-containing heterocycle **28** in good yield. Then, a α-bromination reaction in standard condition using NBS in a mixture of chloroform and acetic acid followed by a three-fold Suzuki cross-coupling reaction with the boronic ester of *p*-methoxytriphenylamine (**12**) afforded the new HTM **BTSe-OMe**.[224] A complete structural characterization of **BTSe-OMe** was carried out using standard spectroscopic techniques such as ^{1}H NMR, ^{13}C NMR, FTIR and mass spectrometry (MALDI-TOF) that confirmed

223 T. Kashiki, S. Shinamura, M. Kohara, E. Miyazaki, K. Takimiya, M. Ikeda, H. Kuwabara, *Org. Lett.* **2009**, *11*, 2473–2475.

224 I. García-Benito, I. Zimmermann, J. Urieta-Mora, J. Aragó, J. Calbo, J. Perles, A. Serrano, A. Molina-Ontoria, E. Ortí, N. Martín, et al., *Adv. Funct. Mater.* **2018**, *28*, 1801734.

unambiguously the presence of **BTSe-OMe**. The ^{1}H NMR spectrum displayed in **Figure 41** showed the corresponding protons expected for **BTSe-OMe** with a singlet at 7.65 ppm that correlate with the β protons of the selenophene rings, and the characteristic signals for para-substituted phenyl rings of the triphenylamine units at 7.50, 7.10, 6.95 and 6.87 ppm with its corresponding methoxy signal at 3.82 ppm. MALDI mass spectrometry (HR-MS) confirms the presence of **BTSe-OMe** with a molecular ion peak $[M]^{+}$ at 1299.1742 m/z (calcd. 1299.1767 m/z) with its typical isotopic distribution.

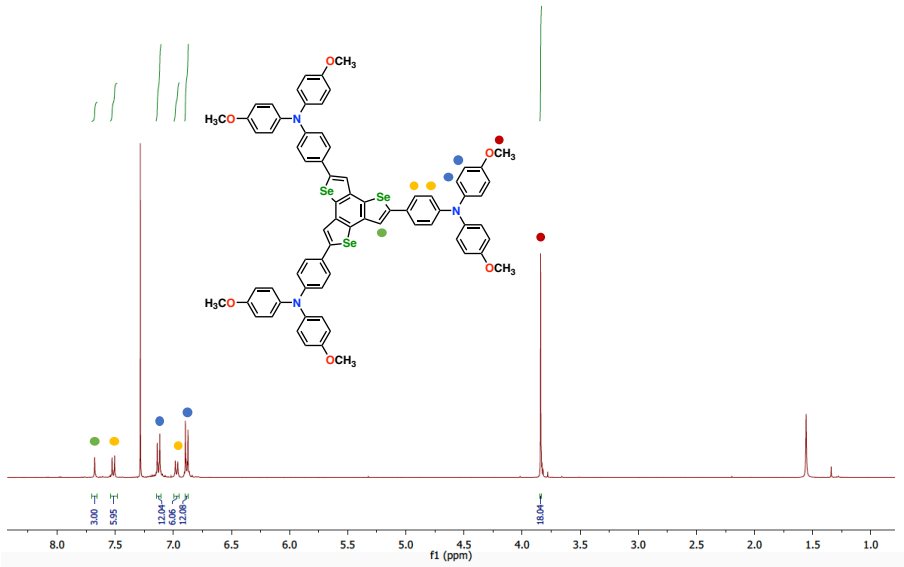

Figure 41. ^{1}H NMR of **BTSe-OMe** in $CDCl_3$ (400 MHz, 298 K).

5.1.11 Optical, electrochemical and thermal characterization of selenium-based BTSe-OMe and its isostructural-related HTMs.

The optoelectronic properties of new HTM **BTSe-OMe** are compared with its isostructural star-shaped HTMs containing nitrogen (**BTP-OMe**), oxygen (**BTF-OMe**) and sulfur-based HTM (**BTT-3**) that were prepared previously in our research group.[102,223]

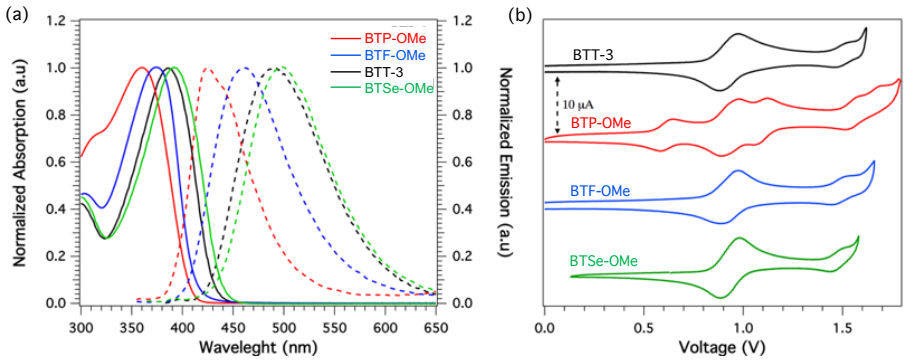

Figure 42. (a) UV-vis absorption spectra (solid line) and fluorescence emission spectra (dashed line) of star-shaped HTMs recorded in CH_2Cl_2; (b) Cyclic voltammetry of star-shaped HTMs in CH_2Cl_2 containing 0.1 M $TBAPF_6$ at a scan rate of 100 mV s^{-1}.

Attending the optical properties of the isostructural HTMs, we recorded the UV-vis absorption and fluorescence emission spectra in dichloromethane solution, as it is shown in **Figure 42a**. The corresponding maximum absorption and emission wavelengths are gathered in **Table 14**. In solution, the absorption maximum ($\lambda_{max,abs}$) of the new **BTSe-OMe** HTM showed a maximum absorption centered at 393 nm ($\varepsilon = 2.1 \times 10^5$ M^{-1} cm^{-1}), which is bathochromically shifted in comparison to the previously prepared HTMs, passing from nitrogen-containing **BTP-OMe** (361 nm, $\varepsilon = 1.4 \times 10^5$ M^{-1} cm^{-1}) to oxygen-containing **BTF-OMe** (376 nm, $\varepsilon = 1.1 \times 10^5$ M^{-1} cm^{-1}) and sulfur-containing **BTT-3** (387 nm, $\varepsilon = 0.9 \times 10^5$ M^{-1} cm^{-1}), which is in agreement with the predicted HOMO-LUMO gap along this series by DFT calculations (**Figure 43**). The higher molar absorption coefficient and the red-shifted absorbance recorded in the case of **BTSe-OMe** can be attributed to its enhanced quinoidal resonance character in the ground state caused by the lower aromaticity of the selenophene.[225] The family of isostructural star-shaped HTMs displays no significant absorption in the visible range. The fluorescence emission spectra of the HTMs showed a similar trend with maximum emission centered at 490 nm for **BTSe-OMe** and systematically blue-shifted maximum in passing from sulfur to oxygen to nitrogen (490, 461 and 425 nm, respectively). The derived optical band gaps (E^{0-0}) were estimated from the intersection of the absorption and emission bands.

[225] H. Yao, L. Ye, H. Zhang, S. Li, S. Zhang, J. Hou, *Chem. Rev.* **2016**, *116*, 7397–7457.

Therefore, star-shaped **BTSe-OMe** showed relatively high energies for the lowest energy 0-0 transition ($E^{0\text{-}0}$) of 2.83 eV (438 nm), which is similar to the isostructural HTMs **BTP-OMe**, **BTF-OMe** and **BTT-3** (3.11, 3.02 and 2.89 eV, respectively).

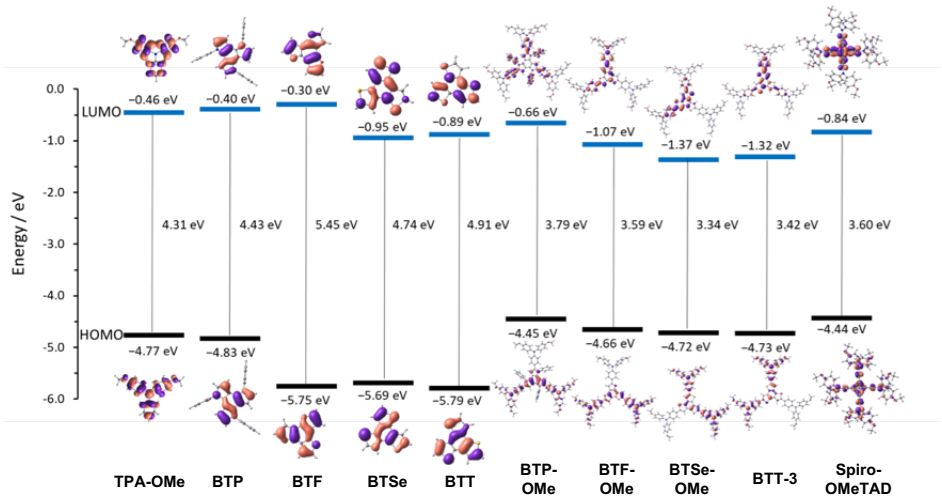

Figure 43. Energy diagram showing the frontier molecular orbitals computed for the star-shaped HTMs and its constituting fragments and the spiro-OMeTAD at the B3LYP/6-31G** level in CH_2Cl_2.

The electrochemical behavior of the **BTSe-OMe** was studied employing cyclic voltammetry (CV) in CH_2Cl_2 solutions using $TBAPF_6$ as supporting electrolyte at a scan rate of 100 mV s^{-1} as illustrated in **Figure 42b**, and it was compared with its isostructural derivatives. The corresponding redox potentials are listed in **Table 14**. **BTSe-OMe** showed an oxidation process at a half-wave potential ($E_{1/2}$) of 0.93 V *vs.* normal hydrogen electrode (NHE), which corresponds to that observed for the previously reported **BTT-3** and involves the extraction of three electrons. Analogously, **BTF-OMe** also exhibited similar redox potential with an oxidation wave at 0.94 V. Thus, HOMO is experimentally calculated at similar energies for **BTSe-OMe** (-5.37 eV), **BTT-3** (-5.37 eV) and **BTF-OMe** (-5.38 eV). In contrast, **BTP-OMe** showed multiple one-electron reversible oxidation waves with $E_{1/2}$ values of 0.61, 0.93 and 1.09 V. As a consequence, **BTP-OMe** presented a stronger electron-donor character in good accord with theoretical predictions (**Figure 43**) in comparison to **BTSe-OMe**, **BTF-OMe**

and **BTT-3**, with higher HOMO energy of -5.05 eV. A stronger donor character could be attributed to the stronger electron donation from the pyrrole moieties, also shown in other systems such as carbazole or triazatruxene. Therefore, **BTSe-OMe**, along with the other isostructural HTMs, featured a suited band alignment with the valence band edge of the compositionally engineered perovskite (*ca.* -5.65 eV), which ensures an efficient hole injection from the perovskite to the HTM. To have a better understanding of the oxidation processes, the oxidized species (up to the trication) of star-shaped HTMs were calculated at the B3LYP/6-31G** level in CH_2Cl_2.

Table 14. Optical and electrochemical properties of isostructural star-shaped HTMs and spiro-OMeTAD.

HTM	$\lambda_{max,abs}$ (nm)[a]	$\lambda_{max,em}$ (nm)[a]	$E^{0\text{-}0}$ (eV)[b]	$E^{ox}{}_{1/2}$ (V)[c]	E_{HOMO} (eV)[d]	E_{LUMO} (eV)[e]
BTSe-OMe	393	496	2.83	0.93	–5.37	–2.54
BTP-OMe	361	425	3.11	0.61	-5.05	-1.94
BTF-OMe	376	461	3.02	0.94	-5.38	-2.36
BTT-3	387	490	2.89	0.93	-5.37	-2.48
spiro-OMeTAD	386	419	3.05	0.72	-5.16	-2.11

[a] λ_{max} of absorption and emission measured in CH_2Cl_2 solutions; [b] $E^{0\text{-}0}$ was determined at the intersection of normalized absorption and emission spectra; [c] Determined from CV measurements *vs.* normal hydrogen electrode (NHE); [d] E_{HOMO} is estimated in eV by E_{HOMO} = -4.44 eV - $E^{ox}{}_{1/2}$; [e] E_{LUMO} was estimated by $E_{LUMO} = E_{HOMO} + E^{0\text{-}0}$.

The evolution upon oxidation indicates that the charge is mainly extracted from the donor units with relevant contributions from the central cores, thus evidencing the electronic communication between the peripheral donor groups and the π-conjugated cores. The ionization energies (IEs) required for passing from the neutral molecule to the cation (IE_1), dication (IE_2) and the trication (IE_3) are predicted to have close values for **BTSe-OMe** (4.65, 4.81 and 4.95 eV), **BTF-OMe** (4.58, 4.79 and 4.94 eV) and **BTT-3** (4.66, 4.80 and 4.92 eV), which is in good agreement with the experimentally observed in the CV, showing only one oxidation wave attributed to the extraction of 3 electrons. In contrast, **BTP-OMe** exhibits the strongest electron-donor character with the smallest IE_1 value

in line with the experimentally measured value and a larger separation between the IE1 (4.32 eV), IE2 (4.70 eV) and IE3 (4.94 eV) energies.

Theoretical calculations performed at the B3LYP/6-31G** level in CH_2Cl_2 of the frontier molecular orbitals calculated star-shaped HTMs and their constituting fragments, as well as the reference spiro-OMeTAD, are displayed in **Figure 43**. As it is expected for the three-armed star-shaped HTMs, the HOMO is destabilized when compared with the respective cores owing to the antibonding interaction with the *p*-methoxytriphenylamine units. **BTSe-OMe**, **BTF-OMe**, and **BTT-3** exhibited doubly-degenerate HOMO and LUMO levels spreading over the donor groups and the central core. For **BTP-OMe**, the HOMO is also doubly-degenerate and presents more important contributions from the BTP core. The energy of the HOMO undergoes a stabilization in passing from **BTP-OMe** (-4.45 eV) to **BTF-OMe** (-4.66 eV), **BTSe-OMe** (-4.72 eV) and **BTT-3** (-4.73 eV) confirming the largest donor character of **BTP-OMe** showing similar value to reference spiro-OMeTAD (−4.44 eV). These values are in concordance with the tendency displayed in the CV measurements. The LUMO experiences a larger stabilization showing a similar trend to the values calculated from the difference between the HOMO energy and the optical band-gap (**Table 14**). Furthermore, hole reorganization energies (λ) were calculated at the B3LYP/6-31G** level in gas phase to assess the capability of the star-shaped for hole-transporting applications rendering values for λ of 0.104, 0.251, 0.104 and 0.098 eV for **BTSe-OMe**, **BTP-OMe**, **BTF-OMe** and **BTT-3**, respectively. **BTSe-OMe** exhibited an excellent value of λ comparable to **BTF-OMe** and **BTT-3** and even lower than the predicted for spiro-OMeTAD (0.139), which confirms, along with an appropriate energy level alignment with the perovskite, the potential of these molecules for hole-transporting applications.

The crystal structure of **BTSe-OMe** was unambiguously elucidated by single-crystal X-ray diffraction (**Figure 44**). Suitable crystals of **BTSe-OMe** (also for **BTF-OMe** and **BTT-3**) were obtained from a toluene solution. The three compounds crystallize in the triclinic space group *P*-1 with one molecule in the asymmetric unit. The selenium-based HTM showed a more distorted central structure due to the presence of a bulkier atom in comparison to the oxygen (more planar structure) and sulfur-based compounds. The triphenylamine benzene rings directly connected to the central BTSe core are slightly twisted

(2.85-16.43°). π-π Interactions were not found in the supramolecular packing of **BTSe-OMe** and **BTT-3** (**BTF-OMe** showed π-π and C-H···O interactions) due to the presence of solvent molecules that were placed nonparallel between the cores of nearby HTM molecules preventing π-π interactions. Nevertheless, relevant interactions between the cores of adjacent **BTSe-OMe** and **BTT-3** molecules could also be developed in the absence of a solvent. Furthermore, intermolecular C-H···O bonds similar to those found in **BTF-OMe** are present from the peripheral *p*-methoxytriphenylamine groups. These interactions connect each **BTSe-OMe** molecule with three adjacent ones and one interstitial toluene molecule.

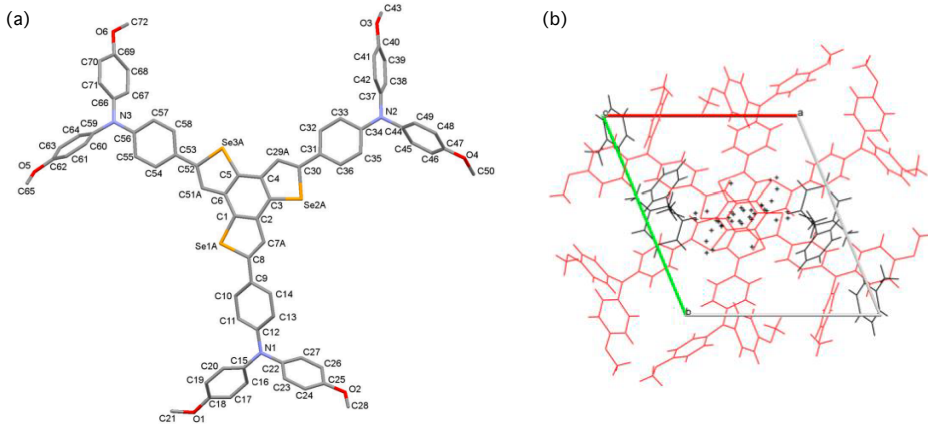

Figure 44. (a) Asymmetric unit in **BTSe-OMe** with atoms labeled (hydrogen atoms and toluene solvent have been omitted); (b) Packing of the **BTSe-OMe** molecules whose centroids are within the unit cell (solvent molecules are depicted in black).

Thermal behavior of the new star-shaped HTMs were evaluated utilizing TGA and DSC (**Figure 45**). A remarkable change in the thermal behavior occurs as a result of the core modification. While **BTSe-OMe** presents a similar thermal stability to the previously reported **BTT-3** with a decomposition temperature (T_{dec}) of 447 and 453 ºC, respectively. **BTP-OMe** is even more stable thermally (T_{dec} of 478 ºC). In contrast, **BTF-OMe** exhibits lower thermal stability with a decomposition temperature of 410 ºC, which is sufficient for its application in PV devices. **Figure 45d** shows the morphological behavior of **BTSe-OMe** after three consecutive heating/cooling cycles under N_2 atmosphere. **BTSe-OMe** features a glass transition at 167 ºC, which was only detected during the second

and third scan. Moreover, during the first cycle, **BTSe-OMe** exhibits a complex thermal behavior with three consecutive processes: a first melting temperature at 269 ºC, followed by a crystallization at 277 ºC and finally another melting temperature at 316 ºC. The high glass transition temperatures observed for **BTSe-OMe** (167 ºC), **BTP-OMe** (183 ºC) and **BTT-3** (162 ºC) reduce the tendency to crystallize upon heating (**Figure 45b-c**). On the other hand, **BTF-OMe** exhibited a reduction of the glass transition and the melting process due to the more crowded structure of **BTP-OMe**.

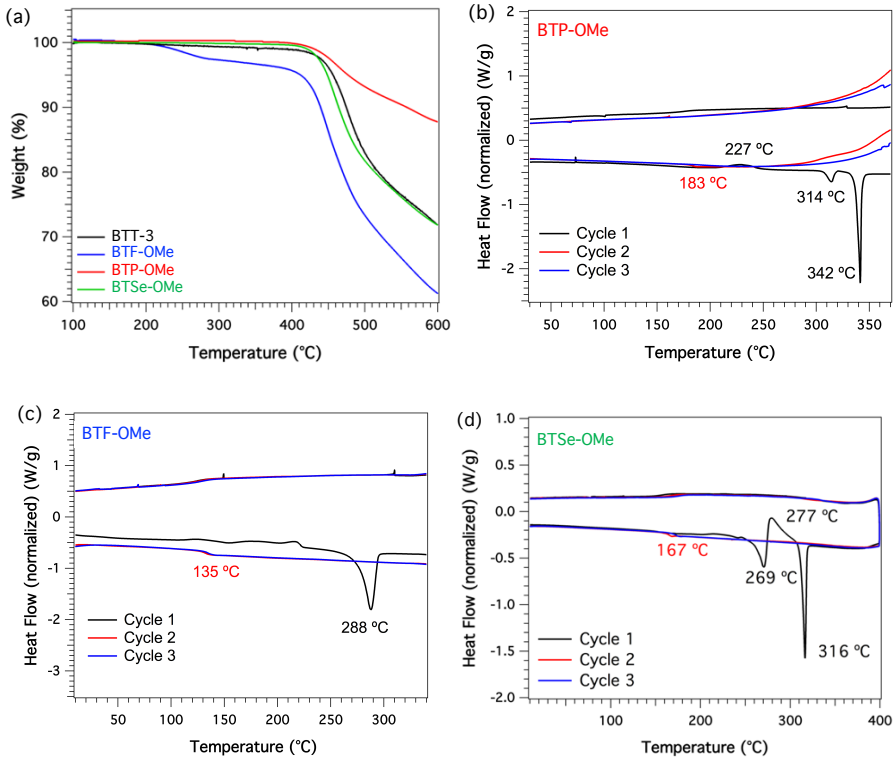

Figure 45. (a) TGA analysis of star-shaped HTMs at scan rate of 10 ºC/min; DSC analysis of (b) **BTP-OMe**, (c) **BTF-OMe** and (d) **BTSe-OMe** with scan rate of 20 ºC/min.

5.1.12 Device performance and characterization of star-shaped HTMs.

The ability of the star-shaped molecules for hole-transporting applications was evaluated incorporating the new HTMs into mesoporous-based perovskite solar

cells employing the mixed cation perovskite $[FAPbI_3]_{0.85}[MAPbBr_3]_{0.15}$. The devices were fabricated from a stack of thin-layers, deposited onto a fluorine-doped tin oxide (FTO) coated glass that can be clearly identified from the cross-section image in SEM image showed in **Figure 46a**. Devices were fabricated following standard procedures and the star-shaped HTMs were deposited from chlorobenzene solutions at concentrations of 30 mM for **BTSe-OMe**, **BTF-OMe** and **BTT-3**, 20 mM for **BTP-OMe** and 70 mM for spiro-OMeTAD under doped conditions (LiTFSI, ^{t}BP and FK-209).

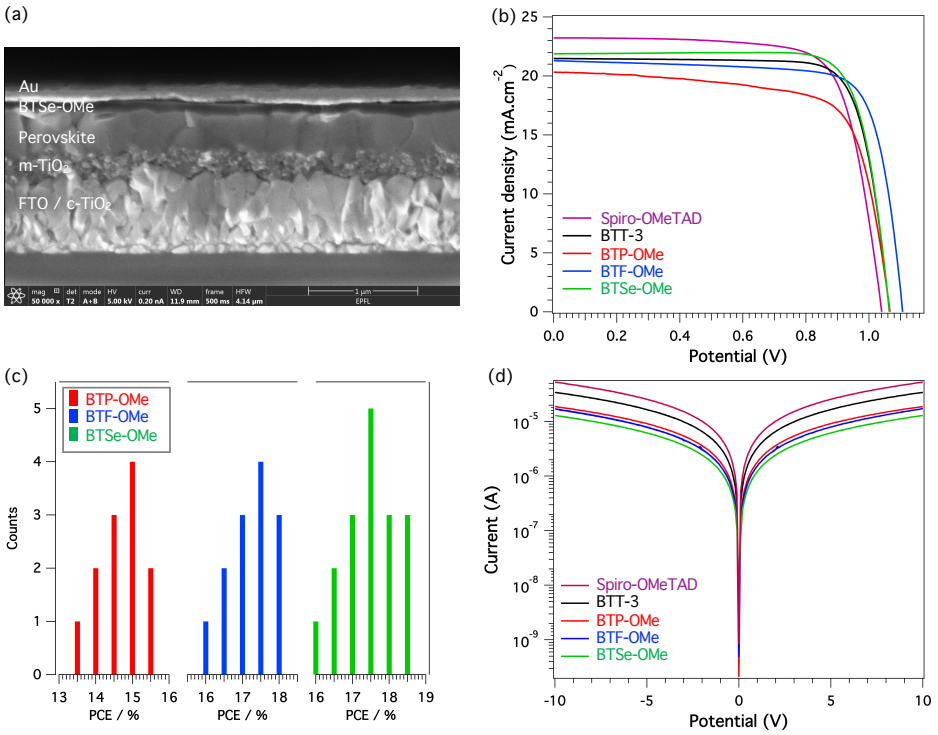

Figure 46. (a) Cross-section image (SEM) of a mesoporous PSC containing **BTSe-OMe**; (b) Current density-voltage (*J-V*) curves of star-shaped HTMs and spiro-OMeTAD in $[FAPbI_3]_{0.85}[MAPbBr_3]_{0.15}$-based PSCs; (c) Efficiency distribution for each HTM; (d) Conductivity of the star-shaped HTMs and spiro-OMeTAD measured on substrates having interdigitated gold electrodes with a channel length of 2.5 μm.

The photovoltaic performance of the star-shaped HTMs was measured under 1 sun and recorded current-voltage (*J-V*) curves, as shown in **Figure 46b**. **BTSe-OMe**-based PSCs displayed the highest PCE value of up to 18.5%, mainly

arising from an enhanced *FF* of 0.80 with a J_{sc} of 21.88 mA cm^{-2} and V_{oc} of 1.07 V (**Table 15**). Nearly performance was observed for devices incorporating **BTF-OMe** as HTM yielding a power conversion efficiency of 18.2%, similar to that measured for the benchmark spiro-OMeTAD used as reference. Moreover, **BTF-OMe** showed a remarkable V_{oc} of 1.1 V and excellent *FF* of 0.77 with a lower J_{sc} of 21.31 mA cm^{-2}. In contrast, **BTP-OMe** exhibited a significantly decreased PCE of 15.5% with reduced values of J_{sc} (20.3 mA cm^{-2}), *FF* (0.71), and V_{oc} (1.06 V). This behaviour is ascribed to the more crowded structure of the central core and the higher reorganization energy calculated for **BTP-OMe**, which may hinder the charge extraction/transport towards the Au electrode and could increase the charge recombination at the interfaces. In summary, **BTSe-OMe**-based devices displayed a more efficient performance, even higher than the sulfur-based **BTT-3** (PCE of 18.0%), the oxygen-based **BTF-OMe**, and the spiro-OMeTAD, confirming the potential of selenium-based molecules for hole-transporting applications. The device statistics obtained using **BTSe-OMe**, **BTF-OMe**, and **BTP-OMe** confirm the superior performance of the selenium-based HTM and similar efficiencies for the oxygen-based compound, as illustrated in **Figure 46c**.

Table 15. Device performance of the star-shaped HTMs and the reference spiro-OMeTAD.

HTM	V_{oc} (V)	J_{sc} (mA cm^{-2})	*FF*	PCE (%)
BTSe-OMe	1.07	21.88	0.80	18.5
BTP-OMe	1.07	20.34	0.71	15.5
BTF-OMe	1.11	21.31	0.77	18.2
BTT-3	1.08	22.02	0.75	18.0
spiro-OMeTAD	1.04	23.23	0.74	18.1

Charge transport properties of the star-shaped HTMs were evaluated using lateral thin-film conductivities on organic field-effect transistor (OFET) substrates. The conductivity value measured for **BTSe-OMe** was 7.88×10^{-5} S cm^{-1} (**Figure 46d**). Contrary to the trend showed in the photovoltaic

performance, the values of lateral conductivity obtained for **BTP-OMe**, **BTF-OMe**, and **BTT-3** were 1.16×10^{-4}, 1.03×10^{-4} and 2.11×10^{-4} S cm^{-1} respectively, showing slightly higher values in comparison to **BTSe-OMe**. The power conversion efficiency and conductivity values are indeed somewhat similar for **BTSe-OMe** and its isostructural **BTF-OMe** and **BTT-3**, suggesting that the device efficiency will not be determined solely by the conductivity of the HTMs. Hence, the better performance of **BTSe-OMe** could be ascribed to the reorganization energy and the electron coupling, which are two critical parameters to take into account for describing the hole transfer rate of different materials. In this regard, the calculated reorganization energy λ for **BTP-OMe** presents the highest value and is conjectured to be responsible for its poor efficiency. **BTSe-OMe** and **BTF-OMe** showed slightly lower conductivity values than **BTP-OMe**, despite possessing a more planar structure and less steric hindrance, as revealed by X-ray data and theoretical calculations for both compounds.

Section 5.2. Synthesis of spiro-like based hole-transporting materials for PSCs.

The strategy of introducing spirocyclic aromatic cores has been extensively used for the preparation of efficient hole-transporting materials for photovoltaics and OLEDs applications. The "spiro-concept" involves two extended π-systems, which are connected to a tetrahedral sp^3-hybridized atom, resulting in an orthogonal arrangement between the aromatic rings. The spiro linkage improves the morphological stability of the chemical structure, whereas the electronic properties of the electroactive units remain intact. Owing to its attractive properties, 9,9'-spirobifluorene has been exploited for organic electronics, mainly for photovoltaic applications, as it has served as a scaffold for the synthesis of the benchmark spiro-OMeTAD. In this section, we have completed the synthesis, characterization, and device implementation of two new families of molecules incorporating a spiro-linkage in the structure (**spiro-POZ-OMe** and **spiro-PTZ-OMe**) and a "spiro-like" C-C linkage (**BX-OMe** and **BTX-OMe**) for the construction of orthogonal-structured hole-transporting materials for PSCs (**Figure 47**).

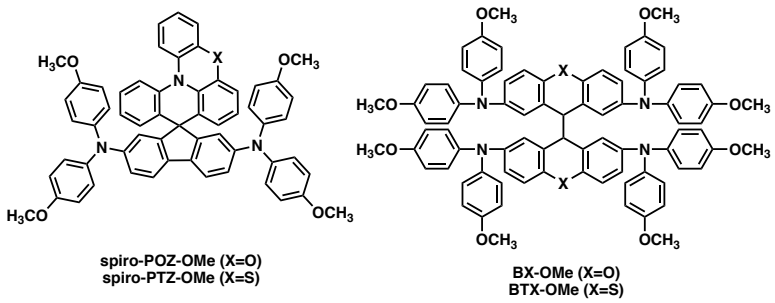

Figure 47. Chemical structure of new HTMs with orthogonal structure.

5.2.1 Synthesis of spiro-phenoxazine and phenothiazine-based HTMs.

Phenoxazine (POZ) and phenothiazine (PTZ) are two well-known heterocyclic scaffolds since the first report of Bernthsen in 1883 that consists of two benzene rings fused through a 1,4-oxazine or 1,4-thiazine, respectively, rendering a butterfly-shaped structure which exhibits remarkable properties for multiple

fields.[226] The optoelectronic properties of POZ and PTZ, such as a large π-conjugated electroactive structure, high molar absorption coefficients, or intense luminescence, make them excellent candidates for photovoltaic or light-emitting diodes (OLEDs) applications. The presence of the different heteroatoms in the structure modifies the electrochemical behavior of these simple units turning them in good electron donor units. Their optoelectronic properties, such as the hole mobility, light absorption capability, thermal stability, or crystallinity, can be modulated by easy and attainable chemical functionalization in different positions of the molecules.[227] Abate and co-workers reported the first implementation of PTZ as a central scaffold in the design of highly-efficient HTMs in 2018.[162]

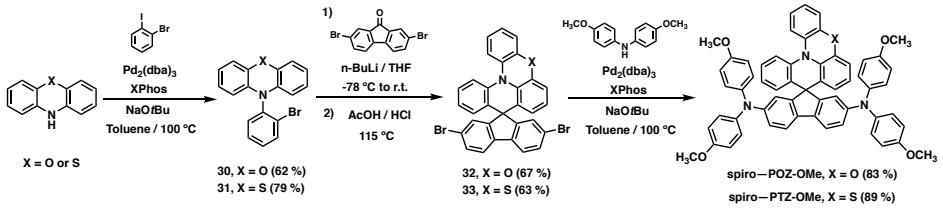

Scheme 6. Synthetic procedure for the preparation of spiro-phenoxazine and spiro-phenothiazine-based HTMs.

Combining the "spiro-concept" and the use of POZ and PTZ units for optoelectronic applications, we have designed two new spiro-like molecules for the synthesis of HTMs. The syntheses of the spiro-phenoxazine (**spiro-POZ-OMe**) and spiro-phenothiazine (**spiro-PTZ-OMe**) based molecules were carried out following previously reported procedures from Jiang, Liao, and co-workers[228,229,230] (**Scheme 6**). Phenoxazine or phenothiazine starting materials were reacted with 2-bromoiodobenzene though a Buchwald-Hartwig carbon-

226 I. J. Al-Busaidi, A. Haque, N. K. Al Rasbi, M. S. Khan, *Synth. Met.* **2019**, *257*, 116189.

227 S. P. Massie, *Chem. Rev.* **1954**, *54*, 797–833.

228 Y.-K. Wang, S.-F. Wu, Y. Yuan, S.-H. Li, M.-K. Fung, L.-S. Liao, Z.-Q. Jiang, *Org. Lett.* **2017**, *19*, 3155–3158.

229 Y.-K. Wang, S.-H. Li, S.-F. Wu, C.-C. Huang, S. Kumar, Z.-Q. Jiang, M.-K. Fung, L.-S. Liao, *Adv. Funct. Mater.* **2018**, *28*, 1706228.

230 H. Jiang, J. Sun, *New J. Chem.* **2013**, *37*, 3161–3165.

nitrogen cross-coupling, giving rise to derivatives **30** and **31**, respectively. Li^+ exchange in the bromoderivative previously prepared at -78 ºC using *n*-butyllithium and subsequent quenching with 2,7-dibromo-9-fluorenone afford the corresponding carbinol derivatives, which were further treated under acidic conditions (AcOH/HCl) towards the formation of the spiranic derivatives **32** and **33**. Finally, two-fold Buchwald-Hartwig reaction for the incorporation of the electron-donor *p*-methoxydiphenylamine units successfully rendered **spiro-POZ-OMe** and **spiro-PTZ-OMe** molecules in excellent yields of 83 and 89%, respectively.

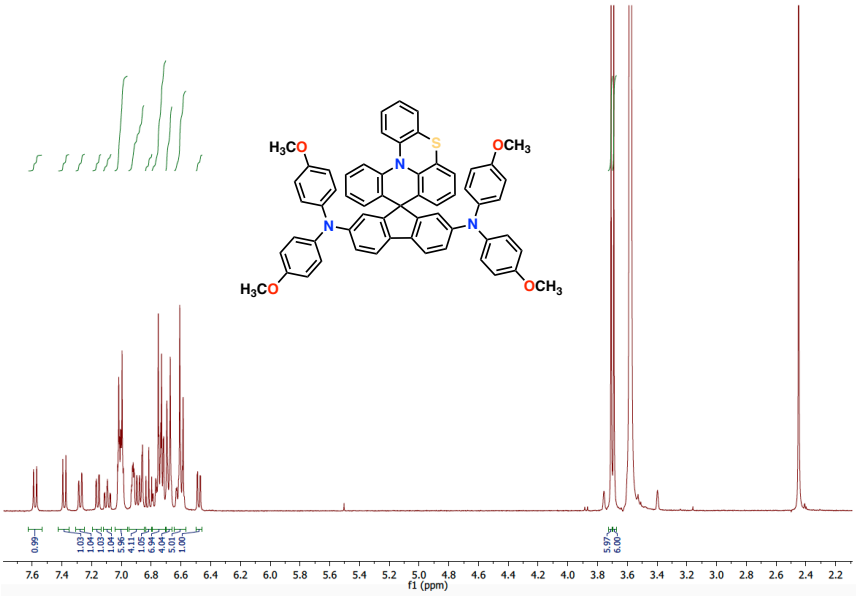

Figure 48. ^{1}H NMR of **spiro-PTZ-OMe** (THF-*d8*, 298 K).

The formation of the desired **spiro-POZ-OMe** and **spiro-PTZ-OMe** were unambiguously confirmed by standard spectroscopic techniques such as ^{1}H and ^{13}C NMR, Fourier transform infrared (FTIR), and high-resolution MALDI-TOF (HR-MS) spectrometry showing the corresponding molecular ion peaks $[M]^+$ at 875.3321 and 892.3208 m/z for **spiro-POZ-OMe** and **spiro-PTZ-OMe**, respectively. The highly asymmetric structure of the spiranic molecules was confirmed by the complexity found in ^{1}H NMR spectra of **spiro-PTZ-OMe** as illustrated in **Figure 48**.

5.2.2 Optical, electrochemical and thermal characterization of spiro-phenoxazine and spiro-phenothiazine-based HTMs.

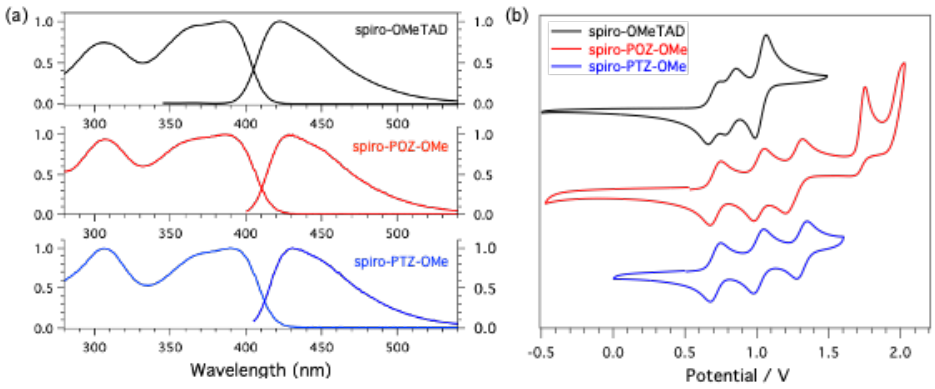

Figure 49. (a) UV-vis absorption spectra (solid line) and emission spectra (dashed line) of **spiro-POZ-OMe**, **spiro-PTZ-OMe** and spiro-OMeTAD in CH_2Cl_2; (b) Cyclic voltammetry of **spiro-POZ-OMe**, **spiro-PTZ-OMe** recorded in CH_2Cl_2 at a scan rate of 100 mV s^{-1}.

The optical properties of the **spiro-POZ-OMe** and **spiro-PTZ-OMe** were evaluated from dichloromethane solutions using UV-vis absorption and fluorescence spectroscopy, and compared to the benchmark spiro-OMeTAD (**Figure 49a**). The optical absorption and emission of the spiro-phenoxazine and spiro-phenothiazine derivatives match completely with that recorded for the spiro-OMeTAD. Spiro-like molecules show a first narrow band at the shorter wavelength, peaking at 300 nm, which is tentatively assigned to the characteristic optical features of the peripheral *p*-methoxydiphenylamine units with enhanced intensity in the case of POZ and PTZ derivatives. A broader band in the range of 350-400 nm is observed for both molecules arising from the π-conjugated structure of the spiranic central core. The emission spectra of **spiro-POZ-OMe** and **spiro-PTZ-OMe** showed a slightly red-shifted maximum wavelength centered at 428 and 431 nm, respectively, in comparison to the benchmark spiro-OMeTAD. The optical band-gap energies ($E^{0\text{-}0}$) were estimated from the intersection of the absorption and emission spectra of each molecule, revealing values of 3.00 and 2.98 eV for **spiro-POZ-OMe** and **spiro-POZ-OMe**, respectively. (**Table 16**)

Table 16. Optical, electrochemical and thermal properties of **spiro-POZ-OMe**, **spiro-PTZ-OMe**, and spiro-OMeTAD.

HTM	$\lambda_{max, abs}$ [nm][a]	$\lambda_{max, em}$ [nm][a]	E^{0-0} [eV][b]	$E^{ox}_{1/2}$ [V][c]	E_{HOMO} [eV][d]	E_{LUMO} [eV][e]	T_{dec} [°C][f]	T_g [°C][g]
spiro-POZ-OMe	387	428	3.00	0.73	-5.17	-2.17	402	152
spiro-PTZ-OMe	390	431	2.98	0.73	-5.17	-2.19	400	166
spiro-OMeTAD	385	419	3.05	0.72	-5.16	-2.11	449	125

[a] λ_{max} of absorption and emission measured in CH_2Cl_2 solutions; [b] E^{0-0} was determined at the intersection of normalized absorption and emission spectra; [c] Determined from cyclic voltammetry measurements *vs* normal hydrogen electrode (NHE); [d] E_{HOMO} is calculated in eV by E_{HOMO} = -4.44 eV - $E^{ox}_{1/2}$; [e] E_{LUMO} were estimated by $E_{LUMO} = E_{HOMO} + E^{0-0}$; [f] Decomposition temperature determined from TGA (5% weight loss under a N_2 atmosphere). [g] Determined from the second cycle of the DSC under a N_2 atmosphere.

Cyclic voltammetry measurements were carried out in order to study the electrochemical behavior of **spiro-POZ-OMe**, **spiro-PTZ-OMe**, and spiro-OMeTAD from CH_2Cl_2 solutions containing 0.1 M of $TBAPF_6$ acting as the electrolyte and at a scan rate of 100 mV s^{-1} (**Figure 49b**). The oxidation potentials of **spiro-POZ-OMe**, **spiro-PTZ-OMe**, and spiro-OMeTAD and the calculated HOMO and LUMO energies are gathered in **Table 11**. Both new molecules display three sequential oxidation waves in the range of 0.7 to 1.30 V with $E^{ox}_{1/2}$ values of 0.73, 1.01, and 1.25 V for **spiro-POZ-OMe** and 0.73, 1.01 and 1.30 V for **spiro-PTZ-OMe**. Thus, from the first oxidation waves located at 0.73 V, the calculated HOMO energies for both molecules are -5.17 eV, which is practically the same as that reported for spiro-OMeTAD (-5.16 eV), ensuring an effective hole transfer of the photogenerated holes from the perovskite material to the HTMs. Moreover, the LUMO energies of both molecules can be estimated using the previously calculated optical band-gap energy and resulted in values of -2.17 and -2.19 eV for **spiro-POZ-OMe** and **spiro-PTZ-OMe**, respectively.

Thermal properties of the spiro-containing molecules were investigated using TGA and DSC under N_2 atmosphere. **Figure 50a** displays the TGA analysis for

spiro-POZ-OMe and **spiro-PTZ-OMe**, confirming the good thermal stability of both molecules with decomposition temperatures (T_{dec}) of 400 ºC which are, however, significantly lower than the T_{dec} of spiro-OMeTAD (449 ºC). DSC analysis of **spiro-POZ-OMe** and **spiro-PTZ-OMe** (**Figure 50b**) indicates a similar morphological behavior for both molecules, exhibiting only glass transition temperatures (T_g) of 152 and 166 °C respectively, after consecutive heating/cooling cycles, which confirms the amorphous nature and reduced tendency to crystallize of **spiro-POZ-OMe** and **spiro-PTZ-OMe**. In contrast, spiro-OMeTAD can exist in both crystalline and amorphous states, with a T_g of 125 °C.

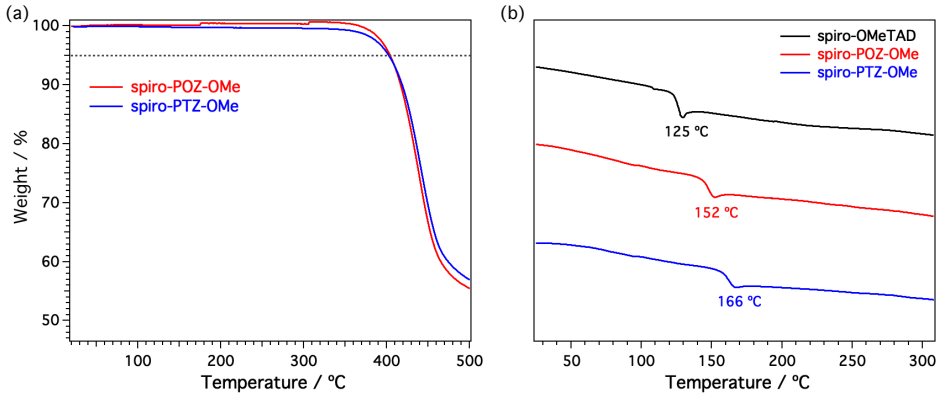

Figure 50. (a) TGA of **spiro-POZ-OMe** and **spiro-PTZ-OMe** under nitrogen at 10 °C min^{-1} of heating rate; (b) DSC curves of **spiro-POZ-OMe**, **spiro-PTZ-OMe** and spiro-OMeTAD under nitrogen at a heating rate of 20 °C min^{-1} (second cycle).

5.2.3 Device performance and characterization of spiro-phenoxazine and spiro-phenothiazine-based HTMs.

The new spiro-phenoxazine and spiro-phenothiazine based HTMs were firstly implemented in standard mesoporous PSCs using a configuration of FTO/c-TiO_2/m-TiO_2/SnO_2/Perovskite/HTM/Au. The HTMs were applied from chlorobenzene solutions with an optimized concentration of 20 and 30 mM for **spiro-POZ-OMe** and **spiro-PTZ-OMe**, respectively. The champion device incorporating **spiro-PTZ-OMe** reached a maximum PCE of 17.28% with an open-circuit voltage (V_{oc}) of 1.06 V, a short-circuit current (J_{sc}) of 23.01 mA cm^{-2} and a *FF* of 0.71 in combination with the triple cation perovskite ($[(FAPbI_3)_{0.87}(MAPbBr_3)_{0.13}]_{0.92}[CsPbI_3]_{0.08}$) (**Figure 51a**). In contrast, the

performance of the devices using **spiro-POZ-OMe** as HTMs was slightly lower due to the reduced values of V_{oc} (1.04 V), J_{sc} (22.94 mA cm^{-2}) and *FF* (0.70) which resulted in a maximum PCE of 16.67% (**Table 17**). The reference of spiro-OMeTAD surpassed both new HTMs reaching a maximum PCE of 18.46% with increased values of V_{oc} (1.08 V), J_{sc} (23.27 mA cm^{-2}) and *FF* (0.74).

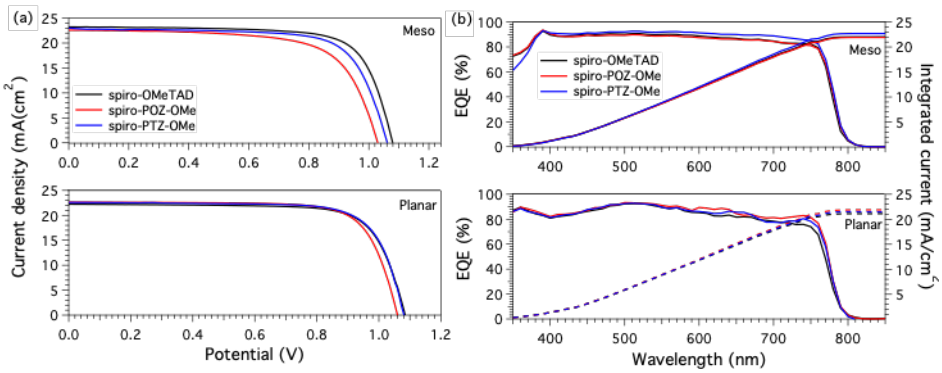

Figure 51. (a) *J-V* curves of **spiro-POZ-OMe**, **spiro-PTZ-OMe** and spiro-OMeTAD in combination with triple cation perovskite in mesoporous (up) and planar (down) devices; (b) External quantum efficiency (EQE) plots of **spiro-POZ-OMe**, **spiro-PTZ-OMe** and spiro-OMeTAD with the corresponding integrated current in mesoporous (up) and planar (down) devices.

In order to improve the photovoltaic performance of **spiro-POZ-OMe** and **spiro-PTZ-OMe**, planar n-i-p devices were prepared using the standard configuration of ITO/SnO_2/Perovskite/HTM/Au. The preparation of planar n-i-p devices is simpler in comparison to the mesoporous devices and requires milder conditions. First, the ITO glass was cleaned by sequentially detergent, deionized water and isopropanol. Before using, the ITO was cleaned by UVO for 15 min. Then, the substrate was spin coated with a thin layer of SnO_2 from a precursor solution in water (2.67%) at 4000 rpm for 30 s, and annealed in ambient air at 150 ºC for 30 min and then cleaned by UVO again for 15 min. The preparation and deposition of the triple cation perovskite, the HTMs and the top electrode were similar to that followed in the mesoporous devices (see *Experimental Section* for more details). Using planar architectures, the photovoltaic performance of **spiro-PTZ-OMe**-based devices at a higher concentration of 50 mM were boosted to a maximum PCE of 18.36% with

improved values of V_{oc} (1.08 V) and *FF* (0.75) (**Table 17**). Following a similar tendency, **spiro-POZ-OMe** displayed a notably improved PCE of 18.14% mainly stemming from the enhanced value of *FF* (0.76) (**Figure 51a**).

Table 17. Photovoltaic parameters of **spiro-POZ-OMe**, **spiro-PTZ-OMe** and spiro-OMeTAD measured from mesoporous and planar devices architectures.

HTM	Configuration	V_{oc} (V)	J_{sc} (mA cm^{-2})	*FF*	PCE (%)
spiro-POZ-OMe	Mesoporous	1.04	22.94	0.70	16.67
	Planar	1.06	22.68	0.76	18.14
spiro-PTZ-OMe	Mesoporous	1.06	23.01	0.71	17.28
	Planar	1.08	22.60	0.75	18.36
spiro-OMeTAD	Mesoporous	1.08	23.27	0.74	18.46
	Planar	1.08	22.30	0.75	18.20

Figure 51b collects the external quantum efficiencies (EQEs) of the devices incorporating **spiro-POZ-OMe**, **spiro-PTZ-OMe** and spiro-OMeTAD as HTM and the theoretical J_{sc} values integrated from the EQE which are consistent with those experimentally measured under 1 sun AM 1.5 G simulated in mesoporous and planar devices. In addition, the statistic distribution of the different photovoltaic parameters for 17 planar devices of each HTM including the reference of spiro-OMeTAD are summarized in **Figure 52**. From the distribution plots it is clearly observed that **spiro-PTZ-OMe** surpass the photovoltaic response of the benchmark spiro-OMeTAD, with a clearly improved tendency of V_{oc}, J_{sc} and PCE despite the reduced *FF*. In sharp contrast, **spiro-POZ-OMe** only shows an improvement in the J_{sc} in comparison with the spiro-OMeTAD

while the rest of PV parameters are decreased, including the distribution on the PCE.

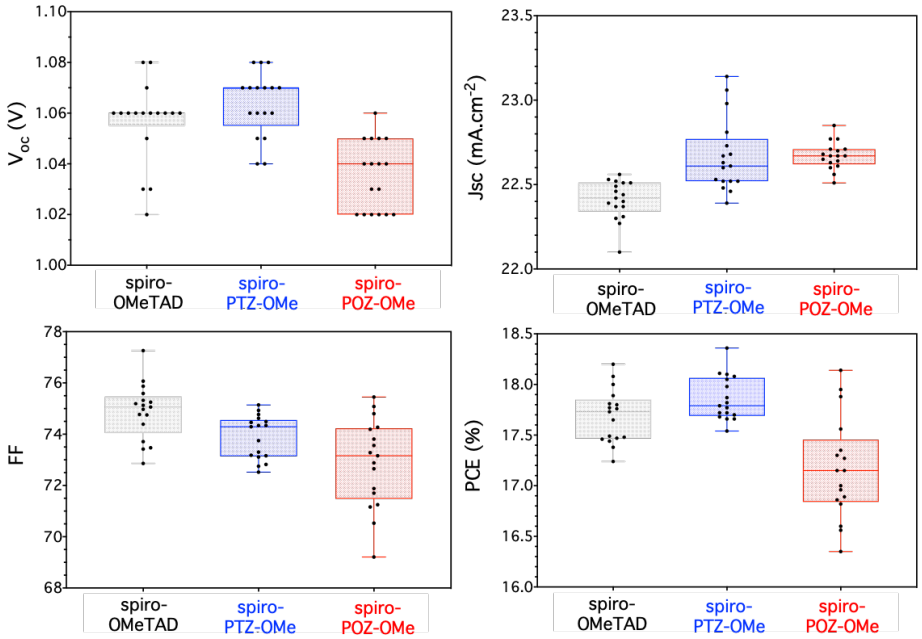

Figure 52. Statistical distribution of the photovoltaic parameters of 17 devices incorporating **spiro-POZ-OMe**, **spiro-PTZ-OMe** and spiro-OMeTAD in planar PSCs.

Likewise, the steady-state photoluminescence was measured in order to investigate the hole extraction ability of **spiro-POZ-OMe** and **spiro-PTZ-OMe** (**Figure 53a**). Upon excitation at 600 nm, the pristine triple cation perovskite film exhibits a strong PL signal centred at 790 nm. After capping the triple cation perovskite layer with the different spiro-based HTMs and spiro-OMeTAD, dramatically decreased PL intensities were observed, which confirm that the photogenerated holes can be efficiently extracted at the perovskite/HTM interface. The quenching of the photoluminescence did not show significant difference for each HTM, showing an increased quenching in the case of spiro-OMeTAD and **spiro-POZ-OMe**, confirming the potential of the new molecules for hole-transport applications.

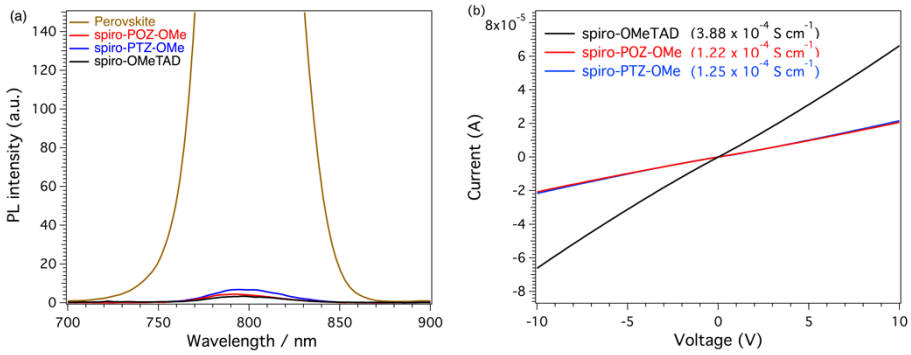

Figure 53. (a) Steady-state PL spectra of pristine triple cation perovskite and perovskite/HTM films; (b) Lateral conductivity measurements of **spiro-POZ-OMe**, **spiro-PTZ-OMe** and spiro-OMeTAD on substrates with interdigitated gold electrodes with a channel length of 2.5 μm.

To further investigate the excellent photovoltaic performance of **spiro-POZ-OMe** and **spiro-PTZ-OMe**, we measured the lateral conductivity of the HTMs on organic field effect transistor (OFETs) substrates (**Figure 53b**). The same optimized concentrations used for the device preparation were applied by adding 6% of FK-209 as dopant for both new HTMs and spiro-OMeTAD. The values for lateral conductivity measured for **spiro-POZ-OMe** (1.22×10^{-4} S cm^{-1}) and **spiro-PTZ-OMe** (1.25×10^{-4} S cm^{-1}) are in the same order in comparison to the benchmark spiro-OMeTAD (3.88×10^{-5} S cm^{-1}) indicating a similar ability for guarantee an efficient current collection.

5.2.4 Synthesis of spiro-like bis-xanthene and thioxanthene-based HTMs.

One of the essential aspects that the spiranic structures offer is the perpendicular arrangement of the two molecular halves connected through a central carbon atom with tetrahedral sp^3-hybridization. The spiro configuration in spiro-OMeTAD renders a rigid structure in an orthogonal arrangement, which efficiently minimizes the molecular interactions between the π-conjugated diphenylamino-substituted fluorenes. However, there is no clear evidence of whether the spiranic structure in spiro-OMeTAD plays an essential role in its outstanding photovoltaic performance in PSCs. As an alternative to the spiro linkage, the molecular design of **BX-OMe** and **BTX-OMe** (**Figure 47** right) incorporates a covalent central C-C bond that connects the two halves of a *p*-methoxydiphenylamino-substituted xanthene or thioxanthene units connected through sp^3-hybridized carbon atoms. This strategy renders a more flexible conformation than those of spiro-based structures, providing a gradual change of the rigidity of the 3D molecular arrangement.

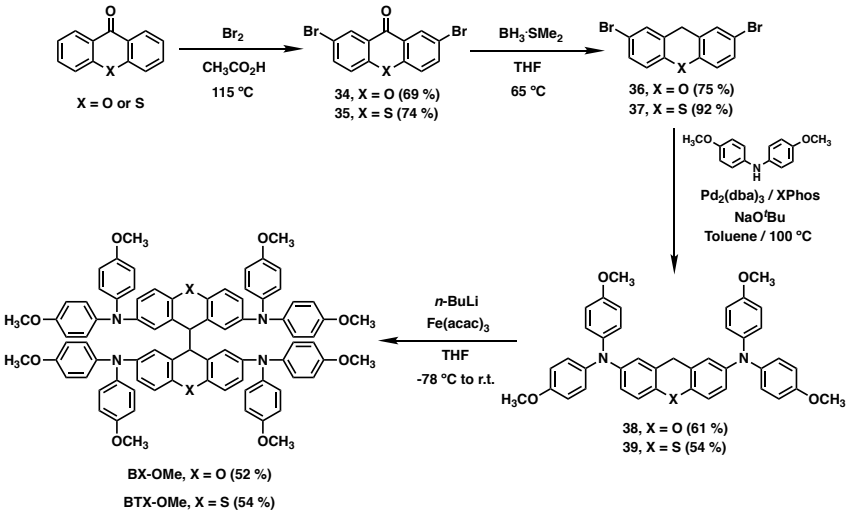

Scheme 7. Synthetic procedure for the preparation of bis-xanthene and thioxanthene-based HTMs.

The preparation of the flexible and symmetric HTMs **BX-OMe** and **BTX-OMe** was carried out by stepwise synthesis following well-established protocols under

standard conditions[231] (**Scheme 7**). The synthesis of both new HTMs starts from the corresponding xanthone or thioxanthone, which underwent a bromination reaction providing the corresponding dibrominated intermediate **34** and **35** in excellent yields.[232,233] The aforementioned intermediates were subjected to a reduction of the carbonyl groups in the presence of borane dimethyl sulfide complex ($BH_3{\cdot}SMe_2$),[234] followed by the carbon-nitrogen cross-coupling Buchwald-Hartwig reaction with *p*-methoxydiphenylamine to form the desired precursors **38** and **39** in moderate yields. Finally, the homocoupling of the two halves was achieved by treating the acid protons of the formed xanthene and thioxanthene with *n*-BuLi in the presence of $Fe(acac)_3$ to obtain the corresponding in **BX-OMe** and **BTX-OMe** in moderate yields. The homocoupling reaction was set up under different metallic ligands such as anhydrous $CoCl_2$ or $CuCl_2$, but the reaction did not take place.

The chemical structures of **BX-OMe** and **BTX-OMe** and its corresponding intermediates were fully characterized by means of standard spectroscopic techniques such as ^1H and ^{13}C NMR and Fourier transform infrared (FTIR). High-resolution MALDI-TOF (HR-MS) spectrometry confirmed the presence of the desired molecules showing the corresponding molecular ion peak for **BX-OMe** ($[M]^+$ at 1270.5081 m/z (calcd. 1270.5086 m/z)) and **BTX-OMe** ($[M]^+$ at 1302.4657 m/z (calcd. 1302.4630 m/z)). As representative spectroscopic features, both HTMs showed the corresponding aliphatic and aromatic signals, as illustrated in **Figure 54**. The protons from the thioxanthene units of the central scaffold are clearly correlated with the signals at 7.52, 6.89, and 6.31 ppm showing the expected multiplicity (doublet, doublet of doublets and doublet, respectively) of tri-substituted phenyl rings and a broad signal (7.11-7.06 ppm) from the *p*-methoxydiphenylamine units. Besides, in the aliphatic region, it is

231 J. Urieta-Mora, I. García-Benito, I. Zimmermann, J. Aragó, P. D. García-Fernández, G. Grancini, A. Molina-Ontoria, E. Ortí, N. Martín, M. K. Nazeeruddin, *Helv. Chim. Acta* **2019**, *102*, e1900056.

232 B. K. Sharma, A. M. Shaikh, R. M. Kamble, *J. Chem. Sci.* **2015**, *127*, 2063–2071.

233 S. Dadashi-Silab, H. Bildirir, R. Dawson, A. Thomas, Y. Yagci, *Macromolecules* **2014**, *47*, 4607–4614.

234 P. M. Bogie, L. R. Holloway, Y. Lyon, N. C. Onishi, G. J. O. Beran, R. R. Julian, R. J. Hooley, *Inorg. Chem.* **2018**, *57*, 4155–4163.

featured two singlets identified as the methoxy protons and the two C-H protons from the bis-thioxanthene central backbone (4.29 ppm).

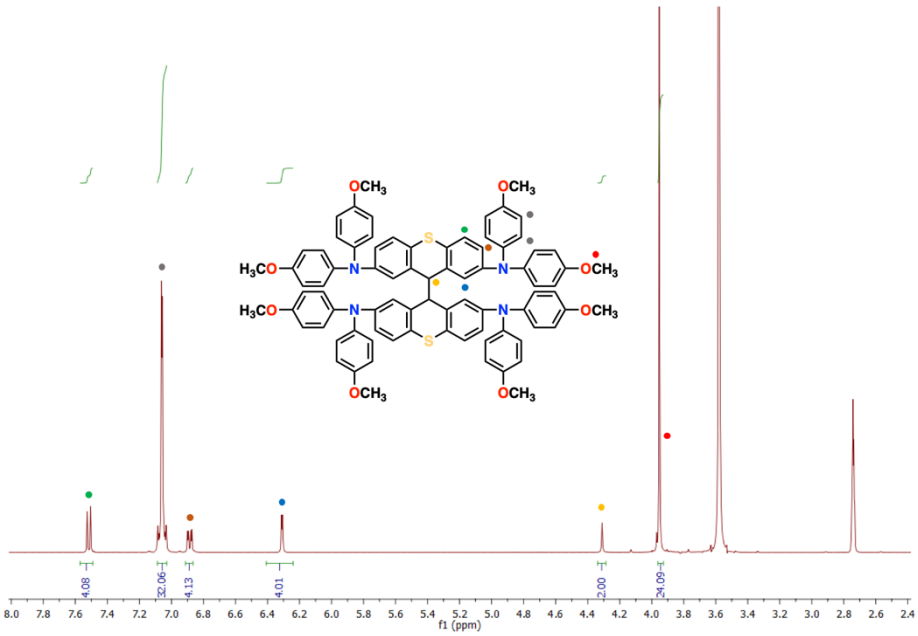

Figure 54. ^{1}H NMR of **BTX-OMe** in THF-*d*$_8$ (400 MHz, 298 K).

5.2.5 Optical, electrochemical and thermal characterization of spiro-like bis-xanthene and thioxanthene-based HTMs.

The structural and electronic properties of the new bis-xanthene and thioxanthene-based HTMs were initially studied through density functional theory (DFT) calculations at the B3LYP/6-31G** level using CH_2Cl_2 as solvent along with its constituting fragments and the spiro-OMeTAD used as reference. In **Figure 55**, the minimum-energy optimized structures calculated for the BX and BTX cores (top) and for the non-planar **BX-OMe** and **BTX-OMe** HTMs (middle) are shown. Clearly, the molecular structure is determined in both cases by the bis-xanthene and thioxanthene units, which are folded along the middle axis of the central heterocyclic ring and orientated different directions (up and down) within the same molecule to minimize the steric interactions. The lack of planarity of the xanthene and thioxanthene moieties is characterized by the folding angle α that defines the tilting of the lateral benzene rings, which

preserve their planarity, with respect to the average molecular plane. Angle α is calculated to have a slightly smaller value in the case of xanthene unit in the BX core (34º) than for the thioxanthene unit in BTX (44º) (**Figure 55a**). The incorporation of the peripheral donor units of diphenylamine to the central cores increases the folding of the xanthene and thioxanthene units, producing higher values for angle α (38º and 47º for **BX-OMe** and **BTX-OMe**, respectively) (**Figure 55b**).

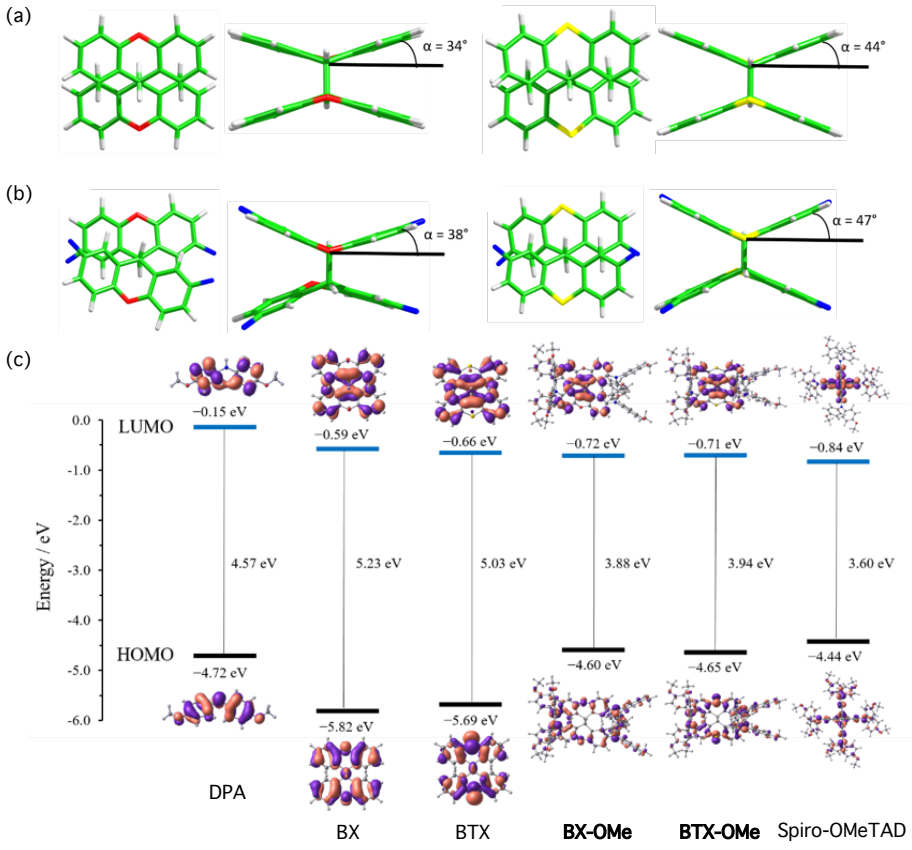

Figure 55. (a) Top and side views of the optimized geometries of BX (left) and BTX (right) cores; (b) Top and side views of the optimized geometries of **BX-OMe** (left) and **BTX-OMe** (right) HTMs; Energy diagram displaying the frontier molecular orbitals of **BX-OMe** and **BTX-OMe**, its constituting fragments and the spiro-OMeTAD as reference computed at the B3LYP/6-31G** level in CH_2Cl_2 solution.

Furthermore, DFT calculations were employed for predicting the frontier molecular orbitals of **BX-OMe** and **BTX-OMe**, its constituting fragments and the spiro-OMeTAD reference compound (**Figure 55c**). The highest-occupied molecular orbital (HOMO) of the BX core shows a weaker electron-donor ability in comparison to the DPA units (computed at -5.84 and -4.72 eV, respectively) while the substitution of oxygen by sulfur in BTX causes a slightly destabilization of the HOMO level enhancing its electron-donor character (-5.69 eV). The attachment of the four *p*-methoxydiphenylamine units to the central cores in **BX-OMe** and **BTX-OMe** induced in a significant destabilization of the HOMO energy, which was computed at -4.60 and -4.65 eV, respectively, thus approaching noticeably to the HOMO level computed for spiro-OMeTAD (-4.44 eV). The HOMO of both **BX-OMe** and **BTX-OMe** spreads mainly over the central cores with contributions from the donor units (mostly from the nitrogen atoms). An important charge transfer was computed from the central bis-xanthene and thioxanthene cores to the external donor moieties with a total net charge of 0.81 e and 0.73 e for **BX-OMe** and **BTX-OMe**, respectively, thus exhibiting an electronic structure markedly polarized.

The optical properties of **BX-OMe** and **BTX-OMe** were evaluated in dichloromethane solution and compared with spiro-OMeTAD (**Figure 56a**). The corresponding maximum absorption and emission wavelengths are summarized in **Table 18**. **BX-OMe** and **BTX-OMe** display a lack of absorption in the visible region with a single absorption band in the range of 280-340 nm (maximum centered at 310 nm for both HTMs) that induced relatively high energy for the lowest energy 0-0 transition ($E^{0\text{-}0}$) for both HTMs, which ensures a good electron-blocking capability. The emission spectra show broad bands with maximum emission peaks centered at 414 and 403 nm for **BX-OMe** and **BTX-OMe**, respectively. The optical absorption and fluorescence of spiro-OMeTAD are shifted towards higher wavelengths compared to **BX-OMe** and **BTX-OMe** owing to the enhanced π-conjugation of the spiro-cyclic central scaffold in spiro-OMeTAD. The derived optical bandgaps ($E^{0\text{-}0}$) were estimated from the intersection of the absorption and emission bands, resulting in values of 3.24 and 3.32 eV for **BX-OMe** and **BTX-OMe**, respectively. An asset of these kind of systems as HTMs for PSCs is their lack of conjugation, which keeps the visible range of the spectrum transparent, in contrast to the spiro-OMeTAD.

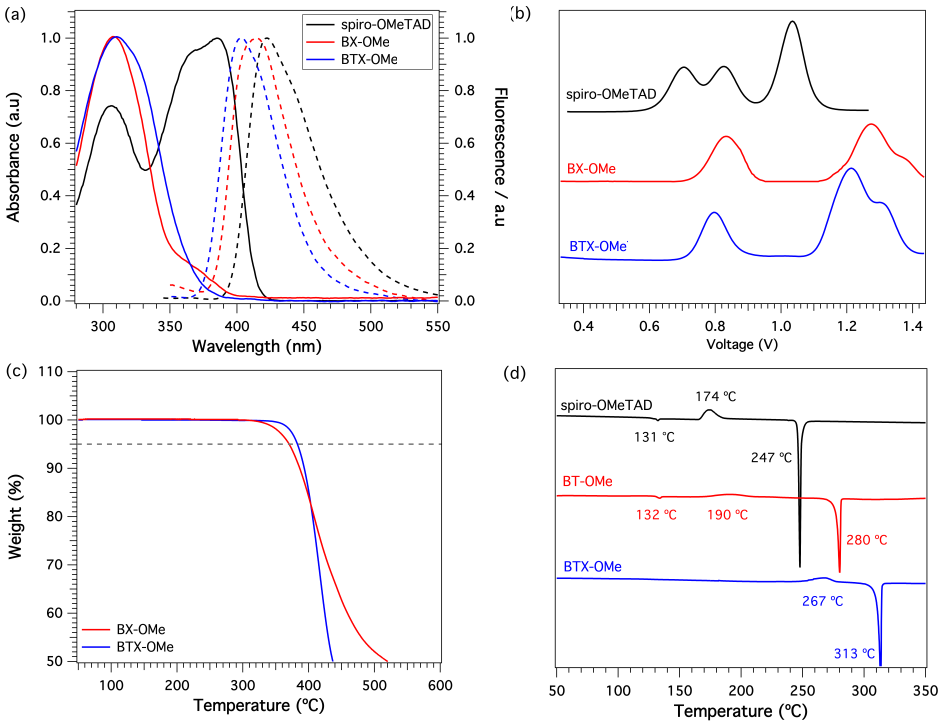

Figure 56. (a) UV-vis absorption spectra (solid line) and emission spectra (dashed line) of spiro-OMeTAD, **BX-OMe**, and **BTX-OMe** in CH_2Cl_2; (b) Differential pulse voltammetry recorded in CH_2Cl_2 containing 0.1 M $TBAPF_6$ at a scan rate of 100 mV s^{-1}; (c) Thermogravimetric analysis curves recorded under nitrogen at 10 °C min^{-1} of heating rate; (d) Differential scanning calorimetry curves under nitrogen at a heating rate of 20 °C min^{-1} (first cycle).

The electrochemical properties of the novel HTMs and spiro-OMeTAD were investigated using differential pulse voltammetry (DPV) in 0.1 M $TBAPF_6/CH_2Cl_2$ solution at a scan rate of 100 mV s^{-1} (**Figure 56b**). As expected from their similar chemical structure, both non-planar HTMs display similar electrochemical behavior with 3 different oxidation waves. In the case of **BX-OMe**, it exhibits the three oxidation waves centered at 0.83, 1.25, and 1.34 V *vs.* normal hydrogen electrode (NHE) (**Table 18**). Substitution of the oxygen atom in the central core by sulfur in **BTX-OMe** resulted in a slight increase of the electron-donor ability of the HTM (0.79, 1.21, and 1.30 V *vs.* NHE). In comparison to the new HTMs, spiro-OMeTAD also shows three oxidation waves centered at 0.70, 0.82, and 1.03 V, with the first oxidation potential cathodically

shifted by 0.09 and 0.13 V when compared to **BTX-OMe** and **BX-OMe**, respectively. The estimated HOMO energies taking into account the first oxidation potential for **BX-OMe**, **BTX-OMe**, and spiro-OMeTAD are -5.27, -5.23, and -5.16 eV, respectively. Therefore, the novel HTMs feature a slightly weaker electron-donor ability in contrast to spiro-OMeTAD but present an excellent band alignment with the valence band edge of common perovskites such as the triple cation $[(FAPbI_3)_{0.87}(MAPbBr_3)_{0.13}]_{0.92}[CsPbI_3]_{0.08}$ (*ca.* -5.7 eV).

Additional theoretical calculations were carried out in order to evaluate the ability of the **BX-OMe** and **BTX-OMe** for hole-transporting applications. Hole reorganization energies (λ) were computed at the B3LYP/6-31G** level in gas phase revealing λ values of 0.120 and 0.124 eV for **BX-OMe** and **BTX-OMe** which are notably smaller than the values calculated for their constituting fragments (0.192, 0.198 and 0.274 eV for the BX and BTX cores and DPA, respectively). The decrease in λ results is ascribed to a charge extraction involving both the core and the DPA units. Furthermore, **BX-OMe** and **BTX-OMe** exhibit low reorganization energies similar to that computed for spiro-OMeTAD (0.139 eV). The small λ values, together with the adequate energy level alignment with the perovskite, indicate the potential of the non-planar bis-xanthene and thioxanthene as HTMs for PSC devices.

Table 18. Optical, electrochemical and thermal properties of **BX-OMe**, **BTX-OMe** and spiro-OMeTAD.

HTM	$\lambda_{max,\ abs}$ [nm][a]	$\lambda_{max,\ em}$ [nm][a]	$E^{0\text{-}0}$ [eV][b]	$E^{ox}{}_{1/2}$ [V][c]	E_{HOMO} [eV][d]	E_{LUMO} [eV][e]	T_{dec} [ºC][f]	T_g [ºC][g]
BX-OMe	309	414	3.24	0.83	-5.27	-2.03	370	132
BTX-OMe	310	403	3.32	0.79	-5.23	-1.91	382	-
spiro-OMeTAD	386	419	3.05	0.70	-5.16	-2.11	449	131

[a] λ_{max} of absorption and emission measured in CH_2Cl_2 solutions; [b] $E^{0\text{-}0}$ was determined at the intersection of normalized absorption and emission spectra; [c] Determined from DPV measurements *vs.* normal hydrogen electrode (NHE); [d] E_{HOMO} is estimated in eV by E_{HOMO} = -4.44 eV - $E^{ox}{}_{1/2}$; [e] E_{LUMO} was estimated by $E_{LUMO} = E_{HOMO} + E^{0\text{-}0}$; [f] Decomposition temperature determined from TGA; [g] Glass transition temperature (T_g) determined from the first cycle from DSC.

To gain insight into the thermal stability of **BX-OMe** and **BTX-OMe**, TGA and DSC were conducted and compared with spiro-OMeTAD (**Figure 56c-d**). Thermogravimetric analysis confirmed the thermal stability of the new HTMs, which show relatively high decomposition temperatures (T_{dec}) of 370 and 382 °C (at a weight loss of 5%) for **BX-OMe** and **BTX-OMe**, respectively, but significantly lower than that measured for spiro-OMeTAD (449 °C) (**Table 18**). The difference in T_{dec} is ascribed to the relatively more rigid structure of spiro-OMeTAD.[235] The morphological study of the new compounds was investigated using DSC analysis and reveals a similar morphological behavior in the case of **BX-OMe** and spiro-OMeTAD. During the first heating scan, both molecules exhibit a discernible glass transition (T_g) and melting temperature (T_m) along with an additional crystallization process (T_c), which is not observed upon cooling. On the other hand, **BTX-OMe** displays a three-step thermal behavior with a crystallization process (T_c of 267 °C) and a sharp endothermic peak corresponding to a melting temperature (T_m) of 313 °C. No crystallization process was observed upon cooling, and only a glass transition (T_g) at 119 °C was discerned during the second heating scan.

5.2.6 Device performance and characterization of spiro-like bis-xanthene and thioxanthene-based HTMs.

The hole-transporting performance of **BX-OMe** and **BTX-OMe** was evaluated in combination with $[(FAPbI_3)_{0.87}(MAPbBr_3)_{0.13}]_{0.92}[CsPbI_3]_{0.08}$ triple cation perovskite in conventional mesoporous devices fabricated from a stack of thin films following the well-stablished procedures described in the *Experimental Section*. On the top of the perovskite layer, the doped HTM layer from a 20 mM solution of the **BX-OMe** and **BTX-OMe** and 70 mM for spiro-OMeTAD in chlorobenzene were deposited. Furthermore, ^{t}BP, Li-TFSI and FK-209 as dopants with an optimized thickness of 100 nm for both molecules were used. The new non-planar HTMs tend to form homogeneous thin films with good morphology. The individual forming-layers of a representative PSC device using

[235] T. Malinauskas, D. Tomkute-Luksiene, R. Sens, M. Daskeviciene, R. Send, H. Wonneberger, V. Jankauskas, I. Bruder, V. Getautis, *ACS Appl. Mater. Interfaces* **2015**, *7*, 11107–11116.

BTX-OMe can be distinguished from the cross-sectional SEM image as shown in **Figure 57a**.

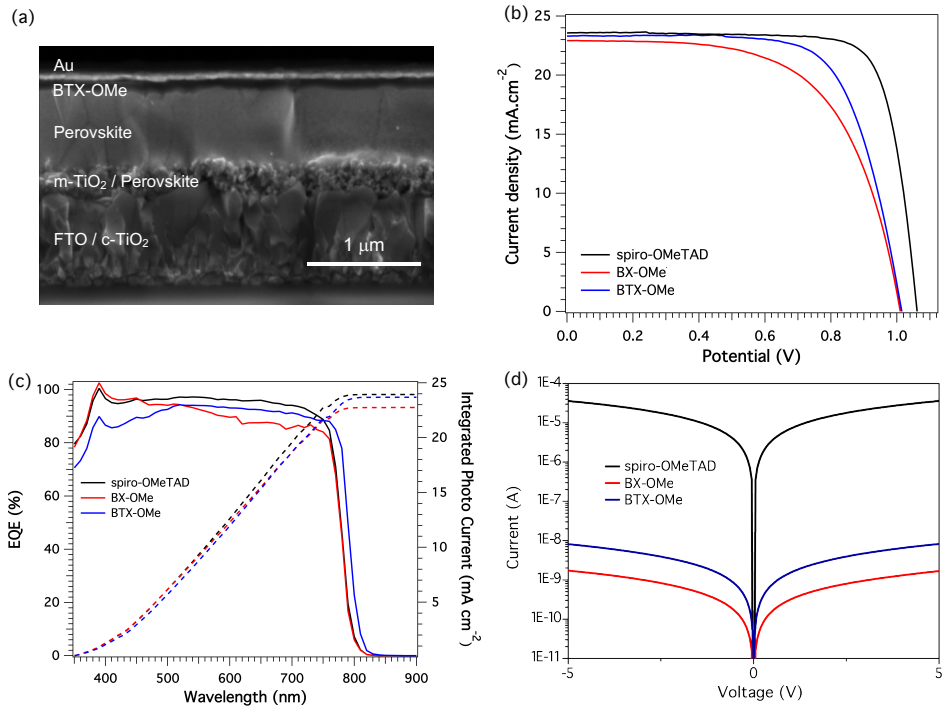

Figure 57. (a) Cross-section image (SEM) of a PSC device using **BTX-OMe** as HTM; (b) *J-V* curves of **BX-OMe**, **BTX-OMe** and spiro-OMeTAD in combination with triple cation perovskite; (c) External quantum efficiency (EQE) plots of **BX-OMe**, **BTX-OMe** and spiro-OMeTAD with the corresponding integrated current; (d) Lateral conductivity measurements of **BX-OMe**, **BTX-OMe** and spiro-OMeTAD measured on substrates with interdigitated gold electrodes with a channel length of 2.5 µm.

The current density-voltage (*J-V*) curves of the best-performing PSCs devices using **BX-OMe**, **BTX-OMe**, and spiro-OMeTAD as HTMs recorded under 1 sun are illustrated in **Figure 57b**, and the corresponding photovoltaic parameters are summarized in **Table 19**. The new spiro-like compounds exhibit a marked difference in terms of efficiency, showing **BTX-OMe**-based PSCs the highest power conversion efficiency up to 16.5%, mainly arising from an enhanced *FF* of 0.70 and an excellent J_{sc} of 23.35 mA cm^{-2}. On the other hand, devices using **BX-OMe** as HTM reached a significantly lower PCE of 14.19% with notably

reduced values for J_{sc} (22.93 mA cm^{-2}) and *FF* (0.61). In sharp contrast, the performance of devices incorporating spiro-OMeTAD exhibited a maximum power conversion efficiency of 19.63% with a notable increase of J_{sc} (23.57 mA cm^{-2}) and *FF* (0.79) that outperformed the spiro-like **BX-OMe** and **BTX-OMe** HTMs. The short circuit currents experimentally found by *J-V* measurements were in perfect agreement with those calculated from the integrated external quantum efficiency (EQE) measurements shown in **Figure 57c** (± 5% mismatch).

Table 19. Device performance of the best PSC devices incorporating **BX-OMe**, **BTX-OMe** and spiro-OMeTAD as HTMs using triple cation perovskite.

HTM	V_{oc} (V)	J_{sc} (mA cm^{-2})	*FF*	PCE (%)
BX-OMe	1.01	22.93	0.61	14.19
BTX-OMe	1.02	23.35	0.70	16.55
spiro-OMeTAD	1.06	23.57	0.79	19.63

To gain insight into the relatively poor performance of the new spiro-like HTMs, we evaluated the electrical conductivity of the HTMs in a lateral configuration between 2.5 μm spaced gold contacts. For this purpose, thin films of the spiro-like HTMs were deposited by spin-coating onto substrates having interdigitated gold electrodes under the same conditions used for the best devices of each HTMs (**Figure 57d**). Low values of lateral conductivity were found for **BX-OMe** and **BTX-OMe** (2.2×10^{-8} and 1.0×10^{-7} S cm^{-1}, respectively), which are remarkably lower than that reported for spiro-OMeTAD (8.7×10^{-5} S cm^{-1}). The low lateral conductivity measured for the spiro-like HTMs is most likely the reason for the low *FF* obtained for their devices, resulting in high series resistance that reduced the power conversion efficiency of the devices incorporating **BX-OMe** and **BTX-OMe**.

Section 5.3 Synthesis of triazatruxene-based HTMs for PSCs.

Nitrogen-based heterocyclic structures represent one of the most featured building blocks for the design of highly efficient donor molecules for OPVs during the years. More recently, they have successfully been used for the synthesis of HTMs for PSCs as it has previously been discussed (see *Background* section). One of the most highlighted structures based on nitrogen heteroaromatic compounds is triazatruxene-based materials since the first report of its synthesis by Bocchi and Palla in 1986.[236] Triazatruxene (TAT) consists of three indole units fused to a central benzene ring in a planar C_{3h} symmetry. It forms a π-extended conjugated structure, which provides high hole mobility owing to its strong π-π intermolecular interactions and electron-donating properties. The introduction of alkyl chains connected through the nitrogen atoms provides excellent solubility to the planar structure. The planar and π-rich structure of TAT derivatives allow the self-assembly into columnar stacks with centers enclosed by the peripheral hydrocarbon chains that confer a coaxial structure in which one-dimensional charge transport is favored by the π-electronic conjugated structure of the molecule. Furthermore, the implementation of TAT-based compounds as hole-transporting materials in PSCs could prevent the perovskite material from the moisture due to its hydrophobic behavior of the alkylated triazatruxene structure. In addition, TAT is one of the most suitable building blocks for photovoltaic applications due to its chemical versatility, which allows easy modification of its optical and electronic properties. Star-shaped triazatruxene derivatives have been successfully introduced as hole-transporting materials for PSCs, reaching remarkable power conversion efficiencies in different works during the last years of research.[158,159,160,237]

[236] V. Bocchi, G. Palla, *Tetrahedron* **1986**, *42*, 5019–5024.

[237] X.-C. Li, C.-Y. Wang, W.-Y. Lai, W. Huang, *J. Mater. Chem. C* **2016**, *4*, 10574–10587.

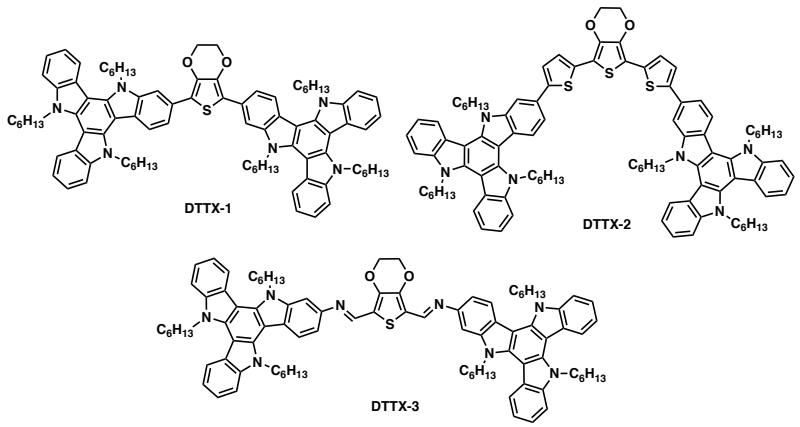

Figure 58. Chemical structures of dumbbell-shape TAT-based HTMs.

Inspired by the promising optoelectronic properties of triazatruxene, we have designed and synthesized three dumbbell-shaped triazatruxene-based derivatives (DTTXs) connected through different simple π-conjugated central units as hole-transporting materials for PSCs (**Figure 58**). The three new TAT-based HTMs can be prepared following a facile strategy, where the central EDOT scaffold is linked to end-capping TAT units to ensure suitable HOMO energy of the molecule as well as to provide excellent solubility in organic solvents.

The new dumbbell-shape materials were synthesized following well-established procedures[158,238] (**Scheme 8**). The triazatruxene unit was prepared by a cyclic trimerization from the condensation of oxindole in the presence of $POCl_3$. Hexyl chains were linked to the nitrogen atom under standard conditions followed by monobromination using NBS under mild conditions to afford intermediate **42**. The preparation of the TAT-boronic derivative **43** was addressed by standard Miyaura borylation reaction, while TAT-amine derivative **44** was synthesized through carbon-nitrogen Buchwald-Hartwig reaction with benzophenone imine and subsequently deprotection in acid media. On a different note, starting 3,4-ethylenedioxythiophene (EDOT) was subjected to a dibromination reaction for the synthesis of **46** followed by consecutive Suzuki-Miyaura cross-coupling and bromination reaction to obtain intermediate **48**. Besides, EDOT starting

[238] I. Bulut, P. Chávez, A. Mirloup, Q. Huaulmé, A. Hébraud, B. Heinrich, S. Fall, S. Méry, R. Ziessel, T. Heiser, P. Lévêque, N. Leclerc, *J. Mater. Chem. C* **2016**, *4*, 4296–4303.

materials reacted in the presence of *n*-butyllithium and DMF for the preparation of dicarboxaldehyde intermediate **49**.

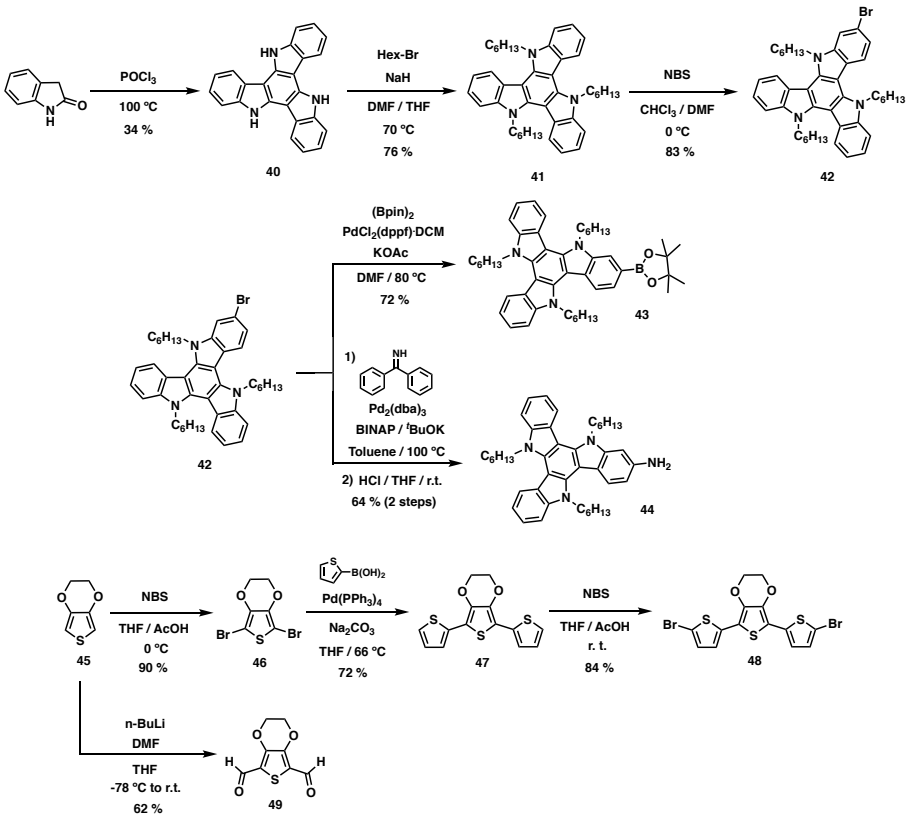

Scheme 8. Synthetic procedures for the preparation of the different intermediates for the synthesis of DTTX molecules.

Finally, TAT-boronic derivative **43** was covalently linked to the dibrominated EDOT (**46**) and π-extended thiophene-substituted EDOT (**48**) through a Suzuki-Miyaura cross-coupling reaction for the synthesis of **DTTX-1** and **DTTX-2** in high yields (84 and 68% respectively) (**Scheme 9**). On the other hand, TAT-amine derivative **44** underwent a condensation reaction with derivative **49** to form the imine-based **DTTX-3** with a high yield (77%).

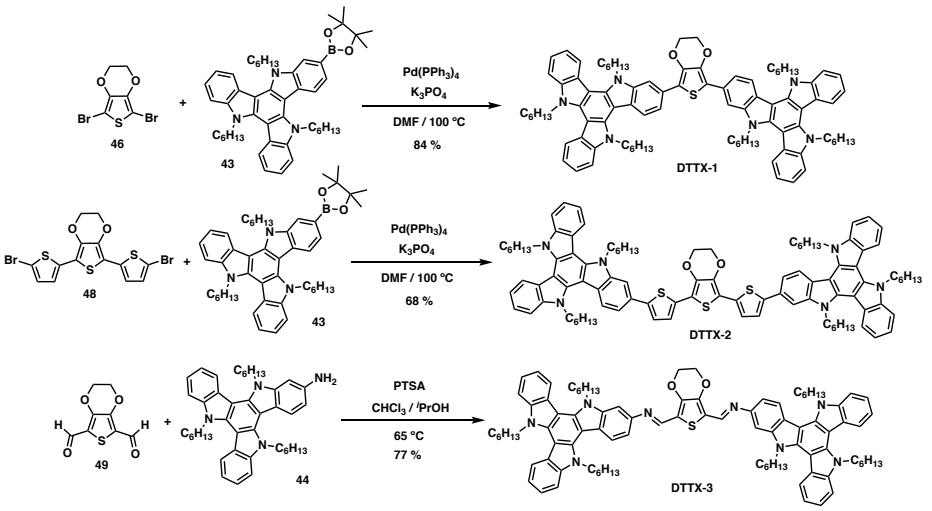

Scheme 9. Synthetic route for the preparation of DTTX molecules.

Complete structural characterization of the DTTXs HTMs was carried out using conventional spectroscopic techniques such as ^{1}H and ^{13}C NMR, FTIR and high-resolution MALDI-TOF (HR-MS) analysis that unambiguously confirmed the presence of new dumbbell-shaped HTMs (see Experimental Section for more details) by their molecular ion peaks $[M]^{+}$ found at 1333.7986 (**DTTX-1**), 1497.7724 (**DTTX-2**) and 1387.8176 (**DTTX-3**) m/z. The three dumbbell-shaped HTMs showed the corresponding aliphatic and aromatic signals, as illustrated in **Figure 59** (**DTTX-2**). Distinctive protons from the thiophene bridge are identified at 8.31 and 7.67 ppm as well as aliphatic protons from the ethylenedioxy-bridge of the EDOT unit (4.52 ppm) and the different signals from the hexyl peripheral chains (5.08, 5.00, 1.96, 1.29, and 0.85 ppm). The aromatic protons of the fused benzene moiety from triazatruxene units linked to the thiophene bridge are identified at 8.00, 7.52, and 7.35 ppm, while the other protons from triazatruxene could not be assigned.

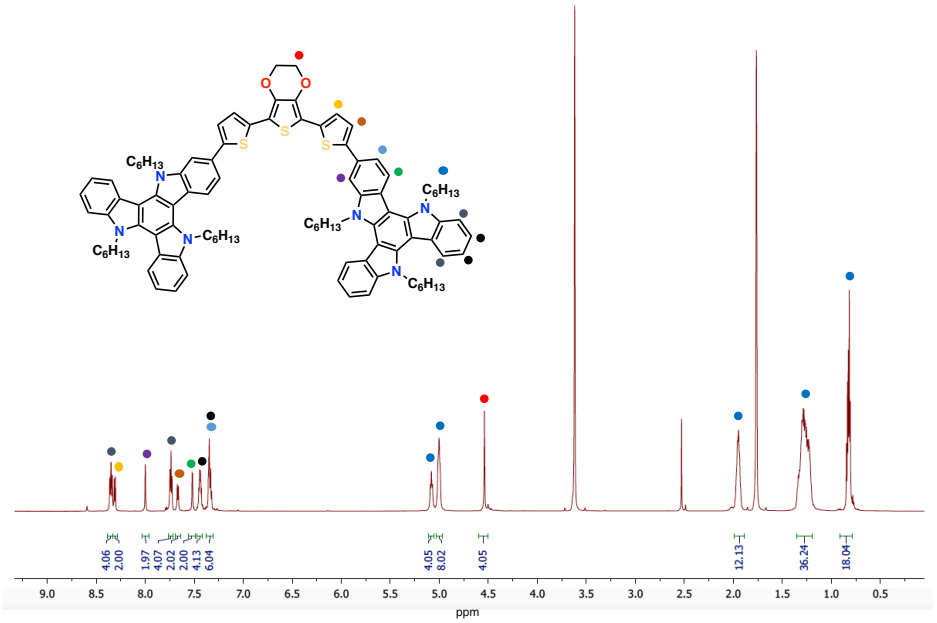

Figure 59. ^{1}H NMR of **DTTX-2** in THF-d_8 (400 MHz, 298 K).

5.3.2 Optical, electrochemical and thermal characterization of triazatruxene-based HTMs.

The optical properties of the dumbbell-shape HTMs were recorded using UV-vis absorption and fluorescence emission spectra in CH_2Cl_2 solution (**Figure 60a**). The new TAT-based HTMs showed strong absorptions in the visible region showing a maximum absorption band located at 315 nm, which is ascribed to the π-π* transitions of the triazatruxene moiety.[239] **DTTX-1** and **DTTX-2** also presented additional intense bands centered at 416 nm ($\varepsilon = 1.3 \times 10^5$ $M^{-1}cm^{-1}$) and 458 nm ($\varepsilon = 0.9 \times 10^5$ $M^{-1}cm^{-1}$), respectively, which are due to the π-extended conjugation (**Table 20**). Regarding **DTTX-3**, a broad absorption band is observed at 497 nm ($\varepsilon = 0.4 \times 10^5$ $M^{-1}cm^{-1}$), which is attributed to an internal charge transfer (ICT) between the electron-donor triazatruxene and the acceptor azomethine-EDOT central scaffold. On the other hand, the emission spectra of **DTTX-1** and **DTTX-2** present a similar outline showing large Stoke

[239] C. Ruiz, E. M. García-Frutos, D. A. da Silva Filho, J. T. López Navarrete, M. C. Ruiz Delgado, B. Gómez-Lor, *J. Phys. Chem. C* **2014**, *118*, 5470–5477.

shifts with a maximum centered at 470 and 480 nm, which is increased until 615 nm in the case of **DTTX-3**. The optical band gaps ($E^{0\text{-}0}$) were estimated from the intersection of the absorption and emission bands. Therefore, TAT-based HTMs present a relative high energies for the lowest energy 0-0 transition ($E^{0\text{-}0}$) of 2.77 (448 nm), 2.66 (466 nm) and 2.37 (523 nm) eV for **DTTX-1**, **DTTX-2** and **DTTX-3**, respectively.

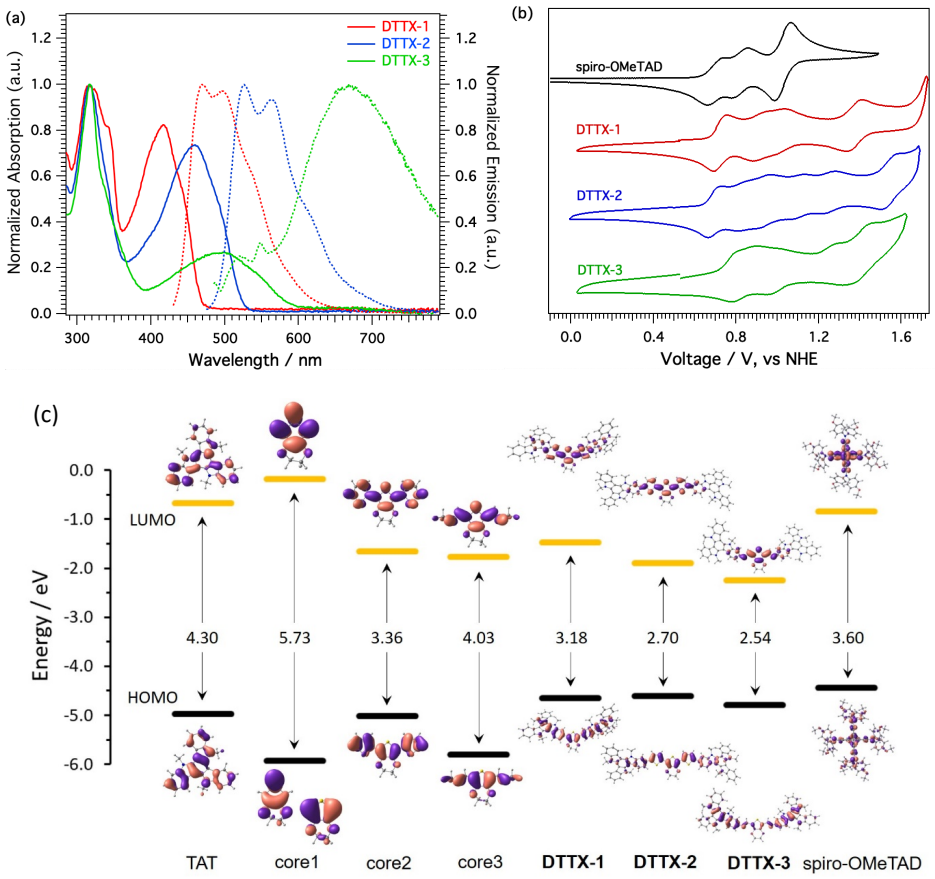

Figure 60. (a) UV-vis absorption spectra (solid line) and fluorescence emission (dashed line) of DTTXs recorded in CH_2Cl_2; (b) Cyclic voltammetry of DTTXs in CH_2Cl_2 containing 0.1 M $TBAPF_6$ at a scan rate of 100 mVs^{-1}; (c) Energy diagram displaying the frontier molecular orbitals computed for the DTTX HTMs, their constituting molecular fragments, and the spiro-OMeTAD reference compound at the B3LYP/6-31G** level in CH_2Cl_2.

The redox properties of the TAT-based HTMs were investigated using cyclic voltammetry (CV) in 0.1 M $TBAPF_6/CH_2Cl_2$ using ferrocene as internal standard at a scan rate of 100 mV s^{-1} (**Figure 60b**). The oxidation potentials and the calculated HOMO energy levels of the TAT-based HTMs are collected in **Table 20**. The cyclic voltammograms of the DTTXs derivatives show a complex electrochemical behavior with multiple oxidation waves for both HTMs. **DTTX-1** and **DTTX-2** display a stronger electron donor character with the first oxidation potential ($E_{1/2}$) placed at 0.73 and 0.69 V *vs* normal hydrogen electrode (NHE) respectively, which represent HOMO energies of -5.17 and -5.13 eV for **DTTX-1** and **DTTX-2** which are almost similar to those measured for reference spiro-OMeTAD (-5.16 eV). Both new HTMs presented a stronger electron donating ability in comparison to **DTTX-3**, which shows an anodically shifted first oxidation potential by 0.11 and 0.15 V ($E_{1/2}$ = 0.84 V), resulting in a lower-lying HOMO energy of -5.28 eV. Hence, an efficient hole extraction from the perovskites to the DTTXs is ensured due to an adequate band alignment with the valence band edge of the perovskite (ca. -5.7 eV). Furthermore, LUMO energies were estimated taking into account the optical band-gap energy ($E^{0\text{-}0}$) calculated before and the HOMO energies estimated from CV measurements.

To gain insight into the structural and electronic properties of the new HTMs DFT calculations at the B3LYP/6-31G** level including solvent effects (CH_2Cl_2) were performed. To simplify the calculations, the hexyl chains attached to the nitrogen atoms of the TAT units were substituted by methyl groups. In **Figure 60c** are displayed the frontier molecular orbitals calculated for the TAT-based HTMs, their constituting fragments, and the spiro-OMeTAD as reference compound. The HOMO energy of the EDOT scaffold in the core-1 (-5.92 eV) increases in energy upon π-extension with imine groups core-3: (-5.82 eV) and especially with thiophene rings forming a terthiophene moiety in core-2 (-5.02 eV). The TAT HOMO is located even higher in energy at –4.97 eV accoding to its electron-donor character. Due to the efficient π -conjugation between the TAT units and the EDOT-type linker, the HOMO in the DTTX HTMs results from a combination of the HOMOs of the three constituting fragments. Noteworthy, the HOMO of **DTTX-1** (-4.64 eV) and **DTTX-2** (-4.60 eV) are only slightly below the HOMO of spiro-OMeTAD (-4.44 eV), supporting them as promising HTMs. The HOMO of **DTTX-3** is however more localized over the TAT units and is calculated lower in energy (-4.79 eV), leading to a slightly

poorer alignment with respect to spiro-OMeTAD. Otherwise, the lowest-unoccupied molecular orbital (LUMO) of the EDOT-linker decreases in energy upon extension of the π-conjugation (from -0.19 eV in core-1 to -1.65 in core-2) and to the incorporation of the electron withdrawing imine groups in core-3 (-1.78 eV eV), and from -1.46 eV in **DTTX-1** to -1.90 and -2.25 eV in **DTTX-2** and **DTTX-3** respectively. As a result, the HOMO-LUMO gap decreases from 3.18 eV in **DTTX-1** to 2.70 and 2.54 eV in **DTTX-2** and **DTTX-3**, respectively. In contrast to the HOMO, the participation of TAT units in the LUMO of DTTX derivatives is marginal, especially for **DTTX-2** and **DTTX-3** (**Figure 60c**).

Table 20. Optical, electrochemical and thermal properties of DTTX derivatives.

HTM	$\lambda_{max,\ abs}$ [nm][a]	$\lambda_{max,\ em}$ [nm][a]	$E^{0\text{-}0}$ [eV][b]	$E^{ox}{}_{1/2}$ [V][c]	E_{HOMO} [eV][d]	E_{LUMO} [eV][e]	T_{dec} [ºC][f]	T_m [°C][g]	T_g [ºC][g]
DTTX-1	315	469	2.77	0.73	-5.17	-2.40	427	210	74
DTTX-2	316	481	2.66	0.69	-5.13	-2.47	420	-	78
DTTX-3	317	615	2.37	0.84	-5.28	-2.91	373	132	-

[a] λ_{max} of absorption and emission measured in CH_2Cl_2 solutions; [b] $E^{0\text{-}0}$ was determined at the intersection of normalized absorption and emission spectra; [c] Determined from CV measurements *vs.* normal hydrogen electrode (NHE); [d] E_{HOMO} is estimated in eV by E_{HOMO} = -4.44 eV - $E^{ox}{}_{1/2}$; [e] E_{LUMO} was estimated by $E_{LUMO} = E_{HOMO} + E^{0\text{-}0}$; [f] Decomposition temperature determined from TGA; [g] Melting and glass transition temperature determined from the first cycle from DSC.

The minimum-energy geometry computed for the DTTX derivatives at the B3LYP/6-31G** level are show in **Figure 61**. The thiophene (EDOT) core exhibits the typical structural pattern of related (oligo)thiophene derivatives, with alternating single and double carbon–carbon bonds forming a π-conjugated pathway. When moving from the isolated core to the corresponding HTMs bearing the TAT units, an enhanced π-delocalization is predicted as indicated by the decrease in the bond length alternation. For example, C−C single bond shortens from 1.440 to 1.431 Å and C=C double bonds lengthen from 1.366 to 1.379 Å in the EDOT moiety in going from the isolated EDOT linker to the π-extended **DTTX-1**. Similarly, moving from **DTTX-1** to the more conjugated **DTTX-2** and **DTTX-3**, an increase in the C=C double bonds length and a

decrease in the C−C single bonds length of the EDOT core support a more effective π-delocalization upon extending the thiophene-based central linker. The TAT unit presents a slightly twisted geometry with out-of-plane distortions due to the steric interactions between the *N*-alkyl groups and the triazatruxene core. In the fused DTTX systems, a good π-conjugation of the constituting TAT−EDOT linker−TAT units is therefore anticipated due to the quasi-planar, highly-conjugated molecular structure, in contrast to that commonly found in HTMs bearing diphenylamino (DPA) and triphenylamino (TPA) peripheral units such as ATT, DBQT, DBST or CoTh based HTMs that were previously investigated.

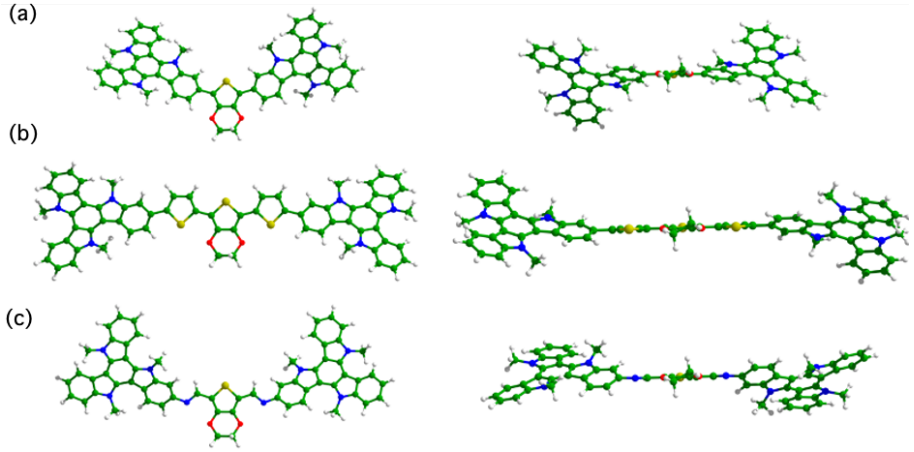

Figure 61. Top (left) and side (right) views of the minimum-energy optimized geometries calculated in CH_2Cl_2 for **DTTX-1** (a), **DTTX-2** (b), and **DTTX-3** (c).

The thermal properties of **DTTX-1**, **DTTX-2**, and **DTTX-3** were determined by means of TGA and DSC under nitrogen atmosphere (detailed thermal features are collected in **Table 20**). The TAT-based HTMs exhibit good thermal stability (5% weight loss under N_2 atmosphere) with decomposition temperatures (T_{dec}) up to 350 °C (**Figure 62a**). Nevertheless, a marked different behavior is observed due to the change in the molecular bridging moieties. On this basis, azomethine-based **DTTX-3** exhibits nearly 60 °C lower thermal stability (T_{dec} of 373 ºC) than all-aromatic backbone-based **DTTX-1** (427 ºC) and **DTTX-2** (420 ºC). Differential scan calorimetry was performed to evaluate the distinct morphological behaviour of the new compounds (**Figure 62b**). During the first scan **DTTX-1** exhibits a low glass transition (T_g) of 74 °C followed by a melting

temperature (T_m) at 210 °C. No crystallization process was observed upon cooling. On the other hand, **DTTX-2** is essentially amorphous and only a low glass transition (T_g) at 78 °C was detected. Finally, during the first cycle of heating, **DTTX-3** exhibits an endothermic peak corresponding to a melting process at 132 °C, without an obvious glass transition during the consecutive cycles.

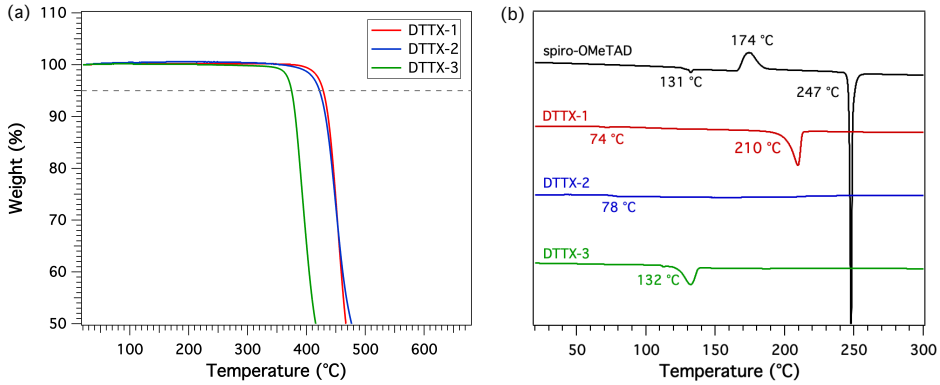

Figure 62. (a) Thermogravimetric analysis curves recorded for DTTX molecules under nitrogen at 10 °C min^{-1} of heating rate; (b) DSC curves of DTTX molecules and spiro-OMeTAD under nitrogen during the first cycle at a heating rate of 20 °C min^{-1}.

5.3.3 Device performance and characterization of triazatruxene-based HTMs.

The dumbbell-shaped DTTX molecules were incorporated as HTMs in solution-processed PSCs and compared to the widely used reference compound spiro-OMeTAD in combination with the triple cation perovskite ($[(FAPbI_3)_{0.87}(MAPbBr_3)_{0.13}]_{0.92}[CsPbI_3]_{0.08}$). The HTMs were deposited by spin-coating from a chlorobenzene solutions (30 mM was the optimized concentration) containing cobalt dopant (FK-209), Li-TFSI and tert-butylpyridine (^{t}BP) as additives (detailed device fabrication can be found in the General Methods in the *Experimental Section*). HOMO energies of TAT-based HTMs feature a perfect match alignment with the valence band edge of the triple cation perovskite for effective hole transport and electron-blocking properties (**Figure 63a**). From the cross-sectional (SEM) image can be distinguished the different layers of the fabricated devices, which showed an optimized layer thickness of 80-100 nm for the DTTX molecules. Although the three

triazatruxene-derivatives possess high solubility in chlorobenzene, which is favorable for obtaining good films and uniform surface coverage of the perovskite, only **DTTX-1** and **DTTX-2** showed a uniform coverage of the perovskite layer as illustrated in **Figure 63b-c**. In contrast, in **DTTX-3** devices were clearly observed pinholes and non-covered zones where the perovskite layer is in direct contact with the gold layer (**Figure 63d** and **Figure 65c**).

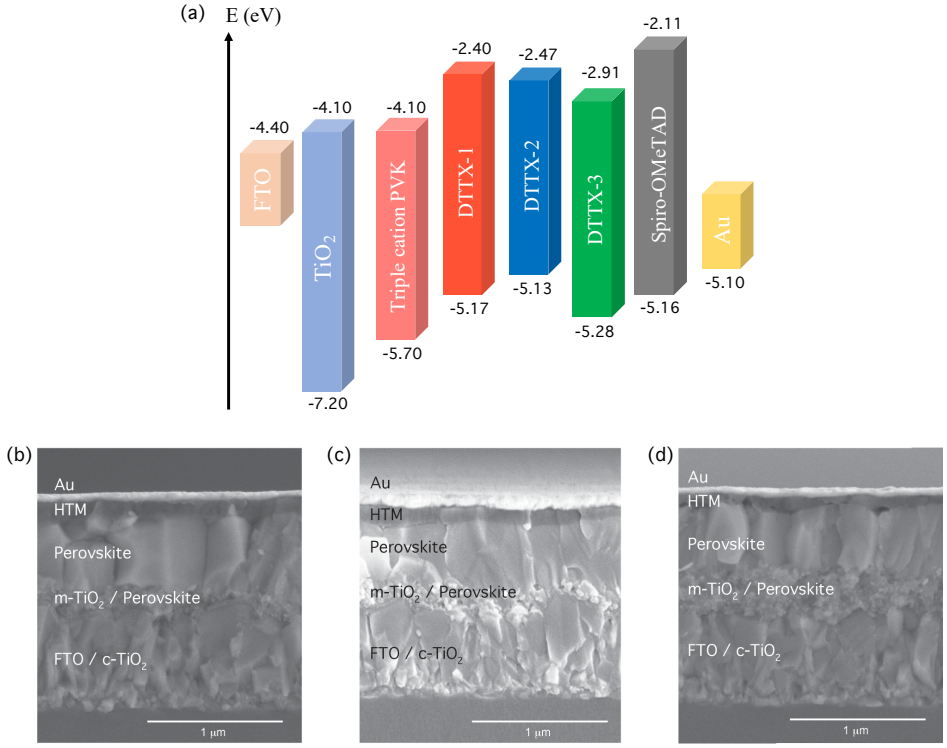

Figure 63. Device characterization: a) Energy diagram of the different components of the PSC; Cross-section scanning electron microscopy (SEM) picture of the mesoporous-PSCs using (b) **DTTX-1**, (c) **DTTX-2** and (d) **DTTX-3** as HTM.

The photovoltaic performance of the TAT-based HTMs was investigated under 1 sun AM 1.5 G simulated illumination at an intensity of 100 mW cm^{-2}. The current density-voltage (*J-V*) curves for the best-performing PSCs are depicted in **Figure 64a**, and the corresponding photovoltaic parameters are collected in **Table 21**. **DTTX-2**-based devices highlighted among the TAT-based HTMs reaching the highest power conversion efficiencies (PCE) of 18.3% with notable

values for V_{oc} (1.06 V), J_{sc} (23.29 mA cm^{-2}) and fill factor (0.74). Closely, **DTTX-1** yielded a maximum PCE of 17.42% (V_{oc} = 1.04 V, J_{sc} = 23.08 mA cm^{-2} and FF = 0.73) which was more dependent of the perovskite's aging. In sharp contrast, devices incorporating azomethine-based **DTTX-3** reached much lower efficiency with a maximum PCE of 12.68%, due to the significantly decreased values for V_{oc} (0.99 V), J_{sc} (22.89 mA cm^{-2}) and, mainly for the fill factor (0.56). The reason for the low FF obtained from the latter is most likely due to the high series resistance (R_s) and low shunt resistance (R_{sh}), which is, therefore, attributed to enhanced interfacial charge recombination.[240] In addition, the low homogeneity of the **DTTX-3** layer on top of the perovskite layer also affects the device performance negatively. The devices using spiro-OMeTAD as reference surpassed the power conversion efficiencies reached by DTTXs derivatives reaching a maximum PCE of 18.92% that arose from the enhanced values of V_{oc} (1.08 V) and J_{sc} (23.44 mA cm^{-2}).

Table 21. Photovoltaic parameters of solution-processed PSC devices using DTTX molecules and spiro-OMeTAD as HTMs.

HTM	V_{oc} (V)	J_{sc} (mA cm^{-2})	FF	PCE (%)
DTTX-1	1.04	23.08	0.73	17.42
DTTX-2	1.06	23.19	0.74	18.30
DTTX-3	0.99	22.89	0.56	12.68
spiro-OMeTAD	1.08	23.44	0.75	18.92

The efficiency distribution of 10 devices incorporating each DTTX HTMs is collected in **Figure 64b**. In the case of **DTTX-1** and **DTTX-2**, a good reproducibility in the efficiency values are observed in comparison to **DTTX-3**, which could be ascribed to the lower homogeneity of **DTTX-3** films on the top of the perovskite that leads to a wider range of efficiencies. **Figure 64c** shows the external quantum efficiencies (EQEs) of the devices incorporating each DTTX as HTM and the theoretical J_{sc} values integrated from the EQE, which are

[240] L. Caliò, S. Kazim, M. Salado, I. Zimmermann, M. K. Nazeeruddin, S. Ahmad, *Sustain. Energy Fuels* **2018**, *2*, 2179–2186.

consistent with those experimentally measured under 1 sun AM 1.5 G simulated illumination in all cases.

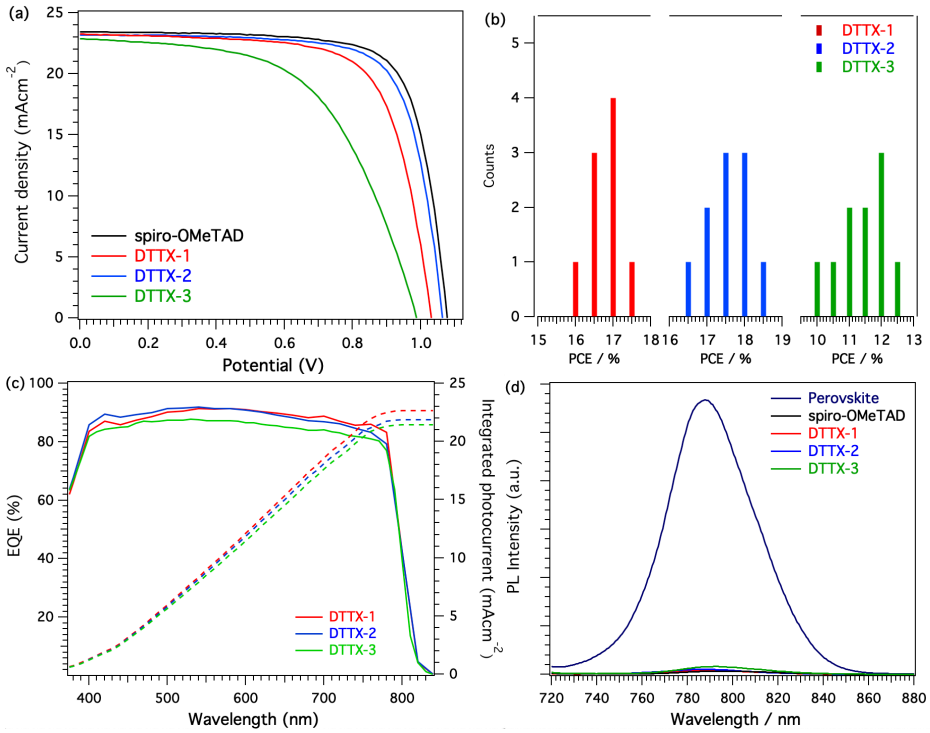

Figure 64. (a) Current density-voltage (*J-V*) curves of DTTXs and spiro-OMeTAD as HTMs in mesoscopic PSCs; (b) Efficiency distribution for 10 devices incorporating DTTX HTMs; (c) External quantum efficiency (EQE) plots of DTTX with the corresponding integrated current; (d) Steady-state PL spectra of pristine triple cation perovskite and perovskite/HTM films.

The suitable band alignment of the HOMO energy levels of the HTMs and the valence band of the perovskite guarantee an efficient extraction of the photogenerated holes at the perovskite/HTM interface. To evaluate the hole-extraction ability of the DTTX molecules, steady-state photoluminescence (PL) measurements were recorded along with reference of spiro-OMeTAD (**Figure 64d**). Upon excitation, the pristine triple cation perovskite film exhibits a strong PL signal centered at 785 nm. After coating the triple cation perovskite layer with the different HTMs and spiro-OMeTAD, a dramatically decreased PL intensity is observed, which confirms that the photogenerated holes can be

efficiently extracted at the perovskite/HTM interface. The quenching of the PL did not show a significant difference for each HTM, obtaining an increased quenching in the case of spiro-OMeTAD and **DTTX-1**.

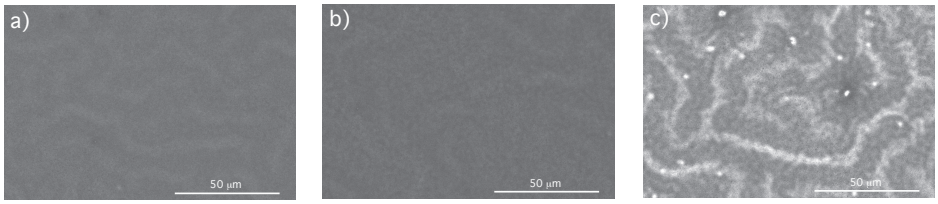

Figure 65. Top-view SEM images of a) **DTTX-1,** b) **DTTX-2**, and c) **DTTX-3** deposited on top of the perovskite film.

Hole extraction and reduce charge recombination are significantly affected by the morphology of the HTMs on top of the perovskite layer. To shed light about the surface morphology of spin-coated films of **DTTX-1**, **DTTX-2**, and **DTTX-3** onto the perovskite, scanning electron microscopy was performed (**Figure 65**). The low magnification top-view SEM images show the quality difference of the DTTX films deposited on top of the perovskite layer. **DTTX-1** and **DTTX-2** layers present an homogeneous and complete surface coverage on top of perovskite. However, the surface of the **DTTX-3** layer contains lot of dots demonstrating the aggregation of the material after spin-coating deposition, which is detrimental for the charge transfer and transport properties and, therefore, to the device performance.

To investigate the charge transport and hole collection properties of **DTTX-1**, **DTTX-2**, **DTTX-3** and spiro-OMeTAD, lateral conductivity was measured by using a two-contact electrical conductivity set-up with organic field-effect transistor (OFET) substrates that were fabricated as described in the *Experimental Section*. Lateral thin-film conductivity of doped **DTTX-1**, **DTTX-2**, and **DTTX-3** was determined to be 1.17×10^{-4}, 4.43×10^{-4} and 4.71×10^{-5} S cm^{-1}, respectively (**Figure 66a**). The conductivity of doped spiro-OMeTAD was determined to be $\sigma = 5.89 \times 10^{-4}$ S cm^{-1}, which is comparable to the values reported in the literature. Although the conductivity values of **DTTX-1** and **DTTX-2** are slightly lower than spiro-OMeTAD, the conductivity of the layer is enough for efficient charge transport. However, the conductivity of **DTTX-3** is one order of magnitude lower than the spiro-OMeTAD value, which explains

the lower PCE of the device. Furthermore, hole mobility was measured on hole-only devices with the structure of glass/ITO/PEDOT:PSS/HTM/Au using the space-charge limited current (SCLC) method according to previous literature.[101] *J-V* curves of hole-only devices of the new HTMs and spiro-OMeTAD were measured in the dark, and the hole mobility (μ_h) was determined using the space-charge limited current method (SCLC) (**Figure 66b**). The hole mobility values of doped **DTTX-1**, **DTTX-2**, **DTTX-3** and spiro-OMeTAD were determined to be 9.41×10^{-5}, 1.84×10^{-4}, 6.70×10^{-5}, and 3.71×10^{-4} cm^2 V^{-1} s^{-1}, respectively, following the same tendency as the lateral conductivity, confirming the potential of **DTTX-1** and **DTTX-2** as alternatives to the benchmark spiro-OMeTAD.

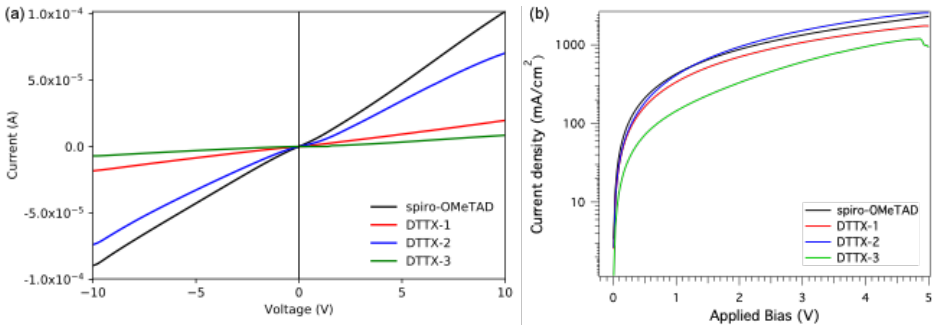

Figure 66. (a) Conductivity measurements of **DTTX-1**, **DTTX-2**, **DTTX-3**, and spiro-OMeTAD measured on OFET substrates; (b) *J-V* plots of hole-only devices based on **DTTX-1**, **DTTX-2**, **DTTX-3** and spiro-OMeTAD.

Section 5.4 Synthesis of disruptive, non-planar nanographene derivatives for hole-transporting applications.

Graphene has attracted the interest of researchers due to its groundbreaking chemical and physical properties that make graphene a potential material for many emerging fields such as batteries, OLEDs, or photovoltaic technologies.[241,242,243,244,245] Nevertheless, the chemical modification of graphene by means of the "top-down" approach alters the lattice of graphene and results in not well-defined chemical structures. In contrast, the "bottom-up" approach uses the organic synthesis, which offers a wide variety of tools to precisely control the chemical structure as well as the geometries of the *"molecular"* nanographenes. Importantly, the latter allows the fabrication of uniform and well-defined molecular structures with new functional properties in comparison to pristine graphene. Molecular nanographenes are compelling choices for molecular electronics and photovoltaic applications since their molecular structures can be precisely designed and synthesized to afford related properties on demand.

The design of molecular, non-planar nanographenes has been recently addressed in our group by using different central scaffolds such as helicenes[156] or corannulene,[246] rendering 3D structures with unique optoelectronic properties. Our chemical design for the construction of a 3D molecular nanographene takes advantage of the previously employed saddle-shaped molecules based on cyclooctatetraphenylene (CoPh) and cyclooctatetrathiophene (CoTh), which are

---

241 K. S. Novoselov, V. I. Fal′ko, L. Colombo, P. R. Gellert, M. G. Schwab, K. Kim, *Nature* **2012**, *490*, 192–200.

242 K. Dirian, M. Á. Herranz, G. Katsukis, J. Malig, L. Rodríguez-Pérez, C. Romero-Nieto, V. Strauss, N. Martín, D. M. Guldi, *Chem. Sci.* **2013**, *4*, 4335–4353.

243 G. Bottari, M. Á. Herranz, L. Wibmer, M. Volland, L. Rodríguez-Pérez, D. M. Guldi, A. Hirsch, N. Martín, F. D'Souza, T. Torres, *Chem. Soc. Rev.* **2017**, *46*, 4464–4500.

244 M. F. El-Kady, Y. Shao, R. B. Kaner, *Nat. Rev. Mater.* **2016**, *1*, 16033.

245 T. Mahmoudi, Y. Wang, Y.-B. Hahn, *Nano Energy* **2018**, *47*, 51–65.

246 J. M. Fernández-García, P. J. Evans, S. Medina Rivero, I. Fernández, D. García-Fresnadillo, J. Perles, J. Casado, N. Martín, *J. Am. Chem. Soc.* **2018**, *140*, 17188–17196.

π-conjugated scaffolds with three-dimensional geometries.[247] (**Figure 67**) Four benzenes or thiophenes are *ortho*-annelated, forming a central eight-membered ring. Due to the different symmetry of the C_6 and the C_4S rings, CoPh exhibits a D_{2d} symmetry, whereas CoTh displays a chiral D_2 point group. Such non-planar structures are excellent building blocks for the preparation of more sophisticated functional π-conjugated materials with the incorporation of 4 units of hexabenzocoronene (HBC) fused to the central scaffolds.

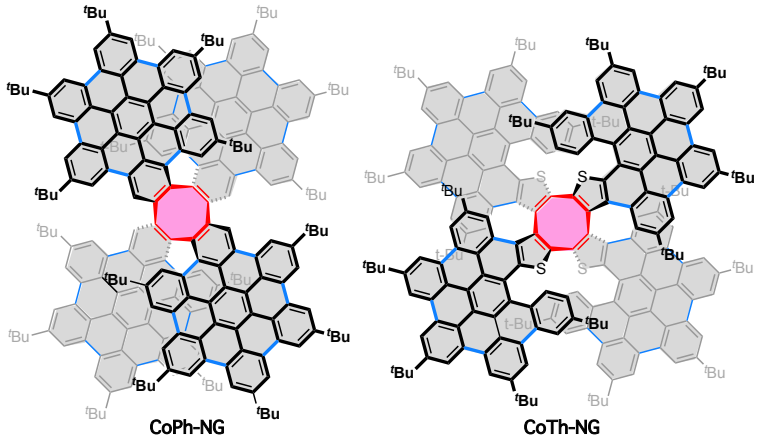

Figure 67. Chemical structure of nanographene-based **CoPh-NG** and **CoTh-NG**.

The synthesis of the tetraphenylene core (CoPh) was conducted following the previously reported procedure, as it is shown in **Scheme 10**.[248] Commercially available 4-methoxyphenylboronic acid and 2-bromo-5-methoxyaniline were subjected to a Suzuki cross-coupling reaction to form derivative **50** in excellent yield. Compound **50** was treated with sodium nitrite and potassium iodide to prepare the iodobiphenyl (**51**) through a Sandmeyer reaction. Derivative **51** underwent a homocoupling palladium-catalyzed direct arylation and cyclization to form the methoxy-substituted tetraphenylene core (CoPh) (**52**). The methyl groups of derivative **52** were cleavaged in the presence of boron tribromide (BBr_3) and subsequently treated with trifluoromethanesulfonic anhydride and

[247] J. Urieta-Mora, M. Krug, W. Alex, J. Perles, I. Fernández, A. Molina-Ontoria, D. M. Guldi, N. Martín, *J. Am. Chem. Soc.* **2020**, *142*, 4162–4172.

[248] C. Zhu, Y. Zhao, D. Wang, W.-Y. Sun, Z. Shi, *Sci. Rep.* **2016**, *6*, 33131.

pyridine gave rise to the formation of 2,7,10,15-tetrakis(trifluoromethanesulfonate)tetraphenylene (**54**) in moderate overall yield of 30% in five synthetic steps.

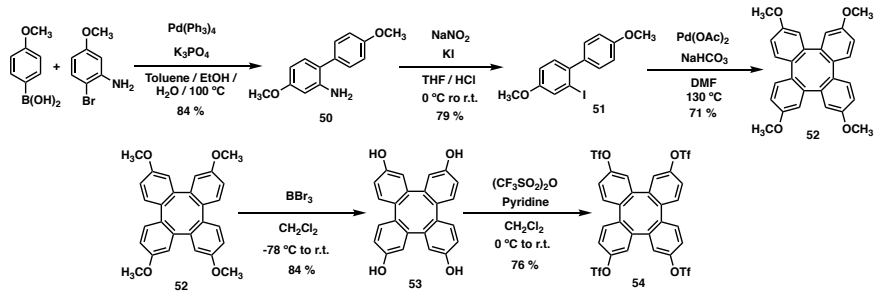

Scheme 10. Synthetic route for the preparation of CoPh core.

The syntheses of **CoPh-NG** and **CoTh-NG** were approached following a straightforward route, as illustrated in **Scheme 11**. The previously prepared 2,7,10,15-tetrakis(trifluoromethanesulfonate)tetraphenylene (**54**) was cross-coupled with 4-*tert*-butylphenylacetylene using a palladium-catalyzed Sonogashira reaction to afford compound **55**. Microwave-assisted [4+2] cycloaddition of **55** with 2,3,4,5-tetrakis(4-*tert*-butylphenyl)-2,4-cyclopentadien-1-one afforded the "open" nanographene derivative **56**, which, subsequently, underwent intramolecular cyclodehydrogenation mediated by $FeCl_3$ (i.e., Scholl reaction) to generate **57** in moderate yields. Oxidative cyclodehydrogenation at 0 °C generated only 23 new carbon-carbon bonds out of the expected 24 new carbon-carbon bonds. Therefore, we carried out the dehydrogenation reaction under harsh oxidative conditions, namely trifluoromethanesulfonic acid (TfOH) and 2,3-dichloro-5,6-dicyano-*p*-benzoquinone (DDQ), which eventually afforded again **57** in higher yields. Compound **57** was subjected to a further one-fold $FeCl_3$-mediated oxidative coupling in refluxing 1,2-dichloroethane to finally lead to **CoPh-NG**. However, gentle heating was needed to yield the complete fusion of all six-membered rings. Under such optimized reaction conditions, derivative **56** was also interconverted into the fully coupled **CoPh-NG**.

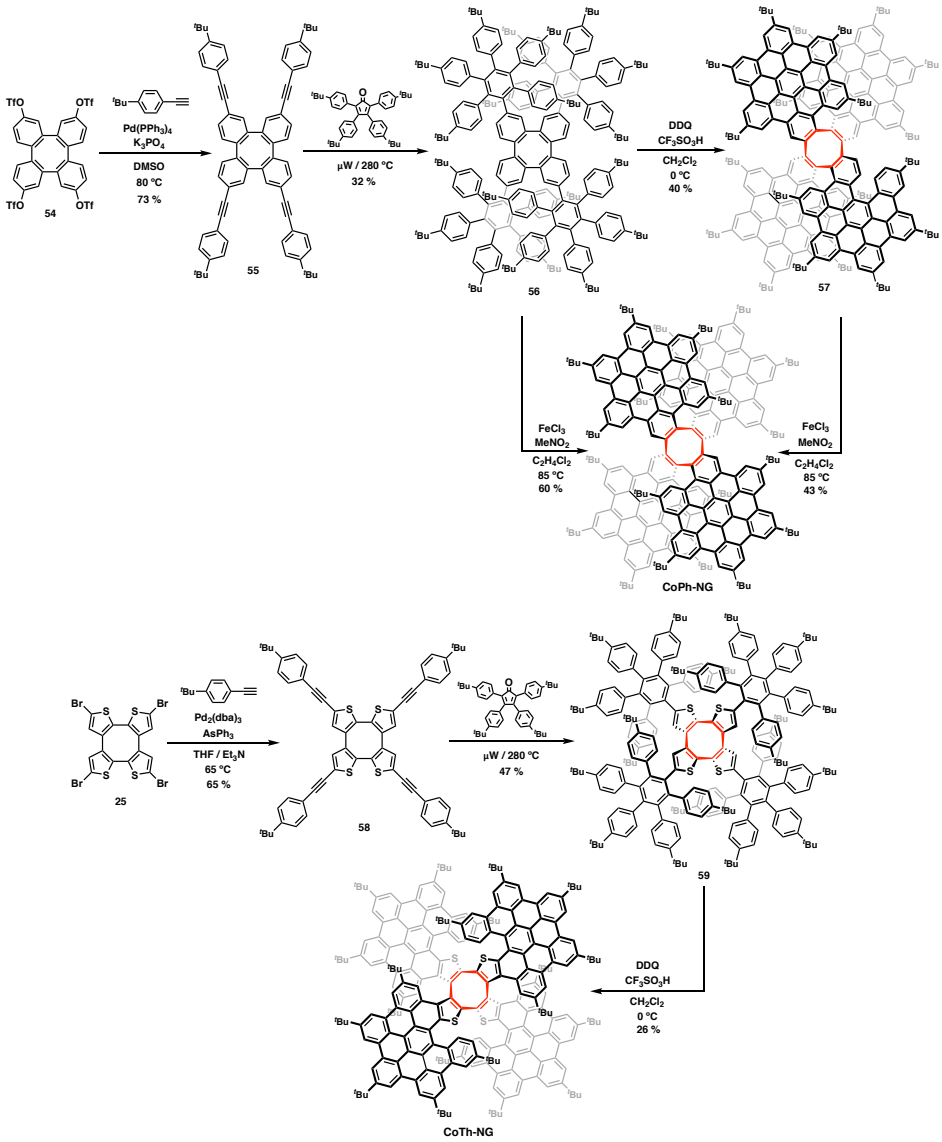

Scheme 11. Synthetic routes for the preparation of nanographenes **CoPh-NG** and **CoTh-NG**.

The conversion of **56** to form **57** and subsequently **CoPh-NG** was followed by ^{1}H NMR spectroscopy (**Figure 68**). As can be observed in the red ^{1}H NMR spectrum, the highly asymmetric structure of derivative **57** leads to a highly complex ^{1}H NMR spectrum with multiple signals for the aromatic protons and

19 different signals for the *tert*-butyl protons (see *Experimental Section*). Once the derivative **57** is fully converted into the more symmetrical **CoPh-NG** (blue line), the signals in the NMR spectrum are reduced to 8 differentiated signals for the aromatic protons and 5 signals for the *tert*-butyl groups.

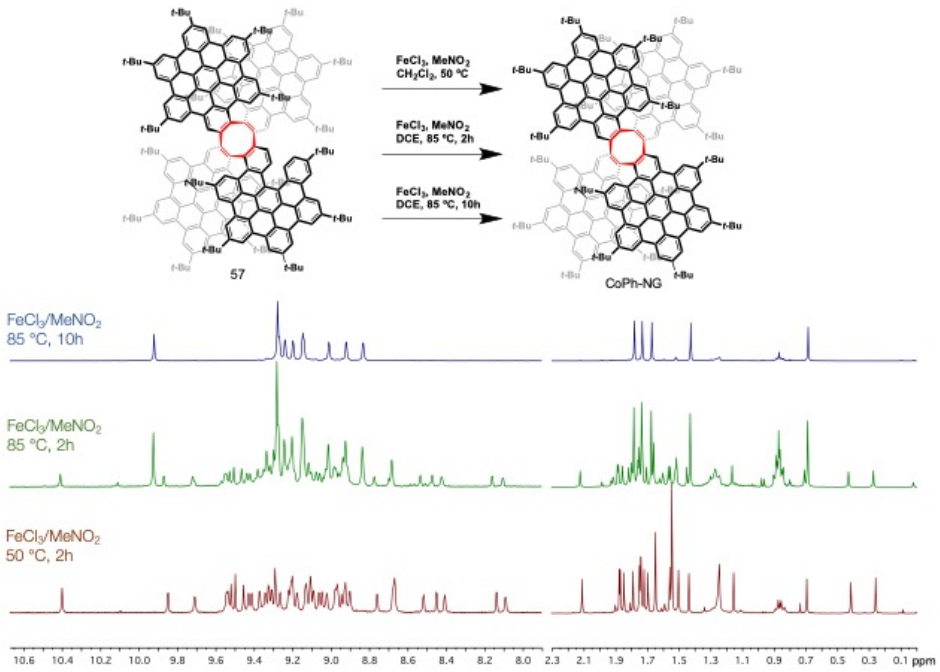

Figure 68. ^{1}H NMRs of the conversion of derivative **57** into **CoPh-NG**.

The synthetic strategy for the preparation of **CoTh-NG** started with the synthesis of 2,5,8,11-tetrabromocycloocta[1,2-*b*:4,3-*b*':5,6-*b*'':8,7-*b*''']tetrathiophene (**25**), which was prepared from 2,2'-dibromo[3,3']bithiophene by an oxidative coupling using $CuCl_2$, as it was explained in section 2.4.1. Compound **25** was subjected to a four-fold palladium-catalyzed Sonogashira reaction with 4-*tert*-butylphenylacetylene to form the intermediate **58**, which reacted under microwave-assisted [4+2] cycloaddition with 2,3,4,5-tetrakis(4-*tert*-butylphenyl)-2,4-cyclopentadiene-1-one to give rise to intermediate **59**. Finally, treating the "open" derivative **59** in the presence of $FeCl_3$ in nitromethane produced the corresponding fully cyclodehydrogenated **CoTh-NG** in moderate yield.

A complete structural characterization of **CoPh-NG**, **CoTh-NG** and the corresponding intermediates was carried out using standard spectroscopic techniques, namely ^{1}H NMR, ^{13}C NMR and FTIR (for more details, see the *Experimental Section*). High-resolution mass spectrometry (MALDI-TOF) confirmed the presence of **CoPh-NG** and **CoTh-NG** with the molecular ion peaks $[M]^{+}$ at m/z 3201.7474 (calcd. for $C_{248}H_{224}$ 3201.7523) and 3233.6390 (calcd. for $C_{240}H_{224}S_4$ 3233.6405), respectively.

5.4.2 Optical, electrochemical and structural characterization of non-planar nanographene-based materials.

The optical characteristics of **CoPh-NG** and **CoTh-NG** were investigated by means of steady-state absorption spectroscopy from CH_2Cl_2 solutions and compared to the reference compound of **HBC** (**Figure 69a**). The absorption spectrum of **HBC** possesses characteristic absorption maxima at 328, 343, 359, and 390 nm. The features at 343, 359, and 390 nm can be correlated to the vibrational fine structure of the symmetry allowed β-transitions,[249,250] and the feature at 328 nm corresponds to the p-bands. The absorption spectrum of **CoPh-NG** features an absorption maximum peaked at 370 nm with additional fine structure at 364, 398, and 407 nm. In general, the absorption spectrum of **CoPh-NG** appears significantly broadened relative to that measured for **HBC**, and the absorption maximum is bathochromically shifted by 11 nm. The extinction coefficients of **CoPh-NG** are less than four times the corresponding values of **HBC**. For example, a value of 4.03 x 10^5 L mol^{-1} cm^{-1} at 370 nm should be compared to 1.71 x 10^5 L mol^{-1} cm^{-1} at 359 nm. Overall, the spectral broadening may contribute to lower extinction coefficients. Attending to the absorption spectra of **CoTh-NG**, broad and overlapping absorption features are observed at 320, 340, 374, 384, 440, and 482 nm. The introduction of thiophenes further reduces the symmetry of the individual moieties, which renders the absorption around 440 nm symmetry allowed.

The fluorescence spectra from CH_2Cl_2 solutions of **CoPh-NG**, **CoTh-NG**, and **HBC** are shown in **Figure 69a** (dashed line). Fine structured HBC-centered

[249] G. Rouillé, M. Steglich, F. Huisken, T. Henning, K. Müllen, *J. Chem. Phys.* **2009**, *131*, 204311.

[250] R. Rieger, K. Müllen, *J. Phys. Org. Chem.* **2010**, *23*, 315–325.

fluorescence is noted for **CoPh-NG** with distinct maxima at 473, 482, 493, 502, 527, and 537 nm. In direct comparison to **HBC**, the fluorescence maxima are red-shifted by around 8 nm (485 nm) with additional distinct maxima at 465, 476, 491, 518, and 527 nm. Additionally, the relative intensity of the short-wavelength maximum is significantly enhanced, which is a manifestation of the reduced symmetry of the asymmetrically-substituted HBCs. Any noteworthy fine structure is lost in the fluorescence spectrum of **CoTh-NG**, and a broad fluorescence maximizing at 530 nm is obtained. The loss of the fine structured spectra is ascribed to the reduced rigidity and distortions within the molecular plane, as suggested by the crystal structures.

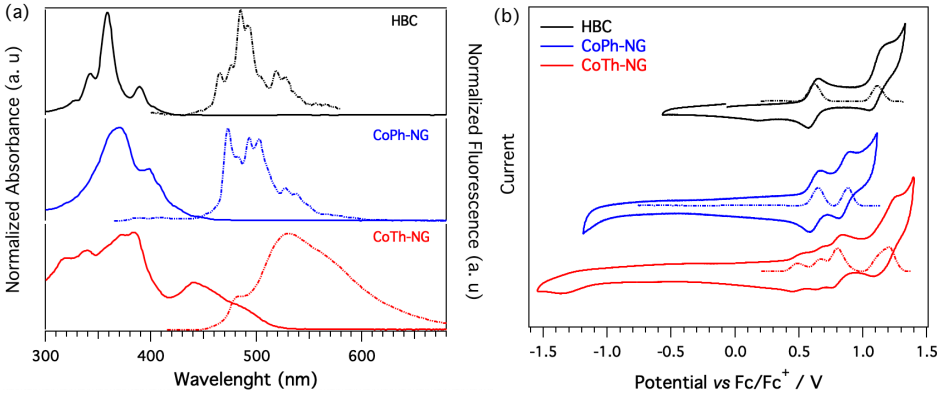

Figure 69. (a) UV-vis absorption spectra (solid line) and fluorescence emission (dashed line) of **CoPh-NG**, **CoTh-NG** and **HBC** recorded in CH_2Cl_2; (b) Cyclic voltammetry of **CoPh-NG**, **CoTh-NG** and **HBC** in CH_2Cl_2 containing 0.1 M $TBAPF_6$ at a scan rate of 100 mVs^{-1}.

The electrochemical properties of **CoPh-NG** and **CoTh-NG** were studied using cyclic voltammetry (CV) and differential pulse voltammetry (DPV), and compared to the most simple nanographene unit, **HBC**. 0.1 M solution of $TBAPF_6/CH_2Cl_2$ was used as supporting electrolyte and **CoPh-NG**, **CoTh-NG**, and **HBC** were measured at a scan rate of 100 mV s^{-1} (**Figure 69b**). The cyclic voltammogram of **CoPh-NG** shows two oxidation waves at +0.62 and +0.85 V *vs.* Fc/Fc^+. These oxidation steps are assigned to two sequential two-electron oxidations, in which a total of four electrons are extracted from the peripheral hexabenzocoronene units of **CoPh-NG** (**Table 22**). The cyclic voltammogram of **CoTh-NG** reveals up to five different oxidation processes where the first

oxidation wave was found cathodically shifted by 0.14 V relative to **CoPh-NG**. This clearly indicates the stronger electron-donating character of **CoTh-NG** due to the presence of the thiophene units. The first three reversible oxidations at +0.48, +0.66, and +0.79 V correspond to one-, one-, and two-electron processes, respectively, and are tentatively assigned to the sequential electron transfer from the thiophene-containing moiety to the peripheral HBC units. The estimated HOMO energies of **CoPh-NG**, **CoTh-NG**, and **HBC** are -5.72, -5.58, and -5.72 eV, respectively.

Table 22. Optical and electrochemical properties of **CoPh-NG**, **CoTh-NG**, and **HBC**.

HTM	$\lambda_{max,\ abs}$ [nm][a]	$\lambda_{max,\ em}$ [nm][a]	$E^{0\text{-}0}$ [eV][b]	$E^{ox}{}_{1/2}$ [V][c]	E_{HOMO} [eV][d]	E_{LUMO} [eV][e]
CoPh-NG	370	493	2.79	0.62	-5.72	-2.93
CoTh-NG	384	530	2.61	0.48	-5.58	-2.97
HBC	359	485	3.00	0.62	-5.72	-2.72

[a] λ_{max} of absorption and emission measured in CH_2Cl_2 solutions; [b] $E^{0\text{-}0}$ was determined at the intersection of normalized absorption and emission spectra; [c] Determined from CV measurements *vs* Fc/Fc^+; [d] E_{HOMO} is estimated in eV by E_{HOMO} = -5.10 eV - $E^{ox}{}_{1/2}$; [e] E_{LUMO} was estimated by $E_{LUMO} = E_{HOMO} + E^{0\text{-}0}$.

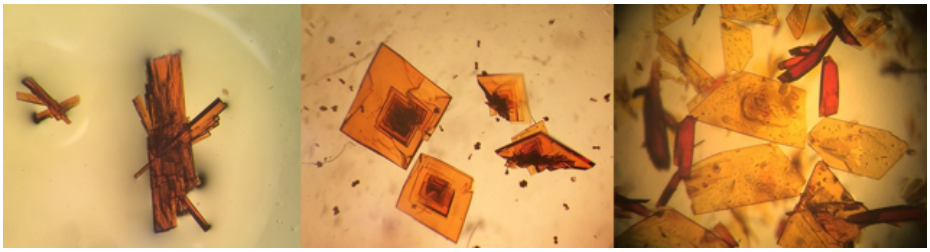

Figure 70. Aggregate of prismatic crystals of **57** (left), laminar crystals of **CoPh-NG** (middle), and both prismatic (2poly) and laminar (2plate) crystals of **CoTh-NG** (right).

A complete structural characterization was carried out using X-ray diffraction. The molecular conformation and crystal packing of **CoPh-NG**, **CoTh-NG**, and compound **57** were unequivocally determined by single crystal X-ray diffraction studies (**Figure 70**). Crystals were obtained by slow diffusion of acetonitrile into their 1,2-dichloroethane solutions. In all cases, the molecular NGs cocrystallize

with solvent molecules (dichloroethane), which display various degrees of disorder. The isolated crystals of **57** (**Figure 70** left) appear as aggregates of orange polyhedra. The crystal structure of **57** was assigned to triclinic *P*-1 space group, with a whole molecule in the asymmetric unit, as depicted in **Figure 71**. The planarity of the four hexabenzocoronene units around the central CoPh ring was quantified by the dihedral angles between the central ring and the peripheral scaffolds. The three hexabenzocoronene fragments in compound **57**, with values ranging from 1.02° to 18.96° are more planar than the fourth fragment of the partially "open" unit (16.26° to 27.56°) as should be expected. The molecular packing of **57** is based on CH-π interactions, as the bulky peripheral tert-butyl (^{t}Bu) substituents prevent the formation of π-π interactions.

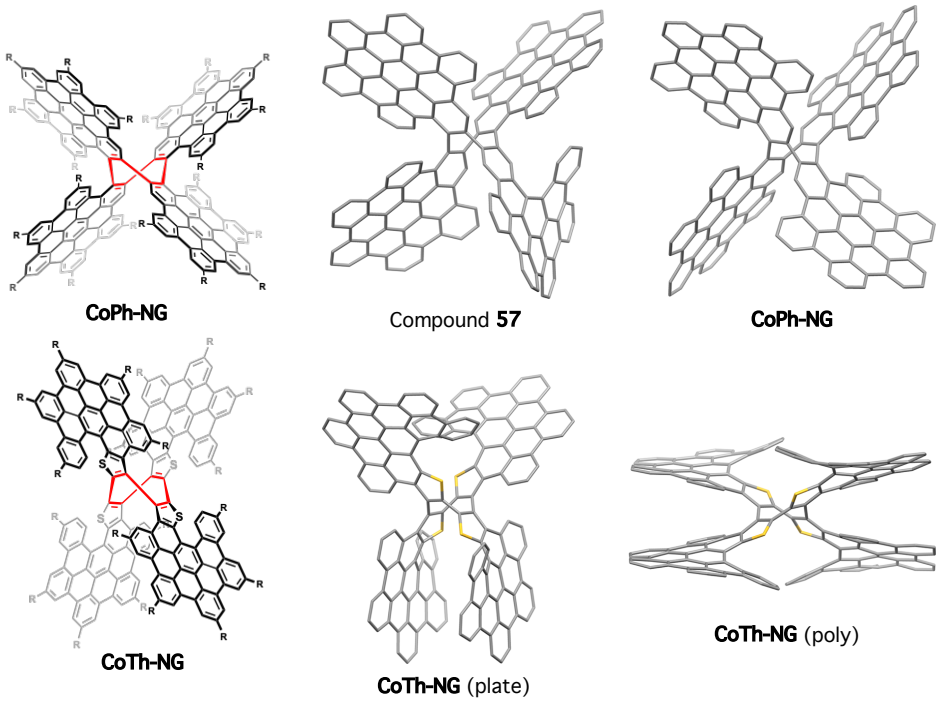

Figure 71. Chemical structures of CoPh-NG and CoTh-NG and their corresponding resolved crystal structures.

Crystals of **CoPh-NG** adopted a laminar morphology (**Figure 70** middle), and the resulting structure is illustrated in **Figure 71**. **CoPh-NG** crystallizes in an orthorhombic *Pnna* space group with half a molecule in the asymmetric unit. Regarding the planarity of the two crystallographically independent arms, two

different hexabenzocoronene fragments are observed, with torsion angles in the range from 7.96° to 16.22° which is considerably less planar than the other one (with values ranging from 3.43° to 10.58°). It is interesting to note that although the CoPh saddle-shaped motif is not chiral, **CoPh-NG** is chiral due to the disposition of the phenyl rings in the HBC arms around the central 8-membered ring. The arrangement of the HBC arms lowers the initial point symmetry to the resulting chiral D_2 point group as they fail to relate to the mirror planes in D_{2d}. Crystals obtained from the racemic mixture are, however, not enantiopure and contain both isomers in a 50:50 ratio. Nevertheless, the different enantiomers of **CoPh-NG** were isolated using chiral high-performance liquid chromatography (HPLC) using a Whelk-O1 (R,R) 5/100 (25 x 1 cm) column with a mixture of *n*-hexane, 2-propanol, and methanol (89/19/1 v/v) as eluent. The optically pure enantiomers of **CoPh-NG** featured a perfect mirror-image circular dichroism (CD) with their corresponding positive and negative Cotton effect at 368 and a shoulder at 353 nm (**Figure 72**).

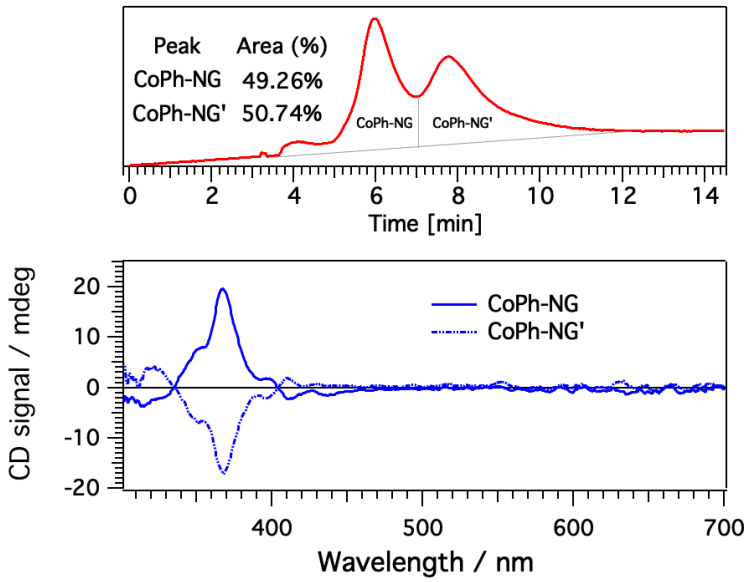

Figure 72. HPLC chromatogram of racemic mixture **CoPh-NG** recorded at 380 nm (eluent, *n*-hexane/2-propanol/methanol, 89/10/1, v/v) and CD spectra for both enantiomers of **CoPh-NG** in CH_2Cl_2.

Furthermore, the molecular packing in the case of **CoPh-NG** is governed by CH-π interactions established by the ^{t}Bu substituents, and π-π interactions were not

observed as it was noted in compound **57**. Indeed, the DFT gas-phase optimized structure of a model compound of **CoPh-NG**, where the bulky ^{t}Bu groups were replaced by methyl groups, confirms the presence of π-π stacking between the HBC arms, which further supports the crucial role of ^{t}Bu groups in preventing close π-π interactions.

On the other hand, two different crystal types were found for **CoTh-NG**: yellow plates and dark orange polyhedra (poly) (**Figure 70** right). Both were isolated and their crystal structures were solved by SCXRD (**Figure 71**). The polyhedra were extremely difficult to handle, because it lost crystallinity rapidly as soon as they were removed from the mother liquors. Crystals of **CoTh-NG**-plate and **CoTh-NG**-poly crystallize in the triclinic *P*-1 space group, with an entire molecule in the asymmetric unit. **CoTh-NG** cocrystallizes with solvent molecules (1,2- dichloroethane or acetonitrile). However, the angles between the hexabenzocoronene arms were found very different in each crystal. While **CoTh-NG**-poly displays a more horizontal disposition of the four arms of the central CoTh, in **CoTh-NG**-plate the substituents are placed in pairs with a V shape, rendering a double helicene-type structure for each side of the molecule. In **CoTh-NG**-poly, similar interactions were observed between two HBC arms and 1,2-dichloroethane, although the solvent was held between the arms of two neighboring **CoTh-NG** molecules. Regarding the planarity of the arms, they display similar torsion angles for most of the rings with maxima of 30.26°, 29.05°, 26.92°, and 30.38° for **CoTh-NG**-plate and 28.35°, 30.02°, 28.68°, and 27.27° for **CoTh-NG**-poly. As mentioned in the crystal structures of **CoPh-NG**, the bulky peripheral ^{t}Bu substituents prevent π-π stacking. The molecular packing in **CoTh-NG**-plate and **CoTh-NG**-poly was driven by CH-π interactions, mostly involving 1,2-dichloroethane in the interstices. **CoTh-NG** is chiral, like the core fragment CoTh, but crystals of **CoTh-NG**-plate and **CoTh-NG**-poly are both in a racemic mixture.

The structure of **CoTh-NG** was further analyzed by means of DFT calculations at the B3LYP-D3/def2-SVP level (**Figure 73**). DFT calculations on models of **CoTh-NG**-plate and **CoTh-NG**-poly, where the bulky ^{t}Bu groups were once again replaced by methyl groups, indicate that both of them are nearly degenerate in the gas-phase with $\Delta E \sim 1$ kcal/mol. This is fully consistent with the presence of both isomers in the solid-state. In both cases, the sulfur atoms of CoTh are

placed far from each other to minimize electronic repulsions between their corresponding lone-pairs. In addition, this particular arrangement enables the occurrence of stabilizing intramolecular n-π non-covalent interactions between the lone-pairs of each sulfur and the adjacent aryl groups of the hexabenzocoronene arms.

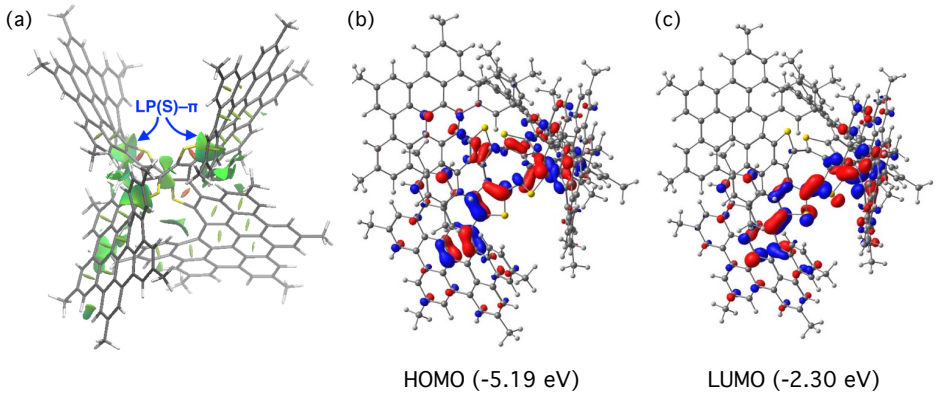

Figure 73. (a) Contour plots of the reduced density gradient isosurfaces for **CoTh-NG-poly** (the green surfaces indicate attractive non-covalent interactions); (b) and (c) Computed molecular orbitals involved in the π-π* transitions for **CoTh-NG** (isosurface value of 0.05 au) computed at the B3LYP-D3/def2-SVP level.

Time-dependent (TD) calculations at the PCM-TD-B3LYP-D3/def2-SVP//B3LYP-D3/def2-SVP level were carried out on **CoTh-NG**. The observed red-shifted broad band of absorption at 482 nm in **CoTh-NG** is ascribed to the involvement of the thiophene moieties. The calculations gave vertical excitation energies at 501 nm, which is in good agreement with the observed experimental value of 482 nm. The vertical transition is mainly associated with the promotion of one electron from the HOMO to the LUMO (**Figure 73b-c**). The HOMO should be viewed as a π-molecular orbital, which is not only located on the hexabenzocoronene arms but also involves the π-system of the four thiophene constituting the CoTh core. Similarly, the LUMO is a fully delocalized π*-molecular orbital which, therefore, confirms the π-π* nature of the red-shifted absorption at 482 nm.

5.4.3 Hole-transporting ability of the molecular nanographene derivatives.

Unfortunately, the new **CoPh-NG** and **CoTh-NG** have not been tested yet for hole-transporting applications. In particular the use of the nanographene-based **CoPh-NG** and **CoTh-NG** materials in PSCs should be approached using non-conventional light absorbing materials due to the low-lying HOMO energies calculated for both molecular NGs (-5.72 and -5.58 eV for **CoPh-NG** and **CoTh-NG** respectively). Hence, perovskite materials such as $MAPbBr_3$ (-5.70 eV),[251] $CsPbBr_3$ (-5.97 eV),[59] $FASnI_3$ (-5.96 eV)[252] or $MA_3Bi_2I_9$ (-5.90 eV)[253] that exhibit an appropriate valence band edge are good candidates for testing molecular NGs as innovative HTMs (**Figure 74**).

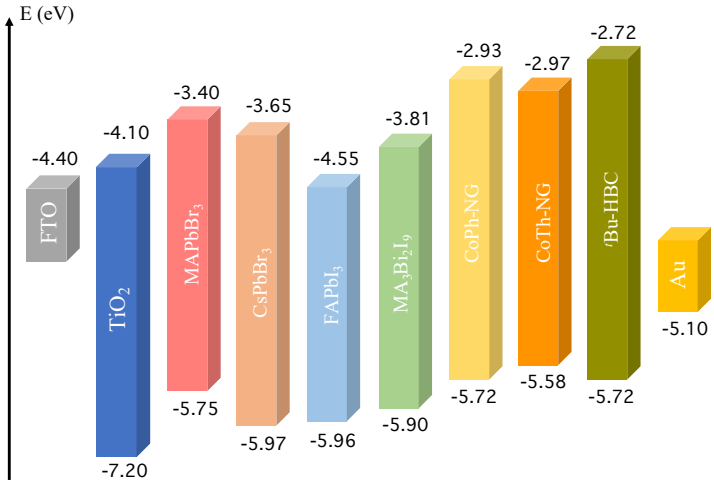

Figure 74. Schematic energy diagram of the different perovskite material with an appropriate valence band edge for nanographene-based molecule.

[251] S. Adjokatse, H.-H. Fang, M. A. Loi, *Mater. Today* **2017**, *20*, 413–424.

[252] T. M. Koh, T. Krishnamoorthy, N. Yantara, C. Shi, W. L. Leong, P. P. Boix, A. C. Grimsdale, S. G. Mhaisalkar, N. Mathews, *J. Mater. Chem. A* **2015**, *3*, 14996–15000.

[253] M. Kong, H. Hu, L. Wan, M. Chen, Y. Gan, J. Wang, F. Chen, B. Dong, D. Eder, S. Wang, *RSC Adv.* **2017**, *7*, 35549–35557.

Conclusions

6. CONCLUSIONS

With the aim of designing new highly efficient HTMs for PSCs, along this thesis different small organic molecules have been synthesized, characterized, and tested in fabricated PSCs devices. Although a clear relationship between the chemical structure of HTMs and its photovoltaic performance has not been clearly established yet, some general remarks could be proposed. Firstly, as it has been explained in the *Results and discussion* section, some requirements for the design of new HTMs must be satisfied. In this regard, an appropriate HOMO energy to ensure an efficient charge transfer of the photogenerated hole from the perovskite to the HTM, a good thermal stability or relatively high values of hole mobility and/or conductivity should be fulfilled. Nevertheless, additional requirements have been observed for achieving high values of efficiency.

One of these additional requirements is the solubility of the HTMs in common solvents for device preparation such as chlorobenzene, 1,2-dichloroethane, or *ortho*-dichlorobenzene. A chemical design that ensures, at least, a moderate solubility of the HTMs was determined as an essential point for the formation of smooth and homogeneous films of the HTMs on top of the perovskite layer. However, it should be noted that a compromise between the solubility and the electronic properties of the HTMs should be reached, as it is beautifully exemplified in the case of the ATT derivatives. As it was explained in the first section, the use of planar π-conjugated scaffolds such as ATT, DBQT, or DBST favors the π-π stacking of the molecules that leads to efficient charge transport. Furthermore, in these sulfur-rich systems, the S···S interactions promote the control of the molecular packing. Due to the low solubility of **ATT-OMe** derivative, different derivatives with increasing alkyl chain length (butyl, hexyl, and decyl) were synthesized. The photovoltaic result showed a sequential adverse effect on the electronic properties of the HTMs (conductivity and charge transfers ability) going from **ATT-OMe** to **ATT-ODec**. Thus, the increasing length of the alkyl chain hinders the molecular interactions and the molecular packing which negatively affect its photovoltaic performance. In contrast, the limited solubility of **DBST-OMe** due to its highly planar structure avoids the preparation of thick enough layers. As a result, the formation of pinholes reduced the performance of the devices. In conclusion, a compromise between the extended molecular structure and its optoelectronic properties and the solubility

must be taken into account. Attaching longer alkyl chains can be envisioned as a complementary strategy to overcome this drawback, but it may affect other properties such as conductivity. Finally, promoting the intermolecular packing through π-π stacking and S···S interactions in sulfur-rich π-conjugated systems as central scaffolds serves as a powerful paradigm for the design of more efficient HTMs

On the other hand, the design of the non-planar and sulfur-rich **CoTh-OMe** with increased processability was conducted using a saddle-shaped cyclooctatetrathiophene (CoTh). Despite its increased solubility derived from its non-planar structure, the saddle-like structure breaks the π-conjugation across the polycyclic core, affecting its electronic properties. The resulting lower performance of **CoTh-OMe** was ascribed to its higher reorganization energy, according to theoretical calculations, the lower lateral conductivity, and its poorer hole extraction ability derived from the PL measurements.

Attending to the incorporation of selenium-containing scaffolds, such as benzotriselenophene (BTSe), presented a positive effect in comparison to the isostructural nitrogen, oxygen, and sulfur-based derivatives, displaying the highest PCE (18.5%) even higher than that measured for the benchmark spiro-OMeTAD. Despite the lower conductivity measured for **BTSe-OMe**, the higher efficiency measured for this derivative, demonstrated that different characteristics such as solubility, hole mobility, or morphology should be taken into account, reaching a compromise between all of them. In the case of **BTSe-OMe**, the larger size of selenium atoms is surmised to passivate the perovskite layer more effectively, thus improving the hole extraction and, therefore, the photovoltaic performance.

The syntheses and photovoltaic application of spiro-based and “spiro-like” HTMs presented different results. On the one hand, phenoxazine and phenothiazine-based HTMs (**spiro-POZ-OMe** and **spiro-PTZ-OMe**) exhibited similar optoelectronic properties than spiro-OMeTAD. Interestingly, mesoporous devices achieved reduced PCEs of 16.67% and 17.28%, respectively, while the incorporation of these HTMs into planar n-i-p devices improved the efficiency up to 18.14 and 18.36% in the case of **spiro-POZ-OMe** and **spiro-PTZ-OMe**, respectively. On the other hand, bisxanthene (**BX-OMe**) and bisthioxanthene-based (**BTX-OMe**) HTMs exhibiting a more flexible

structure in comparison to rigid spiro-containing molecules presented reduced values of PCE (14.19 and 16.55%, respectively). The low conductivity of the HTMs is most likely the reason for the low *FF* obtained for their devices, resulting in high series resistance. Nevertheless, the presence of a more flexible C-C bond connecting the two halves of the HTM core triggers a strong impact on the geometrical and electronic properties and, thereby, on the efficiency of the fabricated PSC devices.

The chemical design using triazatruxene (TAT) as donor units in the preparation of DTTX molecules has been successfully introduced as a new alternative for tuning the electronic properties of the HTMs, and to ensure an efficient hole transfer with the perovskite material. **DTTX-1** and mainly, **DTTX-2** reached values of PCE similar to that measured for the reference of spiro-OMeTAD. In contrast, the presence of the azomethine bond in **DTTX-3** affected negatively to the photovoltaic performance. These results arise mainly from the low *FF* obtained due to the high series resistance (R_s) and low shunt resistance (R_{sh}), which is attributed to enhanced interfacial charge recombination. Lateral conductivity and hole mobility measurements confirmed the potential of **DTTX-1** and **DTTX-2** as alternatives of the benchmark spiro-OMeTAD.

Finally, two molecular nanographenes (**CoPh-NG** and **CoTh-NG**) were synthesized and characterized following a well-stablished approach in three-synthetic steps from their corresponding saddle-shaped cores. From their crystal structure analysis, it was concluded that both molecular NGs are chiral and crystallize as a racemic mixture, which were separated using chiral HPLC in the case of **CoPh-NG**. The hydrocarbon-based structure of **CoPh-NG** and **CoTh-NG** resulted in a low-lying HOMO energy due to the lack of donor groups in the chemical structure. As a result, the low-lying HOMO energy level of these nanographenes does not allow their use as HTMs using conventional perovskites. Therefore, these new derivatives could be tested with non-conventional perovskite materials with deeper valence band energies, such as $CsPbBr_3$ or $FASnI_3$ to assure an efficient hole extraction. Alternatively, a different optoelectronic application, such as organic light emitting diodes (OLEDs) has also been considered for the preparation of functional devices employing these disruptive molecular NGs.

Finally, as a general remark, the present thesis is not focused on a commercial perspective. Although some of the HTMs that have been synthesized have the potential to compete with the reference molecule of spiro-OMeTAD in terms of efficiency/commercial price ratio. In this regard, it is worth highlighting, for example, the **ATT-OMe** or **DBQT-OMe** derivatives that show photovoltaic performances that are comparable to spiro-OMeTAD but with considerably lower estimated production costs (around 38 and 53 €/g respectively in comparison to spiro-OMeTAD or PTAA (> 300 €/g)). In particular, the ATT core, as mentioned above, can be synthesized with an overall yield of 75% without purification steps, allowing its possible application in low-cost technologies. Furthermore, these derivatives did not require additional purification steps such as sublimation, which is a crucial requirement in the case of spiro-OMeTAD.

Experimental Section

7. EXPERIMENTAL SECTION

General Methods. Chemicals and reagents were purchased from commercial suppliers and used as received. All solvents were dried according to standard procedures. Air-sensitive reactions were carried out under nitrogen or argon atmosphere. Flash chromatography was performed using silica gel (Merck, Kieselgel 60, 230-240 mesh or Scharlab 60, 230-240 mesh). Analytical thin layer chromatography (TLC) was performed using aluminum-coated Merck Kieselgel 60 F254 plates. NMR spectra were recorded on a Bruker Advance 300 (^{1}H: 400 MHz; ^{13}C: 101 MHz) spectrometer at 298 K using partially deuterated solvents as internal standards. Coupling constants (*J*) are denoted in Hz and chemical shifts (δ) in ppm. Multiplicities are denoted as follows: s = singlet, d = doublet, dd = doublet of doublets, t = triplet, m = multiplet. FT-IR spectra were recorded on a Bruker Tensor 27 (ATR device) spectrometer. UV-Vis spectra were recorded in a Varian Cary 50 spectrophotometer. Mass spectra Matrix assisted Laser desorption ionization (coupled to a Time-of-Flight analyzer) experiments (MALDI-TOF) were recorded on a MAT 95 thermo spectrometer and a Bruker REFLEX spectrometer respectively. Cyclic voltammetry (CV) experiments were conducted in 0.1 M solution of NBu_4PF_6 (TBAPF) in CH_2Cl_2. Glassy carbon electrode was used as a working electrode and platinum wires were used as counter and reference electrodes. Before each measurement, solutions were deoxygenated with N_2. Ferrocene was added as an internal standard; its oxidation potential in CH_2Cl_2 was positioned at 0.7 V *vs* NHE and HTMs' oxidation potentials were recalculated in reference to NHE. Thermogravimetric analysis (TGA) was performed using a TA Instruments (TGAQ500) with a ramp of 10 °C/min under N_2 from 100 to 1000 °C. DSC was run on a Discovery DSC from TA instruments. Three cycles were recorded under nitrogen, heating (until 400 °C) and cooling (50 °C) at 20 °C/min of scanning rate.

Devices fabrication

Mixed cation perovskite $[FAPbI_3]_{0.85}[MAPbBr_3]_{0.15}$-based mesoporous devices. Conductive FTO glass (NSG10) was subjected to an etching treatment using Zn dust and HCl (3M) and then, sequentially cleaned by sonication in a 2% Helmanex solution, water and isopropanol for 15 min respectively. Before using, the FTO was cleaned by UVO for 15 min A 30 nm titania (TiO_2) blocking layer

was applied on the substrates by spraying a solution of titanium diisopropoxide bis(acetylacetonate) in ethanol at 450 °C. For the 200-300 nm mesoporous TiO_2 layer, 30 NR-D titania paste from Dyesol diluted in ethanol (ratio 1:8 by weight) was applied by spin-coating at 3000 rpm for 15 s followed by a sintering step at 500 °C for 20 min. After cooling down the substrates a Li-treatment was applied by spin-coating 60 µl of a solution of tris(bis(trifluoromethylsulfonyl)imide) (Li-TFSI) in acetonitrile (10 mg/ml) onto the mesoporous layer, followed by a sintering step at 500 °C for 10 min to decompose the Li-salt as previously described.[212] The perovskite layers were fabricated by a single step spin-coating procedure reported by Seok and co-workers.[254] For the perovskite precursor solution, 508 mg of PbI_2 (TCI), 68 mg of $PbBr_2$ (TCI), 180.5 mg of formamidinium iodide (FAI) (Dyesol) and 20.7 mg of methylammonium bromide (MABr) (Dyesol) were dissolved in a 1:4 mixture of DMSO:DMF. The perovskite solution was spun at 5000 rpm for 30 s using a ramp of 3000 rpm s^{-1}. 15 s prior to the end of the spin-coating sequence 100 µl chlorobenzene were poured onto the spinning substrate. Afterwards the substrates were transferred onto a heating plate and annealed at 100 °C for 45 min. The hole-transporting materials were applied from solutions in chlorobenzene. Tert-butylpyridine (TBP), Tris(2-(1H-pyrazol-1-yl)-4-tert-butylpyridine)cobalt (III) (FK-209) and Li-TFSI were added as additives. Equimolar amounts of additives were added for all hole-transporters: 330 mol % TBP, 50 mol % Li-TFSI from a 1.8 M stock solution in acetonitrile and 3 mol % FK-209 from a 0.25 M stock solution in acetonitrile. The final HTM solutions were spin-coated dynamically onto the perovskite layers at 5000 rpm for 20 s. The gold electrodes were deposited by thermal evaporation of 80 nm gold using a shadow mask under high vacuum conditions.

Triple cation perovskite $[(FAPbI_3)_{0.87}(MAPbBr_3)_{0.13}]_{0.92}[CsPbI_3]_{0.08}$-based mesoporous devices. FTO preparation, compact and mesoporous layers of TiO_2 were prepared following the same procedures described for the mixed cation perovskite. In the case of triple cation perovskite, Li-treatment was replaced by a SnO_2 layer applied by spin-coating at 3000 rpm for 30 s.[30] The perovskite was prepared by the solution of 178.94 mg of formamidinium iodide (FAI) (Dyesol), 17.41 mg of methylammonium bromide (MABr) (Dyesol), 57.06 mg of $PbBr_2$

[254] N. J. Jeon, J. H. Noh, Y. C. Kim, W. S. Yang, S. Ryu, S. Il Seok, *Nat. Mater.* **2014**, *13*, 897.

(TCI), 27.02 mg of CsI and 548.60 mg of PbI_2 (TCI) in a 1:3.5 mixture of DMSO:DMF. The perovskite solution was spun at 5000 rpm for 30 s using a ramp of 2000 rpm s^{-1}. 15 s prior to the end of the spin-coating sequence 100 µl chlorobenzene were poured onto the spinning substrate as antisolvent. The substrates were annealed at 100 °C for 1 h. The hole-transporting materials were applied from solutions in chlorobenzene in doped conditions with Tert-butylpyridine (TBP), tris(2-(1H-pyrazol-1-yl)-4-tert-butylpyridine)cobalt (III) (FK-209) and Li-TFSI as additives. Equimolar amounts of additives were added for all hole transporters: 330 mol % TBP, 50 mol % Li-TFSI from a 1.8 M stock solution in acetonitrile and 6 mol % FK-209 from a 0.25 M stock solution in acetonitrile. The final HTM solutions were spin-coated onto the perovskite layers at 4000 rpm for 30 s. The gold electrodes were deposited by thermal evaporation of 80 nm gold using a shadow mask under high vacuum conditions.

Triple cation perovskite $[(FAPbI_3)_{0.87}(MAPbBr_3)_{0.13}]_{0.92}[CsPbI_3]_{0.08}$-based planar devices. Conductive ITO glass was subjected to an etching treatment using Zn dust and HCl (3M) and then, sequentially cleaned with detergent, deionized water and isopropanol. Before using, the ITO was cleaned by UVO for 15 min. Then, the substrate was spin coated with a thin layer of SnO_2 from a precursor solution in water (2.67%) at 4000 rpm for 30 s, and annealed in ambient air at 150 ºC for 30 min and then cleaned by UVO again for 15 min.[255] The perovskite was prepared by the solution of 178.94 mg of formamidinium iodide (FAI) (Dyesol), 17.41 mg of methylammonium bromide (MABr) (Dyesol), 57.06 mg of $PbBr_2$ (TCI), 27.02 mg of CsI and 548.60 mg of PbI_2 (TCI) in a 1:3.5 mixture of DMSO:DMF. The perovskite solution was spun at 5000 rpm for 30 s using a ramp of 2000 rpm s^{-1}. 15 s prior to the end of the spin-coating sequence 100 µl chlorobenzene were poured onto the spinning substrate as antisolvent. The substrates were annealed at 100 °C for 1 h. The hole-transporting materials were applied from solutions in chlorobenzene in doped conditions with Tert-butylpyridine (TBP), tris(2-(1H-pyrazol-1-yl)-4-tert-butylpyridine)cobalt (III) (FK-209) and Li-TFSI as additives. Equimolar amounts of additives were added for all hole transporters: 330 mol % TBP, 50

[255] Q. Jiang, Z. Chu, P. Wang, X. Yang, H. Liu, Y. Wang, Z. Yin, J. Wu, X. Zhang, J. You, *Adv. Mater.* **2017**, *29*, 1703852.

mol % Li-TFSI from a 1.8 M stock solution in acetonitrile and 6 mol % FK-209 from a 0.25 M stock solution in acetonitrile. The final HTM solutions were spin-coated onto the perovskite layers at 4000 rpm for 30 s. The gold electrodes were deposited by thermal evaporation of 80 nm gold using a shadow mask under high vacuum conditions.

Solar cells characterization. High resolution cross-section images of the devices were recorded with a ZEISS Merlin HR-SEM scanning electron microscope. The photovoltaic device performances were evaluated using a VeraSol LED solar simulator (Newport) producing 1 sun AM 1.5 G (100 W cm^{-2}) simulated sunlight. Current density-voltage curves (*J-V*) were measured in air with a potentiostat (Keithley). The light intensity was calibrated with an NREL certified KG5 filtered Si reference diode. The solar cells were masked with a metal aperture of 0.16 cm^2 to define the active area. The current-voltage curves were recorded scanning at 10 or 20 mV s^{-1}. External quantum efficiency (EQE) measurements were performed with an IQE-200B Quantum Efficiency Measurement system from Newport in the range of 350 to 850 nm using a step size of 10 nm.

Lateral conductivity measurements. The different HTMs were spin-coated from their corresponding solutions in chlorobenzene (at the optimized concentration founded for each one) onto substrates having interdigitated gold electrodes with a channel length of 2.5 μm. The same molar concentration as for the device preparation was used and the optimized % of FK-209 were added as dopant. Current-voltage curves (*J-V*) were recorded in the range from -10 to +10 V and the corresponding conductivity values were calculated using Ohms law.

Computational Details. Quantum-chemical calculations were carried out with the Gaussian 16 (revision A.03) software package. All the calculations were performed within the density functional theory (DFT) framework using the B3LYP functional and the 6-31G** basis set. Solvent effects were considered within the self-consistent reaction field (SCRF) theory by using the polarized continuum model (PCM) approach. Vertical electronic transition energies to the lowest-energy singlet excited states of the corresponding HTMs were computed by using the time-dependent DFT (TDDFT) approach. The lowest 30 singlet excited states were calculated at the B3LYP/6-31G** level using the ground-state optimized geometries. Geometry optimizations in gas phase of the radical

cations of each HTMs, their corresponding cores and spiro-OMeTAD were also performed to evaluate the reorganization energy. The intramolecular reorganization energy (λ) consists of two terms related to the geometry relaxation energies of one molecule going from the fully relaxed ground state of the neutral species to the cation state and a neighbouring molecule evolving in the opposite way. For the electrochemical properties, radical cations are treated as open-shell systems and computed within the spin-unrestricted DFT approximation at the UB3LYP/6-31G** level in the presence of CH_2Cl_2. Additionally, dication, trication and tetracation species were also computed in CH_2Cl_2. Molecular orbitals were plotted using the Chemcraft 1.6 software with isovalue contours of ± 0.03 a.u.

7.1 Synthesis of anthra[1,2-*b*:4,3-*b′*:5,6-*b″*:8,7-*b‴*]tetrathiophene (ATT) derivatives

2-[2,4,5-Tris(2-thienyl)phenyl]thiophene[208] (1)

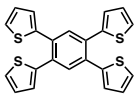

This compound was synthesized according to reported procedure [*Chem. Mater.* **2008**, *20*, 2484-2494] and showed identical spectroscopic properties to those reported therein. ^{1}H NMR (400 MHz, $CDCl_3$, 298 K) δ/ppm: 7.66 (2H, s), 7.30 (4H, dd, J_1 = 1.5 Hz, J_2 = 3.3 Hz), 6.98 (8H, m).

2-Bromo-5-[2,4,5-tris(5-bromo-2-thienyl)phenyl]thiophene[208] (2)

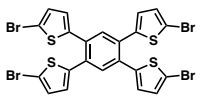

This compound was synthesized according to reported procedure [*Chem. Mater.* **2008**, *20*, 2484-2494] and showed identical spectroscopic properties to those reported therein. ^{1}H NMR (400 MHz, $CDCl_3$, 298 K) δ/ppm: 7.50 (2H, s), 6.97 (4H, d, J = 3.6 Hz), 6.73 (4H, d, J = 3.8 Hz).

2,5,9,12-Tetrabromotrithieno[2′,3′:5,6:3′,2′:3,4:3′,2′:7,8]anthra[1,2-*b*]thiophene[208] **(3)**

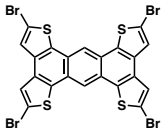

This compound was synthesized according to reported procedure [*Chem. Mater.* **2008**, *20*, 2484-2494] and was used without further purification. Given the low solubility of this compound, ^{1}H NMR and ^{13}C NMR were not possible; Mp > 350 ºC (dec); MALDI calcd for $C_{22}H_6Br_4S_4$ $[M]^+$, 718.15; found 718.09.

ATT-OMe[209]

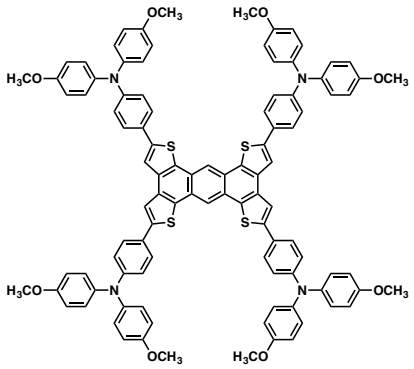

A solution of **3** (250 mg, 0.35 mmol), 4-(4,4,5,5-tetramethyl-1,3,2-dioxaborolan-2-yl)-*N*,*N*-bis(4-methoxyphenyl)aniline (**12**) (675.7 mg, 1.56 mmol), K_3PO_4 (1.78 g, 8.4 mmol) and $Pd(PPh_3)_4$ (80.9 mg, 0.07 mmol) in DMF (8 mL) was degassed for 30 minutes under nitrogen. The reaction was heated at 100 °C for 4 hours. The mixture was cooled to room temperature and water was added. The resulting precipitate was filtered and washed with water and dissolved in hot chloroform. The organic phase was dried over sodium sulfate. The solvent was removed under reduced pressure and the crude product was purified by flash column chromatography (silica gel, CH_2Cl_2 and then CH_2Cl_2:AcOEt (120:1)) to afford **ATT-OMe** as an orange solid (395 mg, 0.25 mmol), yield 72%. ^{1}H NMR (400 MHz, THF-d_8) δ/ppm: 8.67 (s, 2H), 7.99 (s, 4H), 7.70 (d, J = 8.7 Hz, 8H), 7.15-7.11 (m, 16H), 7.01 (d, J = 8.7Hz, 8H), 6.94-6.90 (m, 16H), 3.82 (s, 24H); ^{13}C NMR (101 MHz, $CDCl_3$) δ/ppm: 156.5, 148.9, 144.3, 140.4, 134.6, 133.1, 126.7, 126.5, 125.1, 119.9, 117.38, 114.6, 54.6; FTIR (neat): 2996, 2927, 1603, 1501, 1320, 1276, 1034, 820 cm^{-1}; Mp > 400 ºC (dec); HRMS calcd for $C_{102}H_{78}N_4O_8S_4$ $[M^+]$, 1614.4697; found 1614.4748; Elemental analysis calcd. for $C_{102}H_{78}N_4O_8S_4$, C: 75.81, H: 4.86, N: 3.47, S: 7.94%; found, C: 75.77, H: 4.99, N: 3.46, S: 8.06%.

ATT-OBu[209]

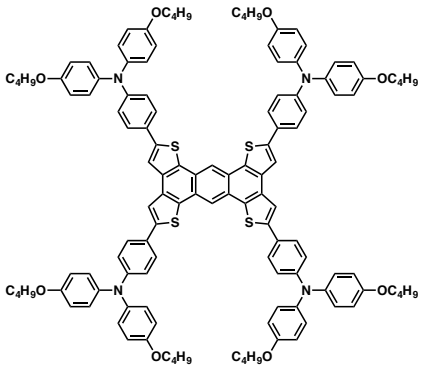

A solution of **3** (178 mg, 0.25 mmol), 4-(4,4,5,5-tetramethyl-1,3,2-dioxaborolan-2-yl)-*N*,*N*-bis(4-butyloxyphenyl)aniline (**13**) (550 mg, 1.06 mmol), K_3PO_4 (1.26 g, 5.95 mmol) and $Pd(PPh_3)_4$ (57 mg, 0.05 mmol) in DMF (6 mL) was degassed for 30 minutes under nitrogen. The reaction was heated at 110 °C for 4 hours. The mixture was cooled to room temperature and water was added. The resulting precipitate was filtered and washed with water and dissolved in hot chloroform. The organic phase was dried over sodium sulfate. The solvent was removed under reduced pressure and the crude product was purified by flash column chromatography (silica gel, CH_2Cl_2 to afford **ATT-OBu** as a yellow solid (245 mg, 0.25 mmol), yield 61%. ^{1}H NMR (400 MHz, THF-d_8) δ/ppm: 8.49 (s, 2H), 7.85 (s, 4H), 7.62 (d, J = 8.7 Hz, 8H), 7.08-7.04 (m, 16H), 6.96 (d, J = 8.7 Hz, 8H), 6.88-6.84 (m, 16H), 3.96 (t, J = 6.6 Hz, 16H), 1.80-1.73 (m, 16H), 1.57-1.48 (m, 16H), 1.01 (t, J = 6.6 Hz, 24H); ^{13}C NMR (101 MHz, $CDCl_3$) δ/ppm: 155.6, 148.4, 143.8, 140.4, 133.8, 133.5, 126.8, 126.7, 126.3, 124.8, 120.2, 117.7, 117.0, 115.3, 67.9, 31.4, 19.3, 13.9; FTIR (neat): 2957, 2934, 1602, 1504, 1488, 1263, 973, 825 cm^{-1}; Mp > 400 ºC (dec); HRMS calcd for $C_{126}H_{126}N_4O_8S_4$, [M^+], 1950.8453; found 1950.8402; Elemental analysis calcd. for $C_{126}H_{126}N_4O_8S_4$, C: 77.50, H: 6.50, N: 2.87, S: 6.57%; found, C: 77.53, H: 6.49, N: 2.89, S: 6.54%.

ATT-OHex[209]

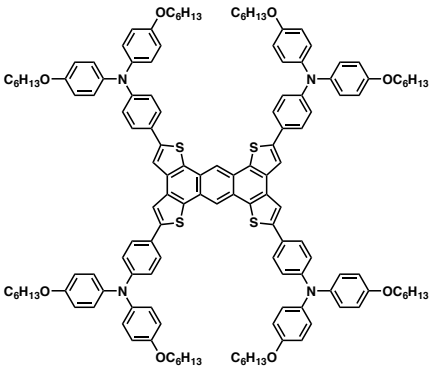

A solution of **3** (207 mg, 0.29 mmol), 4-(4,4,5,5-tetramethyl-1,3,2-dioxaborolan-2-yl) -*N*,*N*-bis(4-hexyloxyphenyl)aniline (**14**) (740 mg, 1.29mmol), K_3PO_4 (1.46 g, 6.91 mmol) and $Pd(PPh_3)_4$ (66.6 mg, 0.06 mmol) in DMF (6 mL) was degassed for 30 minutes under nitrogen. The reaction was heated at 130 °C for 4 hours. The mixture was cooled to room temperature and water was added. The resulting precipitate was filtered and washed with water and dissolved in hot chloroform. The organic phase was dried over sodium sulfate. The solvent was removed under reduced pressure and the crude product was purified by flash column chromatography (silica gel, CH_2Cl_2:Hexane (4:1) to afford **ATT-OHex** as a yellow solid (395 mg, 0.25 mmol), yield 55%. ^{1}H NMR (400 MHz, THF-d_8) δ/ppm: 8.64 (s, 2H), 7.96 (s, 4H), 7.66 (d, J = 8.7 Hz, 8H), 7.09-7.05 (m, 16H), 6.97 (d, J = 8.7Hz, 8H), 6.89-6.85 (m, 16H), 3.95 (t, J = 6.6 Hz, 16H), 1.81-1.75 (m, 16H), 1.54-1.36 (m, 48H), 0.95-0.93 (m, 24H); ^{13}C NMR (101 MHz, $CDCl_3$) δ/ppm: 155.6, 148.5, 143.9, 140.4, 134.0, 133.5, 126.9, 126.8, 126.3, 124.9, 120.2, 117.8, 117.1, 115.3, 68.3, 31.7, 29.4, 25.8, 22.7, 14.1; FTIR (neat): 3037, 2927, 1604, 1500, 1320, 1270, 1235, 1024, 818 cm^{-1}; Mp > 400 ºC (dec); HRMS calcd for $C_{142}H_{158}N_4O_8S_4$ [M^+], 2175.0957; found 2175.1001; Elemental analysis calcd. for $C_{142}H_{158}N_4O_8S_4$, C: 78.34, H: 7.31, N: 2.57, S: 5.89%; found, C: 78.26, H: 7.42, N: 2.62, S: 5.86%.

ATT-ODec[209]

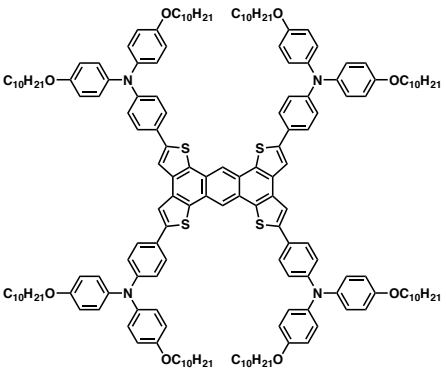

A solution of **3** (175 mg, 0.24 mmol), 4-(4,4,5,5-tetramethyl-1,3,2-dioxaborolan-2-yl)-*N*,*N*-bis(4-decyloxyphenyl)aniline (**15**) (750 mg, 1.09 mmol), K_3PO_4 (1.24 g, 5.84 mmol) and $Pd(PPh_3)_4$ (56.6 mg, 0.05 mmol) in DMF (6 mL) was degassed for 30 minutes under nitrogen. The reaction was heated at 130 °C for 4 hours. The mixture was cooled to room temperature and water was added. The resulting precipitate was filtered and washed with water and dissolved in hot chloroform. The organic phase was dried over sodium sulfate. The solvent was removed under reduced pressure and the crude product was purified by flash column chromatography (silica gel, CH_2Cl_2:hexane (3:7) and then CH_2Cl_2:hexane (7:3) to afford **ATT-ODec** as a yellow solid (292 mg, 0.25 mmol), yield 46%. ^{1}H NMR (400 MHz, THF-d_8) δ/ppm: 8.79 (s, 2H), 8.07 (s, 4H), 7.70 (d, J = 8.7Hz, 8H), 7.10-7.06 (m, 16H), 6.98 (d, J = 8.7Hz, 8H), 6.89-6.85 (m, 16H), 3.96 (t, J = 6.6 Hz, 16H), 1.81-1.29 (m, 64H), 0.90 (t, J = 6.6 Hz, 24H); ^{13}C NMR (101 MHz, $CDCl_3$) δ/ppm: 155.6, 148.5, 143.9, 140.3, 133.9, 133.5, 126.9, 126.8, 126.3, 126.1, 124.9, 120.2, 117.8, 117.1, 115.3, 68.2, 31.9, 29.7, 29.6, 29.5, 29.4, 29.3, 26.1, 22.7, 14.1; FTIR (neat): 2922, 2853, 1601, 1504, 1487, 1238, 852 cm^{-1}; Mp > 400 ºC (dec); HRMS calcd for. $C_{174}H_{222}N_4O_8S_4$ [M^+], 2623.5965; found 2623.6028; Elemental analysis calcd. for $C_{174}H_{222}N_4O_8S_4$, C: 79.59, H: 8.52, N: 2.13, S: 4.88%; found, C: 79.49, H: 8.56, N: 2.20, S: 4.79%.

4-Methoxy-*N*-(4-methoxyphenyl)-*N*-phenylaniline[158] **(4)**

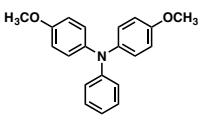

This compound was synthesized according to reported procedure [*J. Am. Chem. Soc.* **2015**, *137*, 16172-16178] and showed identical spectroscopic properties to those reported therein.^{1}H NMR (400 MHz, $CDCl_3$, 298 K) δ/ppm: 7.19 (t, J = 7.6 Hz, 2H), 7.07 (d, J = 6.9 Hz, 4H), 6.96 (d, J = 7.1 Hz, 2H), 6.89 (d, J = 7.1 Hz, 1H), 6.84 (d, J = 8.9 Hz, 4H), 3.82 (s, 6H).

4-Butoxy-*N*-(4-butoxyphenyl)-*N*-phenylaniline[256] (5)

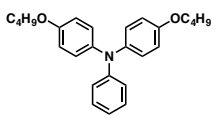

This compound was synthesized according to reported procedure [*J. Mater. Chem. A* **2013**, *1*, 2441-2446] and showed identical spectroscopic properties to those reported therein. ^{1}H NMR (400 MHz, $CDCl_3$) δ/ppm: 7.26-7.07 (m, 2H), 7.06 – 6.96 (m, 5H), 6.90 (dd, J_1 = 15.4, J_2 = 5.8 Hz, 2H), 6.87-6.73 (m, 4H), 3.91 (dt, J_1 = 12.9, J_2 = 6.3 Hz, 4H), 1.80 – 1.65 (m, 4H), 1.55-1.41 (m, 4H), 0.96 (t, J = 7.4 Hz, 6H).

4-Hexyloxy-*N*-(4-hexyloxyphenyl)-*N*-phenylaniline[257] (6)

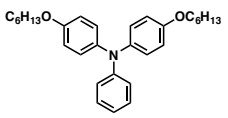

This compound was synthesized according to reported procedure [*Org. Lett.* **2014**, *16*, 106–109] and showed identical spectroscopic properties to those reported therein. ^{1}H NMR (400 MHz, $CDCl_3$) δ/ppm: 7.21-7.16 (m, 2H), 7.08 (d, J = 9.0 Hz, 4H), 6.97 (d, J = 8.0 Hz) 6.90-6.83 (m, 5H), 3.97-3.94 (t, J = 6.5 Hz, 4H), 1.83-1.78 (m, 4H), 1.50 (m, 4H), 1.40 (m, 8H), 0.97 (t, J = 6.5 Hz, 6H).

4-Decyloxy-*N*-(4-decyloxyphenyl)-*N*-phenylaniline[258] (7)

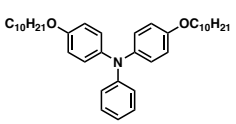

This compound was synthesized according to reported procedure [*Phys. Chem. Chem. Phys.* **2012**, *14*, 8282-8286] and showed identical spectroscopic properties to those reported therein. ^{1}H NMR (400 MHz, $CDCl_3$) δ/ppm: 7.15 (t, J = 7.8 Hz, 2H), 7.02 (d, J = 8.7 Hz, 4H), 6.93 (d, J = 7.8 Hz, 2H), 6.84 (t, J =7.8 Hz, 1H), 6.80 (d, J = 8.7 Hz, 4H), 3.92 (t, J = 6.5 Hz, 4H), 1.77 (m, 4H), 1.45 (m, 4H), 1.26 (m, 24H), 0.88 (m, 6H).

---

[256] J. Zhao, X. Yang, M. Cheng, S. Li, X. Wang, L. Sun, *J. Mater. Chem. A* **2013**, *1*, 2441–2446.

[257] L. Cai, T. Moehl, S.-J. Moon, J.-D. Decoppet, R. Humphry-Baker, Z. Xue, L. Bin, S. M. Zakeeruddin, M. Grätzel, *Org. Lett.* **2014**, *16*, 106–109.

[258] Y. Cao, N. Cai, Y. Wang, R. Li, Y. Yuan, P. Wang, *Phys. Chem. Chem. Phys.* **2012**, *14*, 8282–8286.

4-Iodo-*N*,*N*-bis(4-methoxyphenyl)aniline[158] **(8)**

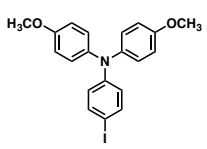

This compound was synthesized according to reported procedure [*J. Am. Chem. Soc.* **2015**, *137*, 16172-16178] and showed identical spectroscopic properties to those reported therein.[1]H NMR (400 MHz, $CDCl_3$) δ/ppm: 7.26 (d, *J* = 8.8 Hz, 2H), 7.05 (d, *J* = 8.5 Hz, 4H), 6.85 (d, *J* = 8.9 Hz, 4H), 6.82 (d, *J* = 8.9 Hz, 2H), 3.82 (s, 6H).

4-Bromo-*N*,*N*-bis(4-butoxyphenyl)aniline[256] **(9)**

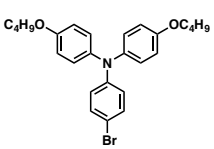

This compound was synthesized according to reported procedure [*J. Mater. Chem. A* **2013**, *1*, 2441-2446] and showed identical spectroscopic properties to those reported therein. [1]H NMR (400 MHz, $CDCl_3$) δ/ppm: 7.20 (d, *J* = 7.8 Hz, 2H), 6.98 (d, *J* = 8.7 Hz, 4H), 6.89 (d, *J* = 7.6 Hz, 2H), 6.79 (d, *J* = 8.5 Hz, 4H), 3.92 (t, *J* = 6.3 Hz, 4H), 1.83 – 1.69 (m, 4H), 1.59 – 1.41 (m, 4H). 0.96 (t, *J* = 7.4 Hz, 6H).

4-Iodo-*N*,*N*-bis(4-hexyloxyphenyl)aniline[257] **(10)**

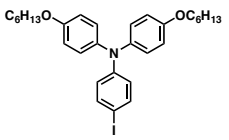

This compound was synthesized according to reported procedure [*Org. Lett.* **2014**, *16*, 106–109] and showed identical spectroscopic properties to those reported therein. [1]H NMR (400 MHz, $CDCl_3$) δ/ppm: 7.43 (d, *J* = 8.7 Hz, 2H), 7.04 (d, *J* = 7.1 Hz, 4H), 6.85-6.83 (d, *J* = 9.0 Hz, 4H), 6.71-6.70 (d, *J* = 7.3 Hz, 2H), 3.94 (t, *J* = 6.5 Hz), 1.83-1.78 (m, 4H), 1.51-1.47 (m, 4H), 1.39 (m, 8H), 0.95 (t, *J* = 6.6 Hz, 6H).

4-Iodo-*N*,*N*-bis(4-decyloxyphenyl)aniline[258] **(11)**

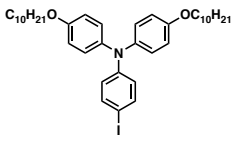

This compound was synthesized according to reported procedure [*Phys. Chem. Chem. Phys.* **2012**, *14*, 8282-8286] and showed identical spectroscopic properties to those reported therein. [1]H NMR (400 MHz, $CDCl_3$) δ/ppm: 7.42 (d, *J* = 8.4 Hz, 2H), 6.99 (d, *J* = 8.7 Hz, 4H), 6.87 (d, *J* = 8.7 Hz,

4H), 6.52 (d, *J* = 8.7 Hz, 2H) 3.92 (t, *J* = 6.5 Hz, 4H), 1.77 (m, 4H), 1.45 (m, 4H), 1.25 (m, 24H), 0.89 (m, 6H).

4-Methoxy-*N*-(4-methoxyphenyl)-*N*-(4-(4,4,5,5-tetramethyl-1,3,2-dioxaborolan-2- yl)phenyl)aniline[158] **(12)**

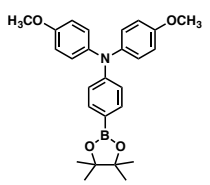

This compound was synthesized according to reported procedure [*J. Am. Chem. Soc.* **2015**, *137*, 16172-16178] and showed identical spectroscopic properties to those reported therein. ^{1}H NMR (400 MHz, $CDCl_3$) δ/ppm: 7.63 (d, *J* = 8.6 Hz, 2H), 7.10 (d, *J* = 8.9 Hz, 4H), 6.90 (d, *J* = 8.6 Hz, 2H), 6.86 (d, *J* = 8.9 Hz, 4H), 3.83 (s, 6H), 1.35 (s, 12H).

4-Butoxy-*N*-(4-butoxyphenyl)-*N*-(4-(4,4,5,5-tetramethyl-1,3,2-dioxaborolan-2-yl)phenyl)aniline[256] **(13)**

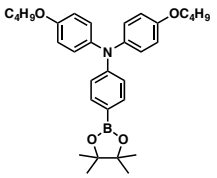

This compound was synthesized according to reported procedure [*J. Mater. Chem. A* **2013**, *1*, 2441-2446] and showed identical spectroscopic properties to those reported therein. ^{1}H NMR (400 MHz, $CDCl_3$) δ/ppm: 7.60 (d, *J* = 8.6 Hz, 2H), 7.08 (d, *J* = 8.9 Hz, 4H), 6.93 (d, *J* = 8.6 Hz, 2H), 6.84 (d, *J* = 8.9 Hz, 4H), 3.92 (t, *J* = 6.3 Hz, 4H), 1.81 – 1.68 (m, 4H), 1.59 – 1.41 (m, 4H). 0.96 (t, *J* = 7.5 Hz, 6H), 1.34 (s, 12H).

4-Hexyloxy-*N*-(4-hexyloxyphenyl)-*N*-(4-(4,4,5,5-tetramethyl-1,3,2-dioxaborolan-2-yl)phenyl)aniline[257] **(14)**

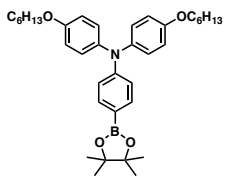

This compound was synthesized according to reported procedure [*Org. Lett.* **2014**, *16*, 106–109] and showed identical spectroscopic properties to those reported therein. ^{1}H NMR (400 MHz, $CDCl_3$) δ/ppm: 7.72 (d, *J* = 8.5 Hz, 2H), 7.14 (d, *J* = 8.8 Hz, 4H), 6.97 (d, *J* = 8.9 Hz, 2H), 6.90 (d, *J* = 8.4 Hz, 4H), 4.00 (t, *J* = 6.5 Hz, 4H), 1.87-1.84 (m, 4H), 1.57-1.54 (m, 4H), 1.45-1.40 (m, 8H), 1.39 (s, 12H), 1.02 (t, *J* = 7.1 Hz, 6H).

4-Decyloxy-N-(4-decyloxyphenyl)-N-(4-(4,4,5,5-tetramethyl-1,3,2-dioxaborolan-2-yl)phenyl)aniline[258] **(15)**

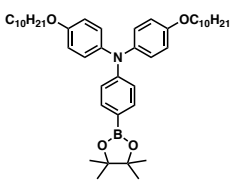

This compound was synthesized according to reported procedure [*Phys. Chem. Chem. Phys.* **2012**, *14*, 8282-8286] and showed identical spectroscopic properties to those reported therein. ^{1}H NMR (400 MHz, $CDCl_3$) δ/ppm: 7.44 (d, J = 8.4 Hz, 2H), 7.03 (d, J = 9.0 Hz, 4H), 6.91 (d, J = 9.0 Hz, 4H), 6.66 (d, J = 8.4 Hz, 2H), 3.91 (t, J = 6.5 Hz, 4H), 1.79 (m, 4H), 1.46 (m, 4H), 1.29-1.22 (m, 36H), 0.89 (m, 6H).

7.2 Synthesis of dibenzoquinquethiophene (DBQT) and dibenzosexithiophene (DBST) derivatives

2,3,4,5-Tetrathienylthiophene[259] **(16)**

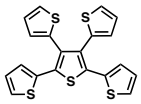

This compound was synthesized according to reported procedure [*Chem. Lett.* **2011**, *40*, 964-966] and showed identical spectroscopic properties to those reported therein. ^{1}H NMR (400 MHz, $CDCl_3$) δ/ppm: 6.90 (dd, J_1 = 1.2, 3.7 Hz, 2H), 6.94 (dd, J_1 = 3.7, J_2 = 5.2 Hz, 2H), 6.96 (dd, J_1 = 3.7, J_2 = 5.2 Hz, 2H), 7.09 (dd, J_1 = 1.2, J_2 = 3.7 Hz, 2H), 7.19 (dd, J_1 = 1.2, J_2 =5.2 Hz, 2H), 7.30 (dd, J_1 = 1.2, J_2 = 5.2 Hz, 2H).

Tetra(5-bromo-2-thienyl)thiophene[259] **(17)**

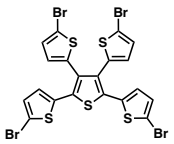

This compound was synthesized according to reported procedure [*Chem. Lett.* **2011**, *40*, 964-966] and showed identical spectroscopic properties to those reported therein. ^{1}H NMR (400 MHz, $CDCl_3$) δ/ppm: 6.67 (d, J = 4.0 Hz, 2H), 6.88 (d, J = 4.0 Hz, 2H), 6.93 (d, J = 4.0 Hz, 2H), 6.96 (d, J = 4.0 Hz, 2H).

259 H. Muraoka, T. Tanifuji, S. Ogawa, *Chem. Lett.* **2011**, *40*, 964–966.

2,5,9,12-Tetrabromodithieno[3,2-*e*:3',2'-*e'*]thieno[2,3-*g*:4,5-*g'*]bis[1] benzothiophene[216] **(18)**

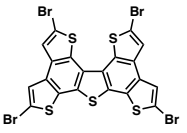

To a solution of compound **17** (330 mg, 0.45 mmol) in warm chlorobenzene (60 mL), $FeCl_3$ (452 mg, 2.79 mmol) in nitromethane (15 mL) was added dropwise. The reaction mixture was stirred at room temperature for 72 hours. The resulting precipitate was filtered and washed several times with hot MeOH and acetone to afford compound **18** as a green solid (yield of 93%), which was used without further purification. Given the low solubility of this compound, ^{1}H NMR and ^{13}C NMR were not possible. MALDI calcd for $C_{20}H_4Br_4S_5$ [M+] 724.27; found, 724.01; Mp > 350 ºC (dec).

DBQT-OMe[216]

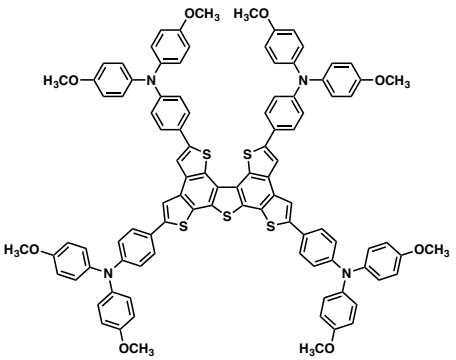

A solution of **18** (200 mg, 0.27 mmol), 4-(4,4,5,5-tetramethyl-1,3,2-dioxaborolan-2-yl)-*N*,*N*-bis(4-methoxyphenyl)aniline (**12**) (512 mg, 1.18 mmol), K_3PO_4 (1.375 gr, 6.5 mmol) and $Pd(PPh_3)_4$ (62 mg, 0.05 mmol) in DMF (8 mL) was degassed for 30 minutes under nitrogen. The reaction was heated at 100 °C for 6 hours. The mixture was cooled to room temperature and water was added. The resulting precipitate was filtered and washed with water and dissolved in hot chloroform. The organic phase was dried over sodium sulfate. The solvent was removed under reduced pressure and the crude product was purified by flash column chromatography (silica gel, CH_2Cl_2 and then CH_2Cl_2:AcOEt (95:2)) to afford **DBQT-OMe** as an orange solid (233 mg, 0.25 mmol), yield 56%. ^{1}H NMR (400 MHz, THF-d_8) δ/ppm: 8.09 (s, 2H), 8.02 (s, 2H), 7.72 - 7.69 (m, 4H), 7.63 - 7.59 (m, 4H), 7.10 - 7.06 (m, 16H), 6.99 - 6.92 (m, 8H), 6.90 - 6.86 (m, 16H), 3.78 (s, 12H), 3.77 (s, 12H); ^{13}C NMR (101 MHz, $CDCl_3$) δ/ppm: 156.1, 155.9(2), 155.8, 148.6, 148.5, 144.1, 142.0, 140.6, 140.5, 140.4, 134.8, 134.4, 130.2, 130.0, 128.7, 127.2, 126.8(2), 126.6, 126.4, 126.3, 125.8, 120.7, 120.3, 119.9, 116.2, 114.8, 114.7, 114.6, 55.49(2); FTIR (neat): 3034, 2996, 2927, 2832, 1602, 1501, 1280, 1238, 1171, 1033, 822, 576

cm^{-1}; Mp > 400 ºC (dec); HRMS calcd for $C_{100}H_{76}N_4O_8S_5$ [M^+], 1620.4261; found 1620.4273; Elemental analysis calcd. for $C_{100}H_{76}N_4O_8S_5$, C: 74.05, H: 4.72, N: 3.45, S: 9.88%; found, C: 74.19, H: 4.73, N: 3.43, S: 9.81%.

2,3,5,6-Tetrabromothieno[3,2-*b*]thiophene[260] (19)

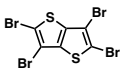

This compound was synthesized according to reported procedure [*Adv. Funct. Mater.* **2012***, 22*, 48-60]. MALDI calcd. for $C_6Br_4S_2$, [M^+] 455.80; found 455.78; Mp : 242 ºC.

2,3,5,6-Tetra(2-thienylthieno)[3,2-*b*]thiophene[261] (20)

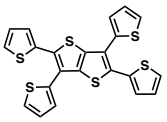

This compound was synthesized according to reported procedure [*New J. Chem.* **2013***, 37*, 1189-1194] and showed identical spectroscopic properties to those reported therein. ^{1}H NMR (400 MHz, acetone-d_6) δ/ppm: 7.64 (d, J = 6.8 Hz, 2H), 7.60 (d, J = 6.8 Hz, 2H), 7.32 (d, J = 4.8 Hz, 2H), 7.29 (d, J = 4.8 Hz, 2H), 7.20 (d, J = 6.8 Hz, 2H), 7.14 (d, J = 6.8 Hz, 2H).

2,3,5,6-Tetra(5-bromo-2thienylthieno)[3,2-*b*]thiophene[216] (21)

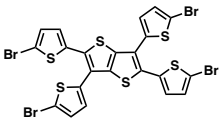

NBS (341.7 mg, 1.92 mmol) was added portionwise to a solution of compound **20** (150 mg, 0.32 mmol) in THF (10 mL) under light exclusion conditions. The reaction was then stirred at room temperature under nitrogen atmosphere. The resulting precipitate was filtered and washed with water and acetone, to afford the derivative **21** (213.3 mg, 0.27 mmol, 85%) as a yellow solid. ^{1}H NMR (400 MHz, $CDCl_3$) δ/ppm: 7.08 (d, J = 3.8 Hz, 2H), 7.01 - 6.99 (m, 4H), 6.95 (d, J = 3.8 Hz, 2H). Given the low solubility of this compound, ^{13}C NMR was not possible. MALDI calcd for $C_{22}H_8Br_4S_6$, [M^+] 784.28; found 784.23.

---

[260] J. Youn, P.-Y. Huang, Y.-W. Huang, M.-C. Chen, Y.-J. Lin, H. Huang, R. P. Ortiz, C. Stern, M.-C. Chung, C.-Y. Feng, L.-H. Chen, A. Facchetti, T. J. Marks, *Adv. Funct. Mater.* **2012**, *22*, 48–60.

[261] Y. Liu, Q. Liu, X. Zhang, L. Ai, Y. Wang, R. Peng, Z. Ge, *New J. Chem.* **2013**, *37*, 1189–1194.

2,5,9,12-Tetrabromodithieno[2',3':4,5;3'',2'':6,7][1]benzothieno[3,2-*b*] dithieno[2,3-*e*:3',2'-*g*][1]benzothiophene[216] **(22)**

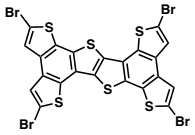

To a solution of compound **21** (215 mg, 0.27 mmol) in warm chlorobenzene (150 mL), $FeCl_3$ (893.8 mg, 5.51 mmol) in nitromethane (15 mL) was added dropwise. The reaction mixture was stirred at room temperature for 72 hours. The resulting precipitate was filtered and washed several times with hot MeOH and acetone to afford compound **22** as a red solid (yield of 98%), which was used without further purification. Given the low solubility of this compound, ^{1}H NMR and ^{13}C NMR were not possible. MALDI calcd for $C_{22}H_4Br_4S_6$, [M^+]: 779.58, found 779.53; Mp > 350 ºC (dec).

DBST-OMe[216]

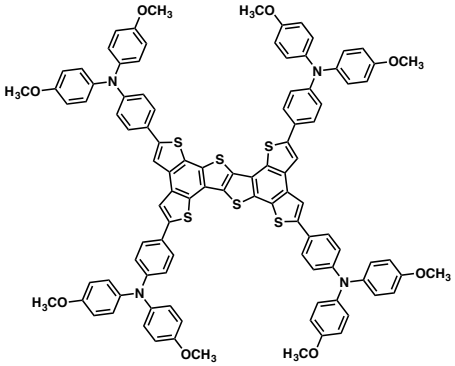

A solution of **13** (150 mg, 0.19 mmol), 4-(4,4,5,5-tetramethyl-1,3,2-dioxaborolan-2-yl)-*N*,*N*-bis(4-methoxyphenyl)aniline (**12**) (375 mg, 0.87 mmol), K_3PO_4 (984 mg, 4.64 mmol) and $Pd(PPh_3)_4$ (45 mg, 0.04 mmol) in DMF (12 mL) was degassed for 30 minutes under nitrogen. The reaction was heated at 100 °C for 6 hours. The mixture was cooled to room temperature and water was added. The resulting precipitate was filtered and washed with water and dissolved in hot chloroform. The organic phase was dried over sodium sulfate. The solvent was removed under reduced pressure and the crude product was purified by flash column chromatography (silica gel, CH_2Cl_2 and then CH_2Cl_2:AcOEt (95:5)) to afford **DBST-OMe** as an orange solid (233 mg, 0.25 mmol), yield 55%. ^{1}H NMR (400 MHz, THF-d_8) δ/ppm: 7.94 (s, 2H), 7.91 (s, 2H), 7.65 - 7.53 (m, 8H), 7.11 - 7.06 (m, 16H), 6.97 - 6.86 (m, 24H), 3.78 (s, 24H); ^{13}C NMR (101 MHz, $CDCl_3$) δ/ppm: 156.0, 155.9, 148.19, 148.1, 143.4, 142.5, 140.5, 140.4, 133.1, 133.0, 132.2, 130.2, 129.9, 128.6, 127.0, 126.8, 126.7, 126.3, 126.0, 123.2, 120.1, 119.8, 116.1, 115.9, 114.7, 114.6, 55.4; FTIR (neat): 3036, 2995, 2929, 2832, 1601, 1502, 1491, 1283, 1237, 1176, 823, 577, 522 cm^{-1}; Mp > 400 ºC (dec); HRMS calcd for $C_{102}H_{76}N_4O_8S_6$,

[M^+], 1676.3982; found 1676.3986; Elemental analysis calcd. for $C_{102}H_{76}N_4O_8S_6$, C: 73.00, H: 4.56, N: 3.34, S: 11.46%; found, C: 73.08, H: 4.49, N: 3.27, S: 11.58%.

7.3 Synthesis of cyclooctatetrathiophene-based (CoTh) derivative

5,5'-Bis(trimethylsilyl)-3,3'-dibromo-2,2'-bithiophene[262] (23)

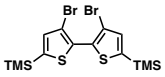

This compound was synthesized according to reported procedure [*J. Am. Chem. Soc.* **2012**, *134*, 8404-8407] and showed identical spectroscopic properties to those reported therein. ^{1}H NMR (400 MHz, $CDCl_3$) δ/ppm: 7.19 (s, 2H), 0.35 (s, 18H).

2,5,8,11-Tetrakis(trimethylsilyl)cycloocta[1,2-*b*:4,3-*b′*:5,6-*b″*:8,7-*b‴*]tetrathiophene[220,263] (24)

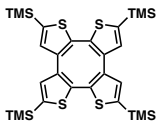

This compound was synthesized according to reported procedure [*Synlett* **2007**, *15*, 2390-2394 and *Chin. J. Chem.* **2015**, *33*, 71-78] and showed identical spectroscopic properties to those reported therein. ^{1}H NMR (400 MHz, $CDCl_3$) δ/ppm: 7.06 (s, 4 H), 0.32 (s, 36 H).

2,5,8,11-Tetrabromocycloocta[1,2-*b*:4,3-*b′*:5,6-*b″*:8,7-*b‴*] tetrathiophene[263] (25)

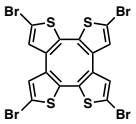

This compound was synthesized according to reported procedure [*Chin. J. Chem.* **2015**, *33*, 71-78] and showed identical spectroscopic properties to those reported therein. ^{1}H NMR (400 MHz, $CDCl_3$) δ/ppm: 6.90 (s, 4H).

---

[262] X. Guo, S. R. Puniredd, M. Baumgarten, W. Pisula, K. Müllen, *J. Am. Chem. Soc.* **2012**, *134*, 8404–8407.

[263] C. Zhao, L. Xu, Y. Wang, C. Li, H. Wang, *Chinese J. Chem.* **2015**, *33*, 71–78.

CoTh-OMe[222]

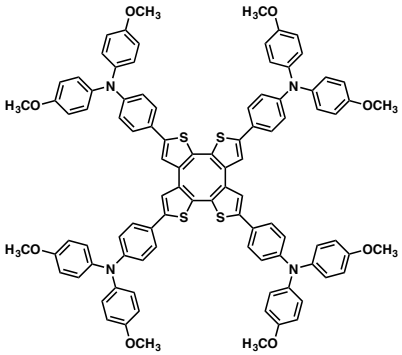

A solution of **25** (100 mg, 0.16 mmol), 4-(4,4,5,5-tetramethyl-1,3,2-dioxaborolan-2-yl)-*N,N*-bis(4-methoxyphenyl)aniline (**12**) (335 mg, 0.77 mmol), K_3PO_4 (790 mg, 3.73 mmol) and $Pd(PPh_3)_4$ (36 mg, 0.03 mmol) in DMF (10 mL) was degassed for 30 minutes under nitrogen. The reaction was heated at 100 °C for 3 hours. The mixture was cooled to room temperature and water was added to the reaction. The resulting precipitate was filtered and washed with water and methanol. The solid was then dissolved in chloroform and dried over sodium sulfate. The solvent was removed under reduced pressure and the crude product was purified by flash column chromatography (silica gel, CH_2Cl_2) to afford **CoTh-OMe** as a bright orange solid (187 mg, 0.12 mmol), yield 78%. ^{1}H NMR (400 MHz, THF-d_8) δ/ppm: 7.40 (m, 8H), 7.20 (s, 4H), 7.04 (m, 16H), 6.85 (m, 24H), 3.75 (s, 24H); ^{13}C NMR (101 MHz, $CDCl_3$) δ/ppm: 167.2, 156.0, 151.2, 148.1, 140.3, 137.9, 136.3, 135.1, 130.0, 125.7, 65.3; FTIR (neat): 3036, 2948, 2832, 1603, 1497, 1462, 1234, 1033, 823 cm^{-1}; HRMS calcd for $C_{96}H_{76}N_4O_8S_4$ [M^+] 1540.45; found 1540.6540; Elemental analysis calcd. for $C_{96}H_{76}N_4O_8S_4$, C: 74.78, H: 4.97, N: 3.63, S: 8.32%; found, C: 74.70, H: 4.99, N: 3.65, S: 8.31%.

7.4 Synthesis of Benzo[1,2-*b*:3,4-*b´*:5,6-*b´´*]triselenophene -based (BTSe) derivative

1,3,5-trichloro-2,4,6-triiodobenzene[264] (26)

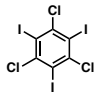

This compound was synthesized according to reported procedures [*Chem. Eur. J.* **1999**, *5*, 29-38] and showed identical spectroscopic

[264] J. J. Wolff, F. Gredel, T. Oeser, H. Irngartinger, H. Pritzkow, *Chem. – A Eur. J.* **1999**, *5*, 29–38.

properties to those reported therein. ^{13}C NMR (101 MHz, $CDCl_3$) δ: 144.9, 97.1 ppm.

1,3,5-Trichloro-2,4,6-tris[(trimethylsilyl)ethynyl]benzene[223] (27)

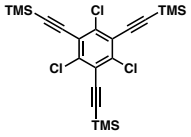

This compound was synthesized according to reported procedure [*Org. Lett.* **2009***, 11,* 2473-2475] and showed identical spectroscopic properties to those reported therein. ^1H NMR (400 MHz, $CDCl_3$) δ/ppm: 0.29 (s, 27 H).

Benzo[1,2-*b*:3,4-*b´*:5,6-*b´´*]triselenophene[223] (28)

This compound was synthesized according to reported procedure [*Org. Lett.* **2009***, 11,* 2473-2475] and showed identical spectroscopic properties to those reported therein. ^1H NMR (400 MHz, $CDCl_3$) δ/ppm: 8.10 (d, *J* =5.6 Hz, 3H), 7.78 (d, *J* = 5.7 Hz, 3H).

2,5,8-tribromobenzo[1,2-b:3,4-b':5,6-b'']triselenophene[224] (29)

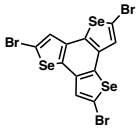

NBS (1.51 g, 8.53 mmol) was added portion wise to a solution of benzo[1,2-*b*:3,4-*b'*:6,5-*b''*]triselenophene (**20**) (500 mg, 2.03 mmol) in a mixture of chloroform and acetic acid (2:1) (15 mL) under light exclusion conditions. The reaction was then heated to reflux under nitrogen atmosphere. The resulting precipitate was filtered and washed with water, MeOH and chloroform to afford the tribromo derivative **21** in 65% yield as a brown solid. ^1H NMR (400 MHz, DMSO-d_6) δ/ppm: 8.29 (s, 1H), 8.26 (s, 1H), 8.10 (s, 1H).

BTSe-OMe[224]

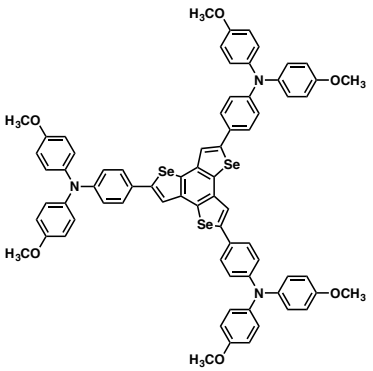

A solution of **29** (300 mg, 0.48 mmol), 4-(4,4,5,5-tetramethyl1,3,2-dioxaborolan-2-yl)-*N*,*N*-bis(4-methoxyphenyl)aniline (**12**) (684 mg, 1.58 mmol), K_3PO_4 (1.84 gr, 8.65 mmol) and $Pd(PPh_3)_4$ (111 mg, 0.09 mmol) in DMF (10 mL) was degassed for 30 minutes under nitrogen. The reaction was heated at 110 °C for 2 hours. The mixture was cooled to room temperature and water was added. The resulting precipitate was filtered and washed with water and dissolved in hot chloroform. The organic phase was dried over sodium sulfate. The solvent was removed under reduced pressure and the crude product was purified by flash column chromatography (silica gel, CH_2Cl_2) to afford **BTSe-OMe** as a yellow solid (165 mg, 0.25 mmol), yield 62%. ^{1}H NMR (400 MHz, $CDCl_3$) δ/ppm: 7.65 (s, 3H), 7.51 - 7.48 (m, 6H), 7.12 - 7.07 (m, 12H), 6.96 - 6.93 (m, 6H), 6.89 - 6.84 (m, 12H), 3.77 (m, 4H), 3.82 (s, 18H); ^{13}C NMR (176 MHz, $CDCl_3$) δ/ppm: 156.2, 148.6, 147.4, 140.1, 137.2, 133.1, 128.0, 127.15, 127.0, 120.6, 120.3, 114.6, 55.5; Mp : 319 ºC; HRMS calcd for $C_{72}H_{57}N_3O_6Se_3$ [M^+] 1299.1767; found 1299.1742; Elemental analysis calcd. for $C_{72}H_{57}N_3O_6Se_3$, C: 66.67, H: 4.43, N: 3.24%; found, C: 66.58, H: 4.31, N: 3.22%.

7.5 Synthesis of spiro-phenoxazine and spiro-phenothiazine-based derivatives

10-(2-Bromophenyl)-10H-phenoxazine[265] (30)

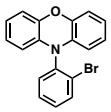

This compound was synthesized according to reported procedure [*ACS Appl. Mater. Interfaces* **2017**, *9*, 24035-24042] and showed identical spectroscopic properties to those reported therein. ^{1}H NMR (400 MHz, $CDCl_3$) δ/ppm: 7.87 (dd, J_1 = 8.0, J_2 = 1.4 Hz,

[265] Y. H. Lee, S. Park, J. Oh, J. W. Shin, J. Jung, S. Yoo, M. H. Lee, *ACS Appl. Mater. Interfaces* **2017**, *9*, 24035–24042.

1H), 7.56 (dd, J_1 = 7.6, J_2 = 1.4 Hz, 1H), 7.47 - 7.36 (m, 2H), 6.75 - 6.60 (m, 6H), 5.81 (d, J = 7.5 Hz, 2H).

10-(2-Bromophenyl)-10H-phenothiazine[266] **(31)**

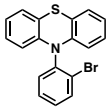

This compound was synthesized according to reported procedure [*Chem. Eur. J.* **2016***, 22,* 17930-17935] and showed identical spectroscopic properties to those reported therein. ^{1}H NMR (400 MHz, $CDCl_3$) δ/ppm: 7.89 (dd, J_1 = 8.0, J_2 = 1.4 Hz, 1H), 7.59 (ddd, J_1 = 7.8, J_2 = 7.3, J_3 = 1.5 Hz, 1H), 7.51 (dd, J_1 = 7.8, J_2 = 1.8 Hz, 1H), 7.41 (ddd, J_1 = 8.0, J_2 = 7.3, J_3 = 1.9 Hz, 1H), 7.02 - 6.94 (m, 2H), 6.89 - 6.76 (m, 4H), 6.09 - 5.99 (m, 2H).

2,7-Dibromospiro[fluorene-9,9'-quinolino[3,2,1-*kl*]phenoxazine][228] **(32)**

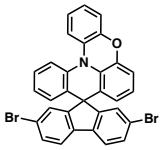

This compound was synthesized according to reported procedure [*Org. Lett.* **2017**, *19*, 3155-3158] and showed identical spectroscopic properties to those reported therein. ^{1}H NMR (400 MHz, $CDCl_3$) δ/ppm: 7.73 (d, J = 8.1 Hz, 1H), 7.65 (s, 2H), 7.49 (m, 3H), 7.36 (s, 2H), 7.22 (m, 1H), 7.07 (m, 3H), 6.85 (m,2H), 6.69 (m,1H), 6.55 (d, J = 3.9 Hz, 1H), 6.12 (d, J = 8.1 Hz, 1H).

2,7-Dibromospiro[fluorene-9,9'-quinolino[3,2,1-*kl*]phenothiazine][230] **(33)**

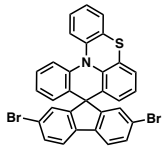

This compound was synthesized according to reported procedure [*New J. Chem.* **2013**, *37*, 3161-3165] and showed identical spectroscopic properties to those reported therein. ^{1}H NMR (400 MHz, $CDCl_3$) δ/ppm: 7.73 - 7.66 (m, 2H), 7.58 - 7.50 (m, 3H), 7.43 - 7.13 (m, 8H), 6.86 - 6.80 (m, 2H), 6.54 (d, J = 8.0 Hz, 1H), 6.36 (d, J = 6.8 Hz, 1H).

[266] C. Poriel, J. Rault-Berthelot, S. Thiery, C. Quinton, O. Jeannin, U. Biapo, D. Tondelier, B. Geffroy, *Chem. – A Eur. J.* **2016**, *22*, 17930–17935.

Spiro-POZ-OMe

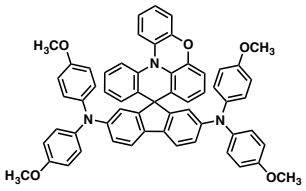

Compound **32** (200 mg, 0.34 mmol), bis(4-methoxyphenyl)amine (174 mg, 0.75 mmol) and XPhos (16 mg, 0.03 mmol) were bubbled with N_2 for 30 minutes in dry toluene (15 mL). Then, $Pd_2(dba)_3$ (16 mg, 0.02 mmol) and Na^{t}BuO (196 mg, 2.04 mmol) were added and the mixture was stirred at 100 °C for 6 hours. After this time, the mixture was cooled down to r.t., filtered through celite and washed with toluene. The organic layer was dried over Na_2SO_4 and the solvent was removed under vacuum. The crude was purified by column chromatography on silica gel (CH_2Cl_2) to afford the desired **spiro-POZ-OMe** as a light yellow solid (253 mg, 0.29 mmol), yield 83%. ^{1}H NMR (400 MHz, THF-d_8) δ/ppm: 7.57 (d, J = 7.8 Hz, 1H), 7.49 (d, J = 8.2 Hz, 1H), 7.34 (d, J = 7.8 Hz, 1H), 7.11 (td, J_1 = 8.3 Hz, J_2 = 1.2 Hz, 1H), 7.05 - 6.97 (m, 6H), 6.90 - 6.82 (m, 5H), 6.77 - 6.70 (m, 12H), 6.65 - 6.60 (m, 5H), 6.29 (dd, J_1 = 6.7 Hz, J_2 = 2.4 Hz, 1H), 3.71 (s 12 H); ^{13}C NMR (101 MHz, $CDCl_3$) δ/ppm: 148.1, 146.5, 137.2, 129.5, 129.1, 127.1, 126.8, 123.6, 123.5, 123.0, 122.5, 120.8, 117.1, 116.8, 114.7, 113.8, 55.4, 55.3; FTIR (neat): 3048, 2952, 2921, 2851, 1608, 1563, 1508, 1465, 1443, 1331, 1280, 1234, 1189, 1027, 832, 772 cm^{-1}; HRMS calcd for $C_{59}H_{45}N_3O_5$ [M$^+$], 875.3334; found 875.3321; Elemental analysis calcd. for $C_{59}H_{45}N_3O_5$, C: 80.89, H: 5.18, N: 4.80%; found, C: 81.01, H: 5.13, N: 4.89%.

Spiro-PTZ-OMe

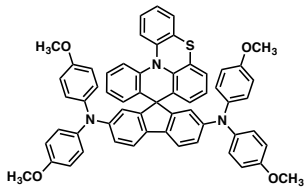

Compound **33** (160 mg, 0.27 mmol), bis(4-methoxyphenyl)amine (135 mg, 0.59 mmol) and XPhos (13 mg, 0.03 mmol) were bubbled with N_2 for 30 minutes in dry toluene (15 mL). Then, $Pd_2(dba)_3$ (12 mg, 0.01 mmol) and Na^{t}BuO (155 mg, 1.62 mmol) were added and the mixture was stirred at 100 °C for 6 hours. After this time, the mixture was cooled down to r.t., filtered through celite and washed with toluene. The organic layer was dried over Na_2SO_4 and the solvent was removed under vacuum. The crude was purified by column chromatography on silica gel (CH_2Cl_2) to afford the desired **spiro-PTZ-OMe** as a light yellow solid (198 mg, 0.24 mmol), yield 89%. ^{1}H NMR

(400 MHz, THF-d_8) δ/ppm: 7.58 (d, J = 8.4 Hz, 1H), 7.38 (d, J = 8.3 Hz, 1H), 7.28 (d, J = 8.2 Hz, 1H), 7.16 (dd, J_1 = 7.7 Hz, J_2 = 1.4 Hz, 1H), 7.11 (td, J_1= 8.4 Hz, J_2 = 1.4 Hz), 7.05 - 6.99 (m, 6H), 6.93 -6.86 (m, 4H), 6.82 (t, J = 7.7 Hz, 1H) 6.79 - 6.72 (m, 7H), 6.63 - 6.58 (m, 5H), 6.48 (dd, J_1 = 7.8 Hz, J_2 = 1.3 Hz, 1H), 7.71 (s, 6H), 3.69 (s, 6H); ^{13}C NMR (101 MHz, $CDCl_3$) δ/ppm: 141.9, 139.0, 128.9, 127.8, 127.6, 127.4, 126.9, 126.4, 125.4, 125.3, 123.9, 123.7, 123.5, 123.3, 119.4, 118.7, 55.4, 55.3; FTIR (neat): 3048, 2952, 2921, 2851, 1608, 1563, 1508, 1465, 1443, 1331, 1234, 1189, 1027, 832, 772 cm^{-1}; HRMS calcd for $C_{59}H_{45}N_3O_4S$ [M^+], 892.026; found 892.3208; Elemental analysis calcd. for $C_{59}H_{45}N_3O_4S$, C: 79.44, H: 5.08, N: 4.71, S: 3.59%; found, C: 79.53, H: 5.00, N: 4.78, S: 3.70%.

7.6 Synthesis of flexible "spiro-like" bis-xanthene and bis-thioxanthene-based derivatives

2,7-Dibromoxanthen-9-one[232] (34)

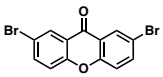

This compound was synthesized according to reported procedure [*J. Chem. Sci.* **2015**, *127*, 2063–2071] and showed identical spectroscopic properties to those reported therein. ^{1}H NMR (400 MHz, $CDCl_3$) δ/ppm: 8.45-8.35 (m, 2H), 7.90 (dd, J_1 = 8.8 Hz, J_2 = 3.2 Hz, 2H). 7.86-7.76 (m, 2H).

2,7-Dibromothioxanthen-9-one[233] (35)

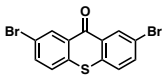

This compound was synthesized according to reported procedure [*Macromolecules* **2014**, *47*, 4607-4614] and showed identical spectroscopic properties to those reported therein. ^{1}H NMR (400 MHz, $CDCl_3$) δ/ppm: 8.75 (d, J = 2.3 Hz, 2H), 7.75 (dd, J_1 = 8.6, J_2 = 2.3 Hz, 2H), 7.48 (d, J = 8.6 Hz, 2H).

2,7-Dibromo-9H-xanthene[234] (36)

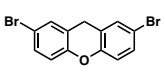

This compound was synthesized by a modified procedure from the bibliography [*Inorg. Chem.* **2018**, *57*, 4155-4163] but showed identical spectroscopic properties to those reported therein. A solution of 2,7-dibromoxanthen-9-one (**34**) (1.30 g, 6.661 mmol) was

dissolved in THF (20 mL) and stirred at room temperature while $BH_3{\cdot}SMe_2$ (0.49 mL, 5.126 mmol) was added dropwise. The mixture was refluxed for 2 hours. After cooling to room temperature, the solution was extracted with chloroform (2x15 mL), and the organic phase was washed with water, $NaHCO_3$ and brine. The organic phase was dried over Na_2SO_4. The solvent was removed under reduced pressure. No further purification was needed. Compound **36** was afforded as a white solid (1.08 g, 3.18 mmol), yield 87%. ^{1}H NMR (400 MHz, $CDCl_3$) δ/ppm: 7.32 (d, J = 6.8 Hz, 4H), 6.94 (d, J = 9.2 Hz, 2H), 4.02 (s, 2H).

2,7-Dibromo-9H-thioxanthene[234] **(37)**

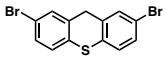

This compound was synthesized by a modified procedure from the bibliography [*Inorg. Chem.* **2018**, *57*, 4155-4163] but showed identical spectroscopic properties to those reported therein. A solution of 2,7-dibromothioxanthen-9-one (**35**) (0.50 g, 1.351 mmol) was dissolved in THF (10 mL) and stirred at room temperature while $BH_3{\cdot}SMe_2$ (0.18 mL, 1.892 mmol) was added dropwise. The mixture was refluxed for 2 hours. After cooling to room temperature, the solution was extracted with chloroform (2x15 mL), and the organic phase was washed with water, $NaHCO_3$ and brine. The organic phase was dried over Na_2SO_4. The solvent was removed under reduced pressure. No further purification was needed. Compound **37** was obtained as a white solid (0.43 g, 1.208 mmol), yield 89%. ^{1}H NMR (400 MHz, $CDCl_3$) δ/ppm: 7.48 (d, J = 1.8 Hz, 2H), 7.35 (dd, J_1 = 8.3 Hz, J_2 = 1.8 Hz, 2H), 7.30 (d, J = 8.3 Hz, 2H), 3.81 (s, 2H).

2,7-Bis[bis(4-methoxyphenyl)amino]-9H-xhantene[231] **(38)**

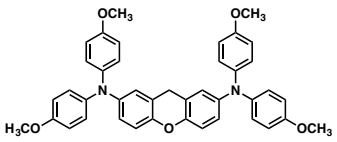

Compound **36** (840 mg, 2.49 mmol), bis(4-methoxyphenyl)amine (1.20 g, 5.23 mmol) and 1M tri-*tert*-butylphosphine solution (0.25 mL) were bubbled with N_2 for 30 minutes in dry toluene (30 mL). Then, $Pd_2(dba)_3$ (114 mg, 0.12 mmol) and Na^tBuO (1.47 g, 14.95 mmol) were added and the mixture was stirred at 100 °C for 6 hours. After this time, the mixture was cooled down to r.t., filtered through celite and washed with water. The organic layer was dried over Na_2SO_4 and the solvent was removed under vacuum. The crude was purified by column chromatography on silica gel (CH_2Cl_2) to afford the desired **38** as a yellowish

solid (973 mg, 1.53 mmol), yield 61%. ^{1}H NMR (400 MHz, $CDCl_3$) δ/ppm: 7.02 - 6.98 (m, 8H), 6.91 (d, *J* = , 2H), 6.87 - 6.78 (m, 8H), 3.81 (s, 12H), 3.75 (s, 2H); ^{13}C NMR (101 MHz, $CDCl_3$) δ/ppm: 155.1, 147.2, 143.9, 141.7, 125.3, 122.8, 122.5, 121.0, 116.9, 114.7, 55.6, 28.4; FTIR (neat): 3000, 2250, 2836, 1600, 1504, 1466, 1234, 1181, 1038, 833, 550 cm^{-1}; HRMS calcd for $C_{41}H_{36}N_2O_5$ [M^+], 636.262; found 635.986.

2,7-Bis[bis(4-methoxyphenyl)amino]-9H-thioxhantene[231] **(39)**

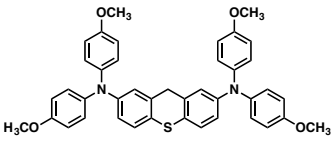

Compound **37** (250 mg, 0.70 mmol), bis(4-methoxyphenyl)amine (354 mg, 1.54 mmol) and 1M tri-*tert*-butylphosphine solution (0.03 mL) were bubbled with N_2 for 30 minutes in dry toluene (15 mL). Then, $Pd_2(dba)_3$ (32 mg, 0.035 mmol) and Na^{t}BuO (412 mg, 4.28 mmol) were added and the mixture was stirred at 100 °C for 6 hours. After this time, the mixture was cooled down to r.t., filtered through celite and washed with water. The organic layer was dried over Na_2SO_4 and the solvent was removed under vacuum. The crude was purified by column chromatography on silica gel (CH_2Cl_2) to afford the desired **39** as a yellowish solid (247 mg, 0.38 mmol), yield 54%. ^{1}H NMR (400 MHz, $CDCl_3$) δ/ppm: 7.19 (d, *J* = 8.4 Hz, 2H), 6.98-7.02 (m, 8H), 6.76-6.84 (m, 12 H), 3.79 (s, 12H), 3.58 (s, 2H); ^{13}C NMR (101 MHz, $CDCl_3$) δ/ppm: 155.7, 147.7, 141.0, 137.3, 127.2, 126.3, 125.3, 120.7, 119.5, 114.7, 55.5, 39.7; FTIR (neat): 3000, 2249, 2898, 2831, 1591, 1504, 1468, 1238, 1034, 829, 608 cm^{-1}; HRMS calcd for $C_{41}H_{36}N_2O_4S$ [M^+], 652.240; found 652.056.

BX-OMe[231]

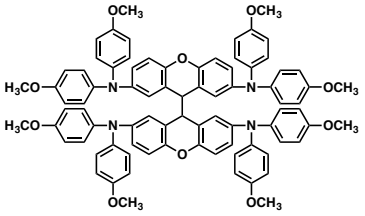

Compound **38** (400 mg, 0.63 mmol) was placed in a 100-mL round-bottomed flask and dissolved in anhydrous THF (30 mL). After the solution was cooled at -78 °C, solution of *n*-BuLi (2.5 M, 0.28 mL, 0.7 mmol) was slowly added and then stirred for 1 h. After that, $Fe(acac)_3$ (325 mg, 0.92 mmol) was added with a N_2 flow and the reaction was stirred at room temperature for 1 h. Then, the mixture was extracted with AcOEt and washed with a saturated NaCl

solution. The combined organic extracts were dried over Na_2SO_4 and concentrated in vacuo. The crude was purified by flash column chromatography (silica gel, CH_2Cl_2) to afford **BX-OMe** as a yellow solid (224 mg, 0.18 mmol), yield 56%. ^{1}H NMR (400 MHz, THF-d_8) δ/ppm: 6.86-6.66 (m, 44H), 3.89 (s, 2H) 3.70 (s, 24H); ^{13}C NMR (101 MHz, $CDCl_3$) δ/ppm: 155.2, 154.9, 148.3, 143.5, 141.8, 140.8, 126.1, 125.9, 125.3, 124.9, 123.9, 123.6, 121.4, 118.6, 117.1, 116.5, 114.9, 114.5, 55.4, 49.7. FTIR (neat): 3037, 2988, 2932, 2902, 2831, 1606, 1501, 1475, 1233, 1174, 1106, 1032, 823, 570, 522 cm^{-1}; HRMS calcd for $C_{82}H_{70}N_4O_{10}$ [M^+], 1270.5086; found 1270.5081; Elemental analysis calcd. for $C_{82}H_{70}N_4O_{10}$, C: 77.46, H: 5.55, N: 4.41%; found, C: 77.58, H: 5.44, N: 4.49%.

BTX-OMe[231]

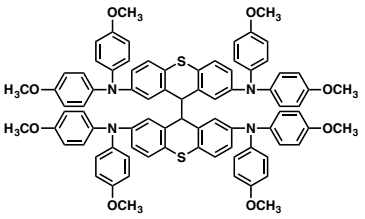

Compound **39** (280 mg, 0.43 mmol) was placed in a 100-mL round-bottomed flask and dissolved in anhydrous THF (25 mL). After the solution was cooled at -78 °C, solution of *n*-BuLi (2.5 M, 0.20 mL, 0.49 mmol) was slowly added and then stirred for 1 h. After that, Fe(acac)$_3$ (228 mg, 0.64 mmol) was added with a N_2 flow and the reaction was stirred at room temperature for 1 h. Then, the mixture was extracted with AcOEt and washed with a saturated NaCl solution. The combined organic extracts were dried over Na_2SO_4 and concentrated in vacuo. The crude was purified by flash column chromatography (silica gel, CH_2Cl_2) to afford **BTX-OMe** as a yellow solid (150 mg, 0.11 mmol), yield 54%. ^{1}H NMR (400 MHz, THF-d_8) δ/ppm: 7.52 (d, J = 8.5 Hz, 4H), 7.11-7.06 (m, 32H), 6.89 (dd, J_1 = 8.5, J_2 = 2.5 Hz, 4H), 6.31 (d, J = 2.5 Hz, 4H), 4.29 (s, 2H), 3.96 (s, 24H); ^{13}C NMR (101 MHz, $CDCl_3$) δ/ppm: 155.8, 146.8, 140.5, 137.9, 127.4, 127.0, 126.7, 123.9, 120.7, 118.1, 114.9, 114.7, 55.5, 48.4. FTIR (neat): 3036, 2933, 2948, 2932, 2903, 2831, 1591, 1502, 1466, 1237, 1176, 1033, 823, 575, 522 cm^{-1}; HRMS calcd for $C_{82}H_{70}N_4O_8S_2$ [M^+], 1302.4630; found 1302.4657; Elemental analysis calcd. for $C_{82}H_{70}N_4O_8S_2$, C: 75.55, H: 5.41, N: 4.30, S: 4.92%; found, C: 75.69, H: 5.29, N: 4.23, S: 4.94%.

7.7 Synthesis of triazatruxene-based (TAT) derivatives

10,15-Dihydro-5H-diindolo[3,2-*a*:3',2'-*c*]carbazole[158] (40)

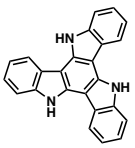

This compound was synthesized according to reported procedure [*J. Am. Chem. Soc.* **2015**, *137*, 16172-16178] and showed identical spectroscopic properties to those reported therein. ^{1}H NMR (400 MHz, DMSO-d_6) δ/ppm: 11.88 (s, 3H), 8.69 (d, J = 7.5 Hz, 3H), 7.74 (d, J = 7.7 Hz, 3H), 7.37 (m, 6H).

5,10,15-Trihexyl-10,15-dihydro-5H-diindolo[3,2-a:3',2'-c]carbazole[158] (41)

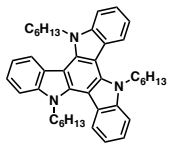

This compound was synthesized according to reported procedure [*J. Am. Chem. Soc.* **2015**, *137*, 16172-16178] and showed identical spectroscopic properties to those reported therein. ^{1}H NMR (400 MHz, $CDCl_3$) δ/ppm: 8.29 (d, J = 8.0 Hz, 3H), 7.64 (d, J = 8.0 Hz, 3H), 7.45 (t, J = 7.5 Hz, 3H), 7.34 (t, J = 7.5 Hz, 3H), 4.98 - 4.86 (m, 6H), 2.08 - 1.86 (m, 6H), 1.40 - 1.11 (m, 18H), 0.81 (t, J = 7.0 Hz, 9H).

2-Bromo-5,10,15-trihexyl-10,15-dihydro-5H-diindolo[3,2-*a*:3',2'-*c*] carbazole[267] (42)

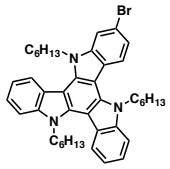

This compound was synthesized according to reported procedure [*RSC Adv.* **2016**, *6*, 6266–6275] and showed identical spectroscopic properties to those reported therein. ^{1}H NMR (400 MHz, $CDCl_3$) δ/ppm: 8.26 (dd, J_1 = 12.7, J_2 = 8.0 Hz, 2H), 8.10 (d, J = 8.6 Hz, 1H), 7.73 (d, J = 1.8 Hz, 1H), 7.63 (dd, J_1 = 8.0, J_2 = 3.4 Hz, 2H), 7.50 - 7.39 (m, 3H), 7.34 (t, J = 7.6 Hz, 2H), 4.96 - 4.78 (m, 6H), 2.07 - 1.82 (m, 6H), 1.39 - 1.13 (m, 18H), 0.83 - 0.79 (m, 9H).

2-(4,4,5,5-Tetramethyl-1,3,2-dioxaborolan-2-yl)-5,10,15-trihexyl-10,15-dihydro-5*H*-diindolo [3,2-*a*:3',2'-*c*]carbazole[267] (43)

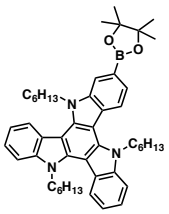

This compound was synthesized according to reported procedure [*RSC Adv.* **2016**, *6*, 6266–6275] and showed identical spectroscopic properties to those reported therein. ^{1}H NMR (400 MHz, $CDCl_3$) δ/ppm: 8.29 (d, *J* = 8.0 Hz, 3H), 8.10 (s, 1H), 7.80 (d, *J* = 8.1 Hz, 1H), 7.64 (d, *J* = 8.1 Hz, 2H), 7.45 (t, *J* = 7.5 Hz, 2H), 7.38 - 7.31 (m, 2H), 5.06 - 4.83 (m, 6H), 2.03 - 1.89 (m, 6H), 1.45 (s, 12H), 1.39 - 1.11 (m, 18H), 0.87 - 0.70 (m, 9H).

2-Amine-5,10,15-trihexyl-10,15-dihydro-5H-diindolo[3,2-*a*:3',2'-*c*] carbazole (44)

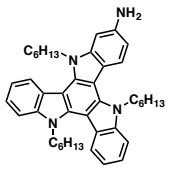

A solution of BINAP (87 mg, 0.19 mmol) and $Pd_2(dba)_3$ (128 mg, 0.19 mmol) in dry toluene under nitrogen atmosphere was stirred at 110 °C for 30 min. Then, the solution was allowed to reach r.t. and **34** (1 g, 1.48 mmol), benzophenone imine (0.5 mL, 2.46 mmol) and K^{t}BuO (332 mg, 2.46 mmol) were added. The mixture was heated at 110 °C for 72 h. The reaction was cooled down to r. t. and filtered through celite. Then, toluene was remove under vacuum and the residue was purified by column chromatography (hexane/ethyl acetate 9:1). Subsequently, the red intermediate (500 mg, 0.64 mmol) was dissolved in a mixture of THF (10 mL) and HCl (2N) (2 mL) and stirred at room temperature for 5 h. The reaction mixture was quenched with water. The resultant solution was extracted with dichloromethane (3x20 mL) and the organic fractions were washed with brine (2x15 mL) and then dried over $NaSO_4$ anhydrous and the solvent was removed under vacuum. The crude was purified by recrystallization in hexane/ethyl acetate 10/1 to afford the amino derivative **36** as a yellow-green solid. (250 mg, 0.41 mmol), yield 64%. ^{1}H NMR (400 MHz, DMSO-d_6) δ/ppm: 10.08 (s, 2H), 8.32 - 8.27 (m, 3H), 7.84 (dd, J_1 = 8.1, J_2 = 3.6 Hz, 2H), 7.74 (d, *J* = 1.4 Hz, 1H), 7.47 (t, *J* = 7.5 Hz, 2H), 7.39 - 7.26 (m, 3H), 4.98 - 4.93 (m, 6H), 1.80 - 1.70 (m, 6H), 1.05 - 0.97 (m, 18H), 0.70 - 0.54 (m, 9H); ^{13}C NMR (101 MHz, DMSO-d_6) δ/ppm: 140.7 (2), 138.6, 138.1, 137.6, 128.5, 123.2,

[267] M. Sang, S. Cao, J. Yi, J. Huang, W.-Y. Lai, W. Huang, *RSC Adv.* **2016**, *6*, 6266–6275.

122.3, 122.2 11.4, 120.0, 114.3, 111.3, 104.9, 103.1, 102.7, 102.3, 46.4, 46.0, 30.6, 28.8, 28.7, 25.4, 25.3, 21.7, 13.6; HRMS calcd. for $C_{42}H_{52}N_4$ [M^+] 612.4192; found 612.115.

2,5-Dibromo-3,4-ethylenedioxythiophene[268] (46)

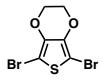

This compound was synthesized according to reported procedure [*Macromolecules* **2008***, 41,* 6012-6018] and showed identical spectroscopic properties to those reported therein. ^{1}H NMR (400 MHz, $CDCl_3$) δ/ppm: 4.13 (s, 4H).

2,5-Bis(2-thyenil)-3,4-ethylenedioxythiophene[269] (47)

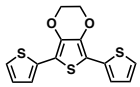

This compound was synthesized according to reported procedure [*Synth. Met.* **2015**, *207*, 65-71] and showed identical spectroscopic properties to those reported therein. ^{1}H NMR (400 MHz, DMSO-d_6) δ/ppm: 7.50 (dd, J_1 = 5.1 Hz, J_2 = 1.1 Hz, 2H), 7.23 (dd, J_1 = 3.6 Hz, J_2 = 1.1 Hz, 2H), 7.08 (dd, J_1 = 5.1 Hz, J_2 = 3.6 Hz, 2H), 4.42 (s, 4H).

2,5-Bis(5-bromo-2-thyenil)-3,4-ethylenedioxythiophene[269] (48)

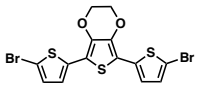

This compound was synthesized according to reported procedure [*Synth. Met.* **2015**, *207*, 65-71] and showed identical spectroscopic properties to those reported therein. ^{1}H NMR (400 MHz, Acetone-d_6) δ/ppm: 7.12 (d, J = 4.0 Hz, 2H), 7.04 (d, J = 4.0 Hz, 2H), 4.49 (s, 4H).

[268] J. Hou, M.-H. Park, S. Zhang, Y. Yao, L.-M. Chen, J.-H. Li, Y. Yang, *Macromolecules* **2008**, *41*, 6012–6018.

[269] I. Imae, K. Korai, Y. Ooyama, K. Komaguchi, Y. Harima, *Synth. Met.* **2015**, *207*, 65–71.

3,4-Ethylenedioxythiophene-2,5-dicarbaldehyde[270] (49)

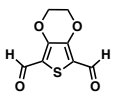

This compound was synthesized according to reported procedure [*Polymer* **2017**, *119*, 274-284] and showed identical spectroscopic properties to those reported therein. ^{1}H NMR (400 MHz, $CDCl_3$) δ/ppm: 10.04 (s, 2H), 4.44 (s, 4H).

DTTX-1

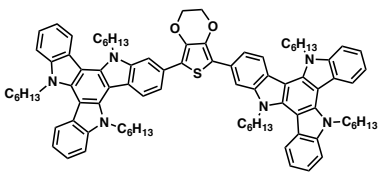

A solution of **46** (100 mg, 0.33 mmol), **43** (530 mg, 0.73 mmol), $Pd(PPh_3)_4$ (38 mg, 0.03 mmol) and K_3PO_4 (839 mg, 3.9 mmol) in dry DMF (10 mL) was degassed for 30 min under nitrogen. The reaction was heated at 100°C for 4 h and followed using TLC. After the reaction is completed, water was added and the formed precipitate was filtered. The solid was dissolved in DCM and washed with water (2x15 mL). The organic fraction was dried over Na_2SO_4 anhydrous and the solvent was removed under vacuum. The crude product was purified by column chromatography on silica gel with hexane/dichloromethane 2:1 as eluent to afford **DTTX-1** as a yellow solid (371 mg, 0.28 mmol), yield 84%. ^{1}H NMR (400 MHz, THF-d_8) δ/ppm: 8.34 - 8.30 (m, 6H), 8.24 (s, 2H), 7.79 (dd, J_1 = 8.3 Hz, J_2 = 0.9 Hz, 2H), 7.72 (dd, J_1 = 7.9 Hz, J_2 = 3.8 Hz, 4H), 7.41 (t, J = 7,6 Hz, 4H), 7.32 - 7.29 (m, 4H), 5.05 - 4.98 (m, 12H), 4.56 (s, 4H), 2.01 - 1.73 (m, 12H), 1.33 - 1.22 (m, 36H), 0.83 - 0.78 (m, 18H); ^{13}C NMR (101 MHz, THF-d_8) δ/ppm: 141.6, 141.3, 141.2, 139.3, 138.8, 138.7 (2), 138.4, 128.1, 123.5, 123.4, 122.6, 122.0, 121.4, 119.5, 118.0, 115.5, 110.6, 110.5, 108.0, 103.5, 103.4, 64.9, 46.7, 46.6, 31.4 (2), 31.3, 29.6, 29.5, 29.4, 26.2 (2), 22.4 (2), 13.4, 13.3; FTIR (neat): 3407, 2924, 2852, 1606, 1562, 1470, 1333, 1235, 1100, 889, 722 cm^{-1}; HRMS calcd. for $C_{90}H_{104}N_6O_2S$ [M^+]: 1333.7968; found 1333.7986; Elemental analysis calcd. for $C_{90}H_{104}N_6O_2S$, C: 81.04, H: 7.86, N: 6.30, S: 2.40%; found, C: 80.95, H: 7.91, N: 6.28, S: 2.37%.

[270] G. Garbay, L. Muccioli, E. Pavlopoulou, A. Hanifa, G. Hadziioannou, C. Brochon, E. Cloutet, *Polymer* **2017**, *119*, 274–284.

DTTX-2

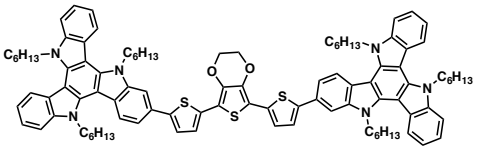

A solution of **48** (86 mg, 0.17 mmol), **43** (267 mg, 0.37 mmol), $Pd(PPh_3)_4$ (20 mg, 0,02 mmol) and K_3PO_4 (432 mg, 2.0 mmol) in dry DMF (8 mL) was degassed for 30 min under nitrogen. The reaction was heated at 100°C for 4 h. After the reaction is completed, water was added and the formed precipitate was filtered. The solid was dissolved in DCM and washed with water (2x15 mL). The organic fraction was dried over Na_2SO_4 anhydrous and the solvent was removed under vacuum. The crude product was purified by column chromatography on silica gel with hexane/dichloromethane 1:1 to afford **DTTX-2** as an orange solid. (173 mg, 0.12 mmol), yield 68%. ^{1}H NMR (400 MHz, THF-d_8) δ/ppm: 8.38 - 8.33 (m, 4H), 8.31 (d, J = 8.2 Hz, 2H), 8.00 (s, 2H), 7.74 (m, 4H), 7.67 (d, J = 8.0 Hz, 2H), 7.52 (d, J = 3.5 Hz, 2H), 7.47 - 7.42 (m, 4H), 7.38 - 7.31 (m, 6H), 5.11 - 5.06 (m, 4H), 5.03 - 4.98 (m, 8H), 4.52 (s, 4H), 1.99 - 1.94 (m, 12H), 1.39 - 1.18 (m, 36H), 0.89 - 0.79 (m, 18H); ^{13}C NMR (101 MHz, THF-d_8) δ/ppm: 143.6, 141.7, 141.3, 141.1, 139.4, 138.9, 138.3, 138.0, 133.3, 129.0, 123.7, 123.4, 123.3, 123.0, 122.7, 122.6, 121.7, 121.5, 121.4, 119.6, 119.5, 117.6, 110.6, 110.5, 109.3, 107.1, 103.5, 103.4, 65.2, 46.7, 46.6 (2), 31.4 (2), 31.3, 29.6, 19.5, 29.4, 26.2, 26.1 (2), 22.4 (2), 13.3 (2); FTIR (neat): 3407, 29243, 2852, 1606, 1565, 1470, 1443, 1406, 1333, 1284, 1100, 792, 722 cm^{-1}; HRMS calcd. for $C_{98}H_{108}N_6O_2S_3$ [M^+]: 1497.7722; found 1497.7724; Elemental analysis calcd. for $C_{98}H_{108}N_6O_2S_3$, C: 78.57, H: 7.27, N: 5.61, S: 6.42%; found, C: 78.70, H: 7.26, N: 5.64, S: 6.36%.

DTTX-3

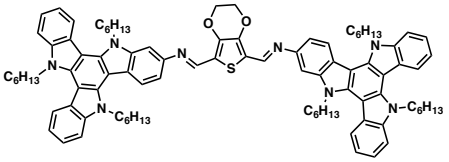

A mixture of **49** (195 mg, 0.32 mmol), **44** (30 mg, 0.15 mmol) and catalytic *p*-toluenesulfonic acid (PTSA) was dissolved in $CHCl_3$ and 2-propanol (6/2 mL) under nitrogen atmosphere. The red colored mixture was heated to reflux for 24 h and then was cooled down to room temperature and extracted with $CHCl_3$. The organic layer was washed with water (2x15 mL), brine (1x15 mL) and dried over $NaSO_4$ anhydrous. The

crude product was purified by column chromatography (dichloromethane:hexane 3:1) to afford **DTTX-3** as a red solid (160 mg, 0.12 mmol), yield 77%. ^{1}H NMR (400 MHz, THF-d_8) δ/ppm: 8.96 (s, 2H), 8.34 - 8.28 (m, 6H), 7.72 - 7.70 (m, 6H), 7.47 - 7.21 (m, 10H), 5.13 - 4.85 (m, 12H), 4.48 (s, 4H), 2.03 - 1.82 (m, 12H), 1.40 - 1.11 (m, 36H), 0.87 - 0.68 (m, 18H); ^{13}C NMR (101 MHz, THF-d_8) δ/ppm: 146.8, 146.4, 143.8, 142.1, 141.3, 141.3, 113.0, 110.6, 110.5, 104.6, 103.6, 103.5, 65.4, 46.7, 46.6, 31.4, 31.4, 29.5, 29.4 (2), 26.2, 26.1, 22.4, 22.3, 13.3, 13.2; FTIR (neat): 3407, 2921, 2848, 1607, 1565, 1464, 1404, 1362, 1331, 1238, 1086, 723 cm^{-1}; HRMS calcd. for $C_{92}H_{106}N_8O_2S$ [M^+]: 1387.8166; found 1387.8176; Elemental analysis calcd. for $C_{92}H_{106}N_8O_2S$, C: 79.61, H: 7.70, N: 8.07, S: 2.31%; found, C: 79.49, H: 7.82, N: 7.98, S: 2.36%.

7.8 Synthesis of nanographenes based on cyclooctatetraphenyl (CoPh) and cyclooctatetrathiophene (CoTh) derivatives

2-Amine-4,4'-methoxy-1,1'-biphenyl[248] (50)

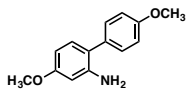

This compound was synthesized according to reported procedure [*Sci. Rep.* **2016**, *6*, 33131] and showed identical spectroscopic properties to those reported therein. ^{1}H NMR (400 MHz, $CDCl_3$) δ/ppm: 7.37 (m, 2H), 7.06 (d, J = 8.3 Hz, 1H), 6.98 (m, 2H), 6.45 (dd, J_1 = 8.4 Hz, J_2 = 2.5 Hz, 1H), 6.39 (d, J = 2.5 Hz, 1H), 3.86 (s, 3H), 3.83 (s, 3H).

2-Iodo-4,4'-methoxy-1,1'-biphenyl[248] (51)

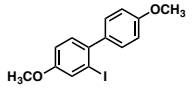

This compound was synthesized according to reported procedure [*Sci. Rep.* **2016**, *6*, 33131] and showed identical spectroscopic properties to those reported therein. ^{1}H NMR (400 MHz, $CDCl_3$) δ/ppm: 7.48 (t, J = 2.1 Hz, 1H), 7.25 (dd, J_1 = 8.0, J_2 = 2.1 Hz, 2H), 7.19 (dd, J_1 = 8.5, J_2 = 1.1 Hz, 1H), 6.96 - 6.91 (m, 3H), 3.86 (s, 3H), 3.82 (s, 3H).

2,7,10,15-Tetramethoxytetraphenylene[248] **(52)**

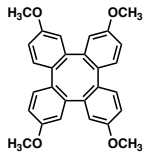

This compound was synthesized according to reported procedure [*Sci. Rep.* **2016**, *6*, 33131] and showed identical spectroscopic properties to those reported therein. ^{1}H NMR (400 MHz, $CDCl_3$) δ/ppm: 7.06 (d, J = 8.4 Hz, 4H), 6.82 (dd, J_1 = 8.4, J_2 = 2.7 Hz, 4H), 6.72 (d, J = 2.7 Hz, 4H), 3.77 (s, 12H).

Tetraphenylene-2,7,10,15-tetraol[248] **(53)**

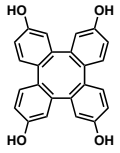

This compound was synthesized according to reported procedure [*Sci. Rep.* **2016**, *6*, 33131] and showed identical spectroscopic properties to those reported therein. ^{1}H NMR (400 MHz, $CDCl_3$) δ/ppm: 8.31 (s, 4H), 6.93 (d, J = 8.3 Hz, 4H), 6.74 (dd, J_1 = 8.3, J_2 = 2.6 Hz, 4H), 6.62 (d, J = 2.5 Hz, 4H).

2,7,10,15-Tetrakis(trifluoromethanesulfonate)tetraphenylene[248] **(54)**

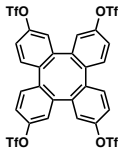

This compound was synthesized according to reported procedure [*Sci. Rep.* **2016**, *6*, 33131] and showed identical spectroscopic properties to those reported therein. ^{1}H NMR (400 MHz, $CDCl_3$) δ/ppm: 7.35 - 7.27 (m, 8H), 7.11 (d, J = 2.3 Hz, 4H).

2,7,10,15-Tetrakis((4-(*tert*-butyl)phenyl)ethynyl)tetraphenylene[247] **(55)**

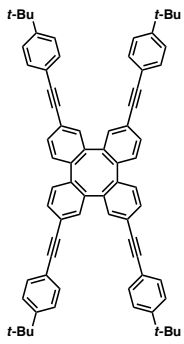

To a dry round bottom flask equipped with a stirrer bar, 2,7,10,15-tetrakis(trifluoromethanesulfonate)tetraphenylene (**54**) (285 mg 0.32 mmol), 4-*tert*-butylphenylacetylene (302 mg, 0.35 mL, 1.91 mmol), $Pd(OAc)_2$ (9 mg, 0.04 mmol), PPh_3 (40 mg, 0.15 mmol), K_3PO_4 (325 mg, 1.52 mmol) were dissolved in anhydrous DMSO (8 mL). The resulting mixture was heated at 85 °C for 16 hours. Then, the reaction was quenched with a saturated solution of NH_4Cl and extracted with $CHCl_3$. The organic extracts were washed with water and dried over Na_2SO_4. The elimination under vacuum of the organic solvent led to the crude product which was purified through flash column

chromatography (eluent; hexane:CH_2Cl_2, 4:1) to afford compound **55** (215 mg, 0.23 mmol) as a white solid, yield 73%. ^{1}H NMR (400 MHz, $CDCl_3$) δ/ppm: 7.49 (dd, J_1 = 7.9, J_2 = 1.7 Hz, 4H), 7.48 - 7.43 (m, 8H), 7.42 (d, J = 1.7 Hz, 4H), 7.40 - 7.34 (m, 8H), 7.19 (d, J = 7.9 Hz, 4H), 1.31 (s, 36H);); ^{13}C NMR (101 MHz, $CDCl_3$) δ/ppm: 151.6, 140.8, 140.6, 132.3, 131.9, 130.8, 129.1, 125.4, 122.9, 120.1, 90.4, 88.3, 34.8, 31.2; FTIR (neat): 3034, 2956, 2903, 1504, 1473, 1266, 830, 560 cm^{-1}; HRMS calcd. for $C_{72}H_{64}$ [M^+] 928.5003; found 928.4971.

Compound 56[247]

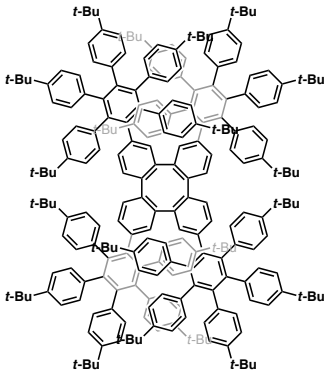

To a 10-mL microwave vial equipped with a magnetic stir bar, compound **55** (200 mg, 0.21 mmol) and tetra 2,3,4,5-tetrakis[4-(1,1-dimethylethyl)phenyl]2,4-cyclopentadien-1-one (655 mg, 1.07 mmol) were added. The reaction mixture was placed in the microwave reactor and heated to 280 °C for 30 minutes. After cooling, the resulting solid was purified through flash column chromatography (eluent; hexane:CH_2Cl_2, 4:1) to afford compound **56** (225 mg, 0.07 mmol) as a pale yellow solid, yield 32%. ^{1}H NMR (400 MHz, $CDCl_3$) δ/ppm: 6.85 - 6.77 (m, 32H), 6.73 - 6.65 (m, 32H), 6.63 - 6.58 (m, 12H), 6.55 (d, J = Hz, 4H), 6.27 (d, J = Hz, 4H), 6.16 (d, J = Hz, 4H), 5.57 (d, J = Hz, 4H), 1.14 (s, 36H), 1.11 (s, 36H), 1.10 (s, 36H), 1.09 (s, 36H), 1.05 (s, 36H); ^{13}C NMR (101 MHz, $CDCl_3$) δ/ppm: 147.5, 147.2, 147.1, 147.0, 140.7, 140.6, 140.4, 140.2, 139.5, 139.55, 139.4, 138.9, 138.6, 138.2, 138.1, 138.0, 137.8, 137.5, 132.3, 131.7, 131.1, 130.9, 130.1, 129.1, 128.5, 123.1, 123.0, 122.9, 122.5, 34.0, 31.7, 31.3, 31.2; FTIR (neat): 2968, 2866, 1660, 1613, 1460, 1361, 1268, 1201, 852, 618 cm^{-1}; HRMS calcd. for $C_{248}H_{272}$ [M^+] 3250.1279; found 3250.1291.

Compound 57[247]

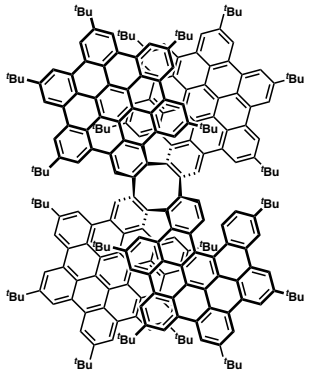

To a dry round bottom flask equipped with a magnetic stir bar compound **56** (110 mg, 0.032 mmol) was dissolved in dry CH_2Cl_2. The solution was cooled at 0 °C and bubbled with N_2 during the reaction. Afterwards, DDQ (767 mg, 3.38 mmol) was added in one portion, followed by the addition of CF_3SO_3H dropwise (2.5 mL). The resulting mixture was stirred for 20 minutes. After that, the mixture was quenched with H_2O and was extracted with CH_2Cl_2. The combined organic layers were dried over Na_2SO_4, filtered and concentrated under vacuum. The crude residue was purified through flash column chromatography (eluent; hexane:CH_2Cl_2, 5:1) to afford compound **57** (44 mg, 0.012 mmol) as a yellow solid, yield 40%. ^{1}H NMR (400 MHz, $CDCl_3$) δ/ppm 10.40 (s, 1H), 9.85 (d, *J* = 1.7 Hz, 1H), 9.71 (d, *J* = 1.7 Hz, 1H), 9.54 - 9.50 (m, 5H), 9.46 - 9.41 (m, 4H), 9.37 - 9.27 (m, 11H), 9.22 - 9.18 (m, 6H), 9.13 - 9.09 (m, 6H), 9.06 (d, *J* = 1.7 Hz, 1H), 9.05 (d, *J* = 1.7 Hz, 1H), 9.02 (d, *J* = 1.7 Hz, 1H), 8.98 - 8.90 (m, 8H), 8.76 (d, *J* = 1.7 Hz, 1H), 8.68 - 8.67 (m, 3H), 8.53 - 8.52 (m, 1H), 8.45 (d, *J* = 1.7 Hz, 1H), 8.51 - 8.50 (m, 1H), 8.14 (d, *J* = 1.7 Hz, 1H), 8.09 (d, *J* = 1.7 Hz, 1H), 2.11 (s, 9H), 1.88 (s, 9H), 1.87 (s, 9H), 1.85 (s, 9H), 1.79 (s, 9H), 1.75 (s, 9H), 1.74 (s, 18H), 1.72 (s, 9H), 1.70 (s, 9H), 1.65 (s, 18H), 1.56 (s, 9H), 1.54 (s, 9H), 1.50 (s, 9H), 1.44 (s, 9H), 1.15 (s, 9H), 0.69 (s, 9H), 0.41 (s, 9H), 0.26 (s, 9H); ^{13}C NMR (176 MHz, CD_2Cl_2) δ/ppm: 149.6 (2) 149.5, 149.4 (2), 149.3 (2), 149.2, 149.1, 149.0, 148.9, 148.5, 147.4, 147.1, 144.1, 143.6, 143.1, 142.9, 139.8, 138.7, 138.3, 132.7, 131.7, 131.20, 130.9 (2), 130.7, 130.6 (2), 130.5, 130.4 (2), 130.3 (2), 130.2 (2), 130.1, 130.0, 129.9 (2), 129.8 (2), 129.7, 129.5, 129.4 (3), 129.2, 129.0, 128.8 (2), 128.6, 128.4, 127.5, 127.0, 126.8, 126.5, 125.8, 124.5, 124.4, 124.3, 124.2, 123.9, 123.7, 123.6, 123.5, 123.2, 123.1, 123.0, 122.9 (2), 122.8, 122.6, 121.7, 121.2, 120.8, 120.7, 120.6, 120.5 (2), 120.4, 120.2, 120.1, 120.0, 119.8, 119.7, 119.4, 119.3, 119.0, 118.9, 118.8, 118.7, 118.5, 118.4, 53.8, 53.7, 53.6, 53.4, 53.2, 53.1, 36.2, 35.8, 35.7 (2), 35.6, 35.5 (3), 35.4 (4), 35.3, 35.1, 34.6, 34.3, 33.7, 32.6, 31.9, 31.7 (2), 31.6 (5), 31.4 (4), 30.6, 30.4, 29.8, 29.6; FTIR (neat): 2958, 2866, 1613, 1580, 1468, 1460, 1361, 1268, 943, 852, 668 cm^{-1}; HRMS calcd. for $C_{248}H_{226}$ [M^+] 3203.7679; found 3203.7605.

CoPh-NG[247]

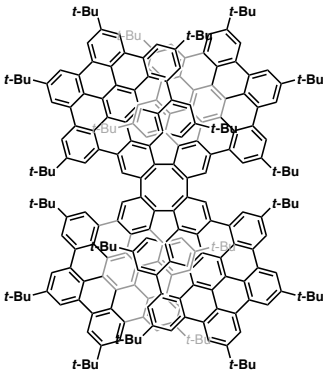

To a dry round bottom flask equipped with a magnetic stir bar compound **56** (100 mg, 0.031 mmol) was dissolved in dry dichloroethane (15 mL). The solution was heated at 85 °C and bubbled with N_2 for 30 minutes. Afterwards, a solution of $FeCl_3$ (502 mg, 3.09 mmol) in $MeNO_2$ (4 mL) was added dropwise. The resulting mixture was stirred for 12 hours at 85 °C. After that, the solvent was removed under reduced pressure and the mixture was washed with H_2O and extracted with CH_2Cl_2. The combined organic layers were dried over Na_2SO_4, filtered and concentrated under vacuum. The crude residue was purified through flash column chromatography (eluent; hexane:CH_2Cl_2, 3:1) to afford the desired compound **CoPh-NG** (44 mg, 0.014 mmol) as a yellow solid, yield 43%. ^{1}H NMR (400 MHz, $CDCl_3$) δ/ppm: 9.90 (s, 4H), 9.26 - 9.24 (m, 12H), 9.22 (bs, 4H), 9.18 (bs, 4H), 9.13 - 9.12 (m, 8H), 8.99 (bs, 4H), 8.90 (bs, 4H), 8.82 (bs, 4H), 1.77 (s, 36H), 1.72 (s, 36H), 1.66 (s, 36H), 1.41 (s, 36H), 0.67 (s, 36H); ^{13}C NMR (176 MHz, CD_2Cl_2) δ/ppm: 149.5, 149.3, 149.2, 149.1, 148.0, 144.1, 140.3, 130.9, 130.7, 130.4 (2), 130.3, 130.1, 130.0, 129.9, 129.7, 129.2, 128.2 (2), 124.5, 124.4, 123.7, 123.6, 123.4, 123.2, 121.0 (2), 120.7, 120.4, 120.3, 120.0, 119.9, 119.3, 119.1 (2), 119.0 (2), 118.7, 53.8 (2), 53.6 (2), 53.5, 53.4, 53.3, 53.1, 35.6 (2), 35.5, 35.4, 34.6, 31.6, 31.5 (2), 30.5; HRMS calcd. for $C_{248}H_{224}$ [M^+] 3201.7523; found 3201.7474.

2,5,8,11-Tetrakis((4-(*tert*-butyl)phenyl)ethynyl)cycloocta[1,2-*b*:4,3-*b′*:5,6-*b″*:8,7-*b‴*]tetrathiophene[247] **(58)**

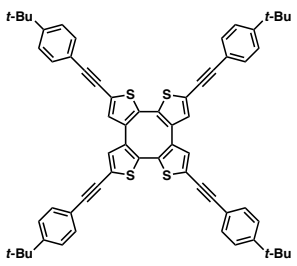

To a dry round bottom flask equipped with a stirrer bar, 2,5,8,11-tetrabromocycloocta[1,2-*b*:4,3-*b′*:5,6-*b″*:8,7-*b‴*]tetrathiophene (**25**) (520 mg 0.81 mmol), 4-tert-butylphenylacetylene (564 mg, 0.64 mL, 3.56 mmol), $Pd_2(dba)_3$ (74 mg, 0.08 mmol), $AsPh_3$ (25 mg, 0.08 mmol), were dissolved in anhydrous THF (20 mL) and anhydrous triethylamine (6 mL). The resulting mixture was heated at 65 °C overnight. The

reaction evolution was monitored by TLC and then allowed to reach room temperature. Then, the reaction was quenched with a saturated solution of NH_4Cl and extracted with $CHCl_3$. The organic extracts were washed with water and dried over Na_2SO_4. The elimination under vacuum of the organic solvent led to the crude product which was purified through flash column chromatography (eluent; hexane:CH_2Cl_2, 4:1) to afford compound **58** (760 mg, 0.80 mmol) as a yellow solid, yield 65%. ^{1}H NMR (400 MHz, $CDCl_3$) δ/ppm: 7.46 - 7.44 (m, 8H), 7.39 - 7.36 (m, 8H), 7.11 (s, 4H), 1.32 (s, 36H); ^{13}C NMR (101 MHz, $CDCl_3$) δ/ppm: 152.3, 136.1, 134.1, 132.8, 131.4, 125.9, 125.6, 119.7, 95.7, 81.3, 77.5, 77.4, 77.2, 76.8, 35.0, 31.5, 31.3; FTIR (neat): 2956, 2865, 1504, 1473, 1362, 1266, 830, 560 cm^{-1}; HRMS calcd. for $C_{64}H_{56}S_4$ [M+] 952.3259; found 952.3224.

Compound 59[247]

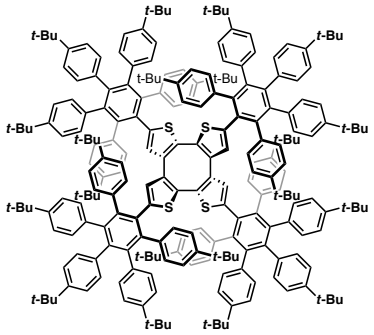

To a 10-mL microwave vial equipped with a magnetic stir bar, compound **58** (120 mg, 0.126 mmol) and tetra 2,3,4,5-tetrakis[4-(1,1-dimethylethyl)phenyl]2,4-cyclopentadien-1-one (383 mg, 0.63 mmol) were added. The reaction mixture was placed in the microwave reactor and heated to 300 °C for 20 minutes. After cooling, the resulting solid was purified through flash column chromatography (eluent; hexane:CH_2Cl_2, 4:1) to afford compound **59** (195 mg, 0.06 mmol) as a yellow solid, yield 47%. ^{1}H NMR (400 MHz, THF-d_8) δ/ppm: 6.93 - 6.90 (m, 20H), 6.84 - 6.78 (m, 26H), 6.72 - 6.70 (m, 10H), 6.63 - 6.58 (m, 24H), 5.05 (s, 4H), 1.20 (s, 72H), 1.10 (s, 72H), 1.08 (s, 36H); ^{13}C NMR (176 MHz, $CDCl_3$) δ/ppm: 147.3, 147.1, 141.1, 140.8, 140.3, 140.2, 138.1, 137.9, 137.5, 134.2, 132.9, 132.8, 132.3, 131.7, 130.9, 130.8, 123.7, 123.0, 122.9, 34.1, 34.0, 31.4, 31.3, 31.2, 31.1, 29.7; FTIR (neat): 2958, 2866, 1510, 1460, 1391, 1361, 1268, 1019, 838, 568 cm^{-1}; HRMS calcd for $C_{240}H_{264}S_4$ [M$^+$] 3273.9535; found 3273.9440.

CoTh-NG[247]

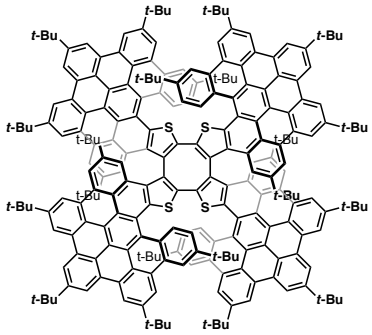

To a dry round bottom flask equipped with a magnetic stir bar compound 5**9** (70 mg, 0.021 mmol) was dissolved in dry CH_2Cl_2. The solution was cooled at 0 °C in an ice water bath and bubbled with N_2 during the reaction. Afterwards, a solution of $FeCl_3$ (347 mg, 2.137 mmol) in $MeNO_2$ (3 ml) and added dropwise. The resulting mixture was stirred for 30 minutes. After that, the solvent was then removed under reduced pressure and the mixture was washed with H_2O and extracted with CH_2Cl_2. The combined organic layers were dried over Na_2SO_4, filtered and concentrated under vacuum. The crude residue was purified through flash column chromatography (eluent; hexane:CH_2Cl_2, 6:1) to afford the desired **CoTh-NG** (18 mg, 0.006 mmol) as an orange solid, yield 26%. ^{1}H NMR (400 MHz, THF-d_8) δ/ppm: 9.37 - 9.30 (m, 12H), 9.27 (d, J = 1.6 Hz, 4H), 9.17 (d, J = 1.6 Hz, 4H), 9.04 (d, J = 8.4 Hz, 4H), 8.86 (d, J = 1.6 Hz, 4H), 8.77 (d, J = 1.6 Hz, 4H), 8.37 (d, J = 1.6 Hz, 4H), 7.53 (d, J = 1.6 Hz, 4H), 7.35 (dd, J = 8.5, 1.6 Hz, 4H); ^{13}C NMR (176 MHz, THF-d_8) δ/ppm: 152.0, 150.5, 150.3, 150.2, 149.2, 140.9, 137.0, 136.4, 134.3, 133.2, 132.0, 131.9, 131.8, 131.7, 131.4, 130.9, 130.4, 129.3, 127.8, 127.5, 124.6, 124.3, 124.0, 123.9 (2), 123.7, 123.2, 123.0, 122.5, 121.6, 121.5, 120.9, 120.2, 120.1, 119.8, 119.5, 119.2, 119.1, 117.5, 36.7, 36.6, 36.5 (2), 36.4, 35.8, 34.5, 33.0, 32.4 (3), 32.3 (3), 32.2 (2), 32.1, 32.0, 31.9, 31.8, 31.7 (2), 31.4, 31.1, 30.8 (2), 30.7 (2), 30.6, 30.5 (2), 23.7, 14.6; FTIR (neat): 2958, 2866, 1613, 1468, 1371, 1260, 943, 855 cm^{-1}; HRMS calcd for $C_{240}H_{224}S_4$ [M^+] 3233.6405; found 3233.6390.

8. References

[1] S. Solomon, G.-K. Plattner, R. Knutti, P. Friedlingstein, *Proc. Natl. Acad. Sci.* **2009**, *106*, 1704 LP – 1709.

[2] I. P. O. C. Change, Special Report of Global Warming of 1.5 ºC, 2018.

[3] U. S. E. I. Administration, "Annual Energy Outlook 2019," can be found under https://www.eia.gov/outlooks/aeo/pdf/aeo2019.pdf, 2019.

[4] A. Extance, *Nature* **2019**, *570*, 429–432.

[5] C. W. Tang, *Appl. Phys. Lett.* **1986**, *48*, 183–185.

[6] B. O'Regan, M. Grätzel, *Nature* **1991**, *353*, 737–740.

[7] M. A. Green, Y. Hishikawa, E. D. Dunlop, D. H. Levi, J. Hohl-Ebinger, M. Yoshita, A. W. Y. Ho-Baillie, *Prog. Photovoltaics Res. Appl.* **2019**, *27*, 3–12.

[8] B. M. Kayes, H. Nie, R. Twist, S. G. Spruytte, F. Reinhardt, I. C. Kizilyalli, G. S. Higashi, in 2011 37th IEEE Photovolt. Spec. Conf., **2011**, pp. 4–8.

[9] J. F. Geisz, M. A. Steiner, I. García, S. R. Kurtz, D. J. Friedman, *Appl. Phys. Lett.* **2013**, *103*, 41118.

[10] P. Jackson, D. Hariskos, R. Wuerz, O. Kiowski, A. Bauer, T. M. Friedlmeier, M. Powalla, *Phys. status solidi – Rapid Res. Lett.* **2015**, *9*, 28–31.

[11] T. K. Todorov, K. B. Reuter, D. B. Mitzi, *Adv. Mater.* **2010**, 22, E156–E159.

[12] W. Wang, M. T. Winkler, O. Gunawan, T. Gokmen, T. K. Todorov, Y. Zhu, D. B. Mitzi, *Adv. Energy Mater.* **2014**, *4*, 1301465.

[13] A. Hagfeldt, G. Boschloo, L. Sun, L. Kloo, H. Pettersson, *Chem. Rev.* **2010**, *110*, 6595–6663.

[14] S. Mathew, A. Yella, P. Gao, R. Humphry-Baker, F. E. Curchod-Basile, N. Ashari-Astani, I. Tavernelli, U. Rothlisberger, M. K. Nazeeruddin, M.

Grätzel, *Nat. Chem.* **2014**, *6*, 242–247.

[15] B. Kippelen, J.-L. Brédas, *Energy Environ. Sci.* **2009**, *2*, 251–261.

[16] S. Günes, H. Neugebauer, N. S. Sariciftci, *Chem. Rev.* **2007**, *107*, 1324–1338.

[17] Q. Liu, Y. Jiang, K. Jin, J. Qin, J. Xu, W. Li, J. Xiong, J. Liu, Z. Xiao, K.Sun, S. Yang, X. Zhang, L. Ding, *Sci. Bull.* **2020**, *65*, 272–275.

[18] H. Zhang, H. Yao, J. Hou, J. Zhu, J. Zhang, W. Li, R. Yu, B. Gao, S. Zhang, J. Hou, *Adv. Mater.* **2018**, *30*, 1800613.

[19] L. Meng, Y. Zhang, X. Wan, C. Li, X. Zhang, Y. Wang, X. Ke, Z. Xiao, L. Ding, R. Xia, H.-L. Yip, Y. Cao, Y. Chen, *Science* **2018**, *361*, 1094.

[20] C.-H. M. Chuang, P. R. Brown, V. Bulović, M. G. Bawendi, *Nat. Mater.* **2014**, *13*, 796.

[21] E. M. Sanehira, A. R. Marshall, J. A. Christians, S. P. Harvey, P. N. Ciesielski, L. M. Wheeler, P. Schulz, L. Y. Lin, M. C. Beard, J. M. Luther, *Sci. Adv.* **2017**, *3*, eaao4204.

[22] A. Kojima, K. Teshima, Y. Shirai, T. Miyasaka, *J. Am. Chem. Soc.* **2009**, *131*, 6050–6051.

[23] N. R. E. L. National Renewable Energy Laboratory, **2018**.

[24] N.-G. Park, *Mater. Today* **2015**, *18*, 65–72.

[25] A. Polman, M. Knight, E. C. Garnett, B. Ehrler, W. C. Sinke, *Science* **2016**, *352*, aad4424-9.

[26] A. Abate, J.-P. Correa-Baena, M. Saliba, M. S. Su'ait, F. Bella, *Chem. – A Eur. J.* **2018**, *24*, 3083–3100.

[27] R. A. B. John W. Anthony Kenneth W. Bladh, Monte C. Nichols, M. S. of America, Handbook of Mineralogy, **2001**.

[28] G. E. Eperon, S. D. Stranks, C. Menelaou, M. B. Johnston, L. M. Herz, H. J. Snaith, *Energy Environ. Sci.* **2014**, *7*, 982–988.

[29] A. D. Jodlowski, C. Roldán-Carmona, G. Grancini, M. Salado, M. Ralaiarisoa, S. Ahmad, N. Koch, L. Camacho, G. de Miguel, M. K.

Nazeeruddin, *Nat. Energy* **2017**, *2*, 972–979.

[30] M. Saliba, T. Matsui, J.-Y. Seo, K. Domanski, J.-P. Correa-Baena, M. K. Nazeeruddin, S. M. Zakeeruddin, W. Tress, A. Abate, A. Hagfeldt, M. Grätzel, *Energy Environ. Sci.* **2016**, *9*, 1989–1997.

[31] M. Saliba, T. Matsui, K. Domanski, J.-Y. Seo, A. Ummadisingu, S. M. Zakeeruddin, J.-P. Correa-Baena, W. R. Tress, A. Abate, A. Hagfeldt, M. Grätzel, *Science* **2016**, *354*, 206.

[32] F. Brivio, K. T. Butler, A. Walsh, M. van Schilfgaarde, *Phys. Rev. B* **2014**, *89*, 155204.

[33] D. B. Mitzi, *Inorg. Chem.* **2000**, *39*, 6107–6113.

[34] S. Kazim, M. K. Nazeeruddin, M. Grätzel, S. Ahmad, *Angew. Chem. Int. Ed.* **2014**, *53*, 2812–2824.

[35] H. S. Jung, N. G. Park, *Small* **2015**, *11*, 10–25.

[36] D. B. Mitzi, in Prog. Inorg. Chem., John Wiley & Sons, Inc., **1999**, pp. 1–121.

[37] Y. Zhao, K. Zhu, *Chem. Soc. Rev.* **2016**, *45*, 655–689.

[38] L. Zheng, Y. Ma, S. Chu, S. Wang, B. Qu, L. Xiao, Z. Chen, Q. Gong, Z. Wu, X. Hou, *Nanoscale* **2014**, *6*, 8171–8176.

[39] T. C. Sum, N. Mathews, *Energy Environ. Sci.* **2014**, *7*, 2518–2534.

[40] Y.-C. Hsiao, T. Wu, M. Li, Q. Liu, W. Qin, B. Hu, *J. Mater. Chem. A* **2015**, *3*, 15372–15385.

[41] F. Li, C. Ma, H. Wang, W. Hu, W. Yu, A. D. Sheikh, T. Wu, *Nat. Commun.* **2015**, *6*, 8238.

[42] Y. Li, W. Yan, Y. Li, S. Wang, W. Wang, Z. Bian, L. Xiao, Q. Gong, *Sci. Rep.* **2015**, *5*, 14485.

[43] Q. Dong, Y. Fang, Y. Shao, P. Mulligan, J. Qiu, L. Cao, J. Huang, *Science* **2015**, *347*, 967.

[44] V. D'Innocenzo, G. Grancini, M. J. P. Alcocer, A. R. S. Kandada, S. D. Stranks, M. M. Lee, G. Lanzani, H. J. Snaith, A. Petrozza, *Nat. Commu*n.

2014, *5*, 3586.

[45] J. C. Blancon, H. Tsai, W. Nie, C. C. Stoumpos, L. Pedesseau, C. Katan, M. Kepenekian, C. M. M. Soe, K. Appavoo, M. Y. Sfeir, S. Tretiak, P. M. Ajayan, M. G. Kanatzidis, J. Even, J. J. Crochet, A. D. Mohite, *Science* **2017**, *355*, 1288.

[46] T. J. Savenije, C. S. Ponseca, L. Kunneman, M. Abdellah, K. Zheng, Y. Tian, Q. Zhu, S. E. Canton, I. G. Scheblykin, T. Pullerits, A. Yartsev, V. Sundström, *J. Phys. Chem. Lett.* **2014**, *5*, 2189–2194.

[47] A. Jha, H.-G. Duan, V. Tiwari, P. K. Nayak, H. J. Snaith, M. Thorwart, R. J. D. Miller, *ACS Photonics* **2018**, *5*, 852–860.

[48] A. Marchioro, J. Teuscher, D. Friedrich, M. Kunst, R. van de Krol, T. Moehl, M. Grätzel, J.-E. Moser, *Nat. Photonics* **2014**, *8*, 250.

[49] J. H. Noh, S. H. Im, J. H. Heo, T. N. Mandal, S. I. Seok, *Nano Lett.* **2013**, *13*, 1764–1769.

[50] H. Zhao, Y. Han, Z. Xu, C. Duan, S. Yang, S. Yuan, Z. Yang, Z. Liu, S. (Frank) Liu, *Adv. Energy Mater.* **2019**, *9*, 1902279.

[51] N. Pellet, P. Gao, G. Gregori, T.-Y. Yang, M. K. Nazeeruddin, J. Maier, M. Grätzel, *Angew. Chem. Int. Ed.* **2014**, *53*, 3151–3157.

[52] N. J. Jeon, J. H. Noh, W. S. Yang, Y. C. Kim, S. Ryu, J. Seo, S. I. Seok, *Nature* **2015**, *517*, 476–480.

[53] A. F. Akbulatov, L. A. Frolova, D. V Anokhin, K. L. Gerasimov, N. N. Dremova, P. A. Troshin, *J. Mater. Chem. A* **2016**, *4*, 18378–18382.

[54] J. Kim, A. J. Yun, B. Gil, Y. Lee, B. Park, *Adv. Funct. Mater.* **2019**, *29*, 1905190.

[55] F. Gagan, G. Deepesh, T. Archana, *Interdiscip. Toxicol.* **2012**, *5*, 47–58.

[56] Z. Shi, J. Guo, Y. Chen, Q. Li, Y. Pan, H. Zhang, Y. Xia, W. Huang, *Adv. Mater.* **2017**, *29*, 1605005.

[57] T. Miyasaka, A. Kulkarni, G. M. Kim, S. Öz, A. K. Jena, *Adv. Energy Mater.* **2019**, *0*, 1902500.

[58] N. K. Noel, S. D. Stranks, A. Abate, C. Wehrenfennig, S. Guarnera, A.-

A. Haghighirad, A. Sadhanala, G. E. Eperon, S. K. Pathak, M. B. Johnston, A. Petrozza, L. M. Herz, H. J. Snaith, *Energy Environ. Sci.* **2014**, *7*, 3061–3068.

[59] W. Ke, P. Priyanka, S. Vegiraju, C. C. Stoumpos, I. Spanopoulos, C. M. M. Soe, T. J. Marks, M.-C. Chen, M. G. Kanatzidis, *J. Am. Chem. Soc.* **2018**, *140*, 388–393.

[60] S. J. Lee, S. S. Shin, Y. C. Kim, D. Kim, T. K. Ahn, J. H. Noh, J. Seo, S. Il Seok, *J. Am. Chem. Soc.* **2016**, *138*, 3974–3977.

[61] X. Liu, K. Yan, D. Tan, X. Liang, H. Zhang, W. Huang, *ACS Energy Lett.* **2018**, *3*, 2701–2707.

[62] L.-J. Chen, C.-R. Lee, Y.-J. Chuang, Z.-H. Wu, C. Chen, *J. Phys. Chem. Lett.* **2016**, *7*, 5028–5035.

[63] C. C. Stoumpos, L. Frazer, D. J. Clark, Y. S. Kim, S. H. Rhim, A. J. Freeman, J. B. Ketterson, J. I. Jang, M. G. Kanatzidis, *J. Am. Chem. Soc.* **2015**, *137*, 6804–6819.

[64] T. Krishnamoorthy, H. Ding, C. Yan, W. L. Leong, T. Baikie, Z. Zhang, M. Sherburne, S. Li, M. Asta, N. Mathews, S. G. Mhaisalkar, *J. Mater. Chem. A* **2015**, *3*, 23829–23832.

[65] M. Chen, M.-G. Ju, H. F. Garces, A. D. Carl, L. K. Ono, Z. Hawash, Y. Zhang, T. Shen, Y. Qi, R. L. Grimm, D. Pacifici, X. C. Zeng, Y. Zhou, N. P. Padture, *Nat. Commun.* **2019**, *10*, 16.

[66] B.-W. Park, B. Philippe, X. Zhang, H. Rensmo, G. Boschloo, E. M. J. Johansson, *Adv. Mater.* **2015**, *27*, 6806–6813.

[67] H.-S. Kim, C.-R. Lee, J.-H. Im, K.-B. Lee, T. Moehl, A. Marchioro, S.-J. Moon, R. Humphry-Baker, J.-H. Yum, J. E. Moser, M. Grätzel, N.-G. Park, *Sci. Rep.* **2012**, *2*, 591.

[68] M. M. Lee, J. Teuscher, T. Miyasaka, T. N. Murakami, H. J. Snaith, *Science* **2012**, *338*, 643–647.

[69] T. Salim, S. Sun, Y. Abe, A. Krishna, A. C. Grimsdale, Y. M. Lam, *J. Mater. Chem. A* **2015**, *3*, 8943–8969.

[70] H. Kim, K.-G. Lim, T.-W. Lee, *Energy Environ. Sci.* **2016**, *9*, 12–30.

[71] L. Meng, J. You, T.-F. Guo, Y. Yang, *Acc. Chem. Res.* **2016**, *49*, 155–165.

[72] W. Yan, S. Ye, Y. Li, W. Sun, H. Rao, Z. Liu, Z. Bian, C. Huang, *Adv. Energy Mater.* **2016**, *6*, 1600474.

[73] T. Matsui, T. Yamamoto, T. Nishihara, R. Morisawa, T. Yokoyama, T. Sekiguchi, T. Negami, *Adv. Mater.* **2019**, *31*, 1806823.

[74] S. D. Stranks, H. J. Snaith, *Nat. Nanotechnol.* **2015**, *10*, 391.

[75] T. Leijtens, G. E. Eperon, N. K. Noel, S. N. Habisreutinger, A. Petrozza, H. J. Snaith, *Adv. Energy Mater.* **2015**, *5*, 1500963.

[76] Q. Fu, X. Tang, B. Huang, T. Hu, L. Tan, L. Chen, Y. Chen, *Adv. Sci.* **2018**, *5*, 1700387.

[77] G. Grancini, C. Roldán-Carmona, I. Zimmermann, E. Mosconi, X. Lee, D. Martineau, S. Narbey, F. Oswald, F. De Angelis, M. Grätzel, M. K. Nazeeruddin, *Nat. Commun.* **2017**, *8*, 15684.

[78] A. Mei, X. Li, L. Liu, Z. Ku, T. Liu, Y. Rong, M. Xu, M. Hu, J. Chen, Y. Yang, M. Grätzel, H. Han, *Science* **2014**, *345*, 295.

[79] S. Guarnera, A. Abate, W. Zhang, J. M. Foster, G. Richardson, A. Petrozza, H. J. Snaith, *J. Phys. Chem. Lett.* **2015**, *6*, 432–437.

[80] G. Niu, W. Li, F. Meng, L. Wang, H. Dong, Y. Qiu, *J. Mater. Chem. A* **2014**, *2*, 705–710.

[81] X. Dong, X. Fang, M. Lv, B. Lin, S. Zhang, J. Ding, N. Yuan, *J. Mater. Chem. A* **2015**, *3*, 5360–5367.

[82] X. Xu, Z. Liu, Z. Zuo, M. Zhang, Z. Zhao, Y. Shen, H. Zhou, Q. Chen, Y. Yang, M. Wang, *Nano Lett.* **2015**, *15*, 2402–2408.

[83] F. Zhang, X. Yang, H. Wang, M. Cheng, J. Zhao, L. Sun, *ACS Appl. Mater. Interfaces* **2014**, *6*, 16140–16146.

[84] M. Jørgensen, K. Norrman, S. A. Gevorgyan, T. Tromholt, B. Andreasen, F. C. Krebs, *Adv. Mater.* **2012**, *24*, 580–612.

[85] F. Matteocci, S. Razza, F. Di Giacomo, S. Casaluci, G. Mincuzzi, T. M. Brown, A. D'Epifanio, S. Licoccia, A. Di Carlo, *Phys. Chem. Chem.*

Phys. **2014**, *16*, 3918–3923.

[86] I. Hwang, I. Jeong, J. Lee, M. J. Ko, K. Yong, *ACS Appl. Mater. Interfaces* **2015**, *7*, 17330–17336.

[87] H. Lin, C. Zhou, Y. Tian, T. Siegrist, B. Ma, *ACS Energy Lett.* **2018**, *3*, 54–62.

[88] G. Grancini, M. K. Nazeeruddin, *Nat. Rev. Mater.* **2019**, *4*, 4–22.

[89] Y. Chen, Y. Sun, J. Peng, J. Tang, K. Zheng, Z. Liang, *Adv. Mater.* **2018**, *30*, 1–15.

[90] H. Tsai, W. Nie, J.-C. Blancon, C. C. Stoumpos, R. Asadpour, B. Harutyunyan, A. J. Neukirch, R. Verduzco, J. J. Crochet, S. Tretiak, L. Pedesseau, J. Even, M. A. Alam, G. Gupta, L. Lou, P. M. Ajayan, M. J. Bedzyk, M. G. Kanatzidis, A. D. Mohite, *Nature* **2016**, *536*, 312–316.

[91] W. Tress, N. Marinova, T. Moehl, S. M. Zakeeruddin, M. K. Nazeeruddin, M. Grätzel, *Energy Environ. Sci.* **2015**, *8*, 995–1004.

[92] E. L. Unger, E. T. Hoke, C. D. Bailie, W. H. Nguyen, A. R. Bowring, T. Heumüller, M. G. Christoforo, M. D. McGehee, *Energy Environ. Sci.* **2014**, *7*, 3690–3698.

[93] S. van Reenen, M. Kemerink, H. J. Snaith, *J. Phys. Chem. Lett.* **2015**, *6*, 3808–3814.

[94] C. Eames, J. M. Frost, P. R. F. Barnes, B. C. O'Regan, A. Walsh, M. S. Islam, *Nat. Commun.* **2015**, *6*, 7497.

[95] H.-S. Kim, I. Mora-Sero, V. Gonzalez-Pedro, F. Fabregat-Santiago, E. J. Juarez-Perez, N.-G. Park, J. Bisquert, *Nat. Commun.* **2013**, *4*, 2242.

[96] V. W. Bergmann, S. A. L. Weber, F. Javier Ramos, M. K. Nazeeruddin, M. Grätzel, D. Li, A. L. Domanski, I. Lieberwirth, S. Ahmad, R. Berger, *Nat. Commun.* **2014**, *5*, 5001.

[97] S. N. Habisreutinger, N. K. Noel, H. J. Snaith, *ACS Energy Lett.* **2018**, *3*, 2472–2476.

[98] S. Maddala, C.-L. Chung, S.-Y. Wang, K. Kollimalayan, H.-L. Hsu, P. Venkatakrishnan, C.-P. Chen, Y. J. Chang, *Chem. Mater.* **2020**, *32*, 127–

138.

[99] N. J. Jeon, H. Na, E. H. Jung, T.-Y. Yang, Y. G. Lee, G. Kim, H.-W. Shin, S. I. Seok, J. Lee, J. Seo, *Nat. Energy* **2018**, 3, 682–689.

[100] M. Saliba, S. Orlandi, T. Matsui, S. Aghazada, M. Cavazzini, J.-P. Correa-Baena, P. Gao, R. Scopelliti, E. Mosconi, K.-H. Dahmen, F. de Angelis, A. Abate, A. Hagfeldt, G. Pozzi, M. Grätzel, M. K. Nazeeruddin, *Nat. Energy* **2016**, *1*, 15017.

[101] B. Xu, J. Zhang, Y. Hua, P. Liu, L. Wang, C. Ruan, Y. Li, G. Boschloo, E. M. J. Johansson, L. Kloo, A: Hagfeldt, A. K.-Y. Jen, L. Sun, *Chem* **2017**, *2*, 676–687.

[102] A. Molina-Ontoria, I. Zimmermann, I. Garcia-Benito, P. Gratia, C. Roldán-Carmona, S. Aghazada, M. Graetzel, M. K. Nazeeruddin, N. Martín, *Angew. Chem. Int. Ed.* **2016**, *55,* 6270–6274.

[103] N. Arora, M. I. Dar, A. Hinderhofer, N. Pellet, F. Schreiber, S. M. Zakeeruddin, M. Grätzel, *Science* **2017**, *358*, 768.

[104] W. Chen, Y. Wu, Y. Yue, J. Liu, W. Zhang, X. Yang, H. Chen, E. Bi, I. Ashraful, M. Grätzel, L. Han, *Science* **2015**, *350*, 944.

[105] G. Kim, J. Lee, G. Kang, T. Kim, T. Park, Adv. *Energy Mater*. **2018**, *8*, 1870018.

[106] Y. S. Kwon, J. Lim, H.-J. Yun, Y.-H. Kim, T. Park, *Energy Environ. Sci.* **2014**, *7*, 1454–1460.

[107] F. Bella, G. Griffini, J.-P. Correa-Baena, G. Saracco, M. Grätzel, A. Hagfeldt, S. Turri, C. Gerbaldi, *Science* **2016**, *354*, 203-206.

[108] M. M. Tavakoli, J. Zhao, R. Po, G. Bianchi, A. Cominetti, C. Carbonera, J. Kong, *Adv. Funct. Mater.* **2019**, *0*, 1905887.

[109] Q. Xiao, J. Tian, Q. Xue, J. Wang, B. Xiong, M. Han, Z. Li, Z. Zhu, H.-L. Yip, Z. Li, *Angew. Chem. Int. Ed.* **2019**, *58*, 17724–17730.

[110] F. Qi, X. Deng, X. Wu, L. Huo, Y. Xiao, X. Lu, Z. Zhu, A. K.-Y. Jen, *Adv. Energy Mater.* **2019**, *9*, 1902600.

[111] K. Walzer, B. Maennig, M. Pfeiffer, K. Leo, *Chem. Rev.* **2007**, *107*,

1233–1271.

[112] J. Urieta-Mora, I. García-Benito, A. Molina-Ontoria, N. Martín, *Chem. Soc. Rev.* **2018**, *47*, 8541–8571.

[113] B. Lüssem, M. Riede, K. Leo, *Phys. status solidi* **2013**, *210*, 9–43.

[114] U. Bach, D. Lupo, P. Comte, J. E. Moser, F. Weissörtel, J. Salbeck, H. Spreitzer, M. Grätzel, *Nature* **1998**, *395*, 583–585.

[115] J. Krüger, R. Plass, L. Cevey, M. Piccirelli, M. Grätzel, U. Bach, *Appl. Phys. Lett.* **2001**, *79*, 2085–2087.

[116] A. Abate, T. Leijtens, S. Pathak, J. Teuscher, R. Avolio, M. E. Errico, J. Kirkpatrik, J. M. Ball, P. Docampo, I. McPherson, H. J. Snaith, *Phys. Chem. Chem. Phys.* **2013**, *15*, 2572–2579.

[117] K. Rakstys, C. Igci, M. K. Nazeeruddin, *Chem. Sci.* **2019**, *10*, 6748–6769.

[118] D.-Y. Chen, W.-H. Tseng, S.-P. Liang, C.-I. Wu, C.-W. Hsu, Y. Chi, W.-Y. Hung, P.-T. Chou, *Phys. Chem. Chem. Phys.* **2012**, *14*, 11689–11694.

[119] M. A. Mahmud, N. K. Elumalai, M. B. Upama, D. Wang, V. R. Gonçales, M. Wright, C. Xu, F. Haque, A. Uddin, *Phys. Chem. Chem. Phys.* **2017**, *19*, 21033–21045.

[120] Q. Liu, L. Fan, Q. Zhang, A. Zhou, B. Wang, H. Bai, Q. Tian, B. Fan, T. Zhang, *ChemSusChem* **2017**, *10*, 3098–3104.

[121] T. Ye, J. Wang, W. Chen, Y. Yang, D. He, *ACS Appl. Mater. Interfaces* **2017**, *9*, 17923–17931.

[122] C. Chen, W. Zhang, J. Cong, M. Cheng, B. Zhang, H. Chen, P. Liu, R. Li, M. Safdari, L. Kloo, L. Sun, *ACS Energy Lett.* **2017**, *2*, 497–503.

[123] J. H. Noh, N. J. Jeon, Y. C. Choi, M. K. Nazeeruddin, M. Grätzel, S. I. Seok, *J. Mater. Chem. A* **2013**, *1*, 11842–11847.

[124] E. J. Juarez-Perez, M. R. Leyden, S. Wang, L. K. Ono, Z. Hawash, Y. Qi, *Chem. Mater.* **2016**, *28*, 5702–5709.

[125] T. P. I. Saragi, T. Spehr, A. Siebert, T. Fuhrmann-Lieker, J. Salbeck, *Chem. Rev.* **2007**, *107*, 1011–1065.

[126] R. G. Clarkson, M. Gomberg, *J. Am. Chem. Soc.* **1930**, *52*, 2881–2891.

[127] X. Li, D. Bi, C. Yi, J.-D. Décoppet, J. Luo, S. M. Zakeeruddin, A. Hagfeldt, M. Grätzel, *Science* **2016**, *353*, 58-62.

[128] W. S. Yang, B.-W. Park, E. H. Jung, N. J. Jeon, Y. C. Kim, D. U. Lee, S. S. Shin, J. Seo, E. K. Kim, J. H. Noh, S. I. Seok, *Science* **2017**, *356*, 1376.

[129] N. J. Jeon, H. G. Lee, Y. C. Kim, J. Seo, J. H. Noh, J. Lee, S. I. Seok, *J. Am. Chem. Soc.* **2014**, *136*, 7837–7840.

[130] L. P. Hammett, *J. Am. Chem. Soc.* **1937**, *59*, 96–103.

[131] L. Calió, S. Kazim, M. Grätzel, S. Ahmad, *Angew. Chem. Int. Ed.* **2016**, *55*, 14522–14545.

[132] Z. Hu, W. Fu, L. Yan, J. Miao, H. Yu, Y. He, O. Goto, H. Meng, H. Chen, W. Huang, *Chem. Sci.* **2016**, *7*, 5007–5012.

[133] L.-H. Xie, F. Liu, C. Tang, X.-Y. Hou, Y.-R. Hua, Q.-L. Fan, W. Huang, *Org. Lett.* **2006**, *8*, 2787–2790.

[134] D. Bi, B. Xu, P. Gao, L. Sun, M. Grätzel, A. Hagfeldt, *Nano Energy* **2016**, *23*, 138–144.

[135] B. Xu, D. Bi, Y. Hua, P. Liu, M. Cheng, M. Grätzel, L. Kloo, A. Hagfeldt, L. Sun, *Energy Environ. Sci.* **2016**, *9*, 873–877.

[136] P. Ganesan, K. Fu, P. Gao, I. Raabe, K. Schenk, R. Scopelliti, J. Luo, L. H. Wong, M. Gratzel, M. K. Nazeeruddin, *Energy Environ. Sci.* **2015**, *8*, 1986–1991.

[137] Y. Wang, T.-S. Su, H.-Y. Tsai, T.-C. Wei, Y. Chi, *Sci. Rep.* **2017**, *7*, 7859.

[138] Y. Wang, Z. Zhu, C. Chueh, K. -Y Jen Alex, Y. Chi, *Adv. Energy Mater.* **2017**, *7*, 1700823.

[139] Y. Lu, X. Zong, Y. Wang, W. Zhang, Q. Wu, M. Liang, S. Xue, *J. Mater. Chem. C* **2019**, *7*, 14306–14313.

[140] S. Kazim, F. J. Ramos, P. Gao, M. K. Nazeeruddin, M. Grätzel, S. Ahmad, *Energy Environ. Sci.* **2015**, *8*, 1816–1823.

[141] J. E. Anthony, J. S. Brooks, D. L. Eaton, S. R. Parkin, *J. Am. Chem. Soc.* **2001**, *123*, 9482–9483.

[142] L. Cabau, I. Garcia-Benito, A. Molina-Ontoria, N. F. Montcada, N. Martin, A. Vidal-Ferran, E. Palomares, *Chem. Commun.* **2015**, *51*, 13980–13982.

[143] H. Choi, K. Do, S. Park, J.-S. Yu, J. Ko, *Chem. – A Eur. J.* **2015**, *21*, 15919–15923.

[144] H. Nishimura, N. Ishida, A. Shimazaki, A. Wakamiya, A. Saeki, L. T. Scott, Y. Murata, *J. Am. Chem. Soc.* **2015**, *137*, 15656–15659.

[145] M. A. Truong, J. Lee, T. Nakamura, J.-Y. Seo, M. Jung, M. Ozaki, A. Shimazaki, N. Shioya, T. Hasegawa, Y. Murata, S. M. Zakeeruddin, M. Grätzel, R. Murdey, A. Wakamiya, *Chem. – A Eur. J.* **2019**, *25*, 6741–6752.

[146] S. Park, J. H. Heo, C. H. Cheon, H. Kim, S. H. Im, H. J. Son, *J. Mater. Chem. A* **2015**, *3*, 24215–24220.

[147] S. Park, J. H. Heo, J. H. Yun, T. S. Jung, K. Kwak, M. J. Ko, C. H. Cheon, J. Y. Kim, S. H. Im, H. J. Son, *Chem. Sci.* **2016**, *7*, 5517–5522.

[148] J. Zhang, Y. Hua, B. Xu, L. Yang, P. Liu, M. B. Johansson, N. Vlachopoulos, L. Kloo, G. Boschloo, E. M. J. Johansson, L. Sun, A. Hagfeldt, *Adv. Energy Mater.* **2016**, *6*, 1601062.

[149] I. Gelmetti, N. F. Montcada, A. Pérez-Rodríguez, E. Barrena, C. Ocal, I. García-Benito, A. Molina-Ontoria, N. Martín, A. Vidal-Ferran, E. Palomares, *Energy Environ. Sci.* **2019**, *12*, 1309–1316.

[150] T. Malinauskas, M. Saliba, T. Matsui, M. Daskeviciene, S. Urnikaite, P. Gratia, R. Send, H. Wonneberger, I. Bruder, M. Grätzel, V. Getautis, M. K. Nazeeruddin, *Energy Environ. Sci.* **2016**, *9*, 1681–1686.

[151] D. Li, J.-Y. Shao, Y. Li, Y. Li, L.-Y. Deng, Y.-W. Zhong, Q. Meng, *Chem. Commun.* **2018**, *54*, 1651–1654.

[152] Q.-Q. Ge, J.-Y. Shao, J. Ding, L.-Y. Deng, W.-K. Zhou, Y.-X. Chen, J.-Y. Ma, L.-J. Wan, J. Yao, J.-S. Hu, Y.-W. Zhong, *Angew. Chem. Int. Ed.* **2018**, *57*, 10959–10965.

[153] X. Sun, Q. Xue, Z. Zhu, Q. Xiao, K. Jiang, H.-L. Yip, H. Yan, Z. Li, *Chem. Sci.* **2018**, *9*, 2698–2704.

[154] M. Ren, J. Wang, X. Xie, J. Zhang, P. Wang, *ACS Energy Lett.* **2019**, *4*, 2683–2688.

[155] Y. Shen, C.-F. Chen, *Chem. Rev.* **2012**, *112*, 1463–1535.

[156] P. J. Evans, J. Ouyang, L. Favereau, J. Crassous, I. Fernández, J. Perles, N. Martín, *Angew. Chem. Int. Ed.* **2018**, *57*, 6774–6779.

[157] F. Liu, F. Wu, Z. Tu, Q. Liao, Y. Gong, L. Zhu, Q. Li, Z. Li, *Adv. Funct. Mater.* **2019**, *29*, 1901296.

[158] K. Rakstys, A. Abate, M. I. Dar, P. Gao, V. Jankauskas, G. Jacopin, E. Kamarauskas, S. Kazim, S. Ahmad, M. Grätzel, M. K. Nazeeruddin, *J. Am. Chem. Soc.* **2015**, *137*, 16172–16178.

[159] P.-Y. Su, L.-B. Huang, J.-M. Liu, Y.-F. Chen, L.-M. Xiao, D.-B. Kuang, M. Mayor, C.-Y. Su, *J. Mater. Chem. A* **2017**, *5*, 1913–1918.

[160] K. Rakstys, S. Paek, P. Gao, P. Gratia, T. Marszalek, G. Grancini, K. T. Cho, K. Genevicius, V. Jankauskas, W. Pisula, M. K. Nazeeruddin, *J. Mater. Chem. A* **2017**, *5*, 7811–7815.

[161] S. Paek, P. Qin, Y. Lee, K. T. Cho, P. Gao, G. Grancini, E. Oveisi, P. Gratia, K. Rakstys, S. A. Al-Muhtaseb, C. Ludwig, J. Ko, M. K. Nazeeruddin, *Adv. Mater.* **2017**, *29*, 1606555.

[162] R. Grisorio, B. Roose, S. Colella, A. Listorti, G. P. Suranna, A. Abate, *ACS Energy Lett.* **2017**, *2*, 1029–1034.

[163] I. Cho, N. J. Jeon, O. K. Kwon, D. W. Kim, E. H. Jung, J. H. Noh, J. Seo, S. I. Seok, S. Y. Park, *Chem. Sci.* **2017**, *8*, 734–741.

[164] M. Daskeviciene, S. Paek, Z. Wang, T. Malinauskas, G. Jokubauskaite, K. Rakstys, K. T. Cho, A. Magomedov, V. Jankauskas, S. Ahmad, H. J. Snaith, V. Getautis, M. K. Nazeeruddin, *Nano Energy* **2017**, *32*, 551–557.

[165] B. Cai, X. Yang, X. Jiang, Z. Yu, A. Hagfeldt, L. Sun, *J. Mater. Chem. A* **2019**, *7*, 14835–14841.

[166] F. Liu, F. Wu, W. Ling, Z. Tu, J. Zhang, Z. Wei, L. Zhu, Q. Li, Z. Li, *ACS Energy Lett.* **2019**, *4*, 2514–2521.

[167] A. Mishra, P. Bäuerle, *Angew. Chem. Int. Ed.* **2012**, 51, 2020–2067.

[168] H. Bronstein, Z. Chen, R. S. Ashraf, W. Zhang, J. Du, J. R. Durrant, P. Shakya Tuladhar, K. Song, S. E. Watkins, Y. Geerts, M. M. Wienk, R. A. Janssen, T. Anthopoulos, H. Sirringhaus, M. Heeney, I. McCulloch, *J. Am. Chem. Soc.* **2011**, *133*, 3272–3275.

[169] J. H. Seo, E. B. Namdas, A. Gutacker, A. J. Heeger, G. C. Bazan, *Adv. Funct. Mater.* **2011**, *21*, 3667–3672.

[170] H. Li, K. Fu, A. Hagfeldt, M. Grätzel, S. G. Mhaisalkar, A. C. Grimsdale, *Angew. Chem. Int. Ed.* **2014**, *53*, 4085–4088.

[171] M. L. Petrus, T. Bein, T. J. Dingemans, P. Docampo, *J. Mater. Chem. A* **2015**, *3*, 12159–12162.

[172] M. L. Petrus, K. Schutt, M. T. Sirtl, E. M. Hutter, A. C. Closs, J. M. Ball, J. C. Bijleveld, A. Petrozza, T. Bein, T. J. Dingemans, T. J. Savenije, H. Snaith, P. Docampo, *Adv. Energy Mater.* **2018**, *8*, 1801605.

[173] F. Zhang, Z. Wang, H. Zhu, N. Pellet, J. Luo, C. Yi, X. Liu, H. Liu, S. Wang, X. Li, Y. Xiao, S. M. Zakeeruddin, D. Bi, *Nano Energy* **2017**, *41*, 469–475.

[174] I. Garcia-Benito, I. Zimmermann, J. Urieta-Mora, J. Arago, A. Molina-Ontoria, E. Orti, N. Martin, M. K. Nazeeruddin, *J. Mater. Chem. A* **2017**, *5*, 8317–8324.

[175] Y.-K. Peng, K.-M. Lee, C.-C. Ting, M.-W. Hsu, C.-Y. Liu, *J. Mater. Chem. A* **2019**, *7*, 24765–24770.

[176] B. Kan, Q. Zhang, M. Li, X. Wan, W. Ni, G. Long, Y. Wang, X. Yang, H. Feng, Y. Chen, *J. Am. Chem. Soc.* **2014**, *136*, 15529–15532.

[177] L. Yuan, Y. Zhao, J. Zhang, Y. Zhang, L. Zhu, K. Lu, W. Yan, Z. Wei, *Adv. Mater.* **2015**, *27*, 4229–4233.

[178] R. Sandoval-Torrientes, I. Zimmermann, J. Calbo, J. Aragó, J. Santos, E. Ortí, N. Martín, M. K. Nazeeruddin, *J. Mater. Chem. A* **2018**, *6*, 5944–5951.

[179] M. Cheng, K. Aitola, C. Chen, F. Zhang, P. Liu, K. Sveinbjörnsson, Y. Hua, L. Kloo, G. Boschloo, L. Sun, *Nano Energy* **2016**, *30*, 387–397.

[180] X. Yin, J. Zhou, Z. Song, Z. Dong, Q. Bao, N. Shrestha, S. S. Bista, R. J. Ellingson, Y. Yan, W. Tang, *Adv. Funct. Mater.* **2019**, *29*, 1904300.

[181] J. Zhou, X. Yin, Z. Dong, A. Ali, Z. Song, N. Shrestha, S. S. Bista, Q. Bao, R. J. Ellingson, Y. Yan, W. Tang, *Angew. Chem. Int. Ed.* **2019**, *58*, 13717–13721.

[182] J. Wang, H. Zhang, B. Wu, Z. Wang, Z. Sun, S. Xue, Y. Wu, A. Hagfeldt, M. Liang, *Angew. Chem. Int. Ed.* **2019**, *58*, 15721–15725.

[183] Y. Shi, K. Hou, Y. Wang, K. Wang, H. Ren, M. Pang, F. Chen, S. Zhang, *J. Mater. Chem. A* **2016**, *4*, 5415–5422.

[184] N. Xu, Y. Li, R. Wu, R. Zhu, J. Zhang, S. M. Zakeeruddin, H. Li, Z.-S. Li, M. Grätzel, P. Wang, *Chem. – A Eur. J.* **2019**, *25*, 945–948.

[185] Y. Cao, Y. Li, T. Morrissey, B. Lam, B. O. Patrick, D. J. Dvorak, Z. Xia, T. L. Kelly, C. P. Berlinguette, *Energy Environ. Sci.* **2019**, *12*, 3502–3507.

[186] H.-Y. Chen, J. Hou, A. E. Hayden, H. Yang, K. N. Houk, Y. Yang, *Adv. Mater.* **2010**, *22*, 371–375.

[187] M. C. Scharber, M. Koppe, J. Gao, F. Cordella, M. A. Loi, P. Denk, M. Morana, H.-J. Egelhaaf, K. Forberich, G. Dennler, R. Gaudiana, D. Waller, Z. Zhu, X. Shi, C. J. Brabec, *Adv. Mater.* **2010**, *22*, 367–370.

[188] R. Xue, M. Zhang, G. Xu, J. Zhang, W. Chen, H. Chen, M. Yang, C. Cui, Y. Li, Y. Li, *J. Mater. Chem. A* **2018**, *6*, 404–413.

[189] A. Yella, C.-L. Mai, S. M. Zakeeruddin, S.-N. Chang, C.-H. Hsieh, C.-Y. Yeh, M. Grätzel, *Angew. Chem. Int. Ed.* **2014**, *53*, 2973–2977.

[190] K. Gao, L. Li, T. Lai, L. Xiao, Y. Huang, F. Huang, J. Peng, Y. Cao, F. Liu, T. P. Russell, R. A. Janssen, X. Peng, *J. Am. Chem. Soc.* **2015**, *137*, 7282–7285.

[191] A. Varotto, C.-Y. Nam, I. Radivojevic, J. P. C. Tomé, J. A. S. Cavaleiro, C. T. Black, C. M. Drain, *J. Am. Chem. Soc.* **2010**, *132*, 2552–2554.

[192] M. Urbani, G. de la Torre, M. K. Nazeeruddin, T. Torres, *Chem. Soc. Rev.* **2019**, *48*, 2738–2766.

[193] S. Chen, P. Liu, Y. Hua, Y. Li, L. Kloo, X. Wang, B. Ong, W.-K. Wong, X. Zhu, *ACS Appl. Mater. Interfaces* **2017**, *9*, 13231–13239.

[194] R. Azmi, U.-H. Lee, F. T. A. Wibowo, S. H. Eom, S. C. Yoon, S.-Y. Jang, I. H. Jung, *ACS Appl. Mater. Interfaces* **2018**, *10*, 35404–35410.

[195] J. Cao, X. Lv, P. Zhang, T. T. Chuong, B. Wu, X. Feng, C. Shan, J. Liu, Y. Tang, *Adv. Mater.* **2018**, *30*, 1800568.

[196] T. Duong, J. Peng, D. Walter, J. Xiang, H. Shen, D. Chugh, M. Lockrey, D. Zhong, J. Li, K. Weber, T. P. White, K. R. Catchpole, *ACS Energy Lett.* **2018**, *3*, 2441–2448.

[197] M. Cheng, Y. Li, M. Safdari, C. Chen, P. Liu, L. Kloo, L. Sun, *Adv. Energy Mater.* **2017**, *7*, 1602556.

[198] Q. Hu, E. Rezaee, M. Li, Q. Chen, Y. Cao, M. Mayukh, D. V McGrath, Z.-X. Xu, *ACS Appl. Mater. Interfaces* **2019**, *11*, 36535–36543.

[199] A. C. Arias, J. D. MacKenzie, I. McCulloch, J. Rivnay, A. Salleo, *Materials and Applications for Large Area Electronics: Solution-Based Approaches*, American Chemical Society, **2010**.

[200] J. L. Delgado, P.-A. Bouit, S. Filippone, M. Á. Herranz, N. Martín, *Chem. Commun.* **2010**, *46*, 4853–4865.

[201] C. Wang, H. Dong, W. Hu, Y. Liu, D. Zhu, *Chem. Rev.* **2012**, *112*, 2208–2267.

[202] S. C. Rasmussen, S. J. Evenson, C. B. McCausland, *Chem. Commun.* **2015**, *51*, 4528–4543.

[203] T. Parker, S. Marder, *Synthetic Methods in Organic Electronic and Photonic Materials*, Royal Society Of Chemistry, **2015**.

[204] N. K. Noel, A. Abate, S. D. Stranks, E. S. Parrott, V. M. Burlakov, A. Goriely, H. J. Snaith, *ACS Nano* **2014**, *8*, 9815–9821.

[205] J. Cao, J. Yin, S. Yuan, Y. Zhao, J. Li, N. Zheng, *Nanoscale* **2015**, *7*, 9443–9447.

[206] Y. Lin, L. Shen, J. Dai, Y. Deng, Y. Wu, Y. Bai, X. Zheng, J. Wang, Y. Fang, H. Wei, W. Ma, X. C. Zeng, X. Zhan, J. Huang, *Adv. Mater.* **2017**, *29*, 1604545.

[207] W.-J. Liu, Y. Zhou, Y. Ma, Y. Cao, J. Wang, J. Pei, *Org. Lett.* **2007**, *9*, 4187–4190.

[208] J. L. Brusso, O. D. Hirst, A. Dadvand, S. Ganesan, F. Cicoira, C. M. Robertson, R. T. Oakley, F. Rosei, D. F. Perepichka, *Chem. Mater.* **2008**, *20*, 2484–2494.

[209] I. Zimmermann, J. Urieta-Mora, P. Gratia, J. Aragó, G. Grancini, A. Molina-Ontoria, E. Ortí, N. Martín, M. K. Nazeeruddin, *Adv. Energy Mater.* **2017**, *7*, 1601674.

[210] K. Rakstys, M. Saliba, P. Gao, P. Gratia, E. Kamarauskas, S. Paek, V. Jankauskas, M. K. Nazeeruddin, *Angew. Chem. Int. Ed.* **2016**, *55*, 7464–7468.

[211] A. N. Sokolov, S. Atahan-Evrenk, R. Mondal, H. B. Akkerman, R. S. Sánchez-Carrera, S. Granados-Focil, J. Schrier, S. C. B. Mannsfeld, A. P. Zoombelt, Z. Bao, A. Aspuru-Guzik, *Nat. Commun.* **2011**, *2*, 437.

[212] F. Giordano, A. Abate, J. P. Correa Baena, M. Saliba, T. Matsui, S. H. Im, S. M. Zakeeruddin, M. K. Nazeeruddin, A. Hagfeldt, M. Grätzel, *Nat. Commun.* **2016**, *7*, 10379.

[213] P. Gratia, A. Magomedov, T. Malinauskas, M. Daskeviciene, A. Abate, S. Ahmad, M. Grätzel, V. Getautis, M. K. Nazeeruddin, *Angew. Chem. Int. Ed.* **2015**, *54*, 11409–11413.

[214] C. Roldán-Carmona, P. Gratia, I. Zimmermann, G. Grancini, P. Gao, M. Graetzel, M. K. Nazeeruddin, *Energy Environ. Sci.* **2015**, *8*, 3550–3556.

[215] E. Mosconi, G. Grancini, C. Roldán-Carmona, P. Gratia, I. Zimmermann, M. K. Nazeeruddin, F. De Angelis, *Chem. Mater.* **2016**, *28*, 3612–3615.

[216] J. Urieta-Mora, I. Zimmermann, J. Aragó, A. Molina-Ontoria, E. Ortí, N. Martín, M. K. Nazeeruddin, *Chem. Mater.* **2019**, *31*, 6435–6442.

[217] J. Aragó, P. M. Viruela, E. Ortí, R. Malavé Osuna, B. Vercelli, G. Zotti, V. Hernández, J. T. López Navarrete, J. T. Henssler, A. J. Matzger, Y.

Suzuki, S. Yamaguchi, *Chem. – A Eur. J.* **2010**, *16*, 5481–5491.

[218] Y. Yao, H. Dong, W. Hu, *Adv. Mater.* **2016**, *28*, 4513–4523.

[219] T. Kauffmann, B. Greving, R. Kriegesmann, A. Mitschker, A. Woltermann, *Chem. Ber.* **1978**, *111*, 1330–1336.

[220] Y. Wang, Z. Wang, D. Zhao, Z. Wang, Y. Cheng, H. Wang, *Synlett* **2007**, *2007*, 2390–2394.

[221] Y. Wang, D. Gao, J. Shi, Y. Kan, J. Song, C. Li, H. Wang, *Tetrahedron* **2014**, *70*, 631–636.

[222] J. Urieta-Mora, I. García-Benito, I. Zimmermann, J. Aragó, J. Calbo, G. Grancini, A. Molina-Ontoria, E. Ortí, N. Martín, M. K. Nazeeruddin, *J. Mater. Chem. C* **2019**, *7*, 6656–6663.

[223] T. Kashiki, S. Shinamura, M. Kohara, E. Miyazaki, K. Takimiya, M. Ikeda, H. Kuwabara, *Org. Lett.* **2009**, *11*, 2473–2475.

[224] I. García-Benito, I. Zimmermann, J. Urieta-Mora, J. Aragó, J. Calbo, J. Perles, A. Serrano, A. Molina-Ontoria, E. Ortí, N. Martín, M. K. Nazeeruddin, *Adv. Funct. Mater.* **2018**, *28*, 1801734.

[225] H. Yao, L. Ye, H. Zhang, S. Li, S. Zhang, J. Hou, *Chem. Rev.* **2016**, *116*, 7397–7457.

[226] I. J. Al-Busaidi, A. Haque, N. K. Al Rasbi, M. S. Khan, *Synth. Met.* **2019**, *257*, 116189.

[227] S. P. Massie, *Chem. Rev.* **1954**, *54*, 797–833.

[228] Y.-K. Wang, S.-F. Wu, Y. Yuan, S.-H. Li, M.-K. Fung, L.-S. Liao, Z.-Q. Jiang, *Org. Lett.* **2017**, *19*, 3155–3158.

[229] Y.-K. Wang, S.-H. Li, S.-F. Wu, C.-C. Huang, S. Kumar, Z.-Q. Jiang, M.-K. Fung, L.-S. Liao, *Adv. Funct. Mater.* **2018**, *28*, 1706228.

[230] H. Jiang, J. Sun, *New J. Chem.* **2013**, *37*, 3161–3165.

[231] J. Urieta-Mora, I. García-Benito, I. Zimmermann, J. Aragó, P. D. García-Fernández, G. Grancini, A. Molina-Ontoria, E. Ortí, N. Martín, M. K. Nazeeruddin, *Helv. Chim. Acta* **2019**, *102*, e1900056.

[232] B. K. Sharma, A. M. Shaikh, R. M. Kamble, *J. Chem. Sci.* **2015**, *127*, 2063–2071.

[233] S. Dadashi-Silab, H. Bildirir, R. Dawson, A. Thomas, Y. Yagci, *Macromolecules* **2014**, *47*, 4607–4614.

[234] P. M. Bogie, L. R. Holloway, Y. Lyon, N. C. Onishi, G. J. O. Beran, R. R. Julian, R. J. Hooley, *Inorg. Chem.* **2018**, *57*, 4155–4163.

[235] T. Malinauskas, D. Tomkute-Luksiene, R. Sens, M. Daskeviciene, R. Send, H. Wonneberger, V. Jankauskas, I. Bruder, V. Getautis, *ACS Appl. Mater. Interfaces* **2015**, *7,* 11107–11116.

[236] V. Bocchi, G. Palla, *Tetrahedron* **1986**, *42*, 5019–5024.

[237] X.-C. Li, C.-Y. Wang, W.-Y. Lai, W. Huang, *J. Mater. Chem. C* **2016**, *4*, 10574–10587.

[238] I. Bulut, P. Chávez, A. Mirloup, Q. Huaulmé, A. Hébraud, B. Heinrich, S. Fall, S. Méry, R. Ziessel, T. Heiser, P. Lévêque, N. Leclerc, *J. Mater. Chem. C* **2016**, *4*, 4296–4303.

[239] C. Ruiz, E. M. García-Frutos, D. A. da Silva Filho, J. T. López Navarrete, M. C. Ruiz Delgado, B. Gómez-Lor, *J. Phys. Chem. C* **2014**, *118*, 5470–5477.

[240] L. Caliò, S. Kazim, M. Salado, I. Zimmermann, M. K. Nazeeruddin, S. Ahmad, *Sustain. Energy Fuels* **2018**, *2*, 2179–2186.

[241] K. S. Novoselov, V. I. Fal′ko, L. Colombo, P. R. Gellert, M. G. Schwab, K. Kim, *Nature* **2012**, *490*, 192–200.

[242] K. Dirian, M. Á. Herranz, G. Katsukis, J. Malig, L. Rodríguez-Pérez, C. Romero-Nieto, V. Strauss, N. Martín, D. M. Guldi, *Chem. Sci.* **2013**, *4*, 4335–4353.

[243] G. Bottari, M. Á. Herranz, L. Wibmer, M. Volland, L. Rodríguez-Pérez, D. M. Guldi, A. Hirsch, N. Martín, F. D'Souza, T. Torres, *Chem. Soc. Rev.* **2017**, *46*, 4464–4500.

[244] M. F. El-Kady, Y. Shao, R. B. Kaner, *Nat. Rev. Mater.* **2016**, *1*, 16033.

[245] T. Mahmoudi, Y. Wang, Y.-B. Hahn, *Nano Energy* **2018**, *47*, 51–65.

[246] J. M. Fernández-García, P. J. Evans, S. Medina Rivero, I. Fernández, D. García-Fresnadillo, J. Perles, J. Casado, N. Martín, *J. Am. Chem. Soc.* **2018**, *140*, 17188–17196.

[247] J. Urieta-Mora, M. Krug, W. Alex, J. Perles, I. Fernández, A. Molina-Ontoria, D. M. Guldi, N. Martín, *J. Am. Chem. Soc.* **2020**, *142*, 4162–4172.

[248] C. Zhu, Y. Zhao, D. Wang, W.-Y. Sun, Z. Shi, *Sci. Rep.* **2016**, *6*, 33131.

[249] G. Rouillé, M. Steglich, F. Huisken, T. Henning, K. Müllen, J. *Chem. Phys.* **2009**, *131*, 204311.

[250] R. Rieger, K. Müllen, *J. Phys. Org. Chem.* **2010**, *23*, 315–325.

[251] S. Adjokatse, H.-H. Fang, M. A. Loi, *Mater. Today* **2017**, *20*, 413–424.

[252] T. M. Koh, T. Krishnamoorthy, N. Yantara, C. Shi, W. L. Leong, P. P. Boix, A. C. Grimsdale, S. G. Mhaisalkar, N. Mathews, *J. Mater. Chem. A* **2015**, *3*, 14996–15000.

[253] M. Kong, H. Hu, L. Wan, M. Chen, Y. Gan, J. Wang, F. Chen, B. Dong, D. Eder, S. Wang, *RSC Adv.* **2017**, *7*, 35549–35557.

[254] N. J. Jeon, J. H. Noh, Y. C. Kim, W. S. Yang, S. Ryu, S. I. Seok, *Nat. Mater.* **2014**, *13*, 897.

[255] Q. Jiang, Z. Chu, P. Wang, X. Yang, H. Liu, Y. Wang, Z. Yin, J. Wu, X. Zhang, J. You, *Adv. Mater.* **2017**, *29*, 1703852.

[256] J. Zhao, X. Yang, M. Cheng, S. Li, X. Wang, L. Sun, *J. Mater. Chem. A* **2013**, *1*, 2441–2446.

[257] L. Cai, T. Moehl, S.-J. Moon, J.-D. Decoppet, R. Humphry-Baker, Z. Xue, L. Bin, S. M. Zakeeruddin, M. Grätzel, *Org. Lett.* **2014**, *16*, 106–109.

[258] Y. Cao, N. Cai, Y. Wang, R. Li, Y. Yuan, P. Wang, *Phys. Chem. Chem. Phys.* **2012**, *14*, 8282–8286.

[259] H. Muraoka, T. Tanifuji, S. Ogawa, *Chem. Lett.* **2011**, *40*, 964–966.

[260] J. Youn, P.-Y. Huang, Y.-W. Huang, M.-C. Chen, Y.-J. Lin, H. Huang, R. P. Ortiz, C. Stern, M.-C. Chung, C.-Y. Feng, L.-H. Chen, A. Facchetti,

T. J. Marks, *Adv. Funct. Mater.* **2012**, *22*, 48–60.

[261] Y. Liu, Q. Liu, X. Zhang, L. Ai, Y. Wang, R. Peng, Z. Ge, *New J. Chem.* **2013**, *37*, 1189–1194.

[262] X. Guo, S. R. Puniredd, M. Baumgarten, W. Pisula, K. Müllen, *J. Am. Chem. Soc.* **2012**, *134*, 8404–8407.

[263] C. Zhao, L. Xu, Y. Wang, C. Li, H. Wang, *Chinese J. Chem.* **2015**, *33*, 71–78.

[264] J. J. Wolff, F. Gredel, T. Oeser, H. Irngartinger, H. Pritzkow, *Chem. – A Eur. J.* **1999**, *5*, 29–38.

[265] Y. H. Lee, S. Park, J. Oh, J. W. Shin, J. Jung, S. Yoo, M. H. Lee, *ACS Appl. Mater. Interfaces* **2017**, *9*, 24035–24042.

[266] C. Poriel, J. Rault-Berthelot, S. Thiery, C. Quinton, O. Jeannin, U. Biapo, D. Tondelier, B. Geffroy, *Chem. – A Eur. J.* **2016**, *22*, 17930–17935.

[267] M. Sang, S. Cao, J. Yi, J. Huang, W.-Y. Lai, W. Huang, *RSC Adv.* **2016**, *6*, 6266–6275.

[268] J. Hou, M.-H. Park, S. Zhang, Y. Yao, L.-M. Chen, J.-H. Li, Y. Yang, *Macromolecules* **2008**, *41*, 6012–6018.

[269] I. Imae, K. Korai, Y. Ooyama, K. Komaguchi, Y. Harima, *Synth. Met.* **2015**, *207*, 65–71.

[270] G. Garbay, L. Muccioli, E. Pavlopoulou, A. Hanifa, G. Hadziioannou, C. Brochon, E. Cloutet, *Polymer* **2017**, *119*, 274–284.